

THE UNIVERSITY OF MANITOBA

Mid-Infrared Biospectroscopic Analysis
of
Biological Systems
In vitro and In situ

by

Pamela Sharon Bromberg

B.Sc. (University of Western Ontario)1990

A thesis submitted to the FACULTY OF GRADUATE STUDIES

in partial fulfillment of the requirements for the degree of

DOCTOR OF PHILOSOPHY

Department of Chemistry

2002

Winnipeg, Manitoba



National Library
of Canada

Acquisitions and
Bibliographic Services

395 Wellington Street
Ottawa ON K1A 0N4
Canada

Bibliothèque nationale
du Canada

Acquisitions et
services bibliographiques

395, rue Wellington
Ottawa ON K1A 0N4
Canada

Your file Votre référence

Our file Notre référence

The author has granted a non-exclusive licence allowing the National Library of Canada to reproduce, loan, distribute or sell copies of this thesis in microform, paper or electronic formats.

The author retains ownership of the copyright in this thesis. Neither the thesis nor substantial extracts from it may be printed or otherwise reproduced without the author's permission.

L'auteur a accordé une licence non exclusive permettant à la Bibliothèque nationale du Canada de reproduire, prêter, distribuer ou vendre des copies de cette thèse sous la forme de microfiche/film, de reproduction sur papier ou sur format électronique.

L'auteur conserve la propriété du droit d'auteur qui protège cette thèse. Ni la thèse ni des extraits substantiels de celle-ci ne doivent être imprimés ou autrement reproduits sans son autorisation.

0-612-79839-9

Canada

THE UNIVERSITY OF MANITOBA
FACULTY OF GRADUATE STUDIES

COPYRIGHT PERMISSION PAGE

MID-INFRARED BIOSPECTROSCOPIC ANALYSIS OF BIOLOGICAL SYSTEMS
IN VITRO AND IN SITU

BY

PAMELA SHARON BROMBERG

A Thesis/Practicum submitted to the Faculty of Graduate Studies of The University
of Manitoba in partial fulfillment of the requirements of the degree
of
Doctor of Philosophy

PAMELA SHARON BROMBERG © 2002

Permission has been granted to the Library of The University of Manitoba to lend or sell copies of this thesis/practicum, to the National Library of Canada to microfilm this thesis and to lend or sell copies of the film, and to University Microfilm Inc. to publish an abstract of this thesis/practicum.

The author reserves other publication rights, and neither this thesis/practicum nor extensive extracts from it may be printed or otherwise reproduced without the author's written permission.

“It is an important and popular fact that things are not always what they seem. For instance, on the planet Earth, man had always assumed that he was more intelligent than dolphins because he had achieved so much - the wheel, New York, wars and so on - whilst all the dolphins had ever done was muck about in the water having a good time. But conversely, the dolphins had always believed that they were far more intelligent than man - for precisely the same reasons.

Curiously enough, the dolphins had long known of the impending destruction of the planet Earth and had made many attempts to alert mankind to the danger; but most of their communications were misinterpreted as amusing attempts to punch footballs or whistle for tidbits, so they eventually gave up and left Earth by their own means before the Vogans arrived.

The last ever dolphin message was misinterpreted as a surprisingly sophisticated attempt to do a double-backwards-somersault through a hoop whilst whistling the ‘Star Spangled Banner’, but in fact the message was this: *So long, and thanks for all the fish.*

In fact there was only one species on the planet more intelligent than dolphins, and they spent a lot of their time in behavioral research laboratories running round inside wheels and conducting frighteningly elegant and subtle experiments on man. The fact that once again man completely misinterpreted this relationship was entirely according to these creatures’ plans.”

Douglas Adams, 1979

Acknowledgements

Foremost I would like to express my gratitude to my PhD thesis advisor Dr. H Duckworth (Head, Department of Chemistry, University of Manitoba) for support and encouragement, especially when I relocated to New York to begin a postdoctoral position, prior to my PhD dissertation. I would also like to thank the other members of my thesis advisory committee, Dr. J. O'Neil (Professor, Department of Chemistry, University of Manitoba), Dr. A. Secco (Head, Faculty of Graduate Studies and Professor, Department of Chemistry, University of Manitoba) and Dr. E. Worobec (Professor, Department of Microbiology, University of Manitoba), for their time, suggestions regarding my research and for carefully going over my written thesis. Finally, wholehearted appreciation is expressed to my external examiner, Dr. A. Shaw (Senior Research Associate, Molecular Spectroscopy Group, Institute for Biodiagnostics, NRCC, Winnipeg, Manitoba) for promptly assessing my thesis, taking the time to give me assistance with my final corrections and encouragement.

Sincere appreciation is expressed towards the Molecular Spectroscopy Group (Dr. H.H. Mantsch, Dr. M.J. Jackson, Dr. C. Schultz, Dr. K-Z. Liu and J. Mansfield) at the Institute for Biodiagnostics, NRCC, Winnipeg, Manitoba, for access to ample instrumentation and data processing software during the first two years of my research and advisement in IR biospectroscopy. Special thanks to Dr. R. Julian (SRC, Stoughton, WI) and Dr. L Miller (NSLS, BNL, Upton NY) for synchrotron beamtime training, support and enthusiasm towards my research. Heartfelt thanks also go to Dr. G.P. Williams (Jefferson Labs, VA, USA) and Dr. P. Dumas (LURE, Paris, France) for advice, stimulating conversations on molecular spectroscopy and synchrotron science and encouragement.

I would like to thank the generosity of my collaborators: Dr. M.A. Moscarello (Biochemistry Division, Hospital for Sick Children, Toronto, ON) for supplying me with the charge isoforms of myelin basic protein, Dr. I.M.C. Dixon (Institute of Cardiovascular Sciences, St. Boniface General Research Centre, Winnipeg, MB) for advisement in cardiomyopathy and for donating the hamster heart tissue for my tissue research and Dr. M.R. del Bigio (Department of Pathology, Health Sciences Research Centre, Winnipeg, MB) for

patiently going over the morphology and AD pathology of the hippocampus, tissue staining and photography and for enthusiasm towards my research.

I would also like to express my appreciation for financial support to: The Manitoba Health Research Council for their Postgraduate Fellowship (1999/2000), the University of Manitoba for the Duff Roblin Graduate Fellowships (1997/1998 and 1998/1999) and the Gordon P. Oslar Graduate Scholarship (1997/1998), and the Faculty of Science for the Dean of Science Graduate Award (1996).

Thanks to the many graduate students I have had the privilege of knowing throughout my years at the Chemistry Department for stimulating conversations (especially at IQs!) and for their support. Special thanks to the members of "Chemistry Climbing Club" for their kindness and for trusting me to set up anchors in times of stress just so that we could all enjoy the Whiteshell from a different perspective.

Ultimately, I would like express my utmost gratitude to my parents, Esther and Lester Glantz, for their patience, understanding and for going that extra mile to bring me care packages containing my Mom's "Norwegian Oatmeal Cookies" in times of desperate need.

Table of Contents

1/ INTRODUCTION.....	1
1.1 FTIR BIOSPECTROSCOPY	1
1.1.1 Chapter overview	1
1.1.2 FTIR spectroscopy, an absorption phenomenon	2
1.1.3 FTIR spectroscopy of biological molecules <i>in vitro</i> and <i>in situ</i>	3
1.2 INSTRUMENTATION AND SAMPLING TECHNIQUES	5
1.2.1 Conventional FTIR spectrometer.....	5
1.2.2 The sample cell for conventional transmission FTIR biospectroscopy.....	7
1.2.3 The attenuated total reflectance accessory for FTIR biospectroscopy	8
1.2.4 The microscope accessory for FTIR microspectroscopy	11
1.2.5 Synchrotron radiation as the source of the IR radiation	12
1.3 SAMPLE PREPARATION	13
1.3.1 Preparation of biological samples in solution for <i>in vitro</i> studies	14
1.3.2 Preparation of dried films for <i>in vitro</i> and <i>in situ</i> studies	17
1.3.3 Preparation of tissue for biological studies <i>in situ</i>	18
1.4 SPECTRAL PROCESSING AND PREPROCESSING	19
1.4.1 Conversion from the Fourier domain to the frequency domain	21
1.4.2 Spectral resolution	23
1.4.3 Spectral noise and apodization of the interferogram	23
1.4.4 Common approaches used in spectral preprocessing to improve spectral quality	24
1.4.5 Band narrowing techniques used to amplify spectral information	26
1.4.6 Non-subjective data reduction techniques	31

1.5 SPECTRAL FEATURES OF TISSUE COMPONENTS <i>IN VITRO</i>	33
1.5.1 Characteristic absorptions of proteins	33
1.5.2 Characteristic absorptions of lipids	40
1.5.3 Characteristic absorptions of nucleic acids	47
1.5.4 Characteristic absorptions of carbohydrates	50
1.6 ANALYSIS OF TISSUES COMPONENTS <i>IN SITU</i>	51
1.7 DATA ANALYSIS	58
1.7.1 Partial least squares analysis for quantitative interpretation of data	59
1.7.2 Structural analysis	60
1.7.3 Multivariate statistical analysis applicable to <i>in situ</i> studies	63
1.7.4 Multidimensional analysis for <i>in situ</i> microspectroscopic studies	64
1.8 OVERVIEW OF THESIS	67
1.9 REFERENCES	72
2/ FTIR SPECTROSCOPIC INVESTIGATION <i>IN VITRO</i>: INTERACTION OF MYELIN BASIC PROTEIN CHARGE ISOFORMS WITH MODEL LIPID SYSTEMS	77
2.1 INTRODUCTION	77
2.1.1 Chapter overview	77
2.1.2 The role of MBP in the myelin sheath of the CNS	81
2.1.3 Studies of the interactions of MBP with model lipid systems	83
2.1.4 Charge isoforms of myelin basic protein	87
2.1.5 Studies of the interactions of MBP charge isoforms with model lipid systems	91
2.1.6 Objectives of the current study	96

2.2 . MATERIALS AND METHODS	98
2.2.1 Materials	98
2.2.2 Sample preparation	99
2.2.3 FTIR spectroscopy	101
2.2.4 Spectral preprocessing and analysis of data	104
2.3 RESULTS AND DISCUSSION	106
2.3.1 The phase behavior of the pure lipid systems	107
2.3.2 The effect of MBP on liposomes of zero surface charge density	115
2.3.3 The effect of MBP on liposomes of negative surface charge density	122
2.3.4 The effect of MBP on liposomes of varied net-negative surface charge density	132
2.3.5 Conformation of MBP charge isoforms in aqueous solution	145
2.3.6 Conformation of MBP charge isoforms upon interaction with neutral lipids	151
2.3.7 Conformation of MBP charge isoforms upon interaction with acidic lipids.....	156
2.3.8 Conformation of MBP isoforms upon interaction with liposomes of altered SCD.....	165
2.4 CONCLUSIONS	174
2.5 REFERENCES	186

3/ COLLAGEN REMODELING IN THE CARDIAC EXTRACELLULAR MATRIX OF THE CARDIOMYOPATHIC SYRIAN HAMSTER AS ASSESSED BY ATR-FTIR.....	191
3.1 INTRODUCTION	191
3.1.1 Chapter Overview	191
3.1.2 Congestive cardiomyopathy	193
3.1.3 The mid-IR fingerprint of fibrous collagens	193
3.1.4 The cardiomyopathic hamster	194
3.1.5 Global data analysis	195
3.1.6 Objectives of the current study	195
3.2 EXPERIMENTAL	196
3.2.1 Materials	196
3.2.2 FTIR-ATR spectroscopy and spectral preprocessing	196
3.2.3 Data analysis	197
3.2.4 Data reduction and LDA	198
3.3 RESULTS AND DISCUSSION	199
3.3.1 Class average spectra, difference spectra and LDA	199
3.3.2 Comparison of the control ventricular tissue	202
3.3.3 Comparison of cardiomyopathic ventricular tissue	205
3.3.4 Collagen remodeling in the right ventricle	207
3.3.5 Collagen remodeling in the left ventricle	210
3.4 CONCLUSIONS	214
3.5 REFERENCES	216

4/ PATHOPHYSIOLOGICAL CHANGES IN ALZHEIMER'S DISEASED HIPPOCAMPUS IMAGED BY SYNCHROTRON FTIR MICROSPECTROSCOPY.....	219
4.1 INTRODUCTION	219
4.1.1 Chapter Overview	219
4.1.2 Alzheimer's Disease	221
4.1.3 Synchrotron FTIR microspectroscopy of the AD and control hippocampus	225
4.1.4 Objectives of current study	226
4.2 MATERIALS AND METHOD	227
4.2.1 Synchrotron FTIR microspectroscopy at the SRC beamline	228
4.2.2 Synchrotron FTIR microscopy at beamline U10B at the NSLS	231
4.2.3 Spectral preprocessing and data analysis	233
4.3 RESULTS AND DISCUSSION	233
4.3.1 FTIR microspectroscopic imaging of control hippocampal tissue ...	234
4.3.2 FTIR imaging of amyloid angiopathy in the AD hippocampus	241
4.3.3 FTIR imaging of diffuse and mature neuritic plaques in the AD hippocampus	248
4.3.4 Detection of Aβ in tissue by FTIR when staining was inconclusive or between plaque regions	274
4.4 CONCLUSIONS	284
4.5 REFERENCES	286
5/ CONCLUDING REMARKS.....	290

List of Figures

Figure 1-1. Simple layout for a conventional FTIR spectrometer.	6
Figure 1-2. Demountable IR cell for liquid studies.....	8
Figure 1-3. The Harrick Scientific SplitPea TM used for ATR-FTIR.....	9
Figure 1-4. The evanescent wave produced in total internal reflection	10
Figure 1-5. Nicolet IR Plan Advantage TM microscope for FTIR microspectroscopy	11
Figure 1-6. Water vapor spectrum with a nominal spectral resolution of 2 cm ⁻¹ ...	16
Figure 1-7. Interconversion between the frequency and Fourier domain	22
Figure 1-8. Fourier self-deconvolution of an IR band	28
Figure 1-9. Second-order derivation of a Lorentzian line.....	30
Figure 1-10. Generalized structure of a phospholipid molecule and organization of amphipathic phospholipids into a bilayer structure.....	41
Figure 1-11. Gel to liquid crystalline phase transition of a phospholipid.	42
Figure 1-12. The DPPG phase transition monitored by the symmetric and asymmetric methylene stretch	44
Figure 1-13. Assignment of IR bands to white matter constituents <i>in situ</i>	54
Figure 2-1. The myelin sheath of the CNS showing the extended oligodendroglial membrane concentrically wrapped around a neuronal axon.....	82
Figure 2-2. Relative positions of myelin basic protein (MBP) at the major dense line and proteolipid protein (PLP) at the intraperiod line of compact myelin.....	83
Figure 2-3. Amino acid sequence of unmodified human and bovine MBP	89
Figure 2-4. Spectral comparison of the amide I band profile of human MBP-C3 when introduced into a liposomal system or when lipid is added directly to the protein/buffer solution to form liposomes	100

Figure 2-5. Calibration of the thermocouple used in the temperature-ramped studies to the waterbath temperature.....	102
Figure 2-6. Boltzmann sigmoidal function used to discern the midpoint of a lipid phase transition.....	108
Figure 2-7. The increase in bilayer hydration upon the gel to $L\alpha$ phase transition as observed by the change in the lipid acyl C=O stretching profile....	109
Figure 2-8. Comparison of the length of the melting interval for d-PC and PG in the 1PG:3d-PC liposomal mixture.....	114
Figure 2-9. Influence of protein interaction on acyl C=O stretch of d-PC.....	118
Figure 2-10. The influence of MBP interaction on the PG acyl C=O band profile.....	127
Figure 2-11. Amide I absorption profile of MBP-C2 at various temperatures.....	149
Figure 2-12. Comparison of the relative intensity of the amide I to the arginine side chain absorption for MBP-C2 and MBP-C8 at 31°C.....	150
Figure 2-13. Amide I band profile of MBP-C2 and MBP-C8 above and below the T_m of d-PC.....	153
Figure 2-14. Comparison of the amide I band profile of MBP-C1-C3, C5 and C8 in aqueous and PG liposomal environments at 55°C.....	160
Figure 2-15. The amide I profile of MBP-C8 in the presence of PG illustrating the gradual gain in α-helical structure with concomitant loss in random coil structure as temperature and the bilayer fluidity increased.....	161
Figure 3-1. Comparison of the class average spectra from the left and right ventricles of the control animals.....	203
Figure 3-2. Comparison of the class average spectra from the left and right ventricles of the CMP animals.....	206
Figure 3-3. Spectral comparison of control and CMP right ventricular tissue indicative of decreased collagen deposition in RV(CMP).....	209
Figure 3-4. Schematic diagram illustrating the difference ventricular collagen content in the CMP and the CON hearts.....	210

Figure 3-5. Spectral comparison of the control and CMP left ventricular tissue indicative of increased collagen deposition in LV(CMP).....	211
Figure 4-1. Schematic illustration of a transverse section of the hippocampus....	222
Figure 4-2. Formation of a mature neuritic plaque with a dense β-amyloid core from diffuse plaque composed of Aβ peptide.	224
Figure 4-3. Schematic representation of a neuron from perikaryon to synapse illustrating the role of microtubule assemblies (and tau) in fast axonal transport mechanisms.....	225
Figure 4-4. Thin tissue section from Alzheimer's hippocampus AD1 on MirrIR slide compared to stained serial section.....	230
Figure 4-5. Photomicrographs of the AD3 tissue section on the MirrIR slide examined spectroscopically prior to and after staining	232
Figure 4-6. Comparison of the mid-IR signature of pyramidal neurons from the CA1, CA2 and CA4 fields to the dentate neuron of the granular layer of the dentate gyrus illustrating the similar lipid to protein ratio	235
Figure 4-7. Comparison of spectra taken of a CA4 pyramidal neuron, the moleculare, radiatum and white matter of the control hippocampal tissue.	236
Figure 4-8. FTIR images of control hippocampus tissue section compared to light microscopy photographs	238
Figure 4-9. The relative contribution of lipid to protein in a CA4 field pyramidal neuron and surrounding neuropil (6 μm spatial resolution).....	240
Figure 4-10. Relative contribution of nucleic acid to protein in CA4 pyramidal neuron in Figure 4-9.....	241
Figure 4-11. Diffuse Aβ peptide deposition peripheral to a blood vessel in AD1..	242
Figure 4-12. Spectral comparison of a focal spectrum taken upon the CA1 blood vessel and that taken on a portion of the diffuse plaque about the vessel periphery	243
Figure 4-13. Detection of β-amyloid angiopathy in CA4 field of hippocampus AD3	245

Figure 4-14. Spectral changes along a blood vessel in AD3 for discrimination of fibrillar amyloid from amorphous deposits of Aβ peptide.....	247
Figure 4-15. FTIR images representative of fibrillar and diffuse amyloid deposition in the CA4 field of hippocampus AD3.....	250
Figure 4-16. Representative spectra of fibrillar amyloid deposits in CA4 field of hippocampus AD3.....	252
Figure 4-17. FTIR image of the CA4 field map presented in Figure 4-15 using an alternative relative intensity profile of the $\nu_s(\text{COO}^-)$ at 1400 cm^{-1} to the $\delta_{\text{as}}(\text{CH}_3)$ at 1455 cm^{-1}.....	255
Figure 4-18. General location of spectral maps 1-9 obtained in the molecule region of hippocampus AD2.....	257
Figure 4-19. Photomicrographs of the unstained and stained region in the molecule where AD2 maps 1 to 6 were collected.	258
Figure 4-20. FTIR imaging of five neighboring tissue areas in the molecule of hippocampus AD2.....	259
Figure 4-21. Representative spectra from the AD2 molecule.....	261
Figure 4-22. Comparison of the phosphomonoester asymmetric stretch, $\nu_{\text{as}}(\text{P-O-C})$, for phosphoserine (967 cm^{-1}), phosphotyrosine (978 cm^{-1}) and phosphothreonine (975 and 952 cm^{-1}).....	264
Figure 4-23. FTIR imaging of two neighboring tissue areas in the molecule and dentate neurons of AD2.....	266
Figure 4-24. Representative spectra from the granular layer of the dentate gyrus accompanied by amyloid deposition in hippocampus AD3.....	267
Figure 4-25. Photomicrographs of the CA1 region examined in hippocampus AD2 unstained and stained.....	268
Figure 4-26. FTIR imaging of a plaque-infested area in the CA1 field of hippocampus AD2.....	269
Figure 4-27. AD2 overview of CA4 field examined, stained and unstained.....	271
Figure 4-28. FTIR imaging in the CA4 field, close to the dentate gyrus of hippocampus AD2.....	272

Figure 4-29. Representative spectra of amyloid deposition in the CA4 field close to the dentate gyrus of hippocampus AD2	273
Figure 4-30. FTIR imaging of diffuse Aβ-deposition in the CA4 field of hippocampus AD2	274
Figure 4-31. Diffuse amyloid deposition detected in the molecule of hippocampus AD3 where staining was inconclusive	276
Figure 4-32. Diffuse amyloid deposition detected in CA4 of hippocampus AD3 where staining was inconclusive	277
Figure 4-33. FTIR imaging of small spectral maps acquired in the CA1 field of AD1 that shows diffuse amyloid deposition that went unrecognized by the staining technique	279
Figure 4-34. FTIR imaging of control hippocampus (CON2) in the CA1 field to delineate the contribution of β-sheet protein to a normal aging hippocampus	280
Figure 4-35. FTIR imaging of control hippocampus (CON1) in the CA1 field to delineate the contribution of β-sheet protein to a normal aging hippocampus	281
Figure 4-36. Abnormal neurons revealed by FTIR imaging in the CA1 field of control hippocampus CON1	283

List of Tables

Table 1-1. Sampling techniques used for mid-infrared biospectroscopy	13
Table 1-2. IR bands due to H ₂ O, D ₂ O and HOD	15
Table 1-3. Literature assignment of components bands of the amide I band profile	36
Table 1-4. Literature values for amino acid side chain absorptions at neutral pD	39
Table 1-5. Characteristic regions in the mid-IR where phospholipids absorb	43
Table 1-6. Example of some IR “marker bands” for distinction of A-, B- and Z-DNA conformers.	49
Table 1-7. Mid-IR spectral subregions frequently used for simultaneous observation of tissue constituents <i>in situ</i>	52
Table 2-1. The relative net-positive charge in the C-terminal and N-terminal half of the MBP isoforms.....	90
Table 2-2. The percent saturation of liposomal negative SCD by each MBP isoform	101
Table 2-3. Comparison of cell temperature at five or ten minutes equilibration time.....	103
Table 2-4. Phase transition temperatures of PG and d-PC in liposomes of varied PG:d-PC composition.	110
Table 2-5. Comparison of the gel and L α state frequency (proportional to energy) for PG and d-PC in the liposomal preparations.	111
Table 2-6. The effect of MBP isoform interaction on T _m (d-PC).	116
Table 2-7. The effect of MBP charge isoforms on d-PC acyl chain order as assessed by the methylene symmetric stretching vibration.....	117
Table 2-8. Influence of MBP on the relative contributions of the H-bonded and free acyl C=O stretch to the acyl C=O stretching profile of d-PC in the L α state (31°C).....	119
Table 2-9. The effect of MBP interaction on the phase transition temperature of PG	123

Table 2-10. The effect of MBP charge isoforms on PG acyl chain order as assessed by the frequency of methylene asymmetric stretching vibration.....	124
Table 2-11. Influence of MBP on the PG acyl band contour in the gel (31°C) and liquid crystalline state (55°C)	125
Table 2-12. Influence of MBP on the relative contributions of the H-bonded and free acyl C=O stretch of PG in the Lα state (55°C).....	126
Table 2-13. The influence of PG on MBP interaction with d-PC in liposomes of various surface charge density	133
Table 2-14. The effect of MBP interaction on T_m(PG) in liposomes of various SCD.....	134
Table 2-15. Acyl chain order of d-PC and PG in the presence of MBP-C1-C3, C5 and C8 for liposomal mixture 3PG:1d-PC	137
Table 2-16. Acyl chain order of d-PC and PG in the presence of MBP-C1-C3, C5 and C8 for liposomal mixture 1PG:1d-PC	138
Table 2-17. Acyl chain order of d-PC and PG in the presence of MBP-C1-C3, C5 and C8 for liposomal mixture 1PG:3d-PC	138
Table 2-18. Temperature dependence of MBP isoform conformation in aqueous solution as determined by the amide I vibration and side chain absorptions.....	147
Table 2-19. The amide I profiles and arginine side chain absorptions of MBP isoforms in the presence of d-PC	152
Table 2-20. Amide I profiles and amino acid side chain absorptions of MBP isoforms in the presence of PG	157
Table 2-21. Amide I band profile of MBP isoforms in 1PG:3d-PC liposomal environment.....	167
Table 2-22. Amide I band profile of MBP isoforms in 1PG:1d-PC liposomal environment.....	171
Table 2-23. Amide I band profile of MBP isoforms in 3PG:1d-PC liposomal environment.....	173
Table 3-1. LDA of control and cardiomyopathic heart tissue using manually spliced spectral subregions.....	200

**Table 3-2. Genetic algorithm-selected spectral subregions that lead to
nonsubjective classification of the heart tissue.....201**

Table 4-1. Hippocampal samples evaluated during doctoral thesis228

Table 4-2. Regions of interest in the hippocampal samples studied at the SRC ...229

Table 4-3. Regions of interest in the hippocampal samples studied at the NSLS .233

ABSTRACT

Fourier transform mid-infrared (FTIR) biospectroscopy, is a versatile analytical tool applicable to studies in biophysics and medicine; if there is a biophysical or biochemical changes within or between specimen(s), structural information can be derived from the spectra data that is difficult or impossible to obtain by another technique. Three independent biological systems were each explored using a different FTIR sampling technique and approach to data analysis. Transmission FTIR was used for an *in vitro* biophysical study of protein-lipid dynamics and interactions. Spectral interpretation provided information on the prevailing interactions between charge isoforms of myelin basic protein (MBP) and liposomes of various net-negative surface charge density (SCD) chosen as simple models for the paranodal and compact myelin membrane. Certain post-translational modifications (*i.e.*, deamidation, phosphorylation and citrullination) alter the net-positive charge of MBP, and excessive MBP charge modification has been thought to be in part responsible for the degradation of the myelin sheath in multiple sclerosis. MBP-mediated adhesion of acidic bilayers (via electrostatic and intercalative interactions), as assessed by the conformational dynamics of the lipid(s) and protein, appeared to be dependent on the saturation of the liposomal negative SCD by the number of positively charged residues on the isoform, rather than by merely MBP net-positive charge. MBP charge modification, especially reduced multivalency of positive charge, was found to have a greater impact on MBP-mediated adhesion of paranodal myelin-like membranes than compact myelin-like membranes. A second project involved the discrimination of cardiomyopathic (CMP) from normal heart tissue using multivariate analysis (LDA) of tissue spectra measured by attenuated total reflectance (ATR) FTIR on the macroscopic level. Left and right ventricular (LV and RV) tissue were sampled from CMP hamsters, known to have pronounced collagen deposition in the LV. Various sets of optimal spectral subregions for LDA classification were chosen by both manual selection and a genetic algorithm. All groups under comparison could be differentiated from one another based on the presence/absence of the mid-IR collagen fingerprint. The relative collagen content within each class was gauged by the spectral differences between class average spectra. The study confirmed that LV collagen increased in the response to the disease but also found that RV collagen decreased. The final project used synchrotron FTIR microspectroscopy to detect the biochemical changes that occur in the Alzheimer's diseased (AD) hippocampus *in situ*. Little is known about the progressive generation of β -amyloid plaques and neurofibrillary tangles in the AD hippocampus. Histochemistry suggests amorphous plaques mature into neuritic plaques with fibrillar amyloid in the core. However, there is conflicting data regarding the quaternary arrangement of the A β -peptide aggregates in diffuse and fibrillar β -amyloid. FTIR images were obtained and visually compared to photomicrographs of the stained tissue. Spectroscopic analysis

revealed that fibrillar amyloid *in situ* was high in aggregate structure while amorphous A β -peptide deposition *in situ* was high in β -sheet structure. Tissue staining correlated with the location of fibrillar amyloid within neurons and regions containing diffuse amorphous plaques. Showing a sensitivity greater than that of conventional histochemistry, FTIR imaging was sensitive enough to detect A β -peptide deposition in regions of AD gray matter at levels approximately 10-20% higher than that in control tissue.

ABBREVIATIONS

Aβ	β -amyloid peptide	MBP	myelin basic protein
AD	Alzheimer's Disease	MCA	multiple component analysis
α	α -helix structure	MCT	mercury-cadmium-telluride detector
AGE	advanced glycation end products	MDL	major dense line
Arg	arginine	mEV	milli-electron volts
Asn	asparagine	mid-IR	mid-infrared
Asp	aspartic acid	MirrIR	Kevley technology reflective slide
ATR	attenuated total reflectance	MS	Multiple Sclerosis
β	β -sheet structure	<i>n</i>	refractive index
βAPP	β -amyloid precursor protein	NFT	neurofibrillary tangle
BNL	Brookhaven National Laboratory, Upton, NY	NMR	nuclear magnetic resonance
C-104	C-terminal fragment of β APP	NSLS	National Synchrotron Light Source, BNL
CCM	idiopathic congestive cardiomyopathy	OCT	Optimal Cutting Temperature Compound
CD	circular dichroism	PA	phosphatidic acid
CHF	chronic heart failure	PC	phosphatidylcholine
CMP	cardiomyopathic	PDMS	polydimethylsiloxane
CNS	central nervous system	PE	phosphatidylethanolamine
CON	control or normal	PG	phosphatidylglycerol
DMP	dimyristoylphosphatidylcholine	PHF	paired helical filaments
C			
DNA	deoxyribonucleic acid	PI	phosphatidylinositol
d_p	penetration depth	PLP	proteolipid protein
d-PC	per-deuterated phosphatidylcholine	PLS	Partial least squares regression
DPPG	dipalmitoylphosphatidylglycerol	Pro	Proline
ECM	extracellular matrix	PS	phosphatidylserine
ESR	electron spin resonance	pSer	phosphoserine
FD	Fourier derivation	pThr	phosphothreonine

FPA	focal plane array	pTyr	phosphotyrosine
FSD	Fourier self-deconvolution	rc	random coil structure
FT	Fourier transform	RAGE	receptor for advanced glycation end products
FTIR	Fourier transform infrared spectroscopy	RNA	ribonucleic acid
GA	genetic algorithm	RV	right ventricle
GAGs	glycosaminoglycans	SCD	surface charge density
Gln	glutamine	Ser	Serine
Glu	glutamic acid	S/N	signal-to-noise
Gly	glycine	SRC	Synchrotron Radiation Center, Stoughton, WI
IPL	intraproton line	t	turn structure
IR	infrared	TEM	transmission electron microscopy
Lα	liquid crystalline state	Thr	Threonine
LDA	linear discriminant analysis	T_m	lipid phase transition temperature
LV	left ventricle	Tyr	Tyrosine
MAP	microtubule-associated protein	U10B	Beamline U10B at NSLS

1 INTRODUCTION

1.1 FTIR BIOSPECTROSCOPY

1.1.1 Chapter overview

Although many spectroscopic methods are available to investigate biological systems, there are numerous advantages in the application of Fourier transform mid-infrared (FTIR) biospectroscopy in biophysical, structural biology and medical research. In contrast to other analytical spectroscopies useful in biology (circular dichroism, optical dichroism, NMR and x-ray crystallography), different FTIR techniques can be used to examine biological samples in any state (*i.e.*, solution, film, solid) on a macroscopic or microscopic scale. Moreover, FTIR can be easily applied to model systems prepared *in vitro* or extracted cells and tissues for *in situ* investigations without the need of internal probes that may compromise the integrity of the sample. Finally, an FTIR spectrum can be collected very quickly (1-2 minutes) on very little sample (μg quantities), the instruments and attachments are rather inexpensive and little technical expertise is required to operate the commercially available spectrometers. However, in spite of its versatility, FTIR biospectroscopy is still somewhat in its infancy and is not yet a commonplace analytical technique used to study biological samples due to the complexity and/or ambiguity of spectral interpretation. For example, in contrast to the rather straightforward analysis of functional group vibrations of simple molecules, biological spectra appear comparatively featureless due to the extensive overlap of numerous vibrations from macromolecules and macromolecular mixtures. However, this decreased resolution of absorptions in mid-IR spectra of biological samples does not imply that pertinent information cannot be obtained from the spectral data. For nearly two decades FTIR biospectroscopists have developed numerous methodologies to deconvolute the massive amounts of information in the mid-IR spectra of biological macromolecules, cells and tissues.

Several recent reviews have been written on FTIR spectroscopy in medicine (Jackson and Mantsch, 1996; Jackson *et al.*, 1997) and on biological macromolecules (Case and Mantsch, 1984; Mendelson and Mantsch, 1986; Mantsch and McElhaney, 1991; Taillandier and Liquier, 1992; Surewitz *et al.*, 1993; Jackson and Mantsch, 1995; Haris and Chapman,

1995). The aim of this introductory chapter is to familiarize the reader with the basics behind the mid-IR absorption phenomenon (section 1.1.2), the benefits and limitations of FTIR biospectroscopy (section 1.1.3), instrumentation and sampling techniques (sections 1.2), sample preparation (section 1.3), preparation of spectra for interpretation (section 1.4), spectral features of biological macromolecules *in vitro* and *in situ* (sections 1.5 and 1.6), and approaches used for global analysis of the data (section 1.7). Finally, at the end of this chapter, the reader will find an overview to the thesis (section 1.8). In this doctoral thesis, FTIR has been applied to three independent projects to further exemplify the utility of FTIR as a sole analytical method, capable of providing unique information on biological systems studied *in vitro* and *in situ*.

1.1.2 FTIR spectroscopy, an absorption phenomenon

When a molecule is irradiated with light of the mid-IR region ($400\text{-}4000\text{ cm}^{-1}$) of the electromagnetic spectrum, the energy from the incident radiation is transferred to the molecule. Energy transference results in excitation from the ground vibrational state to the first excited vibrational state of all or some of the molecular normal modes of vibration. For non-linear molecules, there are $(3N-6)$ normal modes of vibration or fundamental vibrations, N being the number of atoms. In these normal modes, the internuclear bond distances and bond angles change at some natural frequency of the molecule, while the centre of gravity of the molecule remains stationary (for review see Lambert et al., 1987). For a molecule to absorb IR radiation as vibrational excitation energy, there must be a change in the direction or magnitude of the dipole moment of the molecule during that particular vibration (for review see Drago, 1992). The oscillating dipole can interact with the oscillating electric field component of the IR radiation, giving rise to an absorption of radiation at the frequency of the normal mode vibration. In simple molecules (*i.e.*, one functional group) with a center of symmetry (*i.e.*, CO_2), vibrations that do not change the dipole moment of the molecule are not IR-active. For example, in the mid-IR spectrum of CO_2 , the asymmetric stretch can be observed while the symmetric stretch is absent. For more complex molecules the term “group frequencies” is used to refer to the energy absorbed by the individual functional groups (*i.e.*, $\text{C}=\text{O}$, CH_2 , CH_3 , $\text{C}-\text{OH}$, etc.) present in the molecule which experience vibrational excitation at different wavelengths. Initial inspection of the IR spectra of

simple molecules generally involves the assignment of the various bond stretching and deformation vibrations due to the presence of a particular functional group. Clearly, the larger the molecule, the greater the number of atoms and the greater the number of fundamental vibrational modes ($3N-6$). Moreover, the less symmetry a molecule possesses the greater the number of IR-active bands in the mid-IR spectrum (see Lambert *et al.*, 1987). Thus, it is not surprising that in complex biological macromolecules nearly all the modes are IR-active to some extent. However, the asymmetric vibrational mode of a particular functional group (*i.e.*, CH_2 stretching) may be more IR-active than the symmetric vibrational mode and thus higher in relative intensity in the spectrum. Finally, the time scale of the IR experiment (10^{-12} s) is fast enough to yield information on the conformational state of the molecule; the spectra do not experience time scale averaging due to molecular anisotropy (Haris and Chapman, 1995). Environmental effects on the vibrating groups, such as hydrogen bonding, electrostatic association, steric effects, physical state and solvent will change the frequency, bandwidth and intensity of the absorption band (see Lambert *et al.*, 1987). Therefore, the overall absorption band will be a superposition of absorptions from each conformation and thus dependent upon the ratio of conformers present in the sample. However, due to the large number of atoms in macromolecules and their conformational flexibility, the mid-IR spectrum consists of many overlapping absorptions. An absorption band can be assigned to a functional group vibration from the frequency of the band maximum, while conformational information can be extracted from the overall shape of the band contour or profile.

1.1.3 FTIR spectroscopy of biological molecules *in vitro* and *in situ*

The complexity of IR spectra further increases when the common biological macromolecules (proteins, lipids, carbohydrates or nucleic acids) are studied in combination *in vitro*, since each component contributes its own spectrum, and interactions between components cause further changes. That is, intermolecular interactions frequently alter the frequency of a vibration if the microenvironment proximal to the vibrating group has changed (Lambert *et al.*, 1987; Jackson and Mantsch, 1991*b*, 1995; Troullier *et al.*, 2000). For example, an external dipole (*i.e.*, H-bond, salt-bridge, polar solvent) near a vibrating group may extract electron density from the group, allowing the vibration to occur at lower frequency

(*i.e.*, less energy is required). The spectral complexity is further amplified when one studies the mixtures of the biological molecules *in situ*, such as in cells and tissue.

Despite the complexity of the data, IR biospectroscopic analysis can provide simultaneous information on proteins, lipids, carbohydrates and nucleic acids isolated or in their native environments (*i.e.*, cells and tissues). This offers several advantages over other analytical techniques. Spectra of these macromolecules can be acquired in a variety of environments such as aqueous solutions, organic solvents, lipid dispersions, solid state and in tissue. However, care should be taken that the chosen environment is an adequate model for the native environment of the macromolecule. That is, the chosen environment should not induce a conformational change in the macromolecule that is not physiologically relevant (see section 1.3). In the study of macromolecules *in situ*, IR spectroscopy offers advantages over standard biochemical assays used in clinical chemistry and pathology laboratories, because homogenization of the sample is not required and expensive histochemical staining reagents for analysis of components are not utilized, respectively (Jackson *et al.*, 1997). Furthermore, a size limitation on the molecule(s) to be examined does not exist as it does in nuclear magnetic resonance (NMR) spectroscopy, nor do light scattering artifacts associated with turbidity of the sample occur as seen in circular dichroism (CD) spectroscopy (Haris and Chapman, 1995). Therefore, sample mixtures of any combination of molecular weights can be studied, provided that the molecules absorb in different subregions of the mid-IR, even when the preparation has decreased optical transparency. External probe molecules are not required to obtain spectroscopic data as they are in electron spin resonance (ESR) spectroscopy, so samples can be examined without introducing artifacts from contaminants (Haris and Chapman, 1995). Moreover, spectral complexity that arises from time scale averaging of anisotropic motions does not occur as IR is a faster experiment (10^{-12} sec.) in comparison to NMR (10^{-5} sec.) and ESR (10^{-8} sec.). Sample preparation is effortless in comparison to other spectroscopic techniques such as x-ray crystallography where optimal crystallizing conditions can be difficult to delineate as well as time-consuming. Finally, in contrast to other spectroscopic techniques, IR spectroscopy is relatively fast in terms of accumulation and analysis of data while the instrumentation is not nearly as expensive (Haris and Chapman, 1995).

Although FTIR offers several advantages over other analytical techniques, it is equally important to acknowledge the limitations. In contrast to the three dimensional structures at atomic resolution that NMR and x-ray crystallographic techniques can provide and the low resolution three-dimensional structures that can be obtained with transmission electron microscopy, FTIR data cannot be used to delineate a three-dimensional structure of the macromolecule. Moreover, the extensive overlap observed in spectra of macromolecules, cells and tissues, can frequently be troublesome, resulting in a loss of information. Finally, in FTIR studies of intermolecular interactions, isotopic substitution of one of the molecules may be required when the interacting molecules have functional groups that absorb in the same region (*i.e.*, two lipids, two proteins, a protein and a substrate with an amide group). Isotopic substitution greatly increases the expense of the experiment. Moreover, isotopic substitution of the carbons, nitrogen and/or oxygens of a polypeptide backbone typically requires protein expression from bacteria raised on isotopically-substituted glucose and/or amino acids. Such protein expression would be time-consuming and expensive, not to mention it is always possible that the protein expression system is not able to produce sufficient quantities of the labeled protein for a complete set of IR experiments.

1.2 INSTRUMENTATION AND SAMPLING TECHNIQUES

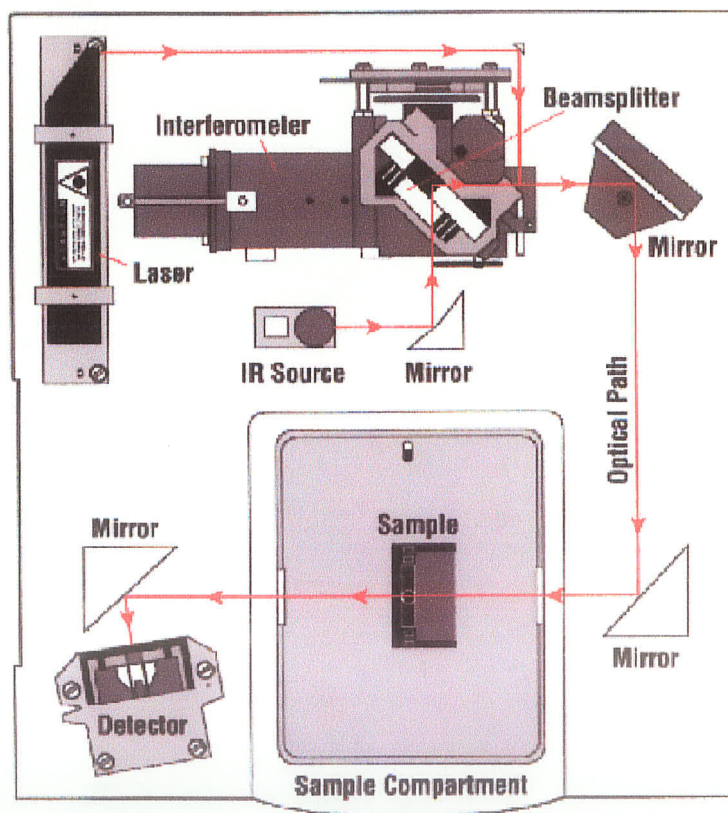
Numerous studies have focused on the analysis of structure, dynamics and interactions of biological molecules utilizing a conventional FTIR spectrometer in the transmission mode. More complex investigations are also possible, requiring accessory equipment for examination of a sample in a particular state or for extraction of unique information. Various accessories are available for use in conjunction with a conventional FTIR spectrometer to analyze samples in different states on either the macroscopic or microscopic scale. The experimental approach taken is largely dependent on whether the application involves study of a prepared sample (*in vitro*) or a tissue sample (*in situ*).

1.2.1 Conventional FTIR spectrometer

A simple layout for a conventional FTIR spectrometer is shown in Figure 1-1. Briefly, a thermal source (globar) emits IR radiation and the beam enters the interferometer. Within the interferometer is a beamsplitter which divides the incoming beam into two optical beams (not shown). One of these optical beams reflects from a fixed mirror, while the

other reflects from a moving mirror at a 90° angle from the fixed mirror. The moving mirror, typically moves only a distance (δ) of a few mm away from the beamsplitter (Lambert *et al.*, 1987). After reflection, these two beams recombine and meet back at the beamsplitter. The interferogram signal that exits the interferometer is therefore a result of these two beams interfering with each other, where the signal intensity is a function of the moving mirror position (Griffiths, 1975). For example, when the optical path difference (*i.e.*, retardation, x) is zero (defined by the relation, $x = 2\delta$, where x is the retardation) the recombined beams are “in phase” and the signal is at a maximum (Griffiths, 1975; Lambert *et al.*, 1987). This is the “centerburst” signal of the conventional FTIR spectrometer. However, when the moving mirror is displaced, the beams will interfere and the signal will fall to zero when $x = \lambda/2$ (Griffiths, 1975; Lambert *et al.*, 1987).

Figure 1-1. Simple layout for a conventional FTIR spectrometer.¹



1. Reprinted with permission from “Introduction to Fourier Transform Infrared Spectrometry” booklet located at the website: <http://www.nicolet.com> provided by Thermo Nicolet Instrument Corporation, 5225 Verona Road, Madison, WI 53711-4495, USA.

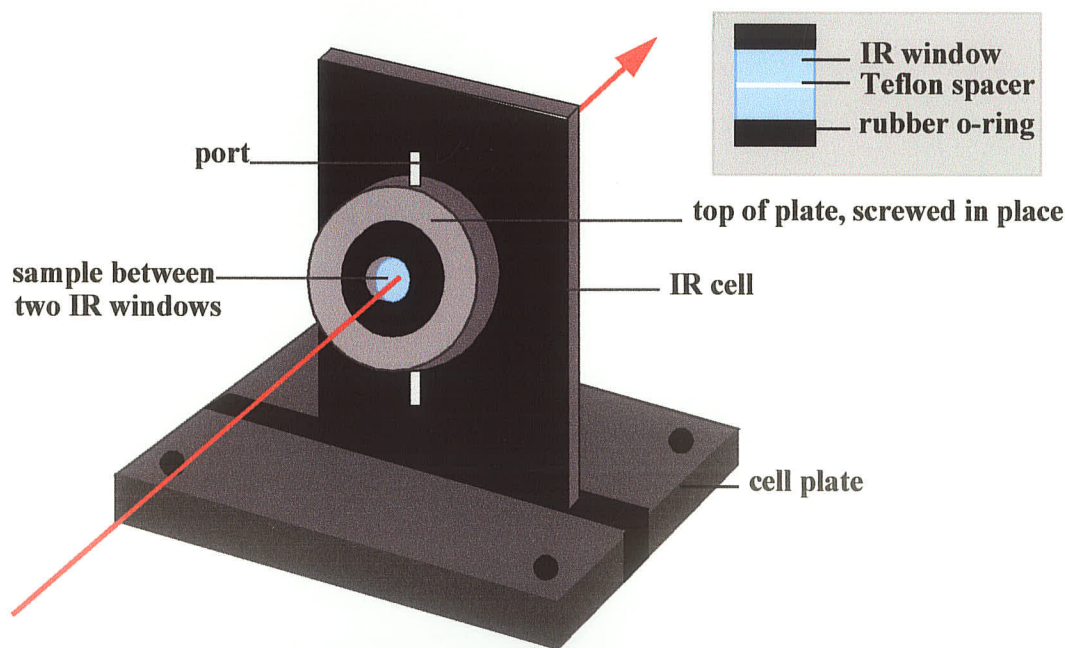
All of the spectral infrared frequencies are simultaneously encoded within this interferogram signal which is then sent forth toward the sample compartment to the sample. The detector then senses the resultant interferogram transmitted or reflected from the sample, and a computer interfaced with the spectrometer calculates the difference in interferogram when compared to the inherent interferogram without absorbance (*i.e.*, the background). In comparison to dispersive instruments, data acquisition takes seconds instead of minutes, a feature known as Fellgett's advantage (Griffiths, 1975). To take full advantage of the interferometry approach, it is essential to have a detector that is highly sensitive and has a fast response time. One commonly used mid-IR detector, which has these characteristics, is the mercury-cadmium-telluride (MCT) pyroelectric bolometer, sensitive from the near infrared (10000 cm^{-1}) to the low end of the mid-IR (400 cm^{-1}). The high sensitivity of FTIR detectors improves the optical throughput (Jacquinot's advantage), while their fast response time allows for co-addition and signal averaging of numerous scans. These two characteristics allow spectra to be acquired with greater signal-to-noise quality in comparison to dispersive instruments (Griffiths, 1975). A helium-neon reference laser (lases in the red) provides internal wavelength calibration for the spectrometer (Connes advantage).

1.2.2 The sample cell for conventional transmission FTIR biospectroscopy

In conventional transmission FTIR spectroscopy a cell or container that is optically transparent is required to hold the sample in the path of the IR beam. For biological samples (aqueous liquid or tissue) the optically transparent windows must have limited solubility in aqueous media and therefore are typically made of either BaF_2 or CaF_2 (Lambert *et al.*, 1987). In the mounting of solution samples, a rubber o-ring and IR transparent window are placed in an open demountable IR cell (see Figure 1-2). Prior to pipetting the sample onto the IR window, an o-ring-shaped Teflon spacer is placed on the IR window for specification of a particular pathlength. For instance, if a prepared protein solution in D_2O was to be analyzed a typical pathlength would be $25\text{-}50\text{ }\mu\text{m}$ while if a nucleic acid solution was to be prepared in H_2O a Teflon spacer of about $10\text{ }\mu\text{m}$ may be the choice as this would minimize the absorption of water in the spectrum (refer to sample preparation section 1.3). Finally, the second IR window is placed on the sample, a second rubber o-ring is added and the

demountable cell is closed such that the IR windows and spacer effectively sandwich the sample while being mounted in a holder that can slide into a sample plate within the sample compartment of the spectrometer (see Figure 1-2). This demountable cell is equipped with external ports which can be used to insert a thermocouple to monitor temperature of the cell contents in dynamic solution studies. Alternatively for small tissue samples, no Teflon spacer is used, but the window itself may be machined to create a central well or depression of reproducible depth (in the range 6 to 10 μm), in which the sample is placed (Jackson and Mantsch, 1996). For dried films prepared on a single IR transparent substrate (section 1.3.2), the same cell plate as that shown in Figure 1-2 can be used to support the IR window, film thickness defining pathlength rather than the Teflon spacer.

Figure 1-2. Demountable IR cell for liquid studies. Inset: shows the arrangement of two IR windows in the cell which effectively sandwich the sample while the Teflon spacer maintains the chosen pathlength.

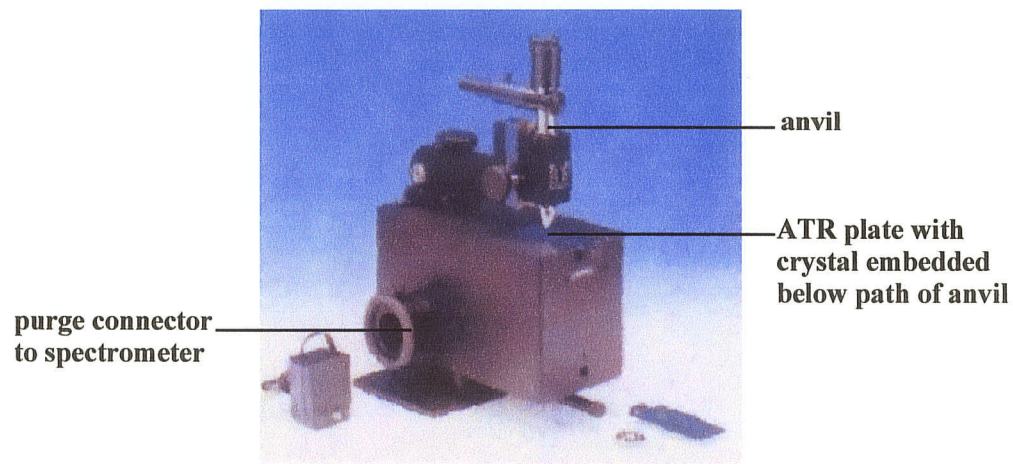


1.2.3 The attenuated total reflectance accessory for FTIR biospectroscopy

Attenuated total reflectance (ATR) FTIR spectroscopy is a convenient method by which samples can be studied in any state (Harrick, 1967). Biospectroscopic investigations can be carried out on liquid, dried film, thin tissue section or bulk tissue samples. Although

gases may also be examined by ATR-FTIR, gases are very rarely studied in FTIR biospectroscopy. Shown in Fig 1-3 is the single point internal reflection accessory the ATR SplitPea™ produced by Harrick Scientific. This ATR accessory is fitted inside the sample compartment of the FTIR spectrometer such that the dry nitrogen air purge is maintained throughout the experiment via connectors to the shutters of the instrument. The sample is placed on the ATR crystal and for bulk tissues the anvil can be lowered at some decided pressure to define tissue thickness for acquisition of reproducible spectra. The spectrum obtained is similar to that acquired in conventional transmission FTIR spectroscopy (section 1.2.2) except that quality is frequently improved because the interfering absorptions due to water vapor (section 1.3.1) and interference fringes are absent (Harrick 1967). The latter can occasionally arise in conventional transmission FTIR when air pockets are present between the two IR windows that sandwich the sample.

Figure 1-3. The Harrick Scientific SplitPea™ used for ATR-FTIR²

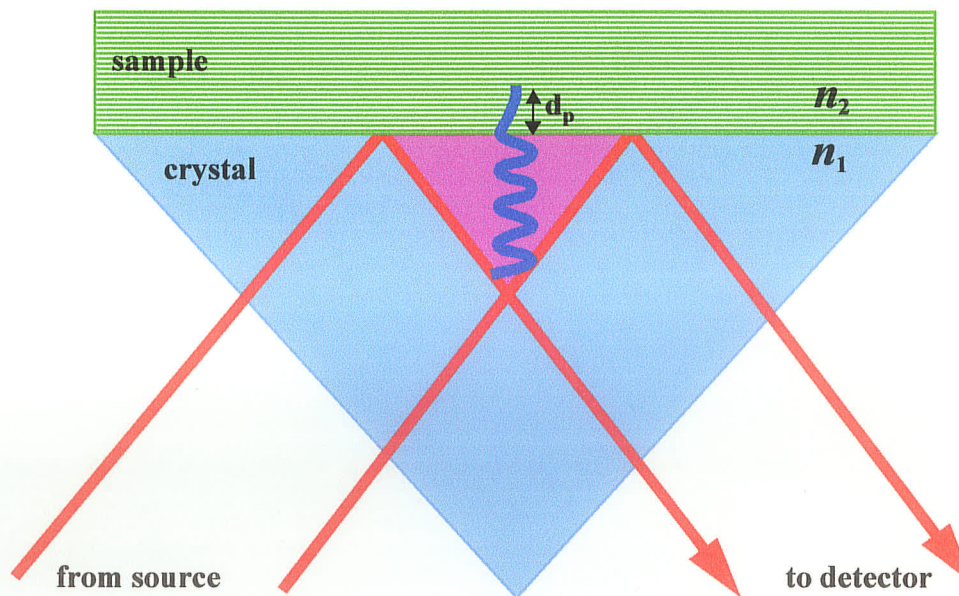


Total internal reflection spectroscopy employs a different phenomenon from that of conventional transmission or specular reflectance IR spectroscopy. In ATR-FTIR, instead of detecting wavelengths transmitted or reflected, the detector monitors the wavelengths which were not totally internally reflected by the crystal due to sample absorption. Inside the ATR accessory the infrared radiation is directed to the ATR reflection element (an opti-

2. Photo reprinted from www.harricksci.com/accessories/splitpea/ with permission from the Harrick Scientific Corporation, 88 Broadway, Ossining, NY 10562, USA

cally transparent prism or hemicylinder for a single point reflection), which is in contact with the sample of lower refractive index, n_2 . As shown in Figure 1-4, the superposition of the incident and reflected IR radiation waves (shown in pink) on the crystal surface creates a standing wave (shown in blue) normal to the surface of this denser medium of higher refractive index, n_1 (Harrick, 1967). As a result, an evanescent or fading, non-propagating field is produced in the rarer medium (lower refractive index, n_2) which energetically decays with distance from the interfacial surface between the ATR reflection element and the sample (Harrick, 1967). At wavelengths at which the sample absorbs there is an energy loss in the evanescent wave that is transferred to the reflected waves and detected upon exit from the ATR accessory. The penetration depth (d_p) of the evanescent field into the rarer medium is proportional to the wavelength of the incident radiation, thus d_p is greater for longer wavelengths (*i.e.*, lower wavenumbers) (Harrick, 1967). Therefore, although ATR spectra resemble conventional transmission spectra, spectral distortion at longer wavelengths (lower cm^{-1}) can be observed since greater penetration means greater absorbance by the sample at those wavelengths.

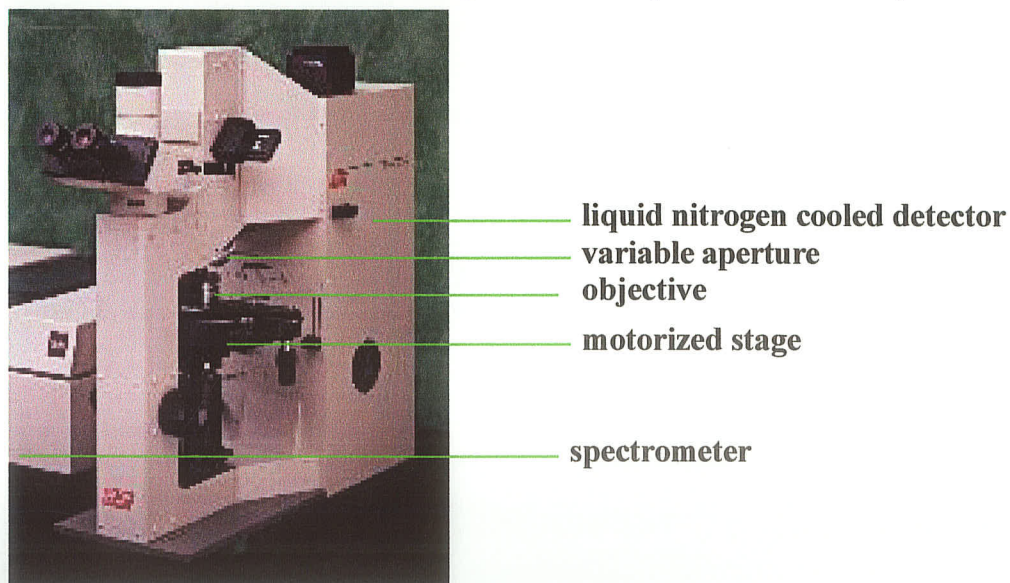
Figure 1-4. The evanescent wave produced in total internal reflection. Abbreviations: refractive index of ATR crystal prism (light blue), n_1 ; refractive index of sample (green), n_2 ; $n_1 > n_2$; penetration depth, d_p .



1.2.4 The microscope accessory for FTIR microspectroscopy

Conventional transmission and ATR-FTIR can be classified as macrosampling techniques, while microscopic sampling requires an external accessory to the FTIR spectrometer, the confocal IR microscope. Shown in Figure 1-5 is the Nicolet IR Plan AdvantageTM microscope. The IR beam exits from the spectrometer to the microscope, and passes through an adjustable variable aperture to the IR transparent objective (32X) which focuses the beam onto a small area of the sample. A diffraction limit of 30-50 μm in diameter can be expected when a globar is used as the source of the IR radiation. Better spatial resolution can be achieved with IR radiation from a synchrotron source (see section 1.2.5). The sample (dried film or thin tissue section) can be placed on an IR transparent substrate such as a BaF_2 or CaF_2 window for data collection in transmission mode or on an IR reflective glass slide for data collection in the reflection mode. Furthermore, spectra can be collected on localized “spots” within the sample or alternatively an array of spectra (“map”) can be collected within a designated sample area. FTIR microspectroscopy is a versatile technique which can be utilized in both *in vitro* and *in situ* studies.

Figure 1-5. Nicolet IR Plan AdvantageTM microscope for FTIR microspectroscopy³



3. Reprinted with permission from website: <http://www.nicolet.com/Microscopy.html> provided by Nicolet Instrument Corporation, 5225 Verona Road, Madison, WI 53711-4495, USA.

1.2.5 Synchrotron radiation as the source of the IR radiation

A conventional FTIR spectrometer utilizes a thermal source (globar) to emit IR radiation (section 1.2.1). Rather than provide a collimated beam as does a laser, a globar source, like a light bulb, emits radiation in all directions. In FTIR microspectroscopy, the IR radiation must pass through an aperture prior to impinging upon the sample (section 1.2.4) and the non-collimated IR radiation that cannot pass through this aperture is lost. Therefore, the number of photons that can reach the detector after absorption utilizing a thermal emission source will be low unless a larger aperture of at least 30 to 50 μm in diameter is utilized (Choo *et al.*, 1996).

Alternatively, improved spatial resolution and faster data collection times can be achieved when synchrotron radiation is utilized as an ultra-bright infrared source in FTIR microspectroscopy (Williams, 1992; Choo *et al.*, 1996; Jamin *et al.*, 1998). Synchrotron infrared light is highly collimated similar to a laser beam, thus it is 1000 times brighter (more photons per cross-sectional area of the beam) than the standard globar used in conventional FTIR microspectroscopy (Williams, 1992). However, unlike a laser it has a broad bandwidth and thus emits a wide range of infrared wavelengths, making FTIR microspectroscopy possible (Williams, 1992). Consequently, this 1000-fold increase in brightness decreases the time required for complete data collection since there is reduction in the number of co-added scans required to produce spectra with a high S/N ratio. Moreover, with synchrotron radiation as the source in FTIR microspectroscopy, the aperture can be decreased to the diffraction limit of 3 to 5 μm for the mid-IR region with improved intensity at the detector (Williams, 1992). In general, as the wavelength of radiation passing through the aperture approaches the diameter of the aperture, the radiation will be scattered radially due to diffraction, resulting in a lower S/N ratio at longer wavelengths (Choo *et al.*, 1996).

A number of synchrotron radiation centres equipped with IR beamline facilities are available worldwide. Those facilities that support FTIR microspectroscopy at their IR ports are: SRC in Daresbury, UK; LURE, Paris, France; ALS, Berkeley, USA; Aladdin, Wisconsin, USA; NSLS, Brookhaven, USA; Max-Lab, Lund, Sweden; and UVSOR, Okasaki, Japan (Williams, 1999). In a synchrotron, energetic electrons are injected into a storage ring kept at high vacuum. Multiple bending magnets are used to keep the electrons circulating

within the ring by imposing changes in direction on them at many locations around the ring. Where a change in direction occurs, synchrotron radiation (white light) is emitted tangent to the arc of the electron path. This emitted synchrotron light is directed down various beamline ports, located along the circumference of the storage ring, which select the light of infrared energies (*i.e.*, block UV, x-rays, gamma rays etc. emitted from the synchrotron source). Radiofrequency cavities (harmonic chambers) replenish the energy lost by emission of synchrotron radiation from the electrons, the effectiveness of which determine the beam lifetime between injections (2-6 hours) as well as the time scale of the source (50-500 picoseconds). Source brightness and stability is variable at the different facilities listed above due to differences in energy at which the ring is operated (MeV) and the radiofrequency cavities utilized to improve beam lifetime (Williams, 1999). Furthermore, these facilities have been developing various approaches in dealing with the source noise that evolves from power supply instability, harmonic chambers, storage ring cooling systems and vibrating pumps (Williams, 1999).

1.3 SAMPLE PREPARATION

Sample preparation for either *in vitro* or *in situ* examination is dependent upon the sampling technique chosen for the investigation. Sampling techniques commonly used for mid-IR biospectroscopy can be divided into four categories: *in vitro* macrosampling, *in vitro* microsampling, *in situ* macrosampling and *in situ* microsampling (Table 1-1). Furthermore, depending upon the state of the sample (solution, dried film, bulk tissue or thin tissue section) the degree of difficulty of sample preparation will vary.

Table 1-1. Sampling techniques used for mid-infrared biospectroscopy

Sample	<i>In vitro</i> (preparations)		<i>In situ</i>	
	Macro	Micro	Macro	Micro
Solution	Transmission			
Dried film	Transmission ATR	Microscopy	Transmission ATR	Microscopy
Tissue			Transmission ATR	Microscopy

1.3.1 Preparation of biological samples in solution for *in vitro* studies

Macrosampling of biological samples prepared *in vitro* in a solution state (*i.e.*, macromolecules in buffer) typically utilizes conventional transmission spectroscopy (section 1.2.2). This sampling technique allows examination of the gross overall spectral characteristics of all of the molecular components in the sample. The choice of solvent for solution studies must maintain the physiological relevance of the model system, and in IR regions where the sample absorbs the molar absorptivity of the solvent relative to that of the solute should be minimal. Physiologically, an aqueous solvent system at neutral pH is the optimum choice as organic solvents such as dimethylsulphoxide and halogenated alcohols can disrupt the native conformation of biological molecules such as proteins (Jackson and Mantsch, 1991a; Jackson and Mantsch, 1992). However, water is a strong IR absorber and interferes with absorptions of biological macromolecules, therefore *in vitro* studies are usually carried out in buffered D₂O which absorbs in regions outside the range of interest for proteins and lipids (Mendelsohn and Mantsch, 1986). The accepted infrared absorption bands of liquid water, D₂O and HOD (Mendelsohn and Mantsch, 1986) are presented in Table 1-2. Finally, the types of functional groups present in the macromolecular component being examined may further direct the choice of solvent. For instance, conformationally diagnostic absorptions of lipids and proteins overlap with the O-H stretching and H-O-H bending vibrations of water, respectively, thus the aqueous solvent of choice is D₂O. However, for nucleic acids and carbohydrates, both D₂O and H₂O absorb in regions of interest, therefore solution spectra may have to be carried out in both H₂O and D₂O in separate experiments for observation of all the relevant macromolecular vibrations (Taillandier and Liquier, 1992). Although, ATR could also be used on solution state biological samples, transmission is the preferred technique when aqueous solutions are used since the closed liquid sampling cell minimizes atmospheric H-D exchange with D₂O. Moreover, ATR can cause distortion of absorption bands on the shorter frequency edge relative to the longer frequency edge of the spectrum (section 1.2.3).

Table 1-2. IR bands due to H₂O, D₂O and HOD⁴

Frequency (cm ⁻¹)	Assignment
3490, 3280	H-O-H stretching, $\nu(\text{O-H})$
3380	H-O-D stretching, $\nu(\text{H-OD})$
2540, 2450	D-O-D stretching, $\nu(\text{O-D})$
2500	D-OH stretching, $\nu(\text{D-OH})$
2125	H ₂ O association band $\nu_A(\text{H}_2\text{O})$
1645	H-O-H bending, $\delta(\text{H}_2\text{O})$
1555	D ₂ O association band, $\nu_A(\text{D}_2\text{O})$
1455	H-O-D bending, $\delta(\text{HOD})$
1215	D-O-D bending, $\delta(\text{D}_2\text{O})$

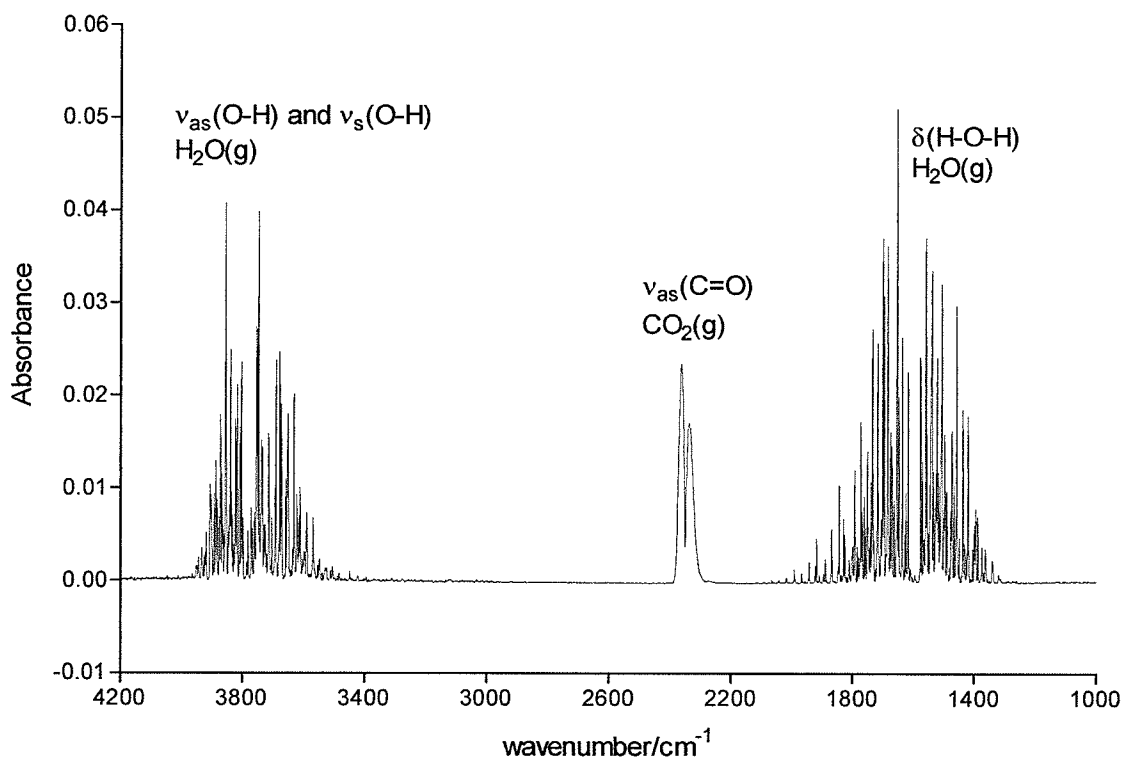
One of the advantages of IR spectroscopy in solution studies is that the sample does not need to be a homogeneous, optically clear solution, as in other types of spectroscopy, such as CD, where light scattering artifacts are a problem. A heterogeneous suspension such as that produced for liposomal mixtures can also be examined, the only limitation being the concentration of the solutes to be detected. The lower limit for substrate concentration in conventional transmission IR spectroscopy is typically 1-10 mg/ml depending on pathlength (Beer-Lambert law applies). For water solutions, shorter pathlengths (*ca.* 6 μm) must be employed along with a higher solute concentration (10 mg/ml), decreasing the intensity of the water bands and allowing them to be more reliably subtracted from the sample spectrum. (Haris and Chapman, 1995; Jackson and Mantsch, 1996). However for samples prepared in D₂O, longer pathlengths (up to 100 μm) and consequently lower solute concentrations (1 mg/ml) can be utilized because D₂O absorptions appear outside the regions of biological interest. (Haris and Chapman, 1995; Jackson and Mantstch, 1996).

Once the liquid sample is placed in the demountable cell (section 1.2.2, Figure 1-2), it is closed to prevent interference by atmospheric water vapor. However, even though the sample compartment is purged with dry nitrogen gas to remove water vapor from out-

4. Band frequency and assignment cited from Table 3 p.114 of Mendelsohn and Mantsch, 1986

side of the cell, traces of H₂O vapor may still be present. A water vapor spectrum (Figure 1-6) should be acquired in the absence of the sample cell for subsequent subtraction from the sample spectrum (section 1.4.4). A water vapor spectrum is usually obtained by breaking the dry N₂(g) purge in the sample compartment (*i.e.*, exposing it to the atmosphere) and taking an absorbance spectrum, using a spectrum of the N₂(g) purged sample compartment as the background spectrum. Therefore, it is not surprising that the asymmetric stretching of carbon dioxide appears near 2400 cm⁻¹, since the atmosphere in most instrument rooms contains CO₂(g) as well as H₂O(g).

Figure 1-6. Water vapor spectrum acquired on a Biorad FTS60 FTIR spectrometer equipped with an MCT detector with a nominal spectral resolution of 2 cm⁻¹. Abbreviations: asymmetric, as; symmetric, s; stretching, v; bending, δ.



1.3.2 Preparation of dried films for *in vitro* and *in situ* studies

As an alternative to solution work, *in vitro* studies may involve the preparation of a dried film on an IR transparent/reflective substrate while the sample is purged with a stream of dry nitrogen gas to minimize hydration from the atmosphere. As shown in Table 1-1, macroscopic sampling of dried films prepared *in vitro* can utilize either conventional transmission (section 1.2.2) or ATR-FTIR (section 1.2.3.) spectroscopy. Unique information, such as orientation of secondary structural elements of a protein with respect to a lipid bilayer prepared on an ATR crystal, can be delineated by observation of bands attenuated or augmented by polarized light (Haris and Chapman, 1995). In contrast to macroscopic sampling techniques, microscopic sampling (section 1.2.4) can reveal differences in sample homogeneity within a prepared dried film. For example, by using IR microspectroscopy on films prepared from clays mixed with different nucleic acids, Franchi *et al.*, 1999, were able to collect spectra at the focal sites of complexation between the nucleic acids and surface-exposed clay molecules. If these clay-nucleic acid films had been examined macroscopically by IR, spectral features due to the chemical change (*i.e.*, complex formation) would have been diluted by the spectral features of the film constituents that did not experience a chemical change. Such “spectral dilution” is a problem with macroscopic sampling techniques of inhomogeneous samples because the “average spectrum” of the sample is obtained, rather than the localized spectrum that is site-specific to the biophysical or chemical change. As a result, macroscopic sampling of inhomogeneous samples can frequently result in a loss of information or perhaps misleading information on the biological system.

Dried films of extracted biological fluids (*i.e.*, blood, urine, *etc.*) can be prepared for IR examination of the solutes “*in situ*”, using transmission or ATR FTIR spectroscopy for macroscopic examination and FTIR microspectroscopy for microscopic examination (Table 1-1). The term “*in situ*” is used rather loosely here because the removal of water from biological fluids may compromise the biological integrity of the solutes. Thus, it may be worthwhile to compare spectra taken of the dried film under a dry stream of nitrogen gas to that under a stream of D₂O vapor that partially rehydrates the film. Direct mid-IR examination of the biological fluid *in situ*, is difficult to carry out unless the fluid is highly concentrated and a low (<10 μm) pathlength is used to minimize the absorptions from water

(see section 1.3.1). More recently, near IR spectroscopy (NIR) has been found to be more suitable than mid-IR spectroscopy for examination of biological fluids (Jackson and Mantsch, 1996; Jackson *et al.*, 1997). Although NIR is out of the scope of this thesis, it should be noted that one of the advantages of NIR over mid-IR spectroscopy is that water overtone and combination absorptions have 10% the intensity of water fundamental vibrations in the mid-IR (Jackson and Mantsch, 1996).

1.3.3 Preparation of tissue for biological studies *in situ*

Biological studies *in situ* more typically involve the analysis of cells and tissues on either the macroscopic or microscopic scale. Transmission (section 1.2.2) and ATR-FTIR spectroscopy (section 1.2.3) as techniques for macrosampling have already been discussed. Sample preparation generally involves the washing of the tissue in a saline solution to remove blood (if the tissue is fresh) or salt-containing solutions (if these have been used to store the tissue post-mortem). Fresh unfixed tissue is preferable so that post-mortem cell autolysis and spectral artifacts due to fixatives can be avoided (Gentner *et al.*, 1998). An appropriately sized piece of the tissue is then cut and placed either between two IR transparent windows with a well (for conventional transmission) or between the crystal and the anvil (for ATR). For microscopic examination (section 1.2.4) however, the tissue must be cut into a very thin section and placed on either an IR transparent substrate or an IR reflective glass slide. The tissue for FTIR microspectroscopy is thinly cut in a fresh-frozen state using a cryostat microtome (Wong and Rigas, 1990; Jackson and Mantsch, 1996). To maintain tissue integrity, fixation should be avoided if possible (*i.e.*, if degradative enzymes are minimal in the tissue). However, formalin fixation is possible without introducing interfering spectral absorptions as long as time is allotted for evaporation of the formalin from the tissue section. Embedding materials that aid in the sectioning of the tissues on a cryostat microtome, such as methyl methacrylate can be utilized but a wash with xylene is recommended as methyl methacrylate absorbs in the mid IR region. The xylene wash will also remove some of the lipid content from the tissue (Jackson and Mantsch, 1996) and thus should only be used when studying tissue of low lipid content (*i.e.*, bone). Embedding with Optimal Cutting Temperature™ (OCT) medium, a mixture of polyvinyl alcohol and polyethylene glycol,⁵ is strongly disfavored as it contains numerous hydroxyl groups (high

molar absorptivity in the mid-IR region) which would produce interfering absorptions with samples of biological interest (Wong and Rigas, 1990; Manoharan *et al.*, 1993; Jackson and Mantsch, 1996). Although OCT is a water-soluble medium it is difficult to completely remove from tissue even after numerous washings with alcohol and vigorous removal will affect the integrity of the endogenous tissue constituents (Wong and Rigas, 1990; Jackson and Mantsch, 1996). Furthermore, unlike methyl methacrylate, OCT is an effective hydrogen bond donor and acceptor and can greatly affect conformation of numerous tissue constituents even after an attempt is made to remove the majority of the OCT (Wong and Rigas, 1990).

1.4 SPECTRAL PROCESSING AND PREPROCESSING

Spectral processing involves the computer-controlled conversion of the detected, signal-averaged and background-subtracted interferogram (recall section 1.2.1) from the Fourier domain to the frequency domain to produce the interpretable IR spectrum. This conversion is mathematically performed by a fast Fourier transform but can be best explained by contrasting the functions that occur upon absorption in the Fourier and frequency domain (section 1.4.1). In addition, certain instrumental parameters, such as the nominal spectral resolution, number of scans collected/coadded and the apodization function applied to the interferogram, give the spectroscopist some control over the signal-to-noise quality in the raw spectrum. This control over spectral quality is better explained by considering what occurs to the interferogram in the Fourier domain (sections 1.4.2 and 1.4.3).

In contrast, spectral preprocessing refers to the IR software programs used by the spectroscopist to improve the quality of the raw spectral data in preparation for spectral interpretation and data analysis. The sequential order in which each preprocessing technique is applied to the raw spectrum is very important. If the spectrum was taken of a sample in solvent (*i.e.*, D₂O buffer), interactive subtraction of the solvent absorption spec-

5. OCT is an embedding material produced by Tissue-TekTM. Tissue-TekTM does not provide the composition of OCT on the container. However, the composition is reported in "Fixation, processing, sectioning and storage of tissues, written by Dr. Beverly Faulkner-Jones, Dept. of Anatomy and Cell Biology, University of Melbourne, Australia, at the website: <http://www.biochemistry.unimelb.edu.au/bfjones/ish/part3.htm>. For further information Dr. Faulkner-Jones can be contacted by email: B.Jones@Anatomy.Unimelb.EDU.AU.

trum from that of the sample in the solvent is performed first, for better visualization of absorption bands due to the solute. Next, if the sample experiences some exposure to H₂O vapor, interactive subtraction of a water vapor spectrum from the solvent-subtracted spectrum can typically improve spectral quality. If there is residual noise after water vapor subtraction, the spectrum may be smoothed but only when absolutely necessary and even then in moderation since over-smoothing can result in a loss of resolution. To correct sloping artifacts in the baseline, an interactive two- or multi-point baseline correction can also be performed. Moreover, if specific spectral subregions are wanted for inspection, band narrowing techniques or global analysis of multiple spectra, the spectrum can be truncated. Finally, in macrosampling applications the concentration of a solute may be slightly different from sample to sample, therefore normalization of the specific absorption band to be compared amongst the spectra will correct for concentration-dependent errors. Further details on these spectral preprocessing techniques, aimed to improve spectral quality or enable direct comparison of absorption bands in multiple spectra, can be found in section 1.4.4. Once the spectroscopist has preprocessed the spectra to improve spectral quality, the next objective may be to amplify the spectral information by increasing the resolution beyond the limits of the instrument (section 1.4.5). For example, band narrowing techniques, such as Fourier self deconvolution (FSD) and derivation (FD), are commonly used to “artificially enhance” the spectral resolution. The term “artificially enhance” is used here because resolution is an instrumental parameter whereas FSD and FD are mathematical techniques that manipulate the resolution after other spectral preprocessing techniques have been applied. FSD and FD operations are performed “interactively” (*i.e.*, user-control of each parameter) on the absorbance spectrum. How these techniques actually narrow band width is best explained by describing the effect of FSD or FD on the interferogram in Fourier domain and converting the result to the frequency domain (as shown in section 1.4.5).

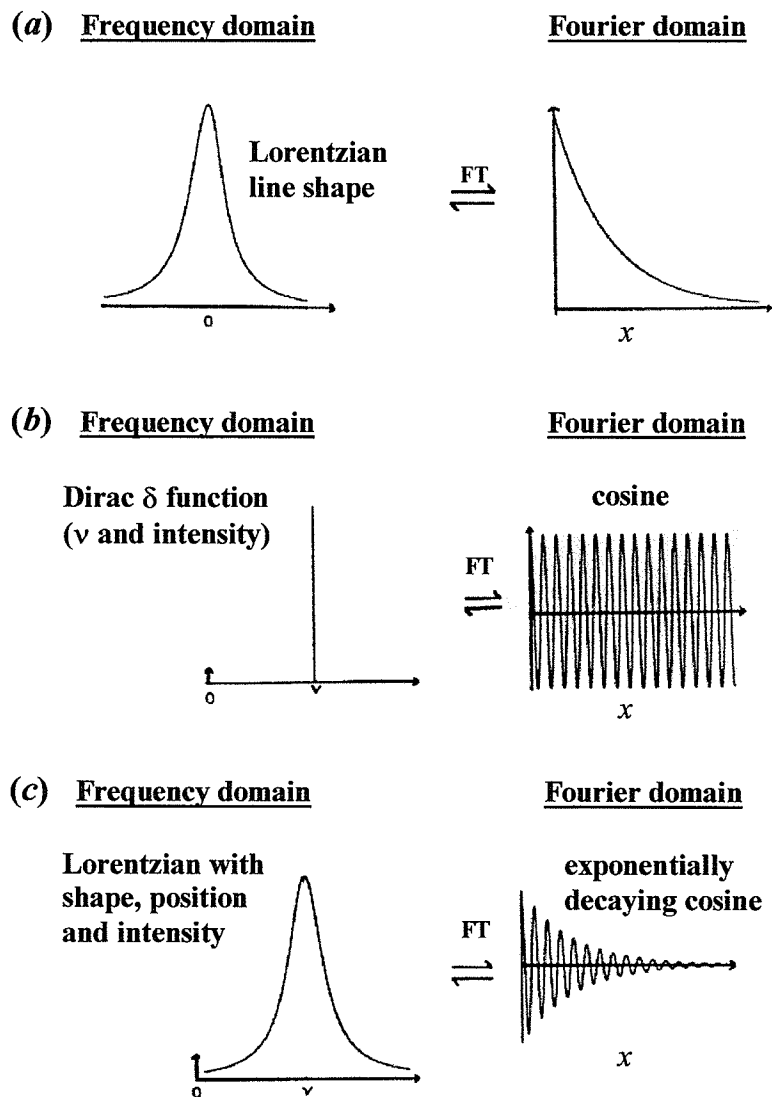
All of these spectral preprocessing techniques are not without a certain level of subjectivity and occasionally several approaches are tried to determine which combination of preprocessing techniques leads to a meaningful result in the global data analysis (section 1.7). This is especially true of truncation of the spectrum (section 1.4.4). That is, user-selection of spectral subregions that contain the most important information for the comparison

of multiple spectra is highly subjective and can result in a loss of pertinent information. This level of subjectivity is not that important for *in vitro* studies, since the spectroscopist knows the composition of the sample. However for *in situ* studies (*i.e.*, tissues), little information is known about the exact composition of the sample(s), increasing the subjectivity in choosing diagnostic subregions or absorptions to differentiate the sample(s). Alternatively, this subjectivity can be lifted by using a computer algorithm to search for the most diagnostic regions of spectra belonging to two or more groups under comparison. One such computer algorithm, a genetic algorithm (GA), coupled to a multivariate analysis algorithm for feedback, searches through the number of possible combinations of diagnostic subregions that can best differentiate between samples (see section 1.4.6.).

1.4.1 Conversion from the Fourier domain to the frequency domain

Once the signal is detected and the information is transferred to a computer interfaced with the spectrometer, the resultant interferogram is converted from the Fourier domain (signal intensity as a function of retardation) to the frequency domain (absorbance as a function of wavenumber) by means of a fast Fourier transform. The interconversion between the Fourier domain and the frequency domain for a single absorption is shown schematically in Figure 1-7. As depicted in Figure 1-7c, Fourier transformation of the interferogram (an exponentially decaying cosine function) produces an absorption band with line shape related to the exponential decay of the cosine and band maximum at frequency, ν , related to the periodicity of the cosine wave (Cameron and Moffatt, 1984). Note, that the faster the rate of exponential decay in the Fourier domain, the greater the bandwidth in the spectral domain. In the frequency domain on the left-hand side of Figure 1-7, a single band in the IR spectrum can be expressed as a convolution of line shape (Figure 1-7a) with a Dirac delta function that describes position and intensity of the absorption (Figure 1-7b). In the Fourier domain on the right-hand side of Figure 1-7, the exponentially decaying cosine wave can be expressed as the vector product of the exponential (Figure 1-7a) and the cosine wave (Figure 1-7b).

Figure 1-7. Interconversion between the frequency and Fourier domains⁶.
 Abbreviations: FT, Fourier transform operation; ν , wavenumbers (cm^{-1}); x , retardation.



6. Figure adapted with permission from Cameron and Moffatt, 1984

1.4.2 Spectral resolution

An IR spectrum consists of numerous absorption bands at different frequencies with different shapes and widths, and is therefore the sum of the fast Fourier transforms performed on each decaying cosine wave of periodicity, ν , in the Fourier domain. Linewidth for a single absorbing group is dependent on the rate of decay of the interferogram, such that a more slowly decaying cosine function is transformed to a narrower line (Cameron and Moffatt, 1984). In addition, a reciprocal relationship exists between spectral resolution and the distance the moving mirror travels (*i.e.*, if the mirror moves 0.25 cm back and forth, the nominal spectral resolution would be $1/(2 \times 0.25 \text{ cm}) = 2 \text{ cm}^{-1}$)⁷ (Griffiths, 1975; Lambert *et al.*, 1987). Therefore, since the detected signal is an exponentially decaying cosine function of the retardation, greater spectral resolution can be obtained at larger displacements of the moving mirror. This sounds wonderful in theory but spectral resolution is also limited by the size of the interferometer (Griffiths, 1975; Lambert *et al.*, 1987). That is, a spectrum cannot be collected with infinite resolution (*i.e.*, very small number of cm^{-1}) unless the size of the interferometer is infinitely large.

1.4.3 Spectral noise and apodization of the interferogram

Although spectral resolution improves at greater retardation, signal intensity wanes and noise becomes overbearing in the spectrum. In the Fourier domain noise remains constant while signal intensity exponentially decays as a function of retardation (Cameron and Moffatt, 1984). Therefore, acquisition of an interferogram is usually followed by multiplication (*i.e.*, dot product) with a chosen apodization function (*i.e.*, boxcar, triangular, Bessel, to name a few). This effectively weights the interferogram closer to the centerburst (*i.e.*, $x = 0$) and truncates the interferogram at a specific retardation, x . The retardation value chosen to be the upper limit in this truncation is dependent upon the spectral resolution selected on the instrument⁷. Co-addition of numerous scans improves the signal-to-noise (S/N) ratio since the signal increases directly with the number of scans collected while the noise, statistical in nature, only increases with the square root of the number of scans collected (Griffiths, 1975).

7. Spectral resolution = $1/2\delta$ (where 2δ is the total distance the mirror moves back and forth). Since retardation, x , is defined by $x = 2\delta$, spectral resolution = $1/x$.

1.4.4 Common approaches used in spectral preprocessing to improve spectral quality

Prior to spectral interpretation, spectral preprocessing techniques, such as the subtraction of water vapor or buffer from the original spectrum, smoothing, baseline correction, truncation and normalization, may have to be applied to the raw spectral data to improve spectral quality or simplify the comparison of multiple spectra. These operations are available in the form of macro-computing programs that are compatible with the software of the instrument. Each preprocessing technique is not without a certain level of subjectivity since the user typically chooses the parameters of the preprocessing calculation. Therefore, it is imperative that the spectroscopist be well practiced in the application and limitations of these techniques, while at the same time being well acquainted with their raw spectral data. Moreover, the sequential order chosen to manipulate the spectra in the overall preprocessing approach is important but under some debate. It is agreed that interactive subtraction of contributions from water vapor and buffer should be done first. Moreover, if the noise level is too high (> 10 mOD units), smoothing should precede FSD or FD, since band narrowing techniques amplify noise (section 1.4.5). Baseline correction can be done prior to truncation as long as the truncated spectrum contains baseline at the extreme ends. Based on personal experience, normalization should be done after any baseline manipulations (subtraction, baseline correction) and smoothing, but prior to band narrowing techniques. Finally, if multiple spectra are to be directly compared in the global data analysis, the sequential order of spectral manipulations must remain constant from spectrum to spectrum and each technique should be carried out in a similar manner with the same parameters.

Spectral preprocessing may involve corrections for unwanted absorptions, such as those due to water vapor and buffer, or for concentration-dependent errors. The interactive subtraction of a water vapor spectrum and buffer spectrum from the raw data is a method based on difference spectroscopy. The scalar weighting factor for subtraction of one spectrum from another is subjective but certain regions in the mid-IR region can be periodically checked to validate the choice. For example, if the region between 1700 - 1800 cm^{-1} is free of the sharp absorptions due to water vapor (section 1.3.1, Figure 1-6), then it is assumed that the correct scaling factor was chosen for the interactive subtraction of water vapor from

the raw spectrum (Jackson and Mantsch, 1995). However, the choice of scaling factor for the interactive subtraction of a buffer spectrum from the original spectrum is validated by observation of a flat zero baseline in regions where neither component (buffer nor solute) absorbs, typically between 1800-1900 cm^{-1} .

Spectral preprocessing may also involve data reduction techniques, such as truncation of the spectral data. For instance, if only a certain region of the spectrum is required for analysis, truncation of the spectrum between two designated wavenumbers is carried out which rids the spectral file of data outside these limits. The decision of which spectral regions are specifically diagnostic is up to the discretion of the spectroscopist. Normally the subjectivity involved in truncation involves merely the selection of obvious regions in the mid-IR in which molecular components absorb, such as the IR fingerprint region (700-1800 cm^{-1})⁸ of the spectrum or the CH, OH and NH stretching region (2800-3600 cm^{-1}). That is, since the region between 1800 and 2800 is typically void of diagnostic absorptions for biological macromolecules this subregion can be omitted from the analysis.

Problems with the spectrometer (*i.e.*, noise) can also be corrected using spectral preprocessing. Should noise be a problem in the spectrum, a smoothing operation (equivalent to apodization discussed in section 1.4.3) could be performed, but extreme care should be taken not to over-smooth as this would result in erroneous interpretation of the spectrum. Additional corrections to the spectral data may also include a correction to the baseline achieved by a variety of methods. For example, the spectroscopist can choose either a two-point or multiple point baseline correction. That is, points on the spectrum can be manually chosen to be considered as part of the overall flat baseline that lies on zero absorption.

Finally, normalization may be required for direct comparison of a number of sample spectra. For example, in macrosampling applications the concentration of a solute may be slightly different from sample to sample, therefore normalization prior to band narrowing techniques will correct for concentration-dependent errors. Normalization involves setting

8. An IR fingerprint refers to the unique arrangement of absorption bands at specific frequencies, with specific relative intensities, that have been assigned to a particular molecule (*i.e.*, collagen fingerprint) much in the same way fingerprints of different individuals are unique. Typically, this unique arrangement of bands occurs in the frequency range of 700-1800 cm^{-1} . Therefore, the 700-1800 cm^{-1} spectral subregion is commonly referred to as the IR fingerprint region in the literature.

the frequency limits of a designated region within a spectrum (*i.e.*, an absorption band, for example) and assigning a specific value for the integrated intensity under the curve. This procedure has to be repeated using the identical parameters (*i.e.*, frequency range and integrated intensity value) on all spectra that are to be compared. Programs that can normalize a group of spectral files simultaneously are available to conserve time in preprocessing. Normalization should also be carried out before using band narrowing techniques to artificially improve the spectral resolution (section 1.4.5).

1.4.5 Band narrowing techniques used to amplify spectral information

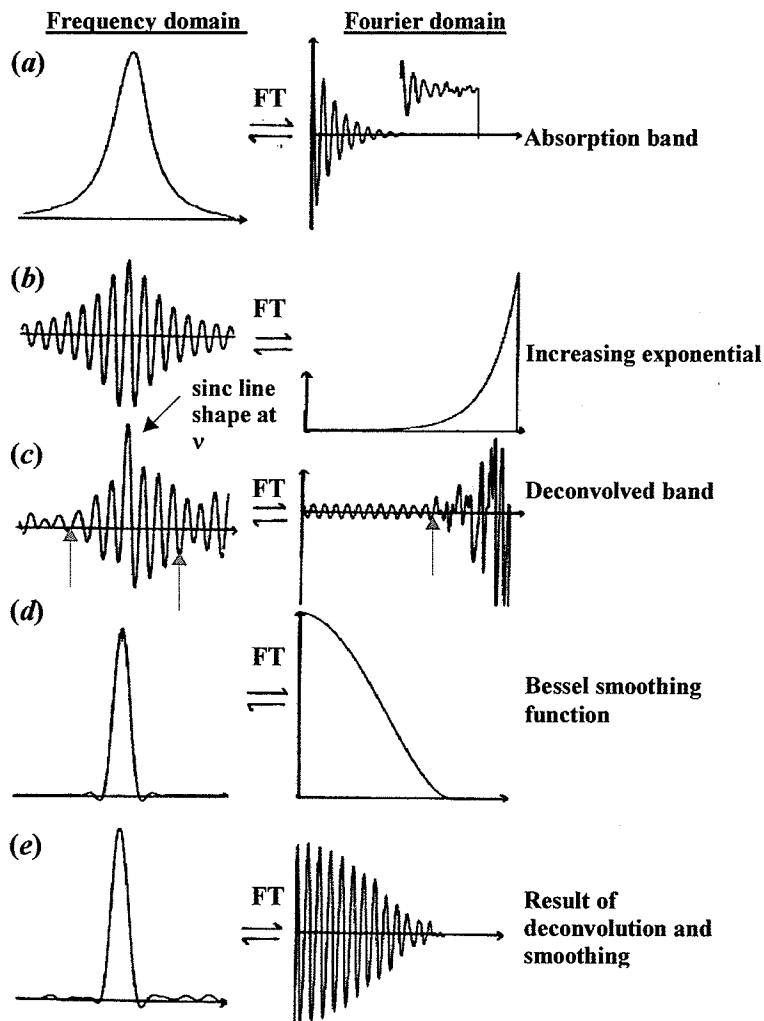
Even though nominal spectral resolution is limited by the instrumentation (section 1.4.2), computational methods are available to artificially enhance the spectral resolution of overlapped band contours. Two such band narrowing techniques, Fourier self-deconvolution (FSD) and Fourier derivation (FD) are commonly used in preparation of IR spectral data for analysis (Kauppinen *et al.*, 1981; Cameron and Moffatt, 1984; Moffatt and Mantsch, 1992; Jackson and Mantsch, 1995). These numerical approaches to spectral preprocessing (use Fourier transforms to) change the shape of the infrared bands and reduce their width to allow for better separation of the individual component bands which comprise the overall band contour (Moffatt and Mantsch, 1992).

One way to illustrate the FSD and FD techniques is diagrammatically by describing their effects on the interferogram in the Fourier domain and converting the result to the frequency domain. First, consider one absorption band (*i.e.*, a Lorentzian of defined shape, intensity and frequency) in the frequency domain and convert (via FT) the spectrum to the Fourier domain (recall Figure 1-7c). In the Fourier domain this Lorentzian is an exponentially decaying cosine function, the wider the Lorentzian band the greater the rate of decay (section 1.4.1). This Lorentzian is a convolution of Lorentzian line shape (recall Figure 1-7a) and a Dirac δ function (recall Figure 1-7b). In an ideal spectrum without noise, the line shape can be deconvolved from the spectrum, by dividing the exponentially decaying cosine function by a decreasing exponential, thus removing the information about line shape from the interferogram. Dividing the interferogram by a decreasing exponential is equivalent to multiplying the interferogram by an increasing exponential. The result in the Fourier domain is a cosine wave that ends at a specific point (*i.e.*, retardation, x) that defines

the original spectral resolution selected on the instrument. Moreover, the inverse Fourier transform of this cosine wave that terminates at some retardation, x , is a sinc line shape (or $[\sin x]/x$) at frequency, ν , similar to the Dirac δ function shown on the left in Figure 1-7b, except that it has a line width defined by the original spectral resolution⁹ with side lobes on either side (see Cameron and Moffatt, 1984). In the Fourier transform of a “real” absorption band (*i.e.*, with noise), the signal intensity decays exponentially while noise remains constant (Figure 1-8a, right). For deconvolution of a Lorentzian line shape from the spectrum, the Fourier transform of the spectrum (Figure 1-8a, right) is multiplied by an increasing exponential (Figure 1-8b, right). Multiplying the signal in the original interferogram by this increasing exponential should result in a cosine wave, similar to that shown on the right in Figure 1-7b. However, when the noise is greater than the signal in the original interferogram, deconvolution results in amplification of the noise exponentially from this point (blue arrow, Figure 1-8c, right). Moreover, noise that has been deconvolved becomes highly periodic upon transformation to the spectral domain (Cameron and Moffatt, 1984). Such highly periodic noise can be seen on either side of the deconvolved absorption band, when the deconvolved interferogram is transformed back to the spectral domain (red arrows, Figure 1-8c, left). To minimize the side lobes of the sinc line shape as well as the noise, the second part of the FSD operation involves the multiplication of the deconvolved interferogram by a smoothing function (Figure 1-8d, right). Smoothing essentially weights the portion of the interferogram that is dominated by signal rather than by noise (Cameron and Moffatt, 1984). In the Fourier domain, the final result of FSD is a smoothly decaying cosine (Figure 1-8e, right) that extends to a greater retardation value than the original interferogram (Figure 1-8a, right). That is, in comparison to the original interferogram, the FSD interferogram has a slower rate of decay. Therefore, upon transformation to the frequency domain, the FSD band has a reduced full width at half maximum (Figure 1-8e, right) because the slower the rate of decay in the Fourier domain the narrower the band in the spectral domain (section 1.4.1).

9. Recall, spectral resolution is defined by $1/2\delta$ (where δ is the displacement of the moving mirror from the beamsplitter in one direction). Also recall, the optical pathlength difference between beams reflected from the moving and fixed mirror, otherwise known as the retardation, x , is defined by $x = 2\delta$. Therefore, spectral resolution is defined by $1/x$.

Figure 1-8. Fourier self-deconvolution of an IR band¹⁰. Inset placed over the Fourier domain in (a) is a magnification of the signal/noise at that retardation of the interferogram. Abbreviations; FT is the Fourier transform operation



When performing the FSD operation on a selected spectral subregion, the user can observe the change in spectral resolution as two parameters, full width at half maximum (choice of the correct increasing exponential) and the percentage of smoothing, are manipulated interactively to achieve maximal resolution enhancement. Maximum resolution enhancement is considered to be obtained when the appearance of periodic noise along the baseline and negative side lobes on the absorption bands are minimized. In general, once

10. Figure adapted with permission from Cameron and Moffatt, 1984.

the estimated bandwidth is greater than the narrowest absorption in the subregion selected for FSD, the negative side lobes of the sinc line shape should disappear (Cameron and Mantsch, 1984). Routine comparison of the spectrum before and after FSD can also be beneficial to ensure that the spectrum has not been over-deconvolved or over-smoothed. However, the FSD operation is not without some drawbacks as choice of these parameters is fairly subjective (Jackson and Mantsch, 1995). In addition, the FSD algorithm makes an assumption of deconvolving the spectrum with a symmetric band shape, usually Lorentzian, but in reality the numerous bands in an IR spectrum may be asymmetric with different shapes (Moffatt and Mantsch, 1992). When the overall band contour is asymmetric due to the overlap of two or more component bands, deconvolution of a symmetric band shape from the spectrum will yield two or more peaks. However, certain experimental techniques, such as ATR-FTIR can distort spectra (section 1.2.3) and deconvolution will augment this distortion leading to erroneous spectral interpretation (Cameron and Moffatt, 1984). Finally, FSD should only be carried out on spectra free from water vapor (section 1.4.4) as water vapor will distort the deconvolved spectrum (Jackson and Mantsch, 1995).

In contrast to FSD, where the interferogram weighting function is an increasing exponential, Fourier second-order derivation uses a quadratic weighting function to narrow bandwidths (Cameron and Moffatt, 1984). As shown in Figure 1-9, the derivative line-shape function in the frequency domain has two positive "intrinsic" lobes and two negative artifact lobes that appear after the weighting function is applied (Cameron and Moffatt, 1984). Rather than using a smoothing function to eradicate the formation of the artifact lobes, simple truncation in the Fourier domain (Figure 1-9c, right) yields the second derivative of the spectrum in the frequency domain. (Cameron and Moffatt, 1984). Similar to FSD, the bandwidth after FD (Figure 1-9c, left) is reduced in comparison to the original Lorentzian (Figure 1-9a, left). That is, the FD calculation decreased the rate of decay of the cosine function in the Fourier domain, narrowing the band in the frequency domain (Figure 1-9c, right). As the second derivative weighting function is negative (Figure 1-9b) this yields a negative second derivative function in the Fourier domain. Therefore, after the second-order FD operation is applied, second derivative spectra are frequently multiplied by a scaling factor of -1 so that the derivative spectrum can be compared more easily to the raw absorbance spectrum.

should in principle give the same result when performed separately on the raw spectrum; that is they should produce the same number of component bands at similar frequencies (Cameron and Moffatt, 1984). However, it is good practice to attempt both band narrowing techniques individually to confirm the presence of the component bands and improve the reliability of the analysis to follow (Jackson and Mantsch, 1995).

1.4.6 Non-subjective data reduction techniques

Truncation of specific spectral subregions from a spectrum by the spectroscopist is entirely subjective (section 1.4.4). Data reduction may involve selection of spectral subregions or specific absorptions within $1000\text{-}1800\text{ cm}^{-1}$ and $2800\text{-}3600\text{ cm}^{-1}$ for comparison of groups/classes of spectra in global analysis of the data (section 1.7.3). In this case, the subjectivity of choosing diagnostic subregions or absorptions can be problematic. Alternatively, this subjectivity can be lifted by utilization of a computer algorithm to search for the most diagnostic regions of spectra belonging to two or more groups under comparison. One such computer algorithm is a genetic algorithm (GA) which searches through the number of possible combinations of diagnostic subregions as it is coupled to a multivariate statistical analysis program (section 1.7.3) that provides feedback to the GA on the success of its selections (Jouan-Rimbaud *et al.*, 1995; Bangalore *et al.*, 1996). An analogy to the GA method of optimal spectral subregion selection is the process of natural selection and gene mutation in which spectral subregions are analogous to “genes”, combinations of such are analogous to “chromosomes” and a multivariate analysis algorithm is utilized as the validation system to discern the most effective “chromosomes” for group comparison.

In the initialization step of a simple GA, each variable (wavelength or spectral subregion) that comprises a “chromosome” is randomly chosen to be used either in the prediction or unused by assigning a value of either one or zero, respectively (Bangalore *et al.*, 1996). This initial “chromosome” goes through a mutation process that randomly varies these values to generate a population of chromosomes for each spectrum, the number in the population designated by the user (Bangalore *et al.*, 1996). In the second step of the GA, the evaluation step, each “chromosome” of this original population pool is tested using multivariate statistical analysis to generate a calibration model (Bangalore *et al.*, 1996). One such multivariate analysis is linear discriminant analysis (LDA) which is used to clas-

sify spectra from two comparable groups (section 1.7.3). For LDA utilizing input data selected by a GA, the spectra are assigned by the user to the class or group of spectra to which they belong and the LDA evaluates whether class separation is achievable using the GA-selected “genes” (subregions) given in each “chromosome” of the original population pool. The overall goal of this evaluation step is to guide the GA to a global optimum for the highest LDA separation attainable, retaining the most effective “chromosomes” for the next generation of the optimization. Retention of the most effective chromosomes is accomplished in the third step of the GA, the “exploitation” step (Bangalore *et al.*, 1996). During “exploitation”, pairs of chromosomes are randomly selected from the original population pool and evaluated, subsequently a clone of the chromosome with the higher LDA separation is placed into a separate pool called the “mating subset”. The pair of chromosomes is replaced in the original population pool and this selection is repeated until the “mating subset” is the same size as the initial population pool. The overall result in the exploitation step of the GA, akin to natural selection, is that there will be many copies of the proficient chromosomes within the “mating subset”, ensuring the minimal appearance of ineffective chromosomes. The final step of the GA is the exploration step which involves mutation and recombination to introduce diversity into the population (Bangalore *et al.*, 1996). In this exploration step, two chromosomes from the “mating subset” are selected and allowed to recombine and exchange genes (subregions) to produce progeny and upon further random mutation these new chromosomes are evaluated by the LDA. The most effective progeny chromosomes are placed into a new population which replaces the original population pool and the process undergoes another iteration (generation) to optimize the LDA separation. The programs are allowed to iterate through a number of generations designated by the user, the final result providing a list of the best genes (subregions) for LDA classification of the spectral groups. The success of GA-selection is evaluated on the basis that the spectral subregions selected are of biodiagnostic value such that assignments of absorptions represented by the selected subregions can be made and rationalized to be attributable to compositional differences between the samples under comparison. Various approaches to spectral preprocessing (normalization FSD, FD, truncation, etc.) may have to be attempted prior to GA-selection of spectral subregions for a meaningful result.

1.5 SPECTRAL FEATURES OF TISSUE COMPONENTS *IN VITRO*

Over the last three to four decades, FTIR spectroscopy has been successfully implemented in studies concerning the structure, interaction and dynamics of isolated tissue components such as proteins (Jackson and Mantsch, 1995), lipids (Mantsch and McElhaney, 1991), carbohydrates (Wong *et al.*, 1991) and nucleic acids (Taillandier and Liquier, 1992). These *in vitro* experiments of the past that concentrated on structural and molecular dynamics analysis and interactions between different macromolecules were facilitated by the observation that these molecules absorb in characteristic regions of the mid-IR due to the presence of unique functional groups. Therefore, a discussion of the typical spectral features of proteins, lipids, carbohydrates and nucleic acids *in vitro* will aid in exemplifying the utility of mid-IR spectroscopy to examine such macromolecules.

1.5.1 Characteristic absorptions of proteins

Implementation of IR spectroscopy in the characterization of protein absorptions useful in structural determination began fifty years ago with the identification of the main absorptions, the amide I and II vibrational modes, sensitive to changes in secondary structural elements of polypeptides, such as α -helices and β -sheets (Elliot and Ambrose, 1950; Ambrose and Elliot, 1951). In tandem to experiment, descriptions of the contribution of different bonds in the amide group to these vibrations and correlations for amide groups in discrete secondary structural arrangements, began to arise from force-field analyses (for review see Jackson and Mantsch, 1995). Examination of protein secondary structure was then further facilitated through the advent of FT technology, and analytical approaches (section 1.7.2) were developed for delineating the quantitative contribution of different secondary structural motifs to the overall amide I absorption profile (Byler and Susi, 1986). For example, curve-fitting algorithms that fit the amide I band profile with component bands assigned to α -helical, β -sheet, turn and random coil structure were used to calculate the percent contribution of each structural element to the overall structure of the protein. However, for the better part of the last decade, quantitative protein structural analysis from curve-fitting the amide I band profile has been seriously questioned, especially when little is known about the structure of the protein (see section 1.7.2). As an alternative to curve fitting, more conservative (*i.e.*, less quantitative) approaches for delineating structural

information from the amide I band profile have been adopted (Surewicz *et al.*, 1993; Haris and Chapman, 1995; Jackson and Mantsch, 1995). For example, a less quantitative approach is to compare and contrast (either visually or by difference spectroscopy) the amide I band profile obtained when the protein is in different environments (*i.e.*, aqueous versus lipid environment) or upon fluctuation of the experimental conditions (*i.e.*, changes in temperature, pH, salt concentration). Regardless of what approach is used to extract information about protein structure from the amide I, they both work on the same underlying principle, namely that changes in the amide I band profile arise from changes in secondary structure. Moreover, the assignment of amide I “component bands” (quantitative approach) or “shoulders” (less quantitative approach) to different protein structural elements is the same. That is, both approaches use literature-accepted frequency ranges to assign features of amide I band profile to particular structural elements of the protein, such as regular secondary structural motifs (α -helices, β -sheets), turn structures, unordered (or random coil) polypeptide segments and peptide aggregates. It is also possible to extract information regarding protein tertiary structure by monitoring the frequency of amino acid side chain absorptions that appear outside the range of the amide I band profile.

Numerous studies that have been carried out over the last fifty years have generated a great deal of information regarding the characteristic absorptions of proteins. The functional group moieties responsible for protein absorption in the mid-IR can be divided into two groups, those due to absorption by the polymeric amide bond moiety of the polypeptide backbone (-CO-NH-) and those due to the various moieties of the amino acid side chains. Both types of absorptions will be conformationally sensitive, the former primarily sensitive to hydrogen bonding effects on the amide C=O and NH, the latter sensitive to the environment in which the amino acid side chain is exposed (section 1.1.1). Therefore, secondary structural changes can be monitored by observation of spectral changes in the polypeptide backbone absorptions and tertiary structural changes can be monitored by changes in the absorptions of amino acid side-chains that appear outside the amide I frequency range.

Absorptions of mid-IR radiation by the polypeptide backbone (-CO-NH-) occur in several regions of the spectrum depending on the functional group or coupling of functional groups in question (for review see Surewicz *et al.*, 1993; Jackson and Mantsch, 1995; Haris

and Chapman, 1995). The so-called amide I vibration, which arises predominantly from C=O stretching of the amide group (minor contribution from C-N stretching, 20%), occurs between 1600 and 1700 cm^{-1} . The amide II absorption arises from amide NH in-plane bending coupled with a contribution from C-N stretching (40%) and appears between 1480-1575 cm^{-1} . Since both the oxygen of the amide carbonyl and the proton of the amide NH are subject to hydrogen bond formation in folded polypeptides, both of these conformationally sensitive absorptions are commonly monitored to assess protein secondary structure. A third, less commonly monitored absorption is the amide III vibration which arises from a variety of coupled vibrations (CN stretching/NH in-plane bending/C-C stretching/C=O in plane bending) and occurs between 1229-1301 cm^{-1} . Finally, NH stretching can be observed to absorb between 3100-3300 cm^{-1} but it is in resonance with the second overtone of the amide II ($2 \times \delta(\text{NH})$), thus it is usually taken as an indication of protein content in mixed samples, rather than a source of information about protein structure.

The amide I vibration essentially arises from one functional group vibration, the amide C=O, therefore the amide I band profile between 1600 and 1700 cm^{-1} is the main spectral subregion of interest for studying protein conformation (Surewicz et al 1993; Jackson and Mantsch, 1995; Haris and Chapman, 1995). The bending vibration of water (1645 cm^{-1}) will obscure the amide I band, which explains why protein solutions prepared *in vitro* for conformational analysis are typically studied in D_2O rather than water. As each amide group in the polypeptide backbone contributes to this absorption, the wide amide I band profile that results is a composite of every amide C=O moiety in the protein backbone. Protein structure and conformational changes can be monitored by analysis of the position and intensity of these overlapping amide I component bands which can be frequently seen as shoulders upon the amide I maximum. These component bands arise due to the different H-bonding patterns in the various secondary structures (α -helices, β -sheets, etc.) adopted by folded proteins. Recall, that vibrational modes are sensitive to external dipoles capable of extracting electron density from the vibrating group, such as hydrogen bonds (sections 1.1.2 and 1.1.3). Therefore, H-bonded amide C=O groups will vibrate at lower frequency than free amide C=O groups. In addition, there is a semi-empirical correlation between the frequency of the amide I component bands and the strength of the H-bond to the carbonyl oxygen: the stronger the H-bond, the more electron density is pulled from the vibrating

group and thus the less energy (*i.e.*, lower the cm^{-1}) required for the C=O stretch of the amide I (Jackson and Mantsch, 1995). Aside from this semi-empirical correlation, studies on homopolypeptides helped to establish where the amide I vibration will absorb for regular secondary structures (α -helices, β -sheets) and unordered polypeptides (Jackson *et al.*, 1989), while studies on cyclic peptides facilitated the assignment of the turn-like structures that occur in folded proteins (Mantsch *et al.*, 1993). Note however, polar homopolypeptides (*i.e.*, poly-L-lysine) tend to be more hydrated than heteropolypeptides (Jackson *et al.*, 1989). In turn, the high dielectric constant of the aqueous solvent (*i.e.*, solvent dipole) can lower the frequency (*ca.*, 5-10 cm^{-1}) of α -helices and β -sheets (Jackson *et al.*, 1989). Therefore, it has been equally important to analyze the amide I band profile of a variety of proteins and peptides with known structures obtained by x-ray crystallography, NMR and CD spectroscopy, in addition to model compounds. As a result of fifty years of experimentation and theoretical correlations, there is a somewhat flexible consensus which directs the assignment of component bands of the amide I band profile to particular protein structures. Shown in Table 1-3 are the expected frequency ranges for various structures commonly found in proteins.

Table 1-3. Literature assignment of components bands of the amide I band profile.¹²

Abbreviations: HF, high frequency; LF, low frequency.

Amide I frequency/ cm^{-1}	Assignment
1680-1685	Antiparallel β -sheet HF component ($50 \text{ cm}^{-1} >$ than LF)
1666	3_1 -helix structural motif due to collagen (poly-Pro helix)
Above 1660	Turns
1648-1660	α -helices
1640-1648	Unordered
1637	3_{10} -helices
1625-1640	Parallel β -sheet and antiparallel β -sheet LF component
1610-1628	Aggregated strands
1619	Low frequency turns (strong H-bonds possibly bifurcated)

12. Literature values in Table 1-3 were compiled from Jackson and Mantsch, 1995, Liu *et al.*, 1996 and Troullier *et al.*, 2000.

As can be seen in Table 1-3, the frequency of the amide I decreases for amide groups accordingly: turns > α -helices > unordered (random coil) > β -sheets > aggregated strands. Following the correlation between H-bond strength and the frequency of the amide I, amide carbonyls involved in strong intermolecular H-bonding, such as those in aggregated proteins, absorb at lower frequencies (1610-1628 cm^{-1}) and frequently exhibit a narrower bandwidth to those involved in weaker and more variable intramolecular H-bonding patterns of regular secondary structures (Table 1-3). For example, parallel β -sheets have non-linear intramolecular H-bonds which are much weaker than linear intermolecular H-bonds and therefore amide I carbonyls involved in this structure absorb at slightly higher frequency range (1625-1640 cm^{-1}) than those in aggregated strands. Although, antiparallel β -sheets have linear intramolecular H-bonds, which are presumably stronger than the non-linear intramolecular H-bonds of parallel β -sheets, antiparallel β -sheets have been reported to absorb in the same frequency range as parallel β -sheets. However, the arrangement of H-bonded amide carbonyls in neighboring strands of antiparallel β -sheets leads to a phenomenon known as "transition dipole coupling" which splits the amide I vibration into two component bands, a high frequency component (HFC) band (1680-1685 cm^{-1}) and a low frequency component (LFC) band approximately 50 cm^{-1} lower (Moore *et al.*, 1975; Chapman and Haris, 1995). Therefore, although the LFC band of antiparallel β -sheets occurs within the same frequency range as a parallel β -sheet component band (1625-1640 cm^{-1}), antiparallel β -sheet structure can be distinguished from parallel β -sheet structure by the presence of the HFC band (1680-1685 cm^{-1}).

As shown in Table 1-3, other high frequency bands are frequently observed which may be attributable to non-H-bonded amide carbonyls such as those found in the bend of a turn which absorb above 1660 cm^{-1} because they do not experience withdrawal of electron density from H-bonding (Mantsch *et al.*, 1993). Furthermore, amide carbonyls involved in the structural motif of collagen, the poly-Pro helix, also absorb at this high frequency as proline cannot provide a H-bonding partner to nearby carbonyl oxygens. However, this high frequency component band (1666 cm^{-1}) is typically accompanied by a lower frequency component band (1628 cm^{-1}) due to amide carbonyls involved in intermolecular H-bonding between cross-linked strands of the collagen triple helix (Liu *et al.*, 1996). Intermediate between the high frequency free carbonyls and those involved in intra- or intermolecular

H-bonding of β -sheets are absorptions of amide I carbonyls in unordered, α -helical and 3_{10} -helical structures (Table 1-3). Jackson and Mantsch, 1991*b*, reported that 3_{10} -helices absorb at higher frequency (1660-1666 cm^{-1}) than α -helices (1648-1660 cm^{-1}) because the H-bonds in 3_{10} -helices are less linear (*i.e.*, weaker) than those in α -helices. However, this observation was made from spectra acquired in chloroform solution, which had a lower dielectric constant than D_2O . Recently, Troullier *et al.*, 2000 observed that amide I carbonyls involved in a 3_{10} -helical structural motif in α -lactalbumin absorb at 1637 cm^{-1} . This assignment for 3_{10} -helices was preferred for entry into Table 1-3 since Troullier *et al.*, 2000 acquired the spectrum of α -lactalbumin in D_2O . It should be noted that it is difficult to distinguish between α -helical and unordered (or random coiled) structures based solely on the frequency of the amide I due to the proximity of their respective spectral ranges for absorption (see Table 1-3). However, due to the conformational flexibility of unordered proteins, the H-bond length is more variable than that in the regular repeat of undistorted α -helical structures. Therefore, the contour of the amide I band profile for unordered proteins is typically wider than that for α -helical structures. Should discrepancy between the two structures still exist, H-D exchange experiments, which monitor the progressive shift of the amide I and amide II vibrations to lower wavenumbers (10-14 cm^{-1} and 100 cm^{-1} , respectively), can provide discrimination since α -helical structures exchange at slower rates than unordered structures (Haris and Chapman, 1995).

The amide I profile is not the only useful IR absorption feature for defining protein structure, as amino acid side chain absorptions that appear just outside the window of the amide I profile can provide information regarding changes in protein tertiary structure. Table 1-4 presents some amino acid side chain absorptions that are useful for monitoring changes in protein tertiary structure. These absorptions, determined in D_2O at neutral pD, all fall in the range 1500-1610 cm^{-1} (Chirgadze *et al.*, 1975). For aspartic and glutamic acids, COO^- symmetric stretching appears at 1584 and 1567 cm^{-1} , respectively, whereas the absorption by the amide moiety of asparagine and glutamine side chains is effectively masked by the amide I absorption. The symmetric stretching absorption of the δ -guanidino group of arginine (1586 cm^{-1}) is near that of aspartic acid, however the asymmetric stretch (1608 cm^{-1}) can be utilized to distinguish between Arg and Asp. Without deuterium exchange, the δ -guanidino group absorptions appear about 50 cm^{-1} higher and would there-

fore be masked by the amide I absorption in tissues or samples prepared in water (Venyaninov and Kalnin, 1990). Finally, the aromatic ring of tyrosine absorbs in the vicinity of low frequency amide I vibrations but the absorption at 1515 cm^{-1} is usually free from other absorbing groups. Other aromatic amino acids (Trp, Phe, His) also absorb in the $1500\text{-}1800\text{ cm}^{-1}$ region of the mid-IR but their absorbances are weak and have not been particularly useful so far (Venyaninov and Kalnin, 1990). Outside of this region, the C-OH stretching of the hydroxyl moiety of Ser, Thr and Tyr can be found between 1160 and 1175 cm^{-1} . Upon glycosylation or phosphorylation of these amino acids, the hydroxyl group cannot H-bond, resulting in a C-O stretching vibration that is more pronounced at 1175 cm^{-1} (Wong *et al.*, 1991).

Table 1-4. Literature values for amino acid side chain absorptions at neutral pD.¹³

Amino acid	Relevant group	Frequency in D ₂ O/cm ⁻¹
Asp	COO ⁻	1584
Glu	COO ⁻	1567
Asn	CONH ₂	1648
Gln	CONH ₂	1635
Arg	[NHCH(NH ₂)=NH ₂] ⁺	1586, 1608
Tyr	Ring C=C	1515, 1615

Anything that alters the microenvironment of the amino acid side chain will change the frequency of that side chain vibration. Hydrogen bonding and electrostatic association would have a similar effect such that the frequency of the absorption would decrease due to electron withdrawing effects upon the vibrating group. For example, electrostatic association between the negatively charged carboxylate group of Asp side chains and the calcium cation found at the active site of a calcium-binding protein such as α -lactalbumin was found to decrease the frequency of the Asp COO⁻ absorption by more than 10 cm^{-1} (Troullier *et al.*, 2000). Furthermore, reduction in dielectric constant of the microenvironment, such as that found in the interior of a folded polypeptide, can decrease the polarization of a vibrating group (C=O, C-OH, COO⁻, etc.), increasing the electron density between the atoms of the vibrating group and thus the frequency of the vibration (Jackson and Mantsch,

13. Literature values in Table 1-4 taken from Chirgadze *et al.*, 1975.

1991*b*, 1995). Therefore, the absorption frequency for amino acid side chains as well as amide C=O groups can vary depending upon whether these groups are surface exposed or buried in the protein interior.

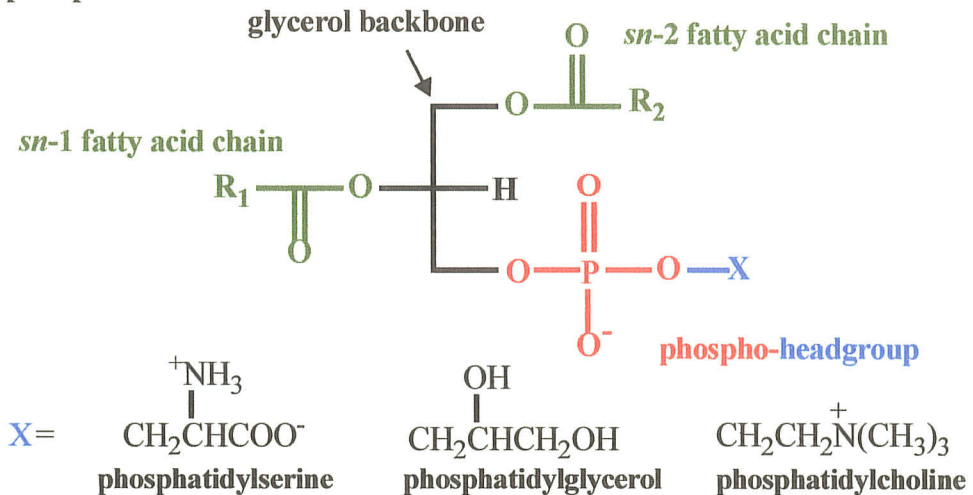
1.5.2 Characteristic absorptions of lipids

Lipids are of fundamental importance to biological systems. Maintenance of a semi-permeable lipid bilayer, the cell membrane, for separation of the internal contents of a cell from the exterior environment is essential for controlling the passage of water, electrolytes and other molecules through the bilayer. Moreover, the fluid bilayer of living systems houses channel and receptor proteins which participate in transport and cell-signaling mechanisms. Therefore, structural characterization of lipids in aqueous environments and in the presence of transmembrane and membrane-associated proteins is of great interest for understanding the function and behavior of the fluid mosaic cell membrane (Singer and Nicolson, 1972). Most spectroscopic techniques do not suffice in this area of study for a variety of reasons previously discussed (section 1.1.2). Differential scanning calorimetry can provide information regarding the thermotropic phase behavior of lipid samples but it does not provide structural information. However, with the advent of FT technology an abundance of FTIR applications in lipid investigations commenced in the late 1970s and the biophysical chemist was furnished with a relatively simple technique that could yield insight into both the structure and thermotropic phase behavior of lipids (Mantsch, 1998).

In general, FTIR investigations of the structure and thermotropic behavior of lipids have focused on the predominant class of lipids which comprises biological membranes, the phospholipids. Phospholipids are amphipathic with a hydrophobic end that consists of two long fatty acid hydrocarbon chains and a hydrophilic end (headgroup) consisting of a derivatized phosphatidic acid (Figure 1-10*a*). The net charge of the phospholipid is dependent on the moiety attached to the phosphate. For example, as shown in Figure 1-10*a*, phosphatidylglycerol (PG) and phosphatidylserine (PS) are both acidic phospholipids (net-negatively charged) while phosphatidylcholine is zwitterionic. Based on the functional groups of a phospholipid, the mid-IR spectrum should possess absorptions due to CH stretching and deformation of the long fatty acid hydrocarbon chains, ester C=O stretching of both acyl groups, phosphate stretching and other vibrations specific to the headgroup.

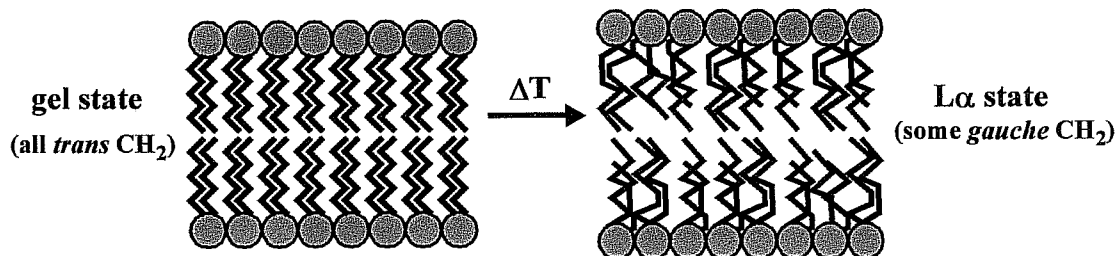
Figure 1-10. Generalized structure of a phospholipid molecule and organization of amphipathic phospholipids into a bilayer structure.

(a) Phospholipid molecule



Phospholipid bilayers are organized such that the headgroups align so as to interact with the aqueous environment, the glycerol backbone and acyl groups of the fatty acids form the interfacial region, and the long fatty acid chains align perpendicular to the membrane surface to form the hydrophobic core of the membrane (Figure 1-11). Shown on the left in Figure 1-11 is a bilayer in the highly ordered gel state in which the methylene groups of the acyl chains are in an “all *trans*” configuration. Upon an increase in temperature, disorder is introduced into the bilayer system such that the long acyl chains become “kinked” (Figure 1-11, right-hand side). The introduction of methylenes in a *gauche* configuration causes “kinking” of the long acyl chains leading to a progressive “kinking” in neighboring chains until the bilayer is in the more fluid, disordered liquid crystalline ($L\alpha$) state. Note however, in the liquid crystalline state not all methylenes of the hydrocarbon chains are in a *gauche* conformation, rather the relative proportion of *gauche* to *trans* methylenes has increased (Casal and Mantsch, 1984; Mendelsohn and Mantsch, 1986; Mantsch and McElhaney, 1991). The midpoint temperature of the highly cooperative gel-to- $L\alpha$ state transition is called the main phase transition temperature (T_m) of the lipid and can be determined experimentally using techniques such as scanning differential calorimetry, FTIR, FT-Raman and NMR (Casal and Mantsch, 1984).

Figure 1-11. Gel to liquid crystalline phase transition of a phospholipid.



Phospholipid absorptions in the mid-IR can be divided into three categories: those due to vibrations of the fatty acid hydrocarbon chains, the fatty acid acyl modes (interfacial region) and the headgroup vibrations (reviewed by Casal and Mantsch, 1984; Mendelsohn and Mantsch, 1986; Mantsch and McElhaney, 1991). The approximate group frequencies expected for the fatty acid hydrocarbon chains, the interfacial region and the headgroup are summarized in Table 1-5. For instance, CH stretching of unsaturated and saturated portions of the long hydrocarbon acyl chains can be distinguished from each other as the former appears between 3010-3050 cm^{-1} and the latter appears between 2800-3000 cm^{-1} . Furthermore, methylene and methyl CH stretching and bending bands are well resolved and for lipids, the ratio of CH₂ stretching (or bending) to that of CH₃ stretching (or bending) is high due to the greater proportion of CH₂ to CH₃ in the long fatty acid hydrocarbon chains. The ester carbonyl stretch of the fatty acid acyl moieties, which reside at the interfacial region of phospholipids in a bilayer, absorbs in a unique subregion of the spectrum, namely 1715-1745 cm^{-1} , while the ester C-O asymmetric (1170 cm^{-1}) and symmetric (1070 cm^{-1}) stretch may be obscured by the solvent or headgroup modes (Table 1-2 and Table 1-5). Finally, the phospholipid headgroups, which reside at the solvent-exposed portion of the bilayer, give rise to vibrations that can be subdivided into two further categories, the vibrations due to the phosphate moiety and those due to the group attached to the phosphate which characterizes the phospholipid (Table 1-5). The phosphodiester moiety gives rise to two strong bands due to asymmetric and symmetric phosphate stretch at about 1228 and 1085 cm^{-1} , respectively, while the phosphate-ester stretch absorbs at 1047 cm^{-1} . Headgroup moieties such as choline, glycerol, ethanolamine (not shown) and serine groups give rise to a variety of vibrational modes shown in Table 1-5 and those groups with exchangeable hydrogens (*i.e.*, ⁺NH₃) will shift to lower wavenumber (*ca.*, 50 cm^{-1}) when D₂O is used as the solvent.

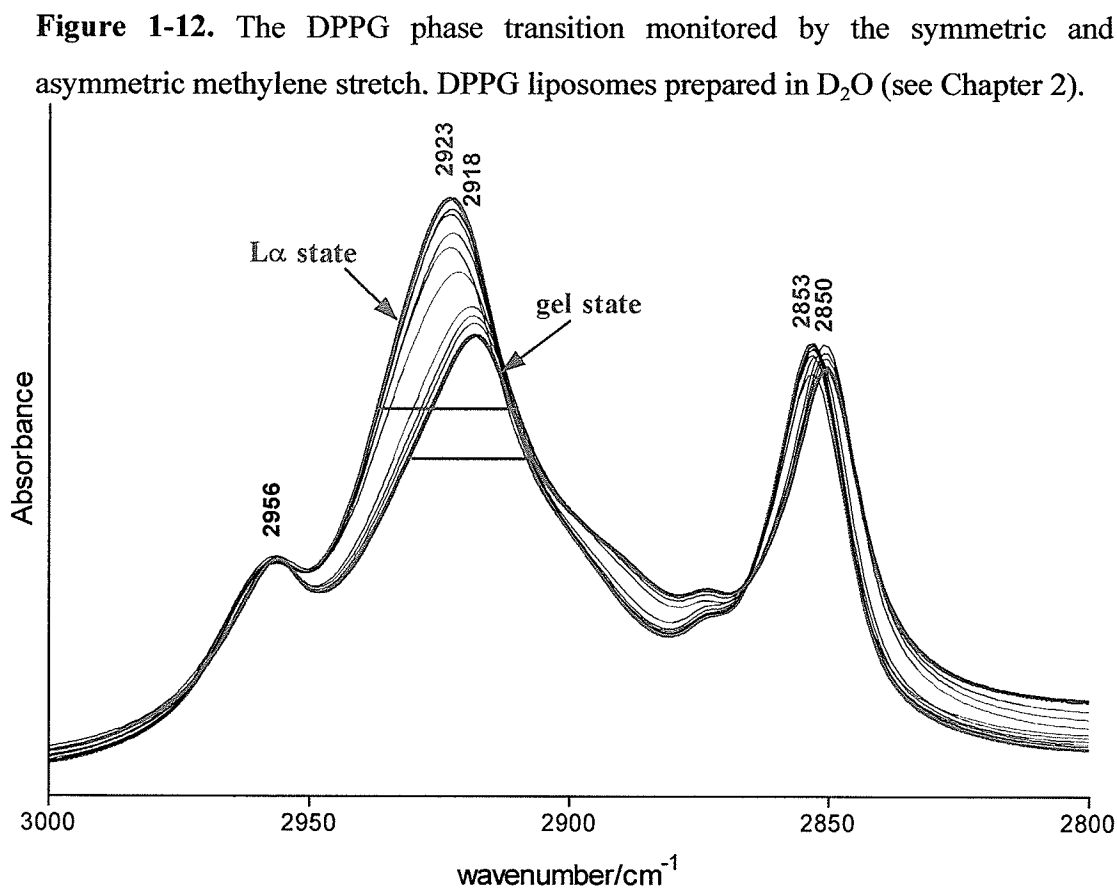
Table 1-5. Characteristic regions in the mid-IR where phospholipids absorb.¹⁴

Phospholipid moiety	Frequency /cm ⁻¹	Assignment
Fatty acid chains		
Unsaturated chains	3010-3050	C=C-H stretching
Saturated chains	2956, 2870	$\nu_{as}(\text{CH}_3)$ and $\nu_s(\text{CH}_3)$
	2920, 2850	$\nu_{as}(\text{CH}_2)$ and $\nu_s(\text{CH}_2)$
	1462-1475	CH ₂ scissoring
	1452-1457	CH ₃ deformation (asym.)
	1380	CH ₃ deformation (sym.)
	1190-1380	CH ₂ wagging procession
	720-1150	CH ₂ rocking/twisting procession
	Acyls	1715-1745
1170 and 1070		ester $\nu_{as}(\text{CO-O-C})$ and $\nu_s(\text{CO-O-C})$
Headgroup		
Phosphodiester	1220-1240, 1085	$\nu_{as}(\text{PO}_4^{2-})$ and $\nu_s(\text{PO}_4^{2-})$
	1047	phosphate-ester stretch, $\nu_s(\text{C-OP})$
Serine	1620 and 1400	$\nu_{as}(\text{COO}^-)$ and $\nu_s(\text{COO}^-)$
	1630 and 1571	$\delta_{as}(\text{NH}_3^+)$ and $\delta_s(\text{NH}_3^+)$
Glycerol	1000-1170	C-O-C and C-O-H
Choline	3050	$\nu_{as}(\text{CH}_3)_3\text{N}^+$
	1405	CH ₃ sym. bend, $\delta_s(\text{CH}_3)_3\text{N}^+$
	971	asym. stretch, $\nu_{as}(\text{C-N}^+-\text{C})$

Since the early 1980s FTIR spectroscopy has been utilized as a convenient tool to monitor phospholipid phase transitions. For example, acquisition of temperature-ramped spectra allows the methylene CH stretching absorptions to be monitored as a function of temperature thereby allowing the gel to L α transition of the lipid to be observed (Casal and Mantsch, 1984; Mendelsohn and Mantsch, 1986; Mantsch and McElhaney, 1991). As shown in Figure 1-12 for the phase transition of DPPG monitored by FTIR, the frequency of the overall band contour of the CH₂ asymmetric and symmetric stretching of DPPG increased upon moving from the gel (blue trace) to L α state (red trace) due to the increase

14. Group frequencies in Table 1-5 compiled from Casal and Mantsch, 1984; Mendelsohn and Mantsch, 1986; and Mantsch and McElhaney, 1991. The serine symmetric COO⁻ stretching frequency is expected to be similar to that of the free carboxylate end of an amino acid or peptide backbone (Chirgadze *et al.*, 1975).

in the *gauche/trans* ratio of CH₂ conformers as the temperature was increased. Furthermore, the band width at half maximum of these contours also increased upon the transition because in the L α -state more conformers contribute to the overall band contour (more fluid and flexible state). For the calculation of T_m, melting curves for this transition can be constructed by plotting the frequency of either $\nu_{as}(\text{CH}_2)$ or $\nu_s(\text{CH}_2)$ as a function of temperature (see Chapter 2). Another useful parameter to measure is the frequency of either extreme state (gel or L α state) in the transition because this is a localized measurement of the stability (*i.e.*, energy is directly proportional to frequency) of each state. Upon interaction with another molecule (*i.e.*, protein), a change in the stability of the gel and L α state of the lipid can then be assessed by the methylene frequency of the gel and L α state. The lower the methylene frequency of the gel and/or L α state, the more the intermolecular interaction has served to stabilize the state (see Chapter 2).



In addition to monitoring the order of the acyl chains, other absorptions can be monitored to establish the state of the phospholipid bilayer (for review see Casal and Mantsch, 1984; Mendelsohn and Mantsch, 1986; Mantsch and McElhaney, 1991). For instance, the ester C=O stretch (1715-1745 cm^{-1}) of the acyl chains can be evaluated to establish the hydration of the bilayer interfacial region, the overall band contour decreasing in frequency as the bilayer becomes more fluid. Upon Fourier self-deconvolution of this overall band contour, two component bands appear, which were initially assigned to the *sn*-1 (*ca.*, 1742 cm^{-1}) and *sn*-2 (*ca.*, 1727 cm^{-1}) C=O moieties of the bilayer interfacial region. It was initially thought that as the lipid approaches the more fluid $L\alpha$ state, the relative intensity of the *sn*-2/*sn*-1 C=O absorption increases since greater hydration at the bilayer interface allows an increase in H-bonding to the *sn*-2 C=O moiety. However, upon isotopic ^{13}C substitution of one acyl group, these component bands have been found to be composed of two further constituent bands, one representing the free C=O at higher frequency and the other the H-bonded C=O at lower frequency (Casal and Mantsch, 1984; Mantsch and McElhaney, 1991). Moreover, when the labeled phospholipid was in one state (gel or $L\alpha$) the frequency of the two acyl chain modes was found to differ by only 4 cm^{-1} when correction was made for the isotopic substitution (Mantsch and McElhaney, 1991). Therefore, it was concluded that the two deconvolved composite bands of the C=O contour of unlabeled phospholipids actually arises due to hydrated C=O groups rather than from the two distinct acyl moieties (Mantsch and McElhaney, 1991). That is, the higher frequency component band arises from free *sn*-1 and *sn*-2 C=O moieties while the lower frequency component band arises from those that are H-bonded. This example of a biologically plausible yet incorrect assumption in band assignment, illustrates the utility of isotopic substitution for progress in FTIR analysis of *in vitro* systems.

Since the two component bands of the acyl C=O profile arise from free (*ca.*, 1740 cm^{-1}) and H-bonded (*ca.*, 1725 cm^{-1}) acyl C=O, the T_m of the lipid may in principle be determined by the temperature-dependence of the relative intensity of these two bands. Since this would involve curve-fitting (section 1.7.2) the acyl C=O stretching profile at each temperature (20-30% error in each curve fit), the preferred method for T_m measurement is to monitor the temperature-dependence of the methylene stretching frequency. However, useful information can be derived from the hydration of the bilayer interfacial

region (*i.e.*, aqueous solvent access to the interface), measured by the relative proportion of the H-bonded C=O to free C=O in each state prior to and after the transition. For example, in the $L\alpha$ state, the relative intensity of the H-bonded C=O to free C=O stretch is higher than in the gel state, thus the hydration of the bilayer interfacial region is greater in the $L\alpha$ state. This is not surprising because the head groups in the $L\alpha$ state of a pure lipid are not as closely aligned to each other due to chain disordering, allowing more solvent access to the interfacial region (Casal and Mantsch, 1984; Mantsch and McElhaney, 1991). Upon interaction with another molecule (*i.e.*, protein), a change in the bilayer interfacial hydration of the gel or $L\alpha$ state of the lipid can provide information about the intermolecular interaction that took place in the state. For example, if the interaction caused the hydration of the $L\alpha$ state lipid to decrease, then the presence of the other molecule blocked solvent access to the interfacial region of the bilayer, perhaps by inserting hydrophobic segments into the bilayer (see Chapter 2).

Other absorptions, such as those due to the headgroup, are less sensitive to the gel to liquid crystalline phase transition of a lipid since the headgroup region of a phospholipid bilayer is already in contact with aqueous solvent (Mantsch and McElhaney, 1991). Therefore, only the methylene and acyl C=O stretching bands are useful for determining the phase behavior of the lipid. However, headgroup moieties are capable of participating in electrostatic interactions with other charged species, such as charged amino acids of a protein extrinsically associated with the lipid, and this interaction can alter the group frequencies of the respective headgroup (Mendelsohn and Mantsch, 1986).

Many of the strong absorptions due to phospholipids (*i.e.*, methylene and ester carbonyl stretching) occur outside regions in which proteins absorb, making them useful in FTIR investigations of protein-lipid interactions and dynamics. In contrast, some head group vibrations are difficult to observe in spectra taken of lipid-protein mixtures, since they are either obscured by the protein absorption (*i.e.*, serine) or absorption due to the aqueous solvent (*i.e.*, glycerol and phosphodiester). Of the phospholipids mentioned, phosphatidylcholine (PC) and phosphatidylglycerol (PG) do not absorb in the region of the amide I and are thus utilized most often in samples prepared *in vitro* in D_2O . Initially, the temperature dependence of the isolated samples is observed. For the lipid sample, the meth-

ylene and ester C=O stretching regions are monitored, while for the protein sample the amide I vibration is monitored. Subsequently, for protein-lipid mixtures, these spectral subregions can be used to simultaneously evaluate the change in the phase behavior of the lipid upon interaction with the protein and the change in protein structure dependent on interactions with the model membrane. Binary lipid mixtures can also be used in protein-lipid studies as long as one of the lipids is per-deuterated. Per-deuteration of one of the lipids allows for simultaneous observation of the asymmetric and symmetric CD₂ stretching vibrations (2193 and 2089 cm⁻¹, respectively) of the per-deuterated lipid, the CH₂ absorptions (2918 and 2850 cm⁻¹) of the other lipid, and the amide I absorption profile (1610-1700 cm⁻¹) of the protein (see Chapter 2).

1.5.3 Characteristic absorptions of nucleic acids

In vitro studies of the structure of nucleic acids by IR methods began in the mid-1900s (for review see Taillandier and Liquier, 1993) alongside the increasing applications to proteins and lipids. Various approaches (conventional FTIR transmission on solution and dried film samples, FTIR microspectroscopy on crystals) have been utilized to establish the characteristic mid-IR absorptions of short oligonucleotides and long polynucleotides, native DNAs and RNAs as well as cleavage products of native nucleic acids. Furthermore, the culmination of nearly fifty years of investigations and the development of pattern recognition programs have facilitated characterization of nucleic acid secondary structures and structural changes in the presence of other bound molecules, such as drugs and proteins. This area of research is extensive, therefore only the general features of FTIR spectra of nucleic acids, along with some of the characteristic mid-IR “marker bands” useful in delineating nucleic acid secondary structure, will be presented in this subsection.

The general mid-IR spectral features of nucleic acids arise from various vibrations within the different segments of the macromolecules. DNA and RNA are polymers of purine and pyrimidine deoxyribonucleotides and ribonucleotides, respectively, which are linked by 3',5'-phosphodiester bridges. The predominant spectral features of nucleic acids are found in the fingerprint region (1800-700 cm⁻¹) of the mid-IR and originate from the ring and C=O stretches of the purine and pyrimidine bases (1800-1500 cm⁻¹), coupled vibrations between the base and the sugar moieties (1500-1250 cm⁻¹), vibrations due to the

phosphate groups and the sugar ($1250\text{-}1000\text{ cm}^{-1}$), and coupled vibrations between the phosphodiester backbone and the sugar moieties below 1000 cm^{-1} (Taillandier and Liquier, 1993). In order to allow observation of all of these spectral subregions important for nucleic acid structural analysis, individual solution samples must be prepared in both H_2O and D_2O as the former obscures absorptions near 1600 cm^{-1} and below 1000 cm^{-1} , while the latter interferes with the absorptions due to the phosphates (Shie *et al.*, 1972; Taillandier and Liquier, 1993). Alternatively, dried films and crystals can be prepared to avoid solvent interferences with nucleic acid absorptions.

Computerized algorithms for pattern recognition have been developed based on a number of conformationally sensitive IR "marker bands" that can distinguish between different conformations of DNA (Taillandier and Liquier, 1993). DNA can adopt several double-helical conformations, such as those found for A-, B- and Z-DNA. Both A-DNA and B-DNA are right-handed double-helical structures (A-DNA is shorter and wider than B-DNA), while Z-DNA is a left-handed double-helix. Changes in temperature, relative humidity, ionic strength of the solvent and the type of counterions present can cause transitions between double- and single-stranded DNA and between the DNA double-helical conformers. For instance, by decreasing the relative humidity of B-DNA a transition from B-DNA to A-DNA can be induced, while a B-DNA to Z-DNA transition can be induced by decreasing the relative humidity in the presence of sodium cations (Taillandier and Liquier, 1993).

For exemplification of the utility of FTIR spectroscopy in the mid-IR for nucleic acid structural studies, Table 1-6 summarizes some of the more discriminating absorptions for A-, B-, and Z-DNA. As shown in Table 1-6, DNA conformers can be distinguished based on alterations in the base stacking arrangement observed by frequency shifts of the in-plane C=O stretching of the bases ($1695\text{-}1720\text{ cm}^{-1}$), absorption patterns from $1300\text{-}1500\text{ cm}^{-1}$ sensitive to the pucker of the deoxyribose sugar ring, and frequency shifts of the asymmetric phosphate absorption ($1215\text{-}1245\text{ cm}^{-1}$) of the phosphodiester linkages (Taillandier and Liquier, 1993). The absorption patterns observable in the $1300\text{-}1500\text{ cm}^{-1}$ region involve a complex coupling between the sugar moieties and the bases that is altered depending upon the pucker of the sugar ring and the orientation of the base to the sugar. For

instance, the sugar-base coupled vibrations between 1408-1425 cm^{-1} have been found to be sensitive to the pucker of the sugar ring which is different for A-DNA (C3'-endo), B-DNA (C2'-endo) and Z-DNA (pyrimidine base, C2'endo; purine base, C3'-endo) conformers (Taillandier and Liquier, 1993). However, the bands located at either 1375 or 1355 cm^{-1} are sensitive to the orientation of a purine base to the sugar (glycosidic torsion angle) where the *anti* geometry persists for A- and B-DNA while the *syn* geometry persists for Z-DNA (Table 1-6). There other numerous IR "marker bands" utilized in the computerized pattern recognition algorithms, the exact positions of bands also highly dependent upon DNA sequence (see Taillandier and Liquier, 1993). These pattern recognition programs have been developed to recognize the presence/absence of absorptions in the spectral subregions specific for distinguishing nucleic acid conformations.

Table 1-6. Example of some IR "marker bands" for distinction of A-, B- and Z-DNA conformers.¹⁵

Conformation			Assignment
A-DNA	B-DNA	Z-DNA	
1705	1715	1695	In plane base C=O stretch
1418, 1401	1425	1408	Deoxyribose pucker
1375	1375	1355	dA: dG anti-glycosidic linkage dA: dG syn-glycosidic linkage
1240	1225	1215	$\nu_{\text{as}}(\text{PO}_2^-)$

In FTIR spectroscopic investigations on *in vitro* preparations of nucleic acids in mixtures with other biological macromolecules there are several subregions which may overlap. For instance, the amide I and amide II vibrations sensitive to changes in protein conformation (section 1.5.1) will overlap with most of the base stretching subregion useful for structural characterization of nucleic acids, except for absorptions above 1700 cm^{-1} . Not surprisingly, absorptions due to carbohydrates (section 1.5.4) overlap with the sugar and phosphate absorptions of nucleic acids. In addition, phosphodiester stretching is typically

15. Values in Table 1-6 extracted from Table 1 in Taillandier and Liquier, 1993. For a comprehensive review of all conformationally sensitive IR "marker bands" see Taillandier and Liquier, 1993.

found in the same region for nucleic acids as it is for phospholipids (section 1.5.2). Therefore, for most FTIR examinations *in situ* (cells and tissues) absorptions due to nucleic acids are masked by the stronger absorptions due to other tissue components of greater concentration, such as proteins, lipids and carbohydrates (section 1.6). However, upon cell death and phagocytosis of cellular debris, tissue studies can typically reveal changes in nucleic acid content by observation of decreased absorptions between 1700-1718 cm^{-1} due to the loss of the nucleic acid base stretching vibrations (Jackson and Mantsch, 1996).

1.5.4 Characteristic absorptions of carbohydrates

Carbohydrates are the final group of biological macromolecules to discuss with respect to FTIR investigation, however unlike proteins, nucleic acids and lipids the acquisition of structural information from FTIR spectra is sparsely covered in the literature. Furthermore, the spectral region in which carbohydrates absorb overlaps with that due to phosphodiester linkages of lipids (section 1.5.2) and with the phosphodiester linkages and sugar moieties of nucleic acids (section 1.5.3). The main focus of FTIR biospectroscopy in this area has been the functional group absorptions of polysaccharides (*i.e.*, glycogen) and glycosylated proteins, in which a complex pattern of bands between 1000-1200 cm^{-1} has been observed (Wong, *et al.*, 1991).

Characteristic carbohydrate spectral features between 1000-1080 cm^{-1} arise from overlapping absorptions of C-O stretching of CH_2OH moieties (1028 cm^{-1}) with coupled vibrational modes for C-O-C stretching and bending of the sugar rings (1048 cm^{-1}), while C-OH stretching of the hydroxyls attached directly to the sugar ring occur in the 1154-1171 cm^{-1} region (Wong *et al.*, 1991). This latter band contour has been described as the overlap of two component bands, the lower frequency vibrational mode assigned to hydrogen-bonded C-OH groups and the higher frequency vibrational mode assigned to C-O vibrations of phosphorylated or O-linked glycosylated amino acids (Wong *et al.*, 1991). For glycogen however, only the C-OH stretching band at the lower frequency of 1148 cm^{-1} is observed as the hydroxyl groups of the polysaccharide are involved in hydrogen bonding (Wong *et al.*, 1991; Bromberg *et al.*, 1999b). Furthermore, for highly glycosylated proteins a similar pattern can be recognized in the spectral region between 1000-1180 cm^{-1} due to carbohydrate residues attached to asparagine (N-linked glycosylation) or serine, threonine,

tyrosine or hydroxyproline (O-linked glycosylation). For instance, IR spectra of the fibrous collagens, type I and type III, *in vitro* and *in situ* display a “fingerprint” pattern of bands at about 1032, 1082 and 1162 cm^{-1} due to carbohydrate residues attached to the numerous hydroxyproline residues of the collagen triple helix (Liu *et al.*, 1996; Liu *et al.*, 1999; Bromberg *et al.*, 1999a).

1.6 ANALYSIS OF TISSUES COMPONENTS *IN SITU*

The wealth of information accumulated over the last four decades by *in vitro* spectroscopic studies of isolated tissue components, and combinations of them, has facilitated the spectroscopic examination of select tissue components *in situ* in their native environments, namely in cells and tissues (Jackson and Mantsch, 1996). A mid-IR spectrum of a cell or a tissue is a sum of all of the IR-active functional group vibrations in the sample in proportion to the relative concentration of these functional groups in the cell or tissue. Although, some of the functional groups in proteins, lipids, nucleic acids and carbohydrates absorb IR radiation in the same spectral subregion, the number of each type of functional group varies from molecular species to molecular species. For example, proteins have the greatest proportion of amide C=O groups while nucleic acids and lipids have the greatest proportion of phosphodiester linkages. Moreover, the relative proportion of the same functional groups can be different for each macromolecule. For example, lipids have the highest proportion of methylene to methyl groups, in comparison to the other three macromolecules. Finally, the relative proportion of the biological macromolecules themselves in the cell or tissue is variable. For example, white matter of the brain contains a predominant amount of lipid while gray matter contains a predominant amount of protein. An understanding of the cell or tissue morphology and biochemical composition is therefore an absolute requirement to assign the various absorptions to functional groups from these four major biological macromolecular components. By careful consideration of all of these principles, numerous IR studies have been able to characterize the spectra of various types of cells and tissues extracted from non-diseased humans and animals (Jackson and Mantsch, 1996; Jackson *et al.*, 1997). Conventional FTIR transmission (section 1.2.2) and ATR-FTIR (section 1.2.3) techniques for macro-sampling have both been used to discern the relative contributions of protein, lipid, carbohydrate and nucleic acid constituents to the over-

all state of tissues. Moreover, for a more localized description of the contributions of protein, lipid, carbohydrate and nucleic acid constituents on the cellular level, micro-sampling of the tissue utilizing FTIR microspectroscopy has been used (section 1.2.4. and 1.2.5). Therefore, despite the spectral overlap of absorptions from different macromolecular constituents of cells and tissues, some information can be extracted that addresses the molecular structure of the sample. Based on the countless FTIR studies that have been carried out biological macromolecules in both *in vitro* mixtures and *in situ*, the spectral subregions of most interest for simultaneous observation of tissue constituents *in situ* are summarized in Table 1-7.

Table 1-7. Mid-IR spectral subregions frequently used for simultaneous observation of tissue constituents *in situ*.

Tissue component	Subregion (cm⁻¹)	Assignment
Protein	1600-1700	amide I
Lipid	2800-3100	CH stretch
	1735-1745	ester C=O
	1450-1470	CH bend
	1000-1300	PO ₂ ⁻
Nucleic acids	1705-1710	Base C=O
	1400-1500	Sugar pucker
	1000-1300	PO ₂ ⁻
Carbohydrates	1000-1200	C-O-C and C-OH

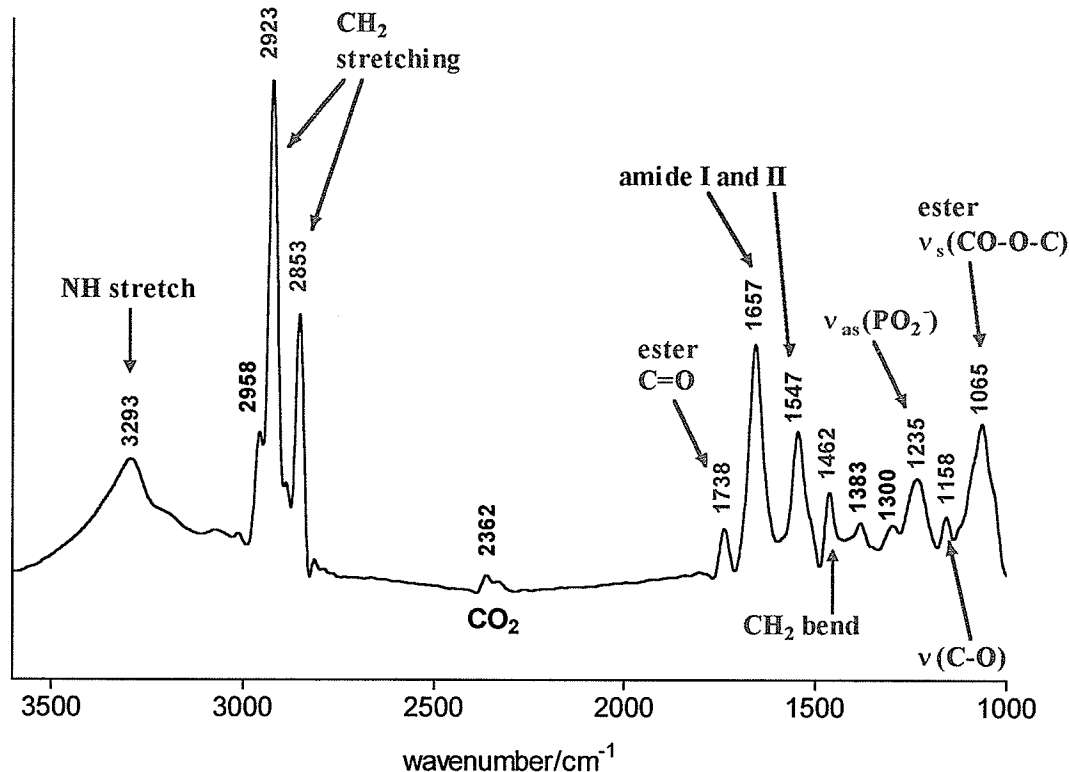
Notice that band assignment in spectra acquired on samples *in situ* can be difficult because some of the subregions summarized in Table 1-7 overlap with subregions of importance to multiple constituents within the sample. For example, phosphodiester stretching vibrations due to lipid and nucleic acid typically overlap, while absorption due to carbohydrates overlaps with that of nucleic acids and carbohydrate bands experience extensive overlap with phosphodiester bands. Since IR is a concentration dependent absorption phenomenon (section 1.3.1) and not all constituents contribute equally to the biochemistry of the sample, the contributions of the individual constituents are reflected by their relative intensities in the IR spectrum. Therefore, regardless of the spectral overlap,

uncertainty can be lifted by considering the relative intensities of the normally strong bands for the suspected components (*i.e.*, proteins, lipids, nucleic acids or carbohydrates).

As an example of recognizing absorptions *in situ* to assess the biochemical makeup of a tissue, consider the mid-IR spectrum acquired on a thin microtomed tissue section of the hippocampus shown in Figure 1-13. This spectrum was acquired using synchrotron FTIR microspectroscopy (section 1.2.5) on a focal region ($18 \times 18 \mu\text{m}^2$) in the white matter (see Chapter 4). Upon visual inspection of the spectrum, the most intense absorptions can be observed in the C-H stretching region ($2800\text{-}3000 \text{ cm}^{-1}$), assigned to the asymmetric (2923 cm^{-1}) and symmetric (2853 cm^{-1}) of methylene groups.¹⁶ The high relative intensity of CH_2 (2923 cm^{-1}) to CH_3 (2958 cm^{-1}) asymmetric stretching and CH_2 (1462 cm^{-1}) to CH_3 (1383 cm^{-1}) deformation, suggests the presence of long hydrocarbon chains in the tissue region examined (see section 1.5.2). Verification that these absorptions arise from the long hydrocarbon acyl chains of lipids comes from presence of a strong ester C=O stretch (1738 cm^{-1}) of fatty acid acyl moieties. Moreover, the high relative intensity of the asymmetric CH_2 (2923 cm^{-1}) to NH stretching (3293 cm^{-1}) suggests that lipid content predominates over protein in the tissue region examined. This is not an unexpected result as the composition of human central nervous system (CNS) white matter is approximately 60% lipid to 40% protein and that of myelin is 70% lipid to 30% protein (Morell *et al.*, 1994). Confirmation that the majority of the lipids belong to the phospholipid family is obtained by observation of strong asymmetric (1235 cm^{-1}) and symmetric (1080 cm^{-1}) phosphodiester stretching absorptions, although the latter is overlapped by ester C-O absorption at 1065 cm^{-1} . It is improbable that these phosphate absorptions arise from a nucleic acid component, because a prominent C=O base stretching absorption between $1710\text{-}1721 \text{ cm}^{-1}$ is absent. The prominence of phospholipid absorption in the tissue is not surprising as the total phospholipid content of CNS white matter accounts for nearly 45% of the lipid content.

16. For a molecule of low symmetry, a symmetric stretch is observed, but just not as IR-active as the asymmetric stretch (section 1.1.2), thus the asymmetric CH_2 stretch in Figure 1-13 is greater in relative intensity to the symmetric CH_2 stretch.

Figure 1-13. Assignment of IR bands to white matter constituents *in situ*.¹⁷



Aside from discerning the relative contribution of lipids to proteins and identifying the predominant lipid class, structural information on these constituents *in situ* can also be obtained (Figure 1-13). The amide I maximum of the total protein in the spectrum is 1657 cm⁻¹, suggesting a predominant contribution from α -helical proteins in the tissue region examined (see section 1.5.1). Proteolipid protein (PLP) and myelin basic protein (MBP) make up 60-80% of the total protein content in CNS myelin, MBP accounting for 30% of the total protein (Morell *et al.*, 1994). PLP is thought to have a number of α -helical domains that span the myelin membrane based on hydrophathy plots of the amino acid sequence (Morell *et al.*, 1994). In contrast, MBP primarily associates with the membrane surface and the structure *in situ* is believed to contain β -sheet, random coil and α -helical structure based on *in vitro* studies (see Chapter 2). The structures of both proteins would have contributed to the amide I band profile of the tissue. However, PLP (30 kDa) is nearly twice as large as

17. Spectrum taken of the white matter of the hippocampus of the human brain using synchrotron FTIR microspectroscopy. Experimental details given in Chapter 4.

MBP (18.5 kDa) (Morell *et al.*, 1994), thus the concentration of PLP amide C=O groups in the tissue would be nearly twice that of MBP amide C=O groups and PLP would have a greater contribution to the amide I band profile of the tissue. As for the molecular structure of the lipid component of the tissue, the frequencies of the methylene asymmetric stretch (2923 cm^{-1}) and symmetric stretch (2853 cm^{-1}) show that the lipids were in a highly fluid $L\alpha$ -state (see section 1.5.2). Transmembrane proteins, such as PLP, cause kinking in neighboring acyl chains which further propagates kinking throughout the bilayer. Such a domino-like phenomenon participates in maintaining fluidity in mammalian membranes, such as myelin. The observation that the membrane was still above its T_m suggests that the native myelin membrane structure was maintained despite the experimental conditions¹⁸.

As illustrated, FTIR is sensitive to the biochemistry and molecular structure of cells and tissues in the normal state. Changes in the biochemistry and molecular structure in diseased tissue are just as easily detected (for review see Jackson and Mantsch, 1996; Jackson *et al.*, 1997). Therefore, FTIR comparison of tissues in normal and diseased states provides a method for direct assessment of the biochemical changes associated with the tissue pathology without chemicals, stains or molecular probes (Jackson and Mantsch, 1996; Jackson *et al.*, 1997). However, to insure that the IR-detected difference(s) are associated with the disease, intact samples are collected from a population representative of each tissue state (*i.e.*, normal and abnormal) because biochemistry can vary within each population. The intact sample collected depends on where the disease is localized in the gross anatomy and/or what specific part of that organ is involved (*i.e.*, heart ventricle, cornea, hippocampal gray matter, *etc.*). In addition, multiple tissue spectra of each intact sample from a population are also required because of “macroscopic heterogeneity” within each intact sample. For example, the distribution of cells and extracellular matrix in an intact sample can be asymmetric. Similarly, the biochemical changes associated with the tissue pathology can be distributed asymmetrically throughout the intact sample. Even if it were possible to take a single IR spectrum of the intact organ, biochemical changes associated with the tissue pathology may be so “diluted” by unaffected portions of the tissue that little

18. The tissue section most likely experiences moisture loss and spectral acquisition was at room temperature, 10-15°C below physiological temperature (see Chapter 4).

spectral difference between the abnormal and normal tissue is observed. Therefore, to avoid spectral “dilution” of the biochemical change, small random samples of normal and abnormal organs are examined. In such an approach, FTIR transmission (section 1.2.2) or FTIR-ATR (section 1.2.3) is chosen for the macroscopic sampling technique (section 1.3.3). However, since numerous spectra are collected for each tissue state, it is impractical to commence data analysis with an assignment of all bands in each spectrum. Instead, data analysis may begin with spectral interpretation of the class average spectrum of each tissue group and the within-group standard deviation spectrum. Note, this is only done to provide the spectroscopist with general information about the two classes of spectra because this is equivalent to “diluting” the biochemistry of each tissue. Nevertheless, comparison of the class average spectrum of the normal group to that of the control group allows for the most biodiagnostic spectral subregions to be selected for the more rigorous approach used for global data analysis (see Chapter 3). The approach used for global data analysis is typically a multivariate statistical analysis performed with a computer algorithm. Such algorithms have certain limitations and are only successful when the spectral data is reduced (section 1.7.3). The most biodiagnostic spectral subregions or absorption bands can be chosen by the spectroscopist (*i.e.*, using the class average spectra as a guide), but this adds to the subjectivity of the study (section 1.4.5). Alternatively, a genetic algorithm (GA) can be used to select the most biodiagnostic spectral subregions or absorption bands non-subjectively when it is coupled to the multivariate analysis algorithm (section 1.4.6). Multivariate statistical analysis serves to classify the “undiluted” tissue spectra as either normal or abnormal for biodiagnostic purposes. Thereafter, to find the biochemical changes associated with the pathology that lead to this classification, the spectroscopist has to return to the class average spectra of each group and assign the bands to particular functional groups. The GA-selected subregions/bands can also be used to find biochemical changes associated with the disease, but a difference spectrum between the class average spectra is still needed to assess whether a tissue constituent increased or decreased as a result of the disease (see Chapter 3).

Differentiation of normal and abnormal tissue using FTIR microspectroscopy (sections 1.2.4 and 1.2.5) follows a different procedure than macro-sampling investigations. Although tissue examination using IR transmission or ATR reduces the “macroscopic het-

erogeneity” in an intact sample, spectral “dilution” still occurs due to “microscopic heterogeneity” in the tissue. That is, tissue morphology and cellular anatomy are asymmetric. Different cell types, cells in different stages of differentiation, extracellular material, *etc.*, contain different macromolecular components in various concentrations. A spectrum collected on an unspecified group of these tissue constituents would be the spectral average and biochemical changes on the cellular level specific to a tissue pathology would be “diluted” or perhaps even misleading (Boydson-White *et al.*, 1999). For example, IR microspectroscopy of individual cells in different phases of the cell cycle has shown that cell DNA absorptions are only detected during replication (S phase), while in later phases (G1 and G2) the DNA is so tightly packed in the nucleus that it is opaque to the IR light (Boydson-White *et al.*, 1999). These observations at the cellular level have serious consequences with respect to numerous macroscopic studies that used IR-detected changes in DNA content to differentiate between diseased and normal tissue. That is, since cells in different phases of cell division are unequally distributed throughout tissue, previous IR investigations may have (by chance) sampled tissue with a greater population of cells in the S phase (Boydson-White *et al.*, 1999). Such “macromolecular heterogeneity” at the cellular level can be addressed using FTIR microspectroscopy with a small aperture ($< 20 \times 20 \mu\text{m}^2$) and a synchrotron IR source (section 1.2.5). Alternatively, high spatial resolution ($< 3 \mu\text{m}^2$) can also be obtained using an IR microscope and focal plane array (FPA) detection, albeit nominal spectral resolution is limited to 16 cm^{-1} (Kidder *et al.*, 1997; Boydson-White *et al.*, 1999; Diem *et al.*, 2000). Depending on which IR microspectroscopic technique is used, hundreds (synchrotron IR) to tens of thousands (FPA detector) of spectra can be collected in each spectral “map” on the tissue section. This in combination with the number of spectral maps/tissue section, the number of sections/tissue and the number of subjects examined, equates to far too many spectra to interpret separately at the onset of data analysis. Instead, each spectral map is analyzed as a single unit using “multidimensional analysis” (see section 1.7.4) to create an FTIR image of the tissue region, prior to spectral interpretation. Thereafter, the tissue section is histochemically stained and the FTIR image of the tissue can be visually compared to the light microscopy images of the tissue prior to and after histochemistry. The spectra that correspond to morphological features in the FTIR image of normal tissue are interpreted and correlated to the corresponding morphological

features of the stained tissue (*i.e.*, cells, parenchyma, blood vessels, *etc.*). In contrast, the spectra that correspond to morphological features in the FTIR image of abnormal tissue are interpreted and correlated to the corresponding pathological features of the stained tissue (*i.e.*, plaques, necrotic cells, fat deposits, *etc.*). Comparison of the FTIR image to the photomicrograph of the unstained tissue is also helpful since stains specific to one tissue component can reduce the contrast of other morphological features in the photomicrograph. Spectral differences between a morphological feature in the normal and diseased state then represent the biochemical change associated with the pathology of the disease.

1.7 DATA ANALYSIS

Analysis of the spectral data acquired can take several approaches dependent upon the overall goal of the study and the method employed to examine the samples. As an initial starting point, regardless of the experimental technique, preliminary data analysis involves band assignment of the preprocessed spectra (or class average spectra) using characteristic group frequencies as a guide for assignments (Jackson *et al.*, 1997). Subsequently, the global analytical approach chosen is dependent upon how the data was acquired (*i.e.*, macro-sampling or micro-sampling, *in vitro* or *in situ*) and the type of information to be extracted from the spectral data. For samples which represent a gross overall condition of a tissue or biological fluid, global data analysis may involve the extraction of quantitative information from the spectral data. For instance, if quantitative information is required, such as the concentration of a particular species in a sample, calibration of the FTIR technique to standard biochemical assays using partial least squares regression analysis, can be utilized for bio-diagnostic purposes (section 1.7.1). Alternatively, for *in vitro* studies, semi-empirical structural information can be extracted and conformational changes of molecular components in the preparation can be monitored as a function of the external conditions (pH, temperature *etc.*) and correlated to physical dynamic events (section 1.7.2). For the extraction of semi-quantitative information on *in situ* studies that employ macro-sampling techniques, tissue constituents can be identified by fingerprint analysis and the state of the tissue (control or diseased) can be differentiated by statistical analysis of the spectral data (section 1.7.3). However, when micro-sampling techniques are utilized, FTIR microspectroscopic data can

be interpreted by multidimensional correlation analysis and visually compared to tissue section histopathology by conventional methods (section 1.7.4).

1.7.1 Partial least squares analysis for quantitative interpretation of data

The extraction of quantitative information for biodiagnostic purposes may involve a single well-resolved absorption band that best represents a molecular species or it may involve a spectral fingerprint of the sample constituents to be quantified. For a single well-resolved band, quantification of the molecular species the band represents would normally proceed with the application of the Beer-Lambert law (see section 1.3.1), where concentration is extracted from the spectral-derived absorbance of the species, its molar extinction coefficient and the pathlength used experimentally. However, biological fluids cannot be studied in their native aqueous state and must be prepared as dried films for FTIR study (section 1.3.2). Since film thickness can vary, the Beer Lambert law cannot be directly applied to find the concentration of a species in the biological film (or tissue) because experimental pathlength is ill-defined. Therefore, a method is required to construct a calibration curve for the molecular species of interest at various concentrations, so that concentration of this species can be determined *in situ*. A simple method is to prepare a number of films *in vitro* at various known standard concentrations of the molecular species of interest as model for the biological film. The integrated intensity of the species-specific band is measured at these various concentrations and a linear calibration curve is constructed from the peak area as a function of known concentrations. If the molar absorptivity of the molecular species in the film prepared *in vitro* is not expected to be different from that in the biological film, the unknown concentration of the species in a biological film can be measured using the calibration curve constructed from the *in vitro* model film. Such a quantitative approach has been reported for determination of daily fluctuations of thiocyanate in saliva. (reviewed by Jackson *et al.*, 1997). Since thiocyanate is normally complexed with proteins in saliva, dried films of protein complexed with various known concentrations of KSCN were prepared to construct a calibration curve for the thiocyanate (2058 cm^{-1}). Thereafter the concentration of thiocyanate was determined in dried films of saliva extracted at various times of the day. Thiocyanate was found to decrease by nearly 75% from early in the morn-

ing to late afternoon; an interesting finding since thiocyanate is normally converted to the antibacterial compound, hypothiocyanite.

Alternatively, the calibration of FTIR spectral data may commence by validation of the technique against a practiced clinical chemistry procedure. In this approach, the concentration of the species is determined by both FTIR and the biochemical assay, the latter providing the “known” measurement of the analyte for what is called the “training set”. Subsequently, biological samples in the “test set” are analyzed “blind” for analyte concentration using the calibration coefficient derived from the “training set”. These calibration-derived FTIR measurements for analyte concentration are then cross-validated to “true” measurements of the “test set” samples using the same standard biochemical assay to check for external validation. Partial least-squares (PLS) regression in this regard provides a means to account for spectral variance in terms of noise, baseline shifts and alterations in analyte concentration (Jackson *et al.*, 1997). PLS methods determine the linear relationship between spectral and clinical measurements while the accuracy of the experimental technique is quantified by the deviation of the linear slope from unity. Furthermore, PLS multiple component analysis (MCA) can be utilized to select spectral subregions that work best in the cross-validation. For example, PLS-MCA has been used to select optimal spectral subregions from spectra of olive oil, sunflower oil and butter, in an ATR-FTIR spectroscopic analysis of fecal lipid content cross-validated to measurements obtained by gravimetric analysis (Franck *et al.*, 1996).

1.7.2 Structural analysis

Structural analysis of a molecular species prepared *in vitro* has generally involved either a semi-empirical approach, curve-fit analysis or pattern recognition analysis. Curve-fitting algorithms and pattern recognition programs are available for quantitative description of molecular structure. These two techniques are not without their drawbacks. In the work described in this thesis, a semi-empirical approach was used to compare protein structures (see Chapter 2). In what follows, the explanation concentrates on approaches relevant to the determination of protein structure.

Much information about protein structure can be obtained from the amide I band profile (section 1.5.1). Application of a semi-empirical approach to structural analysis

involves the band assignment of visible shoulders or component bands within the wide amide I contour. Changes in the external environment, such as pH, temperature, solvent, or interaction with other molecules (*i.e.*, lipids) can then be monitored by following the resulting changes in the overall band contour of the amide I vibration. Increases or decreases in particular secondary structures, turns or aggregation can be followed by changes in the intensity of the component bands along with the appearance of new component bands. For example, upon an increase in temperature proteins in solution may denature and then proceed to form aggregates. This change can be followed by changes in the amide I band profile from possessing component bands due to regular secondary structures such as β -sheets and α -helices to an increase in turn and unordered/random coil structure to the formation of strong intermolecular H-bonds between protein aggregates (see section 1.5.1). Structural analysis is non-quantitative, instead relative changes are noted qualitatively to delineate a physical phenomenon (Jackson and Mantsch, 1995). Numerous biological systems *in vitro* and *in situ* have been studied using this semi-empirical approach, such as investigations in protein folding (Fabian *et al.*, 1994; Troullier *et al.*, 2000), interactions between a protein and another molecular constituent (Haris *et al.*, 1992; Mantsch and McElhaney, 1991; Tailandier and Liquier, 1992) and changes in protein structure as a function of tissue condition (Choo *et al.*, 1996; Jackson and Mantsch, 1996).

Alternatively, for quantitative interpretation of structural details from IR absorptions, algorithms for curve-fitting the amide I band profile are available and have been used extensively in the past and present literature (reviewed by Jackson and Mantsch, 1995). For a quantitative estimate of protein structure, the deconvolved amide I band profile is utilized to provide an estimate of the number of component bands along with their widths, intensities and shapes. These parameters are used as the input data for the curve-fitting algorithm which attempts to reproduce the experimental band profile using an iterative least squares routine (Jackson and Mantsch, 1995). Recall that band-narrowing techniques, such as deconvolution and second-order derivative calculation, use a number of assumptions with respect to band shape (section 1.4.5) and the number of component bands revealed by such techniques may not be an accurate reflection of the number of component bands that comprise the amide I. Errors associated with this assumption, regarding the number of compo-

nent bands, can be minimized if both band-narrowing techniques are used to substantiate the result (section 1.4.5).

Further problems in curve-fitting routines are encountered when it comes to the accurate assignment of the component absorption bands to particular structures within the protein. For instance, a number of amino acid side chain absorptions appear under the amide I band profile (section 1.5.1) which may contribute 10-15% of the total amide I band intensity (Jackson and Mantsch, 1995). Although past researchers have subtracted these amino acid contributions from the overall intensity of the amide I band profile, the molar absorptivity, frequency, and shape of the amino acid side chain absorptions may differ between an amino acid in solution, a homopolypeptide and an amino acid in the sequence of a heteropolypeptide (section 1.5.1). Additional assignment errors arise from discrepancies in assigning specific secondary structures to the particular amide I component bands derived by the curve-fitting algorithm. For example, recall the difficulty in distinguishing α -helical structures from random coils due to the proximity of their absorption frequencies in the mid-IR (section 1.5.1). Finally, the major drawback involved in curve-fitting the amide I band profile is that the molar absorptivities of amide C=O groups involved in a variety of secondary structures are not the same (Jackson and Mantsch, 1995). For instance, experiments performed on poly-L-lysine have revealed that although concentration was held constant, the integrated intensity of the amide I band profile can vary by up to 30% depending upon whether the homopolypeptide was in an unordered (low pH), α -helical (high pH) or aggregated (high temperature) conformation (Jackson *et al.*, 1989).

Instead of a curve-fit analysis for a quantitative estimate of protein structure, approaches based on pattern recognition are available (reviewed by Haris and Chapman, 1995; Jackson and Mantsch, 1995). This type of approach is similar to those used for the estimation of protein secondary structure from other spectroscopic techniques such as CD. In brief, IR spectral features of proteins with known structure derived from X-ray crystallography, NMR and CD spectroscopy comprise the calibration set used to estimate the contribution of secondary structures to IR spectral data of proteins with unknown structure. The quantification is performed by assuming that the experimental spectrum is a linear combination of the reference spectra in the pattern recognition algorithm (Jackson and

Mantsch, 1995). There are several problems associated with these pattern recognition methods. Again the assumption is made that amide C=O groups have the same molar absorptivity regardless of the secondary structure in which they are involved; this oversimplifies the situation in reality (Haris and Chapman, 1995). Amino acid side chain absorptions under the amide I band limit the effectiveness of pattern recognition algorithms in the same manner in which they limit curve-fitting procedures (Haris and Chapman, 1995; Jackson and Mantsch, 1995). Furthermore, the calibration set for pattern recognition may not be large enough to accurately account for the spectral properties seen in the experimental spectrum of a protein with unknown structure (Haris and Chapman, 1995; Jackson and Mantsch, 1995). This latter concern becomes extremely relevant when considering the lack of conformational information on integral membrane proteins. However, in comparison to curve-fit analysis and the semi-empirical approach described above, pattern recognition procedures remove the subjectivity involved in the assignment of component bands of the amide I band profile to particular structures within the protein (Jackson and Mantsch, 1995).

1.7.3 Multivariate statistical analysis applicable to *in situ* studies

For the extraction of semi-quantitative information from *in situ* studies that employ macro-sampling and micro-sampling techniques, tissue constituents can only sometimes be identified by fingerprint analysis. Examples are studies that use the mid-IR collagen fingerprint to monitor changes in the extracellular matrix of a tissue (Liu *et al.*, 1996; Bromberg *et al.*, 1999a; see Chapter 3) or one that uses the silicone (polydimethylsiloxane) fingerprint to check for PDMS leakage into the capsular tissue surrounding breast implants (Hardt *et al.*, 1994). However, fingerprint analysis or the group frequency approach applied alone to a large number of spectra representative of different tissue states (control or diseased) can be potentially subjective. That is, a more rigorous approach (*i.e.*, multivariate analysis) is required to affirm the presence of the molecular fingerprint in each spectrum of each tissue state (section 1.6). Moreover, visual discrimination of the simultaneous absorption changes that ensue due to disease is not always feasible (Jackson *et al.*, 1997). Multivariate analyses (also called “chemometrics”), are approaches in which the chemical problem to be solved,

such as the classification of tissue state based on mid-IR absorptions of molecular species, can be performed objectively (Jackson *et al.*, 1997; Gentner *et al.*, 1998).

There are number of multivariate analysis software programs available that can be applied to spectral data that allow for the differentiation of tissue state (control or diseased) based on pattern recognition. The multivariate statistical analysis can be unsupervised or supervised (Jackson *et al.*, 1997). For example, spectral data can be used as input in commercially available software programs such as Statistica™ for unsupervised methods such as hierarchical clustering. The spectra are then effectively grouped without prior knowledge based on their dissimilarities/similarities to one another. Supervised multivariate analyses however, require some information about the spectral data, such as the group to which they belong (based on tissue state) and the spectral regions of diagnostic significance to the investigation. For example, linear discriminant analysis (LDA) is a supervised multivariate pattern recognition algorithm in which the data is assigned to a group prior to the analysis to “train” the algorithm to recognize the presence/absence of attributes or combination of variables in the test set common to each subset of the data or assigned class (Jackson and Mantsch, 1997). During the “training”, the “leave-one-out” method is typically employed iteratively in which each spectrum in the data set is left out of the “training set” and treated as an unknown with an unassigned class. This continues until LDA classification is optimized (highest separation between classes), the percent separation achieved at the end providing an assessment of how well the groups separate into their defined classes. In a similar manner, the “trained” LDA program can then be used to classify unknown samples. Bias however, can ensue due to overfitting or LDA misclassification, if the number of spectra is less than the number of attributes (wavelengths). Therefore data reduction techniques are frequently employed prior to LDA analysis (Gentner *et al.*, 1998). Spectral subregions can in principle be chosen by the investigator (section 1.4.5) or alternatively for improved objectivity an optimal subregion selection program, such as a genetic algorithm, can be utilized to overcome the data input limitations of LDA (section 1.4.6 and Chapter 3).

1.7.4 Multidimensional analysis for *in situ* microspectroscopic studies

Acquisition of a mapped array of spectra on a tissue section using FTIR microspectroscopy allows the tissue pathology to be examined in its native state and can be utilized

to extract unique chemical information which describes the state of the tissue (sections 1.2.1, 1.2.4, 1.2.5 and 1.3.3). Frequently, when FTIR microspectroscopy is used to gather information on the histopathology of a tissue section, the investigator may want to compare the revealed infrared pathology to that visible in light microscopy images of histochemically-stained tissue for validation of the IR technique. Several software programs have been developed (*i.e.*, OMNICTM, AtlusTM) to create IR images of the tissue area sampled that can be directly compared to the histochemically-stained light microscopy images (see Chapter 4). These IR images are created by the generation of 2D contour plots which chart the spectral relative intensity profiles of specific absorptions as a function of coordinates on the tissue section examined. For example, 2D contour plots can be constructed by the measurement of the integrated intensity of the same absorption band in each spectrum, different colors assigned to variable intensity values at this wavelength and a plot of the colored pixels which represent each spectrum is presented as a function of the tissue map coordinates. Rather than using color to delineate changes in the intensity profile a third dimension can be introduced to produce a three-dimensional surface map of the tissue (Choo *et al.*, 1996; Liu *et al.*, 1999). The selection of absorption band(s) most useful to generate the FTIR image is at present subjective. Numerous strategies are typically employed to generate the best image possible, but most begin with prior knowledge about the tissue composition. For example, if an abnormal peptide aggregate is known to infiltrate the tissue, one way to generate the FTIR image is using the intensity of the amide I band between 1610-1620 cm^{-1} in each spectrum of the map. Thereafter, the spectra belonging to image pixels specific to the highest aggregate content can be inspected and compared to spectra where the aggregate content is low. If another distinct feature of the tissue pathology is suggested by this spectral comparison, then another FTIR image can be generated using the intensity of the new absorption band. This process continues until the FTIR image correlates well with the histochemically-stained tissue. Using the intensity of one absorption band to generate a FTIR image can only be done if a stable global source is used in the IR microspectroscopy. In contrast, the brilliance of a synchrotron IR source is dependent on the stability of the ring. Unfortunately, the once energetic electrons lose energy from emitting synchrotron radiation and even though RF cavities can reduce the rate of energy loss, the beam lifetime rarely exceeds 6 hours (section 1.2.5). As a result, the signal throughput in the IR

microscope also decays with time. Since a spectral map can take hours to collect (1-2 minutes per spectrum), the amount of IR light illuminating the spectra varies dramatically between the beginning of map collection and the end. Therefore, using synchrotron IR microspectroscopy a more preferable profile to use in multidimensional analysis is the relative intensity of two absorption bands per spectrum (see Chapter 4). Correlation profiles may be also calculated from the presence of a combination of absorption bands in each spectrum which represent a specific "IR fingerprint" of the molecular species sought for distribution characterization in the tissue section. Once again, absorption band selection depends initially on what is known about the tissue composition and the relative contribution of each macromolecular component in the tissue region. Numerous 2D contour plots may have to be generated before the FTIR image is optimized. For the comparison of multiple normal and diseased tissue sections, the FTIR images should be generated using a similar profile, so that the relative distribution of the biochemical marker or pathogen can be established. Obviously, if the normal tissue is free of the biochemical marker associated with the disease, imaging based on the prevalence of this marker will not define the morphology of the normal tissue. Similarly, if this biochemical marker is distributed throughout the tissue region sampled, morphological features (*i.e.*, cells) of the diseased tissue will be lost in the FTIR image.

A recent advance in FTIR imaging of tissues has been in the application of unsupervised hierarchical clustering multivariate analysis on large maps (256 x 256) of tissues collected with IR microspectroscopy and FPA detection (Diem *et al.*, 2000). Through hierarchical clustering, spectra that have similar characteristics (frequencies, intensities, bandwidths, relative intensities, relative bandwidths, *etc.*) are classified together at the bottom of an Euclidian tree diagram. The branches of the tree diagram then suggest how similar or dissimilar one class of spectra is from another. Such a multivariate approach requires numerous spectra to be successful. Diem, *et al.*, 2000, applied hierarchical clustering to a third dimension, namely assigning a different color to each class of spectra and importing these results into the 2D contour plot (*i.e.*, each class of spectrum is then localized to specific regions in the tissue section). The IR images generated were strikingly similar to the tissue morphology revealed upon histochemical staining, regardless of whether the tissue was normal or abnormal. Such a process is required for these large FPA detected images

because it is impossible to inspect 66000 spectra/map individually. Representative spectra from a class could be inspected at any time and compared to a class of spectra either closely related (attached by a lower branch in the tree diagram) or veritably unrelated (connection at the top of the tree diagram).

1.8 OVERVIEW OF THESIS

The work presented in this thesis focused on three of the most frequently used techniques for evaluation of biological systems by FTIR spectroscopy in the mid-IR; that is, conventional transmission, ATR and microspectroscopy. Three independent biological systems were evaluated, each project with its own independent hypotheses with respect to the specific biological system studied and the capacity of the chosen FTIR technique to provide data relevant to that biological system. Although three independent biological systems were studied, there was one common overall hypothesis; FTIR biospectroscopy, as a single and diverse analytical tool, will provide unique information on a biological system, provided that a biophysical or biochemical change occurs.

In the first project, a biophysical study, conventional transmission FTIR biospectroscopy was used to monitor protein-lipid dynamics and interactions in model systems prepared *in vitro* (Chapter 2). Specifically, the overall goal was to use FTIR to evaluate the interactions of different charge isoforms of myelin basic protein (MBP) with liposomes of various net-negative surface charge density (SCD) chosen as simple models for the myelin membrane. Due to its highly cationic nature, unfractionated MBP is believed to act as a myelin adhesive in the central nervous system (CNS) by associating with acidic lipids of opposing myelin membrane leaflets. Certain post-translational modifications alter the net-positive charge of the unmodified isoform MBP-C1 (+20), primarily in the C-terminal half of the protein sequence (residues 86-170). MBP-C2 (+19) is deamidated at Gln146, MBP-C3 (+18) is phosphorylated at Thr97 and Ser164, MBP-C5 (+16) is phosphorylated at Ser7, Ser54, Thr97 and Ser164 and MBP-C8 (+14) is citrullinated at Arg35, Arg31, Arg122, Arg130, Arg159 and Arg170. Unfractionated MBP from the CNS myelin of a healthy individual is primarily composed of MBP-C1 and MBP-C2. Excessive MBP charge modification is thought to be in part responsible for the loosening and subsequent degradation of the myelin sheath in demyelinating diseases, such as Multiple Sclerosis. The interaction

between MBP and acidic bilayers has been reported to be highly dependent on the saturation of the negative SCD on the bilayer surface by the 31 positive charges on MBP; the concentration of MBP to acidic lipids in compact myelin being greater than that in non-compact paranodal myelin. Therefore, the overall hypotheses were: (i) Isoforms of greater net-positive charge (C1, C2 and C3) would be more effective at stabilizing acidic liposomes of unsaturated negative SCD (*i.e.*, in paranodal myelin) by electrostatic association, while isoforms of less net-positive charge (C5 and C8) would interact less at the surface and penetrate the bilayer, and (ii) Excessive MBP charge modification would have less of an adverse effect on MBP-mediated adhesion of acidic liposomes of saturated negative SCD (*i.e.*, in compact myelin) than on the adhesion of liposomes of unsaturated negative SCD (*i.e.*, paranodal myelin). Since the concentration of MBP to acidic lipid was to be manipulated by the gradual addition of a zwitterionic lipid (PC) in a binary PG/PC liposomal mixture¹⁹, the type of interaction that occurs between each isoform and liposomes of zero SCD was investigated at the onset of the study. It was proposed that only the isoforms with decreased net-positive charge or electronically neutral segments could stabilize an electronically neutral bilayer surface. It was found that isoforms of decreased net-positive charge (C3, C5 and C8) could indeed associate with electronically neutral PC head groups, while isoforms of increased net-positive charge (C1 and C2) preferred to penetrate the bilayer. MBP association with PC appeared to depend on the number and type of modified residues that could intramolecularly neutralize segments within the MBP sequence; modifications that increased the multivalency of negatively charged residues (*i.e.*, MBP-C3 and C5) were more effective at enhancing this association than modifications that decreased the multivalency of positively charged residues (*i.e.*, MBP-C8). The effects of such charge modifications were more dramatic for MBP interaction with the pure PG bilayer of unsaturated negative bilayer SCD (0.8 mol% MBP to PG). Isoforms of increased net-positive charge (C1, C2 and C3) did interact primarily by electrostatic association with the PG bilayer surface, while those of decreased net-positive charge (C5 and especially C8) extensively penetrated the bilayer. However, rather than net-positive charge affecting only the electrostatic component of the binding interaction, it also affected the synergy between electrostatic

19. Dipalmitoylphosphatidylglycerol (DPPG) and dimyristoylphosphatidylcholine (DMPC) were used.

association and partial penetration of the bilayer interface found to maximize the binding of the MBP-C1 with PG bilayers of unsaturated negative SCD (*i.e.*, paranodal myelin). Specifically, charge modifications that increased the multivalency of negatively charged residues in the C-terminal half of the sequence (MBP-C2 and MBP-C3) were found to decrease the synergy between electrostatic association and partial insertion of residues into the bilayer. Moreover, the additional increased multivalency of negative charges in the N-terminal half of the MBP sequence (MBP-C5) enhanced the intercalative behavior of the isoform. Meanwhile, modifications that reduced the multivalency of positive charges and simultaneously increased the number of hydrophobic residues (MBP-C8) were found to greatly reduce the electrostatic association and enhance bilayer penetration. The adverse effects of MBP charge modification in the adhesion of acidic bilayers did diminish as the liposomal negative SCD was saturated (3.1 mol% MBP to PG). However, improved binding of MBP-C1, C2 and C3 may be promoted by electrostatic association to microdomains of acidic lipids in a compact myelin-like membrane, while improved binding of MBP-C5 and C8 to the membrane may be promoted by surface interaction with acidic and zwitterionic lipids, simultaneously. Moreover, in compact myelin-like membranes, the electrostatic component of MBP-C1 binding to acidic lipid microdomains may be enhanced, whereas MBP-C2 and C3 binding to acidic lipid microdomains is enhanced by an improved synergy between electrostatic association and partial bilayer penetration. Furthermore, the results indicated that since MBP-C5 and C8 were able to simultaneously surface associate to the acidic and zwitterionic lipids, the intercalative behavior of these isoforms is reduced in compact myelin-like membranes. However, reduced multivalency of positive charges in the C-terminal half of MBP (MBP-C8) had a more adverse effect on MBP electrostatic association to compact myelin-like bilayers than increased multivalency of negative charges in the C-terminal half of MBP (MBP-C2, C3 and C5). Consequently, MBP charge modification, especially reduced multivalency of positive charge, may have a greater impact on the MBP-adhesion in paranodal myelin than in compact myelin. Finally, all the isoforms exhibited reduced conformational flexibility upon binding to a compact myelin-like membrane (*i.e.*, conformation did not fluctuate in response to a temperature increase) than to a paranodal myelin-like membrane. Fluctuations between a compact and less com-

compact MBP tertiary structure may be the dynamic mechanism responsible for controlling the amount of cytoplasm in the paranodal loops of myelin during nerve impulse generation.

The second project, a macroscopic investigation *in situ*, involved the non-subjective discrimination of diseased from normal tissue, using ATR-FTIR spectroscopy for sampling and multivariate analysis (LDA) to classify the tissues (Chapter 3). The tissues sampled came from the hearts of a well-characterized line of cardiomyopathic (CMP) hamsters, known to have pronounced collagen deposition in the left ventricle. Classification of the tissue was directed to differentiate between (i) Ventricles (left and right) within an animal class and (ii) Status of the tissue (CMP or control) for each ventricle type. Objectivity was improved by employing a genetic algorithm to select optimal spectral subregions for LDA classification. For comparison of the CMP and control left ventricles, it was hypothesized that the GA would preferentially select spectral subregions where absorptions due to collagen occur. As the final result, all groups under comparison could be differentiated from one another based on the presence or absence of the mid-IR collagen fingerprint (*i.e.*, a series of bands found at *ca.*, 1032, 1082, 1204, 1239, 1283, 1315 and 1338 cm^{-1}). However, the tissue class that possessed enhanced collagen deposition had to be determined by calculation of the difference spectrum between the class average spectra of each two-class comparison. The study confirmed that the CMP animals experienced LV collagen remodeling in the cardiac ECM, but suggested the fibrosis was focal rather than diffuse. Moreover, RV collagen remodeling, denoted by a decreased RV collagen content, was found to accompany the increased LV collagen deposition in the CMP animals.

The final project of this thesis, a microspectroscopic investigation *in situ*, implemented synchrotron FTIR microspectroscopy in the investigation of the pathophysiological changes in Alzheimer's diseased (AD) hippocampus (Chapter 4). Protein aggregates, such as β -amyloid plaques and neurofibrillary tangles, accumulate in various regions of the AD hippocampus. Little is known about the generation of these aggregates during the pathogenesis of AD. Histochemistry of AD suggests that an amorphous diffuse plaque matures into a neuritic plaque with fibrillar amyloid in the core surrounded by diffuse A β -peptide deposits, A β -associated proteins and reactive glial cells. However, there is conflicting data regarding the quaternary arrangement of the A β -peptide aggregates in diffuse and fibrillar

β -amyloid plaque formation. *In vitro* studies have suggested that amyloid fibrils, found at the core of a plaque, are intermolecularly H-bonded β -strands oriented in an antiparallel fashion (the so-called β -sheet-helix structure). *In situ* studies have suggested that the intermolecular H-bonds between β -strands in the fibrils are weaker (*i.e.*, farther apart) than the *in vitro* studies suggest, due to the presence of peripheral proteins and glial cells associated to the plaque. In addition, little is known about whether diffuse A β -peptide deposition can be found in the tissue prior to plaque formation, a query beyond the sensitivity of histochemical methods of analysis. Therefore, it was hypothesized that synchrotron FTIR microspectroscopic imaging is sensitive enough to (i) Discriminate between diffuse and fibrillar amyloid within plaques, (ii) Detect diffuse A β -peptide deposition outside the confines of a plaque and (iii) Discriminate between fibrillar amyloid and the other protein aggregate of the disease, the neurofibrillary tangle (if found) based on their respective spectral features. As a result of this investigation, spectral differences between diffuse and fibrillar amyloid were exploited to generate FTIR images of plaques in the Alzheimer's hippocampus. Two FTIR images were derived for each spectral map and were visually compared a photomicrograph of the stained tissue. Spectroscopic analysis revealed that fibrillar amyloid *in situ* was high in peptide aggregate structure (amide I component band between 1620-1625 cm^{-1}) while amorphous A β -peptide deposition *in situ* was high in β -sheet structure (amide I component band between 1630-1637 cm^{-1}). In addition, a unique spectral feature of fibrillar amyloid was found; a strong COO⁻ stretching absorption (1397-1400 cm^{-1}) attributed to the presence of numerous truncated peptides within the fibrillar amyloid. Tissue staining correlated with the location of fibrillar amyloid within neurons and regions containing diffuse amorphous plaques. Moreover, FTIR imaging was sensitive enough to denote A β -peptide deposition in regions in the AD gray matter where staining was inconclusive. In these regions, the contribution of proteins with β -sheet structure in AD gray matter was approximately 10-20% higher than that in control tissue. The conclusions are only preliminary since a greater sampling of AD and control hippocampus should be carried out. However, this feasibility study is in support of the hypothesis that AD hippocampal tissue has enhanced A β -peptide deposition in seemingly unaffected gray matter in comparison to control gray matter.

1.9 REFERENCES

- Ambrose, E.J., Elliot, A. (1951) Infrared spectroscopic studies of globular protein structure. *Proc. Roy. Soc. Lon. Series A*, 208: 75-90.
- Bangalore, A.S., Shaffer, R.E., Small, G.W., Arnold, M.A. (1996) Genetic algorithm-based method for selecting wavelengths and model size for use with partial least-squares regression: application to near-infrared spectroscopy. *Anal. Chem.*, **68**(23), 4200-4212.
- Boydston-White, S., Gopen, P., Houser, T., Bargonetti, S., Diem, M. (1999) Infrared spectroscopy of human tissue. V. Infrared spectroscopic studies of (ML-1) cells at different phases of the cell cycle. *Biospectroscopy*, **5**(4): 219-227.
- Bromberg, P.S., Gough, K.M., Dixon, I.M.C. (1999a) Collagen remodeling in the extracellular matrix of the cardiomyopathic Syrian hamster as assessed by FTIR attenuated total reflectance spectroscopy. *Can. J. Chem.*, **77**: 1843-1855.
- Bromberg, P.S., Gough, K.M., Ogg, M., Del Bigio, M.R., Julian, R. (1999b) "Synchrotron FTIR microspectroscopy of Alzheimer's diseased brain tissue at the SRC beamline", in Accelerator-based Sources of Infrared and Spectroscopic Applications, G.L. Carr and P. Dumas (editors). *Proc. of SPIE*, **3775**: 118-126.
- Byler, D.M., Susi, H. (1986) Examination of the secondary structure of proteins by deconvolved FTIR spectra. *Biopolymers*, **25**: 469-487.
- Cameron, D.G., Moffatt, D.J. (1984) Deconvolution, derivation and smoothing of spectra using Fourier transforms. *JTEVA*, **12**(2): 78-85.
- Casel, H.D., Mantsch, H.H. (1984) Polymorphic phase behavior of phospholipid membranes studied by infrared spectroscopy. *Biochim. Biophys. Acta*, **779**: 381-401.
- Chirgadze, Y.N., Federov, O.V., Trushina, N.P. (1975) Estimation of amino acid residue side-chain absorption in the infrared spectra of protein solutions in heavy water. *Biopolymers*, **14**: 679-694.
- Choo, L.-P., Wetzel, D.L., Halliday, W.C., Jackson, M., LeVine, S.M., Mantsch, H. H. (1996) In situ characterization of β -amyloid in Alzheimer's diseased tissue by synchrotron Fourier transform infrared microspectroscopy. *Biophys. J.*, **71**: 1672-1679.
- Diem, M., Chiriboga L., Yee, H. (2000) Infrared spectroscopy of human cells and tissue. VIII. Strategies for analysis of mapping data and applications to liver tissue. *Biopolymers*, **57**(5): 282-290.
- Drago, R.S. (1992) Physical Methods for Chemists, 2nd edition, Saunders College Publishing.

- Elliot, A., Ambrose, E.J. (1950) Structure of synthetic polypeptides. *Nature*, **165**: 921-922.
- Fabian, H. Schultz, C., Backmann, J. Hahn, U., Saenger, W., Mantsch, H.H., Naumann, D. (1994) Impact of point mutations on the structure and thermal stability of ribonuclease T1 in aqueous solution probed by Fourier transform infrared spectroscopy. *Biochemistry*, **33**: 10725-10730.
- Franchi, M., Bramanti, E. Morassi Bonzi, L., Luigi Orioli, P., Vettori, C. Gallori, E. (1999) Clay-nucleic acid complexes: characteristics and implications for the preservation of genetic material in primeval habitats. *Orig. Life Evol. Biosphere*, **29**: 297-315.
- Franck, P. Sallerin, J.-L., Schroeder, H., Gelot, M.-A., Nabet, P. (1996) Rapid determination of fecal fat by Fourier transform infrared analysis (FTIR) with partial least-squares regression and an attenuated total reflectance accessory. *Clin. Chem.*, **42(12)**: 2015-2020.
- Gentner, J.M., Wentrup-Byrne, E., Walker, P.J., Walsh, M.D. (1998) Comparison of fresh and post-mortem human arterial tissue: an analysis using FTIR microspectroscopy and chemometrics. *Cell. and Mol. Biol.*, **44(1)**:251-259.
- Griffiths, P. (1975) Chemical Infrared Fourier Transform Spectroscopy, John Wiley & Sons, Inc.
- Hardt, N.S., Yu, L.T., La Torre, G., Steinbach, B. (1994) Fourier transform infrared microspectroscopy used to identify foreign materials related to breast implants. *Mod. Path.*, **7(6)**: 669-676.
- Haris, P.I., Robillard, G.T., van Dijk, A.A., Chapman, D. (1992) Potential of ¹³C and ¹⁵N labeling for studying protein-protein interactions using Fourier transform infrared spectroscopy. *Biochemistry*, **31**: 6279-6284.
- Haris, P.I. and Chapman, D. (1995) The conformational analysis of peptides using Fourier transform IR spectroscopy. *Biopolymers*, **37**: 251-263.
- Harrick, N.J. (1967) Internal Reflection Spectroscopy, Interscience Publishers, 217-222.
- Jackson, M., Haris, P.I., Chapman, D. (1989) Conformational transitions in poly(L-lysine): studies using Fourier transform infrared spectroscopy. *Biochim. Biophys. Acta*, **998**: 75-79.
- Jackson, M., Mantsch, H.H. (1991a) Beware of proteins in DMSO. *Biochim. Biophys. Acta*, **1078**, 231-235.

- Jackson, M., Mantsch, H.H. (1991b) Protein secondary structure from FT-IR spectroscopy: correlation with dihedral angles from three-dimensional Ramachandran plots. *Can. J. Chem.*, **69**, 1639-1642.
- Jackson, M., Mantsch, H.H. (1992) Halogenated alcohols as solvents for proteins: FTIR spectroscopic studies. *Biochim. Biophys. Acta*, **1118**, 139-143.
- Jackson, M., Mantsch, H.H. (1995) The use and misuse of FTIR spectroscopy in the determination of protein structure. *Crit. Rev. Biochem. Mol. Biol.*, **30(2)**, 95-120.
- Jackson, M., Choo, L-P., Watson, P.H., Halliday, W.C., Mantsch, H.H. (1995) Beware of connective tissue proteins: assignments and implications of collagen absorptions in infrared spectra of human tissues. *Biochim. Biophys. Acta*, **1270**, 1-6.
- Jackson, M., Mantsch, H.H. (1996) "FTIR spectroscopy in the clinical sciences" in Bio-medical Applications of Spectroscopy, R.J.H. Clark and R.E. Hester (eds.), John Wiley and Son Ltd., 185-215.
- Jackson, M., Sowa, M.G., Mantsch, H.H. (1997) Infrared spectroscopy: a new frontier in medicine. *Biophys. Chem.*, **68**: 109-125.
- Jamin, N., Dumas, P. Moncuit, J., Fridman, W.-H., Teillaud, J.-L., Carr, G.L., Williams, G.P. (1998) Highly resolved chemical imaging of living cells using synchrotron infrared microspectroscopy. *Proc. Natl. Acad. Sci. USA*, **95**: 4837-4840.
- Kauppinen, J.K., Moffatt, D.J., Mantsch, H.H., Cameron, D.G. (1981) Fourier transforms in the computation of self-deconvoluted and first-order derivative spectra of overlapped band contours. *Anal. Chem.*, **53**: 1454-1457.
- Kidder, L.H., Kalasinsky, V.F., Luke, J.L., Levin, I.W., Lewis, E.N. (1997) Visualization of silicone gel in human breast tissue using new infrared imaging spectroscopy. *Nat. Med. (N.Y.)*, **3**: 235-237.
- Lambert, J.B. Shurvell, H.F., Lightner, D., Cooks, R.G. (1987). Introduction to Organic Spectroscopy, Macmillan Publishing Company, NY, pp.135-239.
- Liu, K.Z., Jackson, M.J., Sowa, M.G., Dixon, I.M.C, Mantsch, H.H. (1996) Modification of the extracellular matrix following myocardial infarction monitored by FTIR spectroscopy. *Biochim. Biophys. Acta*, **1315**, 73-77.
- Liu, K.Z., Dixon, I.M.C., Mantsch, H.H. (1999) Distribution of collagen deposition in Cardiomyopathic hamster hearts determined by infrared microscopy. *Cardiovascular Path.*, **8**, 41-47.

- Manoharan, R., Baraga, J.J., Rava, R.P., Dasari, R.R., Fitzmaurice, M., Feld, M.S. (1993) Biochemical analysis and mapping of atherosclerotic human artery using FT-IR microspectroscopy. *Atherosclerosis*, **103**: 181-193.
- Mantsch, H.H., McElhane, R.N. (1991) Phospholipid transitions in model and biological membranes as studied by IR spectroscopy. *Chem. Phys. Lipids*, **57**, 213-226.
- Mantsch, H.H., Perczel, A., Hollosi, M., Fasman, G.D. (1993) Characterization of β -turns in cyclic hexapeptides in solution by Fourier transform IR spectroscopy. *Biopolymers*, **33**: 201-207.
- Mantsch, H.H. (1998) Vibrational spectroscopy of lipids: a historical perspective. *Chem. Phys. Lipids*, **96**: 3-7.
- McLachlan, G.J. (1992) Discriminant Analysis and Statistical Pattern Recognition, Wiley, New York.
- Mendelsohn, R., Mantsch, H.H. (1986) "Fourier transform infrared studies of lipid-protein interactions", in Progress in Protein-Lipid Interactions, Volume 2, A. Watts and J.J.H.H.M. De Pont (editors), Elsevier Science Publishers, pp.103-146.
- Moffatt, D.J., Mantsch, H.H. (1992) Fourier resolution enhancement of infrared spectral data. *Meth. Enzymol.*, **210**: 192-200.
- Moore, W.K., Krimm, S. (1975) Transition dipole coupling in amide I modes of β -polypeptides. *Proc. Natl. Acad. Sci. USA*, **72**: 4933-4935.
- Morell, P., Quarles, R.H., Norton, W.T. (1994). "Myelin formation, structure and biochemistry", in Basic Neurochemistry, 5th edition, G.J. Siegal, B.W. Agranoff, R.W. Albers and P.B. Molinoff (editors), Raven Press, New York, 117-143.
- Shie, M., Kharitonov, I.G., Tikhonenko, T.I., Chirgadze, Y.N. (1972) New possibilities of investigating nucleic acids and nucleoproteins in aqueous solutions by infrared spectroscopy. *Nature*, **235**: 386-388.
- Singer, S.J., Nicolson, G.L. (1972) The fluid mosaic model of the structure of cell membranes. *Science*, **175**: 720-731.
- Surewicz, W.K., Mantsch, H.H., Chapman, D. (1993) Determination of protein secondary structure by Fourier transform infrared spectroscopy: a critical assessment. *Biochemistry*, **32**(2): 389-394.
- Taillandier, E., Liquier, F. (1992) Infrared spectroscopy of DNA. *Meth. Enzymol.*, **211**, 307-335.

- Troullier, A., Reinstadler, D. Dupont, Y., Naumann, D. Forge, V. (2000) Transient non-native secondary structures during the refolding of α -lactalbumin detected by infrared spectroscopy. *Nat. Struc. Biol.*, **7**(1): 78-86.
- Venyaminov, S.Y., Kalnin, N.N. (1990) Quantitative IR spectrophotometry of peptide compounds in water (H₂O) solutions. I. Spectral parameters of amino acid residue absorption bands. *Biopolymers*, **30**: 1243-1257.
- Williams, G.P. (1992) Infrared synchrotron radiation instrumentation and applications. *Rev. Sci. Instr.*, **63**: 1535-
- Williams, G.P. (1999) "Infrared synchrotron radiation, review of properties and perspectives", in Accelerator-based sources of infrared and spectroscopic applications. G. L. Carr, P. Dumas, editors, *Proc. of SPIE*, **3775**: 2-6.
- Wong, P.T.T., Rigas, B. (1990) Infrared spectra of microtome sections of human colon tissues. *App. Spec.*, **44**: 1715-1718.
- Wong, P.T.T., Cadrin, M., French, S.W. (1991) Distinctive infrared spectral features in liver tumor tissue of mice: evidence of structural modifications at the molecular level. *Expt. Mol. Path.*, **55**, 269-284.

2 FTIR SPECTROSCOPIC INVESTIGATION *IN VITRO*: INTERACTION OF MYELIN BASIC PROTEIN CHARGE ISOFORMS WITH MODEL LIPID SYSTEMS¹

2.1 INTRODUCTION

2.1.1 Chapter overview

Protein-lipid dynamics and interactions have been studied extensively by FTIR biospectroscopy for nearly two decades (for review see Mendelsohn and Mantsch, 1986; Mantsch and McElhaney, 1991). Such studies have demonstrated that the type of interaction that exists between the folded protein and the lipid bilayer can be evaluated by monitoring certain mid-IR frequencies as a function of a chosen independent variable (*i.e.* pH, temperature, salt concentration, *etc.*). Since absorptions that reflect conformational changes of proteins and lipids occur in different sub-regions of the mid-IR (section 1.5.1 and 1.5.2), FTIR examination of mixed systems allows the impact of interaction on separate components of the mixture to be evaluated simultaneously. One purpose of this chapter is to further demonstrate the utility of FTIR biospectroscopy for evaluation of protein-lipid dynamics and interactions in model systems prepared *in vitro*. Specifically, the overall goal of this current work was to use FTIR to evaluate the interactions of different charge isoforms of myelin basic protein (MBP) with liposomes of various net-negative surface charge density (SCD), the latter chosen as simple models for the myelin membrane. Myelin basic protein has a high net-positive charge and is believed to act as a myelin adhesive by associating with acidic lipids of opposing myelin membrane leaflets (section 2.1.2). MBP that has lost the ability to function as a myelin adhesive is thought to be in part responsible for the loosening and subsequent degradation of the myelin sheath in demyelinating diseases, such as multiple sclerosis. The present chapter explores the relative influence of MBP net-positive charge and bilayer composition on myelin stability.

Many of the early attempts to study the interaction of MBP with net-negatively charged lipid systems that model the myelin membrane (section 2.1.3) ignored that MBP

1. The majority of the work in this chapter has been presented at two conferences (Bromberg *et al.*, 1997; Bromberg *et al.*, 1999).

is not a single protein, but instead a collection of several charge isoforms of the same molecular mass (section 2.1.4). MBP charge microheterogeneity arises from post-translational modifications (*i.e.*, deamidation, phosphorylation, and citrullination) of one or more residues in the sequence (section 2.1.4). The unmodified isoform, MBP-C1 carries the most net-positive charge, while net-positive charge decreases by one unit of positive charge in an incremental fashion for MBP-C2 through to C8. Limited research has been carried out on fractionated MBP (primarily MBP-C1, C2 and C8) in an attempt to understand the impact of these various modified residues on the electrostatic binding of the protein to net-negatively charged lipid preparations (section 2.1.5). To date, the atomic structure of MBP (NMR or x-ray crystallography) has not been obtained, making it somewhat more difficult to fully understand its function. CD and IR have confirmed that MBP in aqueous solution is predominantly random coil (section 2.1.4), but out of these two solution techniques IR is more suitable for studying protein structure in a lipid environment. Optical dichroism studies on fractionated MBP with net-negatively charged lipid vesicles have revealed that MBP net-positive charge is not the only factor that can influence the protein/lipid interaction; in particular bilayer negative SCD can also influence the ability of the MBP isoforms to aggregate vesicles (Jo and Boggs, 1995 and Boggs *et al.*, 1997). Such investigations have suggested that electrostatic binding is greater when the relative concentration of MBP to acidic lipid is high (*i.e.*, similar to compact myelin) than low (*i.e.*, similar to paranodal myelin) because there is a stoichiometric saturation of negative charges on the bilayer surface by the positive charges on the protein that maximizes the binding interaction (this is an important distinction because MBP-mediated adhesion in paranodal myelin can be affected by the potassium fluxes generated during an action potential (sections 2.1.3 and 2.1.5)). However, the amount of electrostatic association relative to that of bilayer penetration cannot be assessed by an optical dichroism aggregation assay, nor can aggregation assays provide structural information on the isoforms upon interaction with mixed bilayers. The present study illustrates the unique strengths of FTIR spectroscopy for characterizing the interactions of MBP with model lipid systems; structural changes in several sample constituents have been evaluated simultaneously and the type of intermolecular interaction that prevails amongst the sample constituents can be interpreted from these structural changes.

The experimental design was fairly straightforward (sections 2.2.1, 2.2.2 and 2.2.3). The interactions of MBP-C1, C2, C3, C5 and C8 with acidic, neutral and binary liposomal systems were investigated using transmission FTIR spectroscopy (sections 1.2.1 and 1.2.2). The sensitivity of FTIR to isotopic substitution allowed for simultaneous monitoring of both components in the binary liposomal systems, provided that one lipid was in the per-deuterated form (section 1.5.2). Spectra of proteins, lipids and various protein/lipid mixtures were collected over a temperature range inclusive of the phase transition temperature(s) of the lipid(s). The biophysical behavior of each pure component was first assessed by the temperature-induced changes in the respective spectral signature. In particular, the symmetric methylene CD stretching absorption (*ca.*, 2090 cm^{-1}) of per-deuterated phosphatidylcholine (d-PC) and the asymmetric methylene CH stretching absorption (*ca.*, 2920 cm^{-1}) of phosphatidylglycerol (PG) were monitored as a function of temperature to generate two-state (gel and $L\alpha$ state) transition curves and calculate the phase transition temperature (T_m) of each lipid (section 1.5.2 and 2.3.1). In addition, the acyl chain order (*i.e.*, energy) and hydration of the bilayer interface were assessed to individually characterize the gel and $L\alpha$ state of each lipid. The former was determined from the relative frequencies of the methylene stretch in the two lipid states while the latter was determined from the absorption profile of the acyl carbonyl stretch (*ca.*, 1735 cm^{-1}) in the two lipid states. The phase behavior of d-PC and PG in the binary liposomes was assessed in a similar fashion to that for the pure lipid systems with one exception; bilayer hydration could not be investigated due to spectral overlap of the d-PC and PG acyl C=O stretching profiles (section 2.3.1). Conformational studies of the MBP isoforms in an aqueous environment were carried out using the semi-empirical approach for analysis of the amide I band profile (section 1.5.1, 1.7.2). Isoform conformational flexibility was further characterized by monitoring the temperature-sensitivity of the amide I absorption profile (1600-1700 cm^{-1}) and the δ -guanidino stretching of arginyl residues (*ca.*, 1587 and 1610 cm^{-1}) (section 2.3.5). Thereafter, any detected change in the spectroscopic behavior of the individual components in the protein-lipid samples was interpreted to suggest the type of interaction that prevailed between an isoform and the bilayer. A change in the $T_m(\text{lipid})$ in the presence of protein was taken as unequivocal evidence for interaction. The acyl chain order and hydration of the bilayer interfacial region (single lipid systems only) of the two

lipid states (gel and $L\alpha$) were both used to estimate the relative contributions of (i) bilayer stabilization by isoform electrostatic association and (ii) bilayer destabilization by isoform penetration. The acyl chain order of the d-PC and PG $L\alpha$ states was also used to determine which of the two lipids an isoform exhibited a binding preference for, and whether the isoform could induce PG microdomain formation in the binary liposomes. Finally, the isoform conformations and conformational flexibilities in aqueous solution (section 2.3.5) were compared to those in neutral (section 2.3.6), acidic (section 2.3.7) and binary (section 2.3.8) liposomal environments. These comparisons established the effect each lipid has on the individual MBP isoforms and verified whether the isoform exhibited a preference for interaction with PG and/or d-PC.

In brief, isoforms of decreased positive charge (C3, C5 and C8) did indeed interact with the electronically neutral d-PC surface, while isoforms of increased positive charge (C1 and C2) tended to penetrate the bilayer. However, decreased net-positive charge was not the only factor involved in MBP association with the d-PC bilayer surface. Instead, association with d-PC appeared to depend on both the number and type of post-translational modified residues. The effect of such post-translational modifications was most dramatic for MBP interaction with the pure PG bilayer of unsaturated negative bilayer SCD (0.8 mol% MBP to PG). Isoforms of increased net-positive charge (C1, C2 and C3) did interact primarily by electrostatic association with the PG bilayer surface, while those of decreased net-positive charge (C5 and especially C8) penetrated the bilayer extensively. However, a synergy between electrostatic association and partial penetration of the bilayer interface was found to maximize the binding strength of the most positively charged isoforms (C1 and C2) with PG. Rather than net-positive charge alone affecting MBP electrostatic association to PG, it was the impact of net-positive charge modulating the balance between electrostatic association and partial penetration of the bilayer interface that affected MBP-mediated adhesion of PG bilayers with unsaturated negative SCD (*i.e.*, paranodal myelin). As the liposomal negative surface charge density was decreased by the addition of a neutral lipid (d-PC), the adverse effects of MBP charge modification in the adhesion of acidic bilayers diminished. Saturation of the liposomal negative SCD by the positive charges on an isoform enhanced the relative contribution of stabilizing MBP electrostatic associations (as opposed to bilayer penetration) and allowed the protein to adopt a more compact and

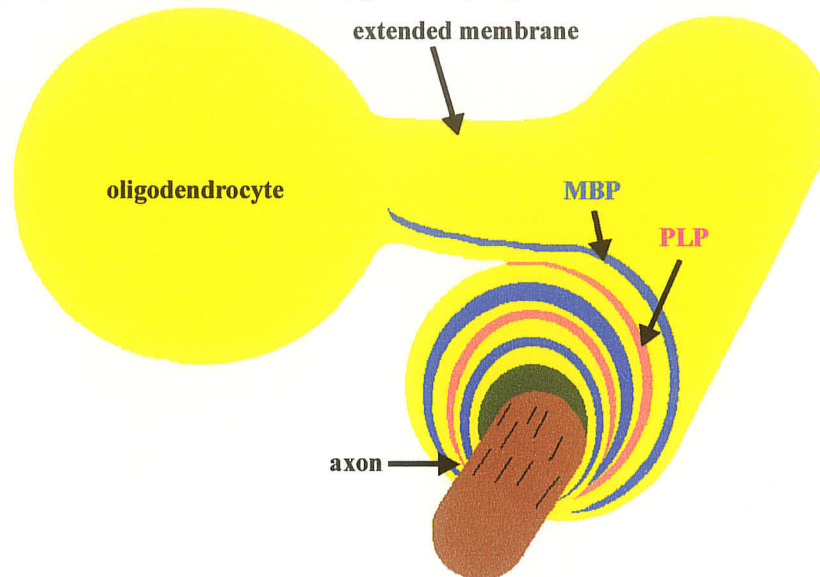
ordered (increased β -sheet and α -helix) structure. As long as charge modifications did not (i) affect the multivalency of positive charges available on the C-terminal half of the isoform or (ii) alter the net charge on the N-terminal half of the isoform, binding to a compact myelin-like membrane was optimal and perhaps initiated by the formation of acidic lipid microdomains in the mixed bilayer (applies to C1, C2 and C3). Interestingly, the least positively charged isoforms, MBP-C5 and C8 were able to surface associate simultaneously to both lipids (acidic and neutral) in a mixed bilayer. It was proposed that preferential interaction between the N-terminal halves of these isoforms and the neutral lipid component reduces the intercalative behavior of these isoforms, optimizing their binding to a compact myelin-like membrane. Consequently, MBP charge modification - especially polycitrullination of arginine residues - most likely has a greater impact on the adhesive properties of MBP in paranodal myelin than in compact myelin. That is, a greater ratio of the uncitrullinated isoforms to MBP-C8 may be more critical for maintaining a proper balance between MBP electrostatic association and bilayer penetration in paranodal myelin than in compact internodal myelin. However, fluctuations between a compact and less compact MBP tertiary structure may be the dynamic mechanism responsible for controlling the amount of cytoplasm in the paranodal loops of myelin during nerve impulse generation. Moreover, the amphipathic character of MBP-C8 and the preference of this isoform for interaction with neutral lipids, suggests that the delicate balance between neutral and acidic phospholipids in the myelin membrane may also play a part in MBP-mediated adhesion of myelin.

2.1.2 The role of MBP in the myelin sheath of the CNS

The myelin sheath, comprised of multilamellar stacks of lipid bilayers compactly held in place by protein-lipid interactions, serves as the insulator of the nervous system. CNS myelin is the extended plasma membrane of a glial cell called an oligodendrocyte, which concentrically wraps around the axon in a tight spiral fashion to form the compact myelin sheath (Figure 2-1). Numerous oligodendroglial membranes typically wrap the length of an axon resulting in alternating segments of the myelin sheath and the myelin-bare nodes of Ranvier (Morell *et al.*, 1994). Proximal to the nodes of Ranvier, paranodal myelin contains the residual cytoplasm of the flattened oligodendrocyte that has been compressed from the compact internodal myelin (Morell *et al.*, 1994). Without myelin, neuro-

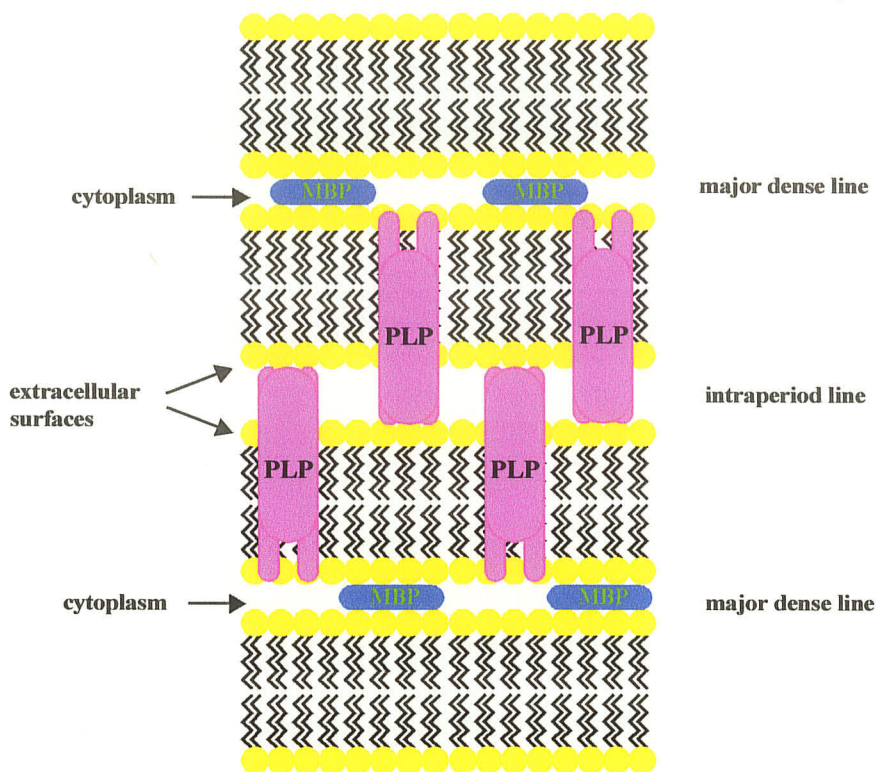
logical conduction is comparatively slow and uses up more energy (Morell *et al.*, 1994). Demyelinating diseases, such as multiple sclerosis (MS), where neurological conduction is compromised, may be understood in part by studying the protein-lipid interactions which compact the extended oligodendroglial membrane to form the myelin sheath.

Figure 2-1. The myelin sheath of the CNS showing the extended oligodendroglial membrane concentrically wrapped around a neuronal axon. Abbreviations: MBP, myelin basic protein; PLP, proteolipid protein.



Myelin basic protein (MBP), an extrinsically associated protein of the myelin membrane, is thought to play a substantial role in the formation, maintenance and degradation of the myelin sheath. MBP was first isolated and characterized by gel electrophoresis in the 1960s following acidic extraction from purified myelin and precipitation of the basic protein from the aqueous supernatant using ethanol (Lowden, Moscarello and Morecki, 1966). Since then, MBP has been localized to the cytoplasmic face of the myelin membrane (major dense line) where the net-positively charged protein is believed to interact via electrostatic association with acidic phospholipid head groups of the inner bilayer leaflet (Morell *et al.*, 1994). The extended oligodendroglial membrane is thought to be flattened by MBP association while the other major protein of the myelin membrane, proteolipid protein, is thought to participate in the adherence of concentric layers (intrapertiod line) of the flattened membrane into the compact myelin sheath (Figures 2-1 and 2-2).

Figure 2-2. Relative positions of myelin basic protein (MBP) at the major dense line and proteolipid protein (PLP) at the intraperiod line of compact myelin. Acyl hydrocarbon chains are shown in the all *trans* conformation for simplicity.



2.1.3 Studies of the interactions of MBP with model lipid systems

Over the last three decades numerous studies have explored the interactions of unfractionated MBP with model lipid systems utilizing differential scanning calorimetry (Papahadjopoulos *et al.*, 1975; Boggs and Moscarello, 1978; Boggs *et al.*, 1981; Reinl and Bayerl, 1993; Nabet *et al.*, 1994), UV/visible absorbance spectrophotometry (Chieftetz and Moscarello, 1985; Jo and Boggs, 1995; Boggs *et al.*, 1997), infrared spectroscopy (Jackson *et al.*, 1993; Reinl and Bayerl, 1993; Nabet *et al.*, 1994), NMR spectroscopy (Deber *et al.*, 1986; Reinl and Bayerl, 1993; Roux *et al.*, 1994); electron spin resonance spectroscopy (Boggs and Moscarello, 1978), hydrophobic photolabeling (Boggs *et al.*, 1988; Boggs *et al.*, 1999a) to name a few. Such studies have demonstrated that electrostatic interaction of MBP with acidic lipids involves association of the basic residues of MBP (lysine and arginine) with the negatively charged lipid head groups (Deber *et al.*, 1986).

However, some debate has endured in whether this interaction between MBP and acidic lipids was mediated solely by electrostatic association or by a combination of association and hydrophobic intercalation with the bilayer acyl chains. Although Reiny and Bayerl, 1993, found that the phase transition temperature of acidic lipids was raised in the presence of MBP indicating predominantly electrostatic association, other studies found that it decreased upon MBP interaction (Papahadjopoulos *et al.*, 1975; Boggs and Moscarello, 1978; Boggs *et al.*, 1981; Nabet *et al.*, 1994). A lowering of a lipid phase transition temperature in this manner supports the hypothesis that MBP interaction with acidic lipids proceeds through a combination of electrostatic association and hydrophobic interaction.

The combination of electrostatic and hydrophobic interactions between MBP and acidic phospholipids is highly supported in the literature by parameters more localized in nature than the phase transition temperature of the lipid. For example, poly-L-lysine, which interacts purely by electrostatic association with acidic phospholipids (Boggs *et al.*, 1981), is not labeled to the same extent with a hydrophobic label as that of MBP proteins (Boggs *et al.*, 1988), indicating that the MBP proteins can both associate with and perturb the bilayer of acidic lipids. Boggs *et al.*, 1988 found that upon binding to acidic phospholipids (PS, PG, PA), the extent of hydrophobic labeling was 5 to 7 times greater for MBP than for poly-L-lysine. Insertion of MBP into acidic bilayers was further confirmed using FTIR spectroscopy where MBP was observed to decrease the hydration of the bilayer interfacial region as monitored by the shift of the lipid acyl C=O profile to higher frequency upon MBP interaction (Nabet *et al.*, 1994). While partial insertion of hydrophobic side chains of MBP may occur during the interaction of this protein with acidic lipids, it appears to be well accepted that the majority of the protein is localized at the surface of the bilayer with its basic residues involved in electrostatic interactions with the negatively charged headgroups of the lipid.

The interaction of MBP with neutral lipids or with binary lipid mixtures of acidic and neutral lipids is somewhat less clear. Boggs *et al.*, 1988, did detect greater hydrophobic labeling of MBP than poly-L-lysine in the presence of zwitterionic lipids (PC), but the degree of hydrophobic labeling was decreased by a factor of 2 to 4 over that of MBP in the presence of acidic lipids. This latter observation may indicate that electrostatic association can further promote membrane insertion. It has also been proposed that while MBP can

still interact electrostatically with binary lipid systems composed of both acidic and neutral phospholipids, protein association with neutral lipids alone is unlikely (Reinl and Bayerl, 1993). Reinyl and Bayerl, 1993, further implied that a demixing or phase separation of binary neutral/acidic lipid mixtures upon MBP interaction did not occur since both lipids were affected by MBP presence. However, Reinyl and Bayerl, 1993, refrained from proposing an explanation of the effect of MBP on neutral PC of the binary mixture or the type of protein-PC interaction that might occur. More recently, MBP was found to penetrate more extensively into neutral phospholipid bilayers than net-negatively charged bilayers, suggesting hydrophobic interactions between MBP and neutral lipid bilayers was possible (Roux *et al.*, 1994). Moreover, MBP was found to disrupt multilamellar bilayers of neutral phosphatidylcholine in the absence of acidic lipid (PS), while PS interaction with the protein prevented disruption of the PS/PC bilayers (Roux *et al.*, 1994). Roux *et al.*, 1994, also found that MBP-induced fragmentation of multilamellar PS/PC bilayers occurred when divalent cations were used to neutralize the negative charge of the acidic lipid in the binary mixture. The results of Roux *et al.*, 1994, suggest that hydrophobic interactions of MBP with neutral lipids diminish when preferential electrostatic interactions between MBP and acidic lipids is possible.

It should be noted that most studies on MBP interaction with binary lipid systems have been carried out using high concentrations of MBP to acidic lipid (> 3 mol% MBP), resulting in a saturation² of the bilayer net-negative SCD by the positive charges available on MBP. Such studies may model compact internodal myelin, where the MBP to acidic lipid concentration is nearly high enough to fully neutralize the net-negative SCD, but ignore that the myelin sheath is not composed of one homogeneous concentration of MBP to acidic lipid (Morell *et al.*, 1994; Jo and Boggs, 1995; Boggs *et al.*, 1997). For example, the MBP to acidic lipid concentration is much lower in paranodal myelin.³ Since insufficient MBP is present to fully neutralize the negative charges on the bilayer surface, paran-

2. MBP has 31 positively charged residues (net positive charge of +20). Therefore one MBP molecule could potentially neutralize 20 to 31 negatively charged lipid head groups. Depending on whether some negative charged residues shield some of the positive charges of MBP, a MBP to acidic lipid concentration of 3 to 5 mol% MBP is considered to saturate (*i.e.*, neutralize) the net-negative SCD of an acidic bilayer.

3. Boggs *et al.*, 1997, used 3.7 mol% MBP-to-PS and 1.2-0.2 mol% MBP-to-PS for samples to mimic the concentration of MBP-to-acidic lipid in compact and paranodal myelin, respectively.

odal myelin takes on a non-compact ultrastructure due to charge repulsion between opposing bilayer leaflets (Jo and Boggs, 1995). Specifically, Jo and Boggs, 1995, found that low concentrations of MBP to acidic lipid (< 3 mol% MBP) did not sufficiently aggregate PS/PC vesicles but aggregation greatly increased when the mixture was exposed to moderate concentrations of KCl (50-100 mM). Therefore, moderate concentrations of potassium shield the excess negative SCD on the MBP-vesicle surface enhancing aggregation (Jo and Boggs, 1995). However, excessive KCl (100-150 mM) promoted dissociation of the MBP-vesicle aggregates, suggesting that once the vesicle negative SCD was neutralized, potassium then interferes with the electrostatic association between positively charged residues of MBP and negatively charged lipid head groups (Jo and Boggs, 1995). In contrast to the experiments aimed at modeling paranodal myelin, MBP-mediated aggregation of PS/PC vesicles with saturated net-negative SCD (> 3 mol% MBP to PS) occurred with lower concentrations of KCl (10-50 mM) and dissociation occurred once the aggregates were exposed to 90 mM KCl (Jo and Boggs, 1995; Boggs *et al.*, 1997). Even though a high MBP concentration was used to neutralize the negative charges of the acidic lipid in the PS/PC vesicles, some potassium was still required to neutralize the 11 negatively charged residues on the surface of the MBP-vesicles (Jo and Boggs, 1995; Boggs *et al.*, 1997). Therefore, MBP-adhesion to lipid bilayers is highly dependent on whether MBP saturates the bilayer SCD or leaves some negatively charged lipid head groups on the surface of opposing leaflets free to repel one another. Interestingly, the effect of 50-100 mM KCl on the MBP-vesicle complexes prepared with a low concentration of MBP to acidic lipid, is physiologically significant. For example, paranodal myelin is susceptible to potassium ion fluxes (60-75 mM) since potassium channels in the membrane can transiently take up the potassium released from the nodes of Ranvier during an action potential (Hille and Catterall, 1994; Jo and Boggs, 1995; Boggs *et al.*, 1997). Such potassium fluctuations in the residual cytoplasm of the paranodal loops may alter MBP-adhesion in paranodal myelin, allowing MBP to regulate the volume of the cytosol during neuronal activity (Jo and Boggs, 1995; Boggs *et al.*, 1997).

2.1.4 Charge isoforms of myelin basic protein

The basic nature of human myelin basic protein (170 amino acids, 18.5 kDa) can be accounted for by the high content of basic amino acids (12 lysines and 19 arginines) (Deber *et al.*, 1986). Due to charge repulsion, MBP has been found to be a highly unorderd protein with virtually no tertiary structure in aqueous solution at physiological pH (Morell *et al.*, 1994). However, under alkaline conditions electrophoretic studies have shown that the major species of mammalian MBP (18.5 kDa) can be resolved into several component bands suggesting that this species exists as a number of isoforms that differ in their net-positive charge (Martenson *et al.*, 1969). This charge microheterogeneity is believed to arise by a variety of post-translational modifications such as phosphorylation (Chou *et al.*, 1976; Deibler *et al.*, 1975; Martenson *et al.*, 1983), loss of C-terminal arginine (Deibler *et al.*, 1975), deamidation (Chou *et al.*, 1976; Martenson *et al.*, 1983), methylation at arginine 106 (Morell *et al.*, 1994), and deimination of some of the positively charged arginyl residues to zwitterionic citrulline (Wood and Moscarello, 1989).

Isolation of the individual charge isoforms of MBP, on larger scale than that achieved by alkaline gel electrophoresis, can be carried out using CM52 columns at pH 10.6 in which the components elute from the column in the order of increasing net-positive charge (Chou *et al.*, 1976). The least positively charged isoform, now designated as component 8 (or C8) can be found in the void volume, whereas components C1-C5 must be released from the carboxymethylcellulose cation exchange resin using a linear salt gradient, with C1 the most positively charged isoform eluting last (Moscarello *et al.*, 1986). Upon further analysis of the unbound fraction in the CM52 chromatography, C8 was found to be composed of four myelin basic proteins, high (18.5 kDa) and low (17.3 kDa) molecular weight components A and B, designated as C8-A(H), C8-A(L), C8-B(H) and C8-B(L) (Boulias *et al.*, 1995). Boulias *et al.*, 1995, further reported that 70% of unfractionated MBP from normal human white matter is composed of C1, C2, C3, C8-A and C8-B (relative abundance *ca.*, 17, 11, 15, 10 and 10%, respectively), while the remaining 30% of unfractionated MBP is predominantly composed of C4 and C5.

Amino acid analysis of the unmodified isoform, MBP-C1, has shown that the positive charged residues are almost equally distributed between the N-terminal half (residues 1-85) and C-terminal half (residues 86-170) of the protein, while the number of negatively

charged residues in the N-terminal half are nearly double that in the C-terminal half (Figure 2-3). The N-terminal half of MBP-C1 has 15 basic residues (5 lys and 10 arg) and 7 acidic residues (6 asp and 1 glu) while the C-terminal half has 16 basic residues (7 lys and 9 arg) and 4 acidic residues (3 asp and 1 glu). Although the net-positive charge of unmodified MBP-C1 is +20, the net-positive charge of the C-terminal half (+12) is 50% greater than that in the N-terminal half (+8). Interestingly, hydrophobic photolabeling studies have shown that the N-terminal half of MBP-C1 has a greater propensity to insert hydrophobic amino acid side-chains into lipid bilayers than the C-terminal half (Boggs *et al.*, 1999a). For the modified isoforms, MBP-C2, C3, C5 and C8, some discrepancy has arisen on the type and site of post-translational modifications in the amino acid sequence. The decrease of one net-positive charge for MBP-C2 was originally thought to originate from deamidation of either a glutamine or asparagine (Chou *et al.*, 1976). The decrease of two in net-positive charge for MBP-C3 had been proposed to arise from a combination of phosphorylation and deamidation (Chou *et al.*, 1976; Moscarello, 1990). More recently, capillary electrophoresis-mass spectrometry on MBP isoforms extracted from bovine brain determined that MBP-C2 is deamidated at Gln146 while MBP-C3 is phosphorylated at Thr97 and Ser164 (Zand *et al.*, 1998). Zand *et al.*, 1998, also found that the post-translational modification responsible for the charge reduction in MBP-C4 and C5 was phosphorylation; MBP-C4 was found to be phosphorylated at Ser54, Thr97 and Ser160, accounting for a decrease of three in net-positive charge; MBP-C5 was found to be phosphorylated at Ser7, Ser54, Thr97 and Ser164 accounting for a decrease of four in net-positive charge. Finally, MBP-C8 has been shown to have six arginines deaminated to neutral citrulline at Arg25, Arg31, Arg122, Arg130, Arg159 and Arg170, resulting in the loss of six positive charges in the protein sequence (Wood and Moscarello, 1989). Taking the results of Wood and Moscarello, 1989, and Zand *et al.*, 1998, into account, the majority of the post-translational modifications that alter the net-positive charge of unmodified MBP-C1 occur in the C-terminal half of the protein (Figure 2-3). The type and site of post-translational modification(s) in MBP-C2, C3, C5 and C8 are highlighted in Figure 2-3.

Figure 2-3. Amino acid sequence of unmodified human and bovine MBP. The two amino acid sequences are aligned as suggested in Zand *et al.*, 1998. Basic residues (K and R) are labeled in blue and acidic residues (D and E) are labeled in red. Citrullinated arginines in MBP-C8 are highlighted with a yellow circle (Wood and Moscarello, 1989). Deamidated Gln146 in MBP-C2 is highlighted with a green square. (Zand *et al.*, 1998). Phosphorylated residues in MBP-C3 (Thr97 and Ser164) and MBP-C5 (Ser7, Ser54, Thr97 and Ser164) are highlighted with a pink circle.

human A S Q K R₅ P S Q R H₁₀ G S...K Y L₁₅ A T...A S T₂₀ M D...H A R₂₅ H G.....F L P₃₀ R H
bovine A A Q K R₅ P S Q R.....S₁₀ K Y L...A S₁₅ A S T...M D₂₀ H A R...H G₂₅ F L P.....R H₃₀

human R D T₃₅ G I.....L D S₄₀ I G...R F F₄₅ G G...D R G₅₀ A P...K R G₅₅ S G...K D S₆₀ H H
bovine R D T.....G I₃₅ L D S...I G₄₀ R F F...G S₄₅ D R G...A P₅₀ K R G.....S G₅₅ K D G...H H₆₀

human P A R₆₅ T A...H Y G₇₀ S L...P Q K₇₅ S H.....G R T₈₀ Q...D E N P₈₅ V...V H F F₉₀ K N
bovine A A R...T T₆₅ H Y G...S L₇₀ P Q K...A Q₇₅ H G R P...Q₈₀ D E N P...V₈₅ V H F F...K₉₀ N

human I V T₉₅ P.....R T P P₁₀₀ P.....S Q G K₁₀₅ G...R G L S₁₁₀ L.....S R F S₁₁₅ W...G A E G₁₂₀ Q
bovine I V T.....P₉₅ R T P P.....P₁₀₀ S Q G K...G₁₀₅ R G L S...L₁₁₀ S R F S...W₁₁₅ G A E G...Q₁₂₀

human R P G F₁₂₅ G.....Y G G R₁₃₀ A...S D Y K₁₃₅ S.....A H K G₁₄₀ F.....K G V D₁₄₅
bovine R P G F...G₁₂₅ Y G G R...A₁₃₀ S D Y K.....S₁₃₅ A H K G...L₁₄₀ K G H D

human A.....Q G T L₁₅₀ S.....K I F K₁₅₅ L...G G R D₁₆₀ S...R S G S P M A R R₁₇₀
bovine A₁₄₅ Q G T L...S₁₅₀ K I F K...L₁₅₅ G G R D...S₁₆₀ R S G S P M A R R

The total net-positive charge of each isoform compared to the net-positive charge of the N-terminal half and the C-terminal half of each isoform is summarized in Table 2-1. The N-terminal half of MBP-C1, C2 and C3 are identical, therefore these isoforms differ from one another in the C-terminal half of the sequence. The reduced net-positive charge of MBP-C2 and C3 in the C-terminal half of the sequence by 10% and 20%, respectively, may reduce the electrostatic association of these isoforms with negatively charged head groups on a bilayer surface. Although the C-terminal half of MBP-C3 and C5 have the

same net-positive charge, the two additional sites of phosphorylation on Ser7 and Ser54 in MBP-C5 reduces the net-positive charge of the N-terminal of MBP-C5. In turn, this 25% reduction of net-positive in the N-terminal half of MBP-C5 may further promote insertion of N-terminal half segments into a bilayer surface. Finally, the net-positive charge of the C-terminal half of MBP-C8 is reduced by 33% in comparison to unmodified MBP-C1, while the net-positive charge of the N-terminal half of MBP-C8 is similar to that of MBP-C5. In comparison to the uncitrullinated residues, strength of electrostatic association of the C-terminal half of MBP-C8 to acidic bilayers would be greatly compromised, especially under conditions where the net-negative SCD of the bilayer surface is not fully neutralized by the available positive charges on the protein (section 2.1.5).

Table 2-1. The relative net-positive charge in the C-terminal and N-terminal half of the MBP isoforms. Shown in brackets is the net-positive charge normalized to value for MBP-C1.

Isoform	Net-positive charge	Net-positive charge in N-terminal half	Net-positive charge in C-terminal half
C1	+20 (1.0)	+8 (1.0)	+12 (1.0)
C2	+19 (1.0)	+8 (1.0)	+11 (0.9)
C3	+18 (0.9)	+8 (1.0)	+10 (0.8)
C5	+16 (0.8)	+6 (0.8)	+10 (0.8)
C8	+14 (0.7)	+6 (0.8)	+8 (0.7)

The existence of the individual charge isoforms of MBP has been thought to have a physiological significance with regards to development and maintenance of the myelin sheath, and an upset balance may be responsible for the demyelination involved in diseases such as MS (Cheifetz and Moscarello, 1985). For example, myelin isolated from the white matter of individuals with chronic multiple sclerosis (MS) has been shown to exhibit a less cationic character than that obtained from unaffected individuals (Moscarello *et al.*, 1994; Wood *et al.*, 1996). Specifically, the ratio of the citrullinated MBP-C8 to that of the most cationic MBP-C1 increased more than two-fold for chronic MS myelin and more than six-fold for fulminating MS myelin of the Marburg type (Wood *et al.*, 1996). The distribution of the charge isoforms of MBP in normal human myelin has also

been proposed to vary within the tissue. For example, the least cationic isomer, MBP-C8, which comprises 20% of the total MBP, has been localized to the intraperiod line by immunogold electron microscopy using an antibody specific for citrulline (McLaurin *et al.*, 1993). McLaurin *et al.*, 1993 found that this was contrary to the localization of an antibody that recognized unfractionated MBP to both the major dense line and the intraperiod line (recall Figure 2-2). Perhaps the upset balance in the proportion of MBP-C8 to MBP-C1 in the myelin extracted from individuals with MS (Wood *et al.*, 1996), affects both the cationic character of MBP needed for adhesion of the myelin membrane and the distribution of MBP required for normal CNS myelin ultrastructure. Finally, an upset balance amongst charge isoforms may have different effects in paranodal myelin and compact myelin (sections 2.1.3 and 2.1.5). That is, a decrease in the net-positive charge of MBP (*i.e.*, when MBP-C8/C1 is high) may affect adhesion more in paranodal myelin, where the concentration of MBP to acidic lipid is low, than in compact myelin, where the concentration of MBP to acidic lipid is high (Boggs *et al.*, 1997).

2.1.5 Studies of the interactions of MBP charge isoforms with model lipid systems

Although the numerous studies on unfractionated MBP have been informative (section 2.1.3), greater understanding of MBP adhesion to the myelin membrane can be obtained by investigating the behavior of the individual MBP isoforms with model lipid systems. However, studies on the interaction of individual charge isoforms of MBP with model lipid systems are not as numerous as those on unfractionated MBP. To date, the literature has focused on MBP isoform interaction with acidic lipids (Choo, 1992; Jackson *et al.*, 1993; Boggs *et al.*, 1999a), neutral lipids (Boggs *et al.*, 1999a), binary lipid mixtures of net-negative charge (Cheifetz and Moscarello, 1985; Jo and Boggs, 1995; Boggs *et al.*, 1997; Boggs *et al.*, 1999b) and myelin-like membranes (Jo and Boggs, 1995; Boggs *et al.*, 1997) to name a few. The underlying objective in many of these investigations has been to understand the effect of the various post-translational modifications on myelin adhesion. In general, research has sought to define the role of net-positive charge on the interaction between the isoforms and acidic lipids, the type of interaction (electrostatic and/or hydrophobic) that occurs between the isoforms and various lipid systems, and the segments of the proteins that participate in the interaction.

The role of net-positive charge on the interaction of MBP with acidic lipids has been intensely studied for nearly two decades. The reduction of MBP net-positive charge has been shown to decrease the ability of the protein to bind and aggregate net-negatively charged lipid vesicles. For example, by measuring the optical density at 450 nm, Cheiftez and Moscarello, 1985, found that decreasing MBP net positive charge by *in vitro* phosphorylation of MBP-C1 and C2 reduced the ability of the proteins to aggregate PC vesicles containing 7.8% PS. Since a high concentration of MBP to acidic lipid was used in this study of Cheiftez and Moscarello, 1985, (*ca.*, 5.4 mol% MBP-to-PS), the negative charges on the vesicles would have been saturated⁴ by the positive charges available on MBP-C1 and C2. As the proteins were phosphorylated and negative charges were introduced onto the proteins, the extent of vesicle aggregation rapidly declined (Cheiftez and Moscarello, 1985). Cheiftez and Moscarello, 1985, suggested that inhibition of vesicle aggregation upon the phosphorylation of MBP-C1 and C2 was due to a charge repulsion between MBP and the negatively charged headgroups of acidic vesicles. A few years later, in a circular dichroism investigation, *in vitro* phosphorylation of the MBP isoforms was shown to increase the β -sheet structure of the proteins (Ramwani *et al.*, 1989). Given that a conformational change occurs upon extensive phosphorylation, Ramwani *et al.*, 1989, suggested that the positive charged residues on MBP-C1 and C2 available for association with acidic lipids may have been neutralized or shielded by the introduced phosphorylated amino acids. Therefore, Ramwani *et al.*, 1989, proposed that the inhibition of PS/PC vesicle aggregation by hyperphosphorylated MBPs, observed by Cheiftez and Moscarello, 1985, was caused by a reduction in the number of positively charged residues available for electrostatic association with PS. However, under the saturating conditions imposed by Cheiftez and Moscarello, 1985, it is more likely that the binding of hyperphosphorylated MBP to a vesicle would impart a net-negative charge on the vesicle surface and repulsion between these net-negatively charged vesicles inhibited aggregation (Jo and Boggs, 1995; Boggs *et al.*, 1997). Under conditions where the MBP to acidic lipid concentration does

4. The number of positive charges on MBP is 31. MBP-C2 (deamidated at Gln146) and *in vitro* phosphorylation products of MBP-C1 and C2 still have 31 positive charges potentially available to associate with PS. The 5.4 mol% of MBP to PS in the study of Cheiftez and Moscarello, 1985 would produce a positive-to-negative charge ratio of 1.7, well saturating the negative charges of the lipid.

not saturate the negative charges on the vesicle surface (0.2 mol% MBP to PS), the ability of MBP-C1, C2, C3, C4, C5 and C8 to mediate aggregation of PS/PC vesicles in 100 mM KCl decreases as net-positive charge decreases and isoform/vesicle dissociation in 150 mM KCl increases as isoform net-positive charge decreases (Boggs *et al.*, 1997). Boggs *et al.*, 1997 also found that the difference in the ability of MBP-C1, C2, C3, C4 and C5 to mediate vesicle aggregation in 100 mM KCl decreased when higher concentrations of protein (1.2 mol% MBP-to-PS) were used, whereas MBP-C8 mediated aggregation at 100 mM KCl was still markedly lower than that of the uncitrullinated MBPs. At first it was thought that the number of residues modified to carry a negative charge (via deamidation or phosphorylation) caused charge repulsion between these negatively charged residues and the excess negative charge on the lipid vesicles (Boggs *et al.*, 1997). However, once saturating⁵ concentrations of the MBP isoforms (3.7 mol% MBP-to-PS) were used, the KCl-induced increase in vesicle aggregation was not as dramatic and did not vary for MBP-C1,C2,C3, C4 and C5 (Boggs *et al.*, 1997). Therefore, repulsion from the negatively charged residue(s) on MBP-C2, C3, C4 and C5 caused by deamidation and phosphorylation was not responsible for their decreased ability to mediate aggregation at lower protein to acidic lipid ratios (Boggs *et al.*, 1997). Instead, Boggs *et al.*, 1997, suggested that the post-translational modifications on MBP-C2, C3, C4 and C5 reduce the extent of electrostatic binding between these isoforms and the PS head groups of the binary vesicles. MBP-C8 mediated aggregation of the PS/PC vesicles using 3.7mol% MBP was not carried out, however using 1.2 mol% MBP, vesicle aggregation in the presence of MBP-C5 was 30-40% greater than that in the presence of MBP-C8 (Boggs *et al.*, 1997). Boggs *et al.*, 1997, concluded that a decrease in the total number of positively charged residues in the protein sequence (*i.e.*, via citrullination) had a greater effect than a decrease in the net-positive charge by phosphorylation. Reduction in the multivalency of positive charges available for neutralization of negative charges on the bilayer surface is a different concept than decreased net-positive charge due to any post-translational modification. In addition, from the decreased difference in the ability of MBP-C1, C2, C3, C4 and C5 to mediate

5. Maximum aggregation was found using a 3.7 mol% of MBP-to-PS (vesicle composition of 9PC:1PS), which converts to a mole ratio of PS to MBP of 25, almost equal to the number of positive charged residues on MBP and saturation of the negative charges on the vesicle surface.

vesicle aggregation when high concentrations of MBP were used, Boggs *et al.*, 1997 proposed that an upset balance amongst these isoforms would likely have less of an effect on myelin adhesion in compact internodal myelin than in paranodal myelin.

Although the predominant interaction between unfractionated MBP and acidic lipids is believed to be electrostatic, the relative contribution of electrostatic association and hydrophobic interaction has yet to be quantified for each isoform. Several studies, however, have indicated that the MBP isoforms have differing degrees of amphipathic behavior towards net-negatively charged bilayers, such that partial insertion accompanies electrostatic association. For example, Choo, 1992, and Jackson *et al.*, 1993, reported FTIR spectra taken at 10°C and 30°C of a 1.1 mol% MBP to DMPG⁶ liposomal mixture, indicating that the most cationic isoforms exhibit a greater degree of electrostatic association with the bilayer surface and fewer penetrations of bilayer interfacial region than MBP-C5 and C8 (Choo, 1992; Jackson *et al.*, 1993). Strong association between isoform and the PG head groups was inferred by minimal difference in the acyl chain order of PG at 10°C and 30°C (Choo, 1992; Jackson *et al.*, 1993). Such an observation suggests that the acyl chains of the lipid remain ordered even upon the phase transition due to stabilization of the bilayer surface by electrostatic association with MBP-C1, C2, C3 or C4. The phase transition temperature of PG in the presence of the isoforms was not calculated by Choo, 1992, or Jackson *et al.*, 1993, but their inferred absolute abolition of the PG phase transition is not in agreement with the other studies that report a decrease in the phase transition temperature of acidic lipids upon MBP interaction (see Boggs *et al.*, 1999, for review). In contrast to the more cationic isoforms, MBP-C5 and C8 resulted in some dehydration of the bilayer interfacial region as observed by the decrease in the PG acyl C=O stretching profile (Jackson *et al.*, 1993). This latter observation indicates that the less cationic isoforms partially penetrate into the interfacial region. However, the acyl C=O absorption profile was not Fourier self-deconvolved, nor was it compared to that of the

6. Conditions where the PG negative SCD would be unsaturated. MBP-C1 has 31 positively charged residues available or a net charge of +20 which means that the negative SCD of PG would be 34% (0.011×31) or 22% (0.011×20) saturated depending on whether negatively charged amino acids shield some of the basic residues. MBP-C8 has 25 positively charged residues available or a net charge of +14 and the negative SCD of PG liposomes would be 34% or 15% saturated.

lipid in the absence of protein, making it impossible to make further inferences about the relative proportions of H-bonded C=O to free C=O in the bilayer interface upon isoform interaction. Jackson *et al.*, 1993, also reported that only the most cationic isoforms adopted some α -helical, β -sheet and turn structure along with random coil structure upon PG association. In the aggregation assays performed by Boggs *et al.*, 1997, using myelin-like⁷ vesicles and a sub-saturating concentration of each isoform (1.2 mol% MBP to acidic lipid), the degree of vesicle aggregation mediated by MBP-C8 upon exposure to 100 mM KCl, more closely resembled that observed for the other isoforms. Moreover, at higher concentrations of KCl (150-400 mM) little dissociation of the isoform-vesicle aggregates was observed when the vesicle composition more closely resembled that of myelin (Boggs *et al.*, 1997). Resistance to dissociation by high concentrations of KCl implied that other forces aside from electrostatic association were involved in the binding of the MBP isoforms to myelin-like membranes, such as H-bonding of the protein to lipid headgroups and penetration of hydrophobic amino acid side chains into the bilayer (Boggs *et al.*, 1997). The existence of membrane-interacting domains or segments of the MBP-C1 and C2 has been substantiated by the hydrophobic photolabeling studies of Boggs *et al.*, 1999a. For example, upon interaction with PG, MBP-C1 and C2 were labeled more on the N-terminal half than on the C-terminal half of the sequence, suggesting that the hydrophobic interacting segments are located in the N-terminal half of the protein (Boggs *et al.*, 1999a). Boggs *et al.*, 1999a, further noted that the N-terminal half of these MBP proteins still contained more hydrophobic label than the C-terminal half when the proteins interacted with a neutral lipid like PC. These were interesting findings, since it is the C-terminal half of MBP which is more susceptible to the host of post-translational modifications documented for the different isoforms (see section 2.1.4, Figure 2-3). For example, the site of deamidation is located in the C-terminal half of the MBP-C2 sequence (Gln146 to Glu146), resulting in a gain of one negative charge in the solvent accessible portion of MBP-C2. Thus, since the N-terminal half of MBP-C1 and C2 are identical, net-positive charge has little effect on the penetration of MBP isoforms into the bilayer of lipids

7. Myelin-like vesicles were composed of 44 mol% cholesterol, 27 mol% PE, 13 mol% PS, 11 mol% PC, 3 mol% sphingomyelin and 2 mol% PI akin to the lipid composition of the cytoplasmic leaflet of myelin. Thus, these vesicles contain 15 mol% acidic lipid.

(Boggs *et al.*, 1999a), while the ability of MBP-C2 to aggregate acidic vesicles is slightly reduced by the reduced number of available positive charges in the C-terminal half of the MBP-C2 for electrostatic binding (Cheifetz and Moscarello, 1985; Boggs *et al.*, 1997). Hydrophobic photolabeling of the more modified isoforms have not yet been reported for comparison. However, a more recent vesicle aggregation study has been carried out to investigate whether citrullination increases the amphipathic behavior of MBP (Boggs *et al.*, 1999b). Boggs *et al.*, 1999b, examined the ability of MBP-C1, C8 and poly-citrullinated MBP-Cit(18)⁸ to aggregate large multilayered net-negatively charged lipid vesicles. Similar to the earlier aggregation assay, MBP-C1 interaction increased the absorbance at 450 nm more than that of MBP-C8, indicating greater aggregation is mediated by MBP-C1, but MBP-Cit(18) actually decreased ΔA^{450} of the lipid vesicles (Boggs *et al.*, 1999b). Boggs *et al.*, 1999b, found that upon size exclusion chromatography and electron microscopy it was found that MBP-Cit(18) actually fragmented the large vesicles into smaller ones (Boggs *et al.*, 1999b). Boggs *et al.*, 1999b, concluded that extensive citrullination caused MBP-Cit(18) to act more like an apolipoprotein rather than an extrinsically associated protein. Moreover, it was suggested that although fragmentation of the large vesicles did not occur, 6 citrullines may still increase the amphipathic character of MBP-C8 (Boggs *et al.*, 1999b).

2.1.6 Objectives of the current study

It was the aim of the current study to use FTIR spectroscopy to investigate the interactions of the various charge isoforms of MBP (C1, C2, C3, C5 and C8) with binary lipid systems composed of dipalmitoylphosphatidylglycerol (PG) and per-deuterated dimyristoylphosphatidylcholine (d-PC).⁹ Since it is unclear whether MBP can indeed interact with a zwitterionic lipid such as PC, isoform interaction with d-PC was examined to ascertain if PG and d-PC in the binary liposomes could compete for interaction with the

8. Extracted from the myelin of individuals that died from fulminating (Marburg-type) MS, MBP-Cit(18) has 18 or 19 arginyl residues deaminated to citrulline.

9. Although phosphatidylserine (PS), the predominant acidic phospholipid of myelin (Morell *et al.*, 1994), would have been the ideal choice for the acidic lipid in the model system rather than PG, the PS head group absorbs at 1620-1630 cm^{-1} , making conformational analysis of the amide I band profile of MBP impossible (see section 1.5.2).

protein(s). It was proposed that only the isoforms with decreased net-positive charge or electronically neutral segments could stabilize an electronically neutral bilayer surface. If surface interaction with d-PC is possible, preferential interaction of the less positively charged isoforms with d-PC may depend on the proportion of d-PC in the binary liposomes. Another objective of the present study was to evaluate the role of net-positive charge on the interaction of MBP with acidic liposomes, when the negative SCD of the bilayer was unsaturated by the positive charges on the protein. PG liposomes with 0.8 mol% MBP were used to model the interaction between MBP and an acidic bilayer with a negative SCD that is unsaturated by the 31 positive charges on the unmodified protein (*i.e.*, paranodal myelin). It was hypothesized that the isoforms of greater net-positive charge (C1, C2 and C3) would be more effective at stabilizing the PG bilayer by electrostatic association, while isoforms of less net-positive charge (C5 and C8) would interact less at the surface and penetrate the bilayer. To investigate the influence of saturating the negative SCD of an acidic bilayer, the concentration of MBP to acidic lipid was gradually increased by raising the d-PC content in binary PG/d-PC liposomes. The greater the concentration of MBP to PG, the greater the saturation of the net-negative SCD on the PG/d-PC bilayer surface by the positive charges on the protein. PG/PC liposomes with 3.1 mol% MBP to PG were used to model the interaction between MBP and an acidic bilayer with a net-negative SCD that is nearly saturated by the 31 positive charges on the unmodified protein (*i.e.*, compact myelin). It was hypothesized that saturation of the net-negative SCD of the binary liposomes by the positive charges on MBP would enhance the electrostatic association of the isoforms with the PG and possibly lead to the formation of PG microdomains in the binary liposomes.

All protein-lipid interactions can be evaluated by the change in the phase behavior of the lipid(s) in the presence of each isoform, and the change in isoform conformation upon interaction with the lipid(s). The gel to $L\alpha$ state phase transition of the lipids alone and in the presence of each isoform can be examined by monitoring the temperature dependence of the lipid methylene stretching vibrations (see section 1.5.2). A protein interacting with a lipid bilayer by intercalation should result in a decrease of the lipid phase transition temperature (T_m). In contrast, an increase in T_m is observed when the interaction is more purely electrostatic since tight association to the lipid head groups in

the absence of bilayer penetration restricts the conformational freedom of the lipid acyl chains. However, MBP has been shown to result in a decrease in the T_m of acidic lipids because a combination of electrostatic association and bilayer penetration is believed to occur (see sections 2.1.3 and 2.1.5). To investigate the relative proportion of stabilization by MBP electrostatic association to destabilization by MBP bilayer penetration, the acyl chain order of the lipid in both states was examined. That is, the greater the acyl chain order (lower frequency), the greater the relative proportion of stabilization by MBP electrostatic association to destabilization by MBP penetration into the bilayer. Further information on the extent of MBP penetration can be obtained by examination of the hydration of the bilayer interface, interpreted from the acyl C=O stretching profile (*ca.* 1738 cm^{-1}) of the PG or d-PC liposomes in the presence of each isoform (see section 1.5.2). For example, upon protein penetration, solvent access to the interfacial region of the fluid bilayer is reduced and the lipid acyl C=O band contour should shift to higher frequency (*i.e.*, dehydration effect). Finally, structural changes of the isoforms upon interaction with the lipid(s) will be observable by monitoring the amide I band profile and the δ -guanidino stretching profile of arginine side chains (see section 1.5.1). The conformational changes observed for the isoforms in a PG or d-PC environment, compared to those observed upon interaction with the binary liposomes, will provide further insight on the preferential interaction of the isoforms with either d-PC or PG.

2.2 . MATERIALS AND METHODS

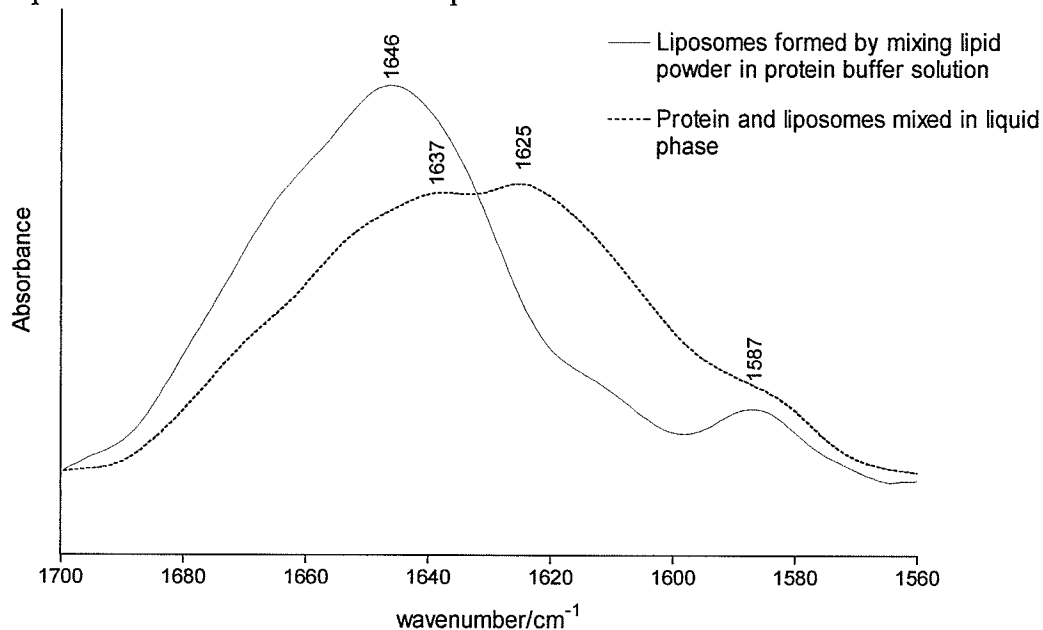
2.2.1 Materials

Myelin basic protein charge isoforms C1-C3, C5 and C8, isolated and purified from bovine brain by the method of Chou *et al.*, 1976, were obtained from the laboratory of M.A. Moscarello (University of Toronto, Canada). The sodium salt of dipalmitoylphosphatidylglycerol (PG) from Sigma and per-deuterated phosphatidylcholine (d-PC) from Avanti Polar Lipids were used without any further purification ($MW_{PG} = 744.96 \text{ g/mol}$; $MW_{d-PC} = 732.38 \text{ g/mol}$). All materials were kept in a -30°C freezer until the liposomal samples were to be prepared.

2.2.2 Sample preparation

Liposomes of PG:d-PC in various compositions (1:0, 3:1, 1:1, 1:3 and 0:1 by weight) were prepared in phosphate buffer saline solution (PBS powder, from Sigma) using D₂O as the solvent (pD=7.4) to a lipid concentration of 50 mg/ml. The lipid solution was briefly sonicated until a milky solution was formed, and then repetitive cycles of heating the sample with hot water (near the phase transition temperature of the pure lipid), vortexing while warm and then cooling under tap water were carried out to ensure full hydration. Solutions of MBP C1-C3, C5 and C8 alone were prepared in PBS/D₂O (pD=7.4) to a protein concentration of 10 mg/ml, the lower limit for IR detection for a pathlength of 25 μ m (section 1.3.1), so that the conformation of the protein in aqueous solution could be assessed and compared to that in the presence of lipid. Introduction of a protein solution to the prepared liposomal solution resulted in the appearance of predominant amide I absorption at 1615-1620 cm^{-1} , which signified that the protein preferred to aggregate under such conditions. The amide I component band due to aggregated strands was then minor if not absent when this sample preparation was tested spectroscopically. Spectroscopic comparison of the two methods is shown in Figure 2-4, where human myelin basic protein, isoform C3, was examined in a preliminary study. The band due to aggregation at 1624 cm^{-1} , found when protein and lipid were introduced to one another in the liquid phase, is absent in the spectrum of the protein mixed with lipid powder. Since MBP does not denature below 80°C, it was concluded that preparation of the liposomes in a protein/buffer solution could proceed as described. Therefore, the protein-lipid samples were prepared by replacement of PBS/D₂O used previously in the lipid only samples with a protein/ PBS/D₂O solution, maintaining a lipid to protein ratio of 5:1 by weight. D₂O was used instead of H₂O so that sample absorption bands in the IR would not be obscured by the interfering bands of H₂O (section 1.3.1). However, it should be noted that D₂O solutions could cause a 0.2-0.4°C increase in the main phase transition temperature of a lipid (Casal and Mantsch, 1984). Moreover, per-deuteration of acyl chains of phospholipids (as in the case of d-PC used in this study) is known to cause a 4-5°C decrease in the T_m of the lipid (Peterson *et al.*, 1975)

Figure 2-4. Spectral comparison of the amide I band profile of human MBP-C3 when introduced into a liposomal system or when lipid is added directly to the protein/buffer solution to form liposomes.



The mole ratio of MBP to PG for liposomes of various negative surface charge density were 1:130 (0.8 mol%), 1:98 (1.0 mol%), 1:65 (1.5 mol%) and 1:32 (3.1 mol%) for the liposomes prepared with 1:0, 3:1, 1:1, 1:3 PG:d-PC by weight, respectively. By taking into account the multivalency of positive charges available and the net-positive charge of each MBP isoform, the percent saturation of the negative surface charge density of the pure PG and binary PG:d-PC liposomes was calculated (Table 2-2). As shown in Table 2-1, the 1:3 PG:d-PC liposomal composition (3.1 mol% MBP to PG) represents a near saturation of the negative surface charge density by the available positively charged residues in MBP-C1, C2, C3 and C5 and to a lesser extent in MBP-C8. Thus, the 1:3 PG:d-PC mixture is proportioned in a way for comparison to other MBP examinations as nearly saturating concentrations of MBP to acidic lipid (compact myelin), whereas interaction of MBP with the other liposomal mixtures is comparable to situations where the MBP concentration is rather low (paranodal myelin).

Table 2-2. The percent saturation of liposomal negative SCD by each MBP isoform.

Both the multivalency of positive charges available on the isoform and the overall net-positive charge (in parentheses) were taken under consideration.

Mol% MBP to PG	Saturation by C1	Saturation by C2	Saturation by C3	Saturation by C5	Saturation by C8
0.8 mol%	25% (16%)	25% (15%)	25% (14%)	25% (13%)	20% (11%)
1.0 mol%	31% (20%)	31% (19%)	31% (18%)	31% (16%)	25% (14%)
1.5 mol%	47% (30%)	47% (29%)	47% (27%)	47% (24%)	38% (21%)
3.1 mol%	96% (62%)	96% (59%)	96% (56%)	96% (50%)	78% (43%)

2.2.3 FTIR spectroscopy

FTIR spectroscopy was carried out using a BioRad FTS-60 spectrometer equipped with a liquid nitrogen cooled MCT detector, belonging to the Molecular Spectroscopy Division of the Institute for Biodiagnostics (IBD), National Research Council of Canada, Winnipeg, Manitoba. Temperature-ramped IR spectra were acquired on MBP C1-C3, C5 and C8 in buffer and on the PG:d-PC liposomes (1:0, 3:1, 1:1, 1:3 and 0:1) alone and in the presence of each MBP isoform. When preparation was complete, 10 μ l of sample was placed between two BaF₂ windows separated by a 25 μ m Teflon spacer and the demountable IR cell (section 1.2.2) made by Harrick ScientificTM was sealed and placed in a thermostated metal jacket located in the sample compartment of the spectrometer. A computer-interfaced thermocouple was placed in the port of the IR cell to monitor the temperature of the sample during spectral acquisition. The thermocouple was calibrated to the temperature of the waterbath used to heat the thermostated metal jacket in 2 $^{\circ}$ C increments.

Calibration was accomplished by monitoring the temperature recorded by the thermocouple in the waterbath as a function of the set water bath temperature and fitting the curve to a second-order polynomial on Graph Pad PrismTM software (Figure 2-5). This procedure was carried out frequently to ensure accurate calibration of the thermocouple. Once calibrated, heat loss from the water bath to the sample compartment during spectral acquisition was then corrected by placing this polynomial equation in Microsoft ExcelTM and

using the recorded thermocouple temperature to derive the actual temperature of the IR cell in the sample compartment. Since the water bath was connected to the thermostated cell jacket by means of a one metre insulated tube, the time required to allow the cell to reach the temperature set by the waterbath had to be established. It was established that a ten minute equilibration time was preferable to that of five minutes to heat the sample cell to the desired waterbath set temperature (Figure 2-5). As shown in Figure 2-5, either equilibration time was suitable for the cell temperature to reach that of the waterbath in the lower temperature range of 15-30°C. At higher temperatures however, the cell temperature began to lag behind, a lag that was less pronounced using a longer equilibration time (Table 2-3). From these initial measurements it was decided that at least ten minutes was required for the IR cell inside the sample compartment to reach the water bath set temperature and achieve thermal equilibrium. An equilibration time greater than ten minutes was not considered to be practical since there was a risk of sample evaporation at the higher temperatures. Therefore, the use of the thermocouple to monitor the temperature of the cell was imperative since some heat loss from the water through the insulated tubing to the thermostated jacket was unavoidable.

Figure 2-5. Calibration of the thermocouple used in the temperature-ramped studies to the waterbath temperature.

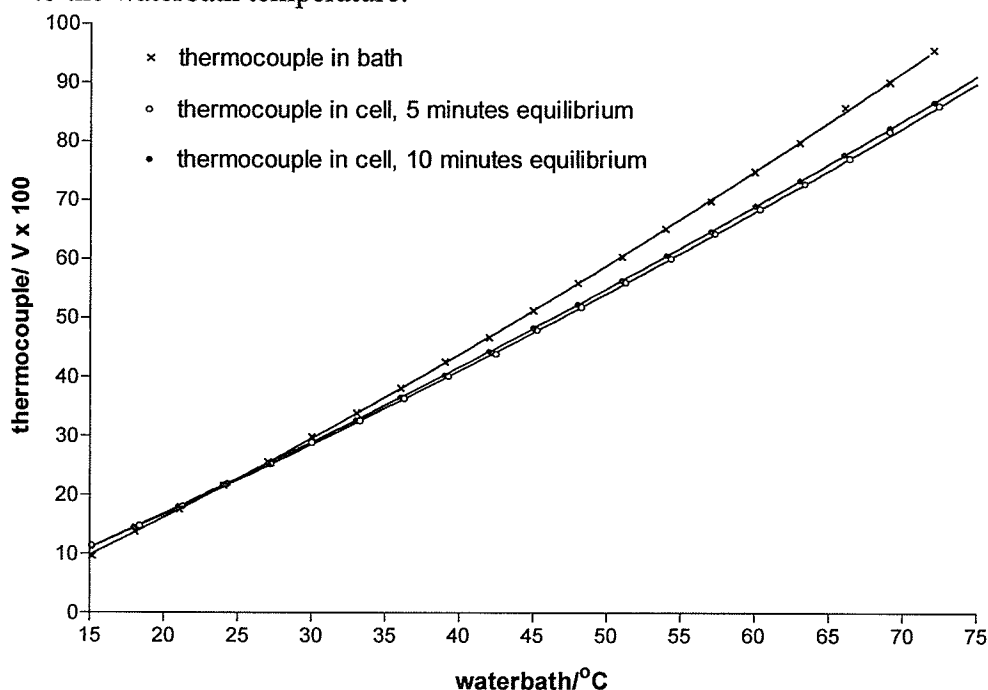


Table 2-3. Comparison of cell temperature at five or ten minutes equilibration time.

The cell temperatures were recorded by the calibrated thermocouple located in the port of the IR cell.

$T_{\text{bath}}/^{\circ}\text{C}$	$T_{\text{cell}}(5 \text{ min.})/^{\circ}\text{C}$	$\Delta T (5 \text{ min.})$	$T_{\text{bath}}/^{\circ}\text{C}$	$T_{\text{cell}}(10 \text{ min.})/^{\circ}\text{C}$	$\Delta T (10 \text{ min.})$
15.14	16.30	1.16	15.18	16.14	0.96
18.40	8.88	0.48	17.98	18.72	0.74
21.28	21.42	0.14	20.99	21.42	0.43
24.29	24.29	0.00	23.99	24.14	0.15
27.27	26.82	-0.45	27.05	26.89	-0.16
30.03	29.45	-0.85	30.02	29.60	-0.42
33.30	32.11	-1.19	33.01	32.26	-0.75
36.27	34.80	-1.47	36.03	34.94	-1.09
39.30	37.45	-1.85	39.02	37.59	-1.43
42.29	40.06	-2.23	42.02	40.33	-1.69
45.29	42.76	-2.53	45.03	43.03	-2.00
48.28	45.42	-2.86	48.02	45.68	-2.34
51.30	48.11	-3.19	51.01	48.30	-2.71
54.36	50.75	-3.61	54.03	51.07	-2.96
57.35	53.42	-3.93	57.03	53.68	-3.35
60.35	56.06	-4.29	60.02	56.37	-3.65
63.38	58.72	-4.66	63.03	59.09	-3.94
66.39	61.34	-5.05	66.01	61.76	-4.25
69.08	64.11	-4.97	69.09	64.46	-4.63
72.45	66.72	-5.73	72.09	67.07	-5.02
75.44	69.35	-6.09	75.10	69.76	-5.34
78.43	71.95	-6.48	78.06	72.35	-5.71

Once the methodology had been established, the computer-controlled water bath was set to ramp the temperature by 2°C increments allowing 10 minutes for thermal equilibrium of the sample at each temperature prior to each spectral acquisition. Mid-infrared spectra were collected on a Bio-Rad FTS 60 spectrometer equipped with a liquid nitrogen cooled MCT detector. For each spectrum collected 256 interferograms were co-added and signal averaged using a nominal resolution of 2 cm^{-1} . The thermocouple temperature recorded at the beginning and end of each spectral acquisition (acquisition time per spectrum = 150 sec.) was stable. The thermocouple temperature recorded during the first scan was corrected using the calibration curve described above and the temperature of the sample was calculated to an experimental error of 0.1°C . Re-calibration of the thermocouple was done periodically between temperature-ramped experiments.

2.2.4 Spectral preprocessing and analysis of data

Spectra were buffer-subtracted and the spectrum of water vapor was interactively subtracted from all spectra (see sections 1.2.2 and 1.4.4) using WIN-IR™ software (Bio-Rad). Second-order derivative spectra, calculated using 13 points for smoothing, were utilized in evaluation of the temperature dependence of the methylene asymmetric CH and CD stretching vibration of PG and d-PC, respectively. Fourier self-deconvolved (FSD) spectra (WIN-IR™ array basic program parameters: FWHH = 17.2 cm⁻¹, smoothing = 66.5%) were utilized to assess the conformation of the protein in aqueous solution and in a liposomal environment by observation of changes in the amide I band profile and amino acid side chain absorptions (1700-1550 cm⁻¹). Second-order derivative spectra (21 points) were also calculated to confirm the presence of component bands in the amide I band profiles (see section 1.4.5 for description of band narrowing techniques). Hydration at the bilayer interfacial region for the MBP:PG or MBP:d-PC samples was assessed by comparison of the lipid acyl C=O absorption profile when in the presence of each isoform to that found for pure PG or pure d-PC above and below the T_m of the lipid.

The main transition temperatures of the lipids were estimated and the energy of the gel and L α states were found by using a Boltzmann sigmoidal function¹⁰ (Graph Pad Prism™ software) to fit the curve of methylene vibrational frequency (cm⁻¹) as a function of temperature. The energy (proportional to cm⁻¹) of the gel and L α states were derived from their mean frequencies in the plateau regions of the two state transition calculated by the Boltzmann sigmoidal function. It should be noted that this method used to calculate the main phase transition temperature of a lipid based on the temperature dependence of the methylene stretching frequency is an approximation. It has been discussed in the literature that the temperature dependence of the methylene stretching bands tends to exhibit a non-

10. Boltzmann sigmoidal function as defined by Graph Pad Prism™ software, where “V50” is the mid-point of the transition, “slope” refers to the slope of the transition interval (*i.e.*, cooperativity of the transition) and “Top” and “Bottom” define the horizontal portions of the plot for the L α and gel state frequencies, respectively.

$$Y = \frac{\text{Bottom} + (\text{Top} - \text{Bottom})}{1 + \exp[(V50 - X)/\text{slope}]}$$

linear functional relationship to the temperature dependence of the fraction of lipid molecules in the liquid crystalline state (Dhuly *et al.*, 1983; Lasch *et al.*, 1998). This nonlinear relationship arises due to the superposition of both lipid populations in one absorption band (Dhuly *et al.*, 1983). However, these two component bands cannot be resolved experimentally, nor by FSD or FD calculations. Instead, the calculation of T_m proposed by Dhuly *et al.*, 1983, proceeds by defining a band shape for each lipid population (gel and $L\alpha$ state) and then calculating the contribution of these lipid populations to absorption profiles within the melting interval. Such model calculations use experimentally derived band parameters, such as intensity, full width at half maximum and frequency to deduce the fraction of lipid molecules in the liquid crystalline state at each temperature yielding a more meaningful T_m of the lipid. These methylene stretching band parameters for the lipid molecules in both of the pure states (gel and $L\alpha$) are extrapolated from the extremes of the melting interval and then used to calculate each absorption profile (linear combination of each pure state) within the melting interval. Once the calculated absorption profile matches that band contour obtained experimentally, the proportion of molecules in the $L\alpha$ state needed to produce the curve-fit is plotted as a function of temperature and the midpoint of the transition is derived from a Boltzmann sigmoidal fit of the melting curve. In this manner, the calculation proposed by Dhuly *et al.*, 1983, results in a Boltzmann sigmoid that has horizontal upper and lower states and a defined slope within the melting interval connecting the two states which allows for direct comparison of midpoints from different samples. This model calculation was not performed to derive the lipid phase transition temperatures in this current study mainly to avoid curve-fitting IR absorption bands (see Chapter 1). In addition, the pure lipid phase transition temperatures calculated in the current study using the Boltzmann sigmoidal function were found to be in agreement with the accepted literature values for DPPG and d-DMPC, taking into account the effects of isotopic substitution and the use of D_2O as the solvent (see section 2.3.1).

2.3 RESULTS AND DISCUSSION

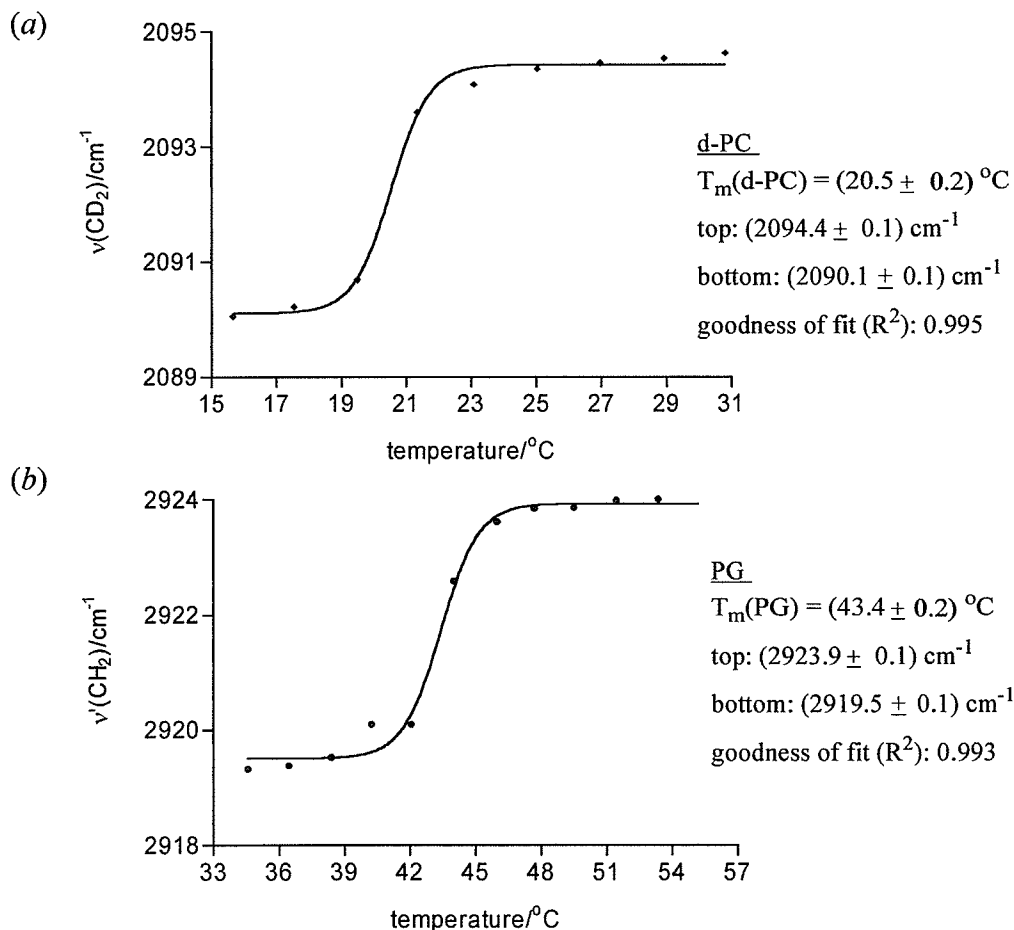
The FTIR spectra collected of each lipid, protein-lipid and protein sample provided the data to evaluate changes in lipid dynamics and in protein structure upon protein-lipid interaction. Analysis of the phase behavior of the lipid systems in the absence of protein provided a starting point in this research endeavor and therefore is presented first in section 2.3.1. Three parameters were used to evaluate the phase behavior of either pure PG or d-PC; namely the phase transition temperature, the acyl chain order of each lipid state (*i.e.*, energy determined by the proportion of methylenes in the *trans* and *gauche* conformation) and acyl carbonyl stretching profile of each lipid state. Two parameters were used to analyze the phase behavior of PG and d-PC in the binary liposomes, the phase transition temperature and the lipid acyl chain order. Once the phase behavior of the lipid systems had been evaluated, the phase behavior of the lipids were used to evaluate the interaction between each MBP isoform and d-PC (section 2.3.2), PG (section 2.3.3) and PG:d-PC liposomes of various net-negative SCD (section 2.3.4). A change in the phase behavior of either lipid upon protein presence was taken as unequivocal evidence for interaction. Aside from monitoring variations in the phase temperature of PG and d-PC upon protein presence, alterations in the acyl chain order of PG and d-PC were examined as a more localized parameter to define each state of the lipid. Changes in the $T_m(\text{lipid})$, acyl chain order of each lipid state and bilayer interfacial hydration of each lipid state (pure liposomes only) were used together to establish the type of protein-lipid interaction that predominates and to ascertain whether MBP could induce the formation of PG microdomains in binary PG:d-PC liposomes. Finally, the conformation of the MBP isoforms in aqueous solution (section 2.3.5) was compared to the conformation in a neutral d-PC (section 2.3.6), acidic PG (section 2.3.7) and binary PG:d-PC liposomal environments of reduced negative SCD (section 2.3.8). The conformational changes observed for the isoforms in a PG or d-PC environment were compared to those observed upon interaction with the binary liposomes to verify preferential interaction with either d-PC or PG.

2.3.1 The phase behavior of the pure lipid systems

As the temperature is increased a lipid undergoes a two-state transition from the highly ordered gel state to the more fluid liquid crystalline state (section 1.5.2). Such a transition was followed in the current study by monitoring the frequency of methylene CH and CD stretching of PG and d-PC, respectively, as a function of temperature. A plot of frequency as a function of temperature was then fitted to the Boltzmann sigmoidal function (described in section 2.2.4) to derive the phase temperature of the lipid. The methylene asymmetric CH stretch of PG (*ca.* 2916-2924 cm^{-1}) was used preferentially in the Boltzmann sigmoidal calculation as the symmetric methylene stretch at 2850-2852 cm^{-1} was subject to more interference from the strong, broad D-O-D stretching (*ca.* 2800-2100 cm^{-1}) of the solvent (see section 1.3.1). Similarly due to solvent interference, it was concluded that the methylene symmetric CD stretch of d-PC (*ca.* 2089-2095 cm^{-1}) was a more reliable source of information to determine the acyl chain order than the symmetric stretch at 2189-2193 cm^{-1} .

Examples of Boltzmann sigmoidal fitted curves used to calculate the lipid phase transition temperatures and the wavenumbers of the gel and $L\alpha$ states are given in Figure 2-6. The literature values for the main phase transition temperature of the sodium salt of DPPG at neutral pH and DMPC are 41.5 and 23.5°C, respectively (CRC Handbook of Lipid Bilayers, 1990). In comparison to the literature value, our experimentally determined $T_m(\text{PG})$ was found to be 43.4 °C and was thus within agreement considering experimental error and that our measurement was carried out in D_2O which typically increases the T_m of a lipid by 0.2-0.4°C (Casal and Mantsch, 1984; Lasch *et al.*, 1998). For the per-deuterated DMPC utilized in this study, it was expected that per-deuteration of the acyl chains would cause a 4-5°C decrease in the phase transition temperature of DMPC in combination with the 0.2-0.4°C increase observed when measurements are carried out in D_2O (Peterson *et al.*, 1975). Our experimentally determined $T_m(\text{d-PC})$ of 20.5°C was thus found to coincide with the accepted literature value.

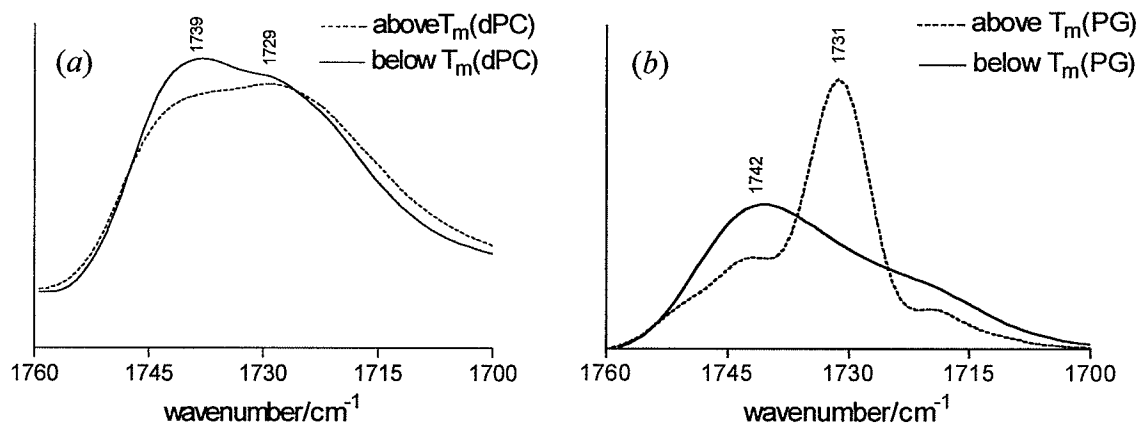
Figure 2-6. Boltzmann sigmoidal function used to discern the midpoint of a lipid phase transition. Shown are the melting curves for (a) d-PC; methylene symmetric stretch, $\nu(\text{CD}_2)$, as a function of temperature and (b) PG; methylene asymmetric stretch, $\nu(\text{CH}_2)$, as a function of temperature.



Aside from the phase transition temperature of the pure lipid systems, the temperature dependence of the lipid acyl C=O stretch can also provide information regarding the hydration of the bilayer interfacial region and thus the state of the lipid (section 1.5.2). The acyl C=O stretch of both the *sn*-2 and the *sn*-1 chains comprise the overall acyl C=O stretching profile. However, IR studies on lipids with one acyl chain ^{13}C -labeled have revealed that the frequency of the two acyl chain modes while in one state actually differ by only 4 cm^{-1} and that the two composite bands revealed upon FSD of the C=O contour of unlabeled phospholipids arises due to differences in hydration (Mantsch and McElhaney, 1991). That is, the higher frequency component band arises from free acyl C=O moieties

while the lower frequency component band arises from those that are H-bonded. The relative intensity of the H-bonded C=O component band to that of the free C=O increases in response to an increase in bilayer fluidity and the increase in hydration at the bilayer interfacial region. This increase in the relative intensity of the H-bonded C=O band to the free C=O band is shown for d-PC and PG in Figure 2-7. For pure d-PC liposomes the low frequency H-bonded C=O stretch (1729 cm^{-1}) increased in relative intensity to the high frequency free C=O stretch (1739 cm^{-1}) in response to the lipid phase transition (Figure 2-7a). A more dramatic increase in the relative intensity of the H-bonded C=O (1731 cm^{-1}) to free C=O (1742 cm^{-1}) was observed for PG (Figure 2-7b). The choline head group ($^+\text{N}(\text{CH}_3)_3$) of d-PC is more hydrophobic than the polar glycerol headgroup of PG. In comparison to PG, the moderate state of hydration of the $L\alpha$ state d-PC bilayer interfacial region may be due to the increased hydrophobicity at the surface of the d-PC bilayer.

Figure 2-7. The increase in bilayer hydration upon the gel to $L\alpha$ phase transition as observed by the change in the lipid acyl C=O stretching profile. (a) The acyl C=O stretch of d-PC below and above $T_m(\text{d-PC})$ at 15°C and 31°C , respectively. (b) The acyl C=O stretch of PG below and above $T_m(\text{PG})$ at 31°C and 55°C , respectively.



Evaluation of the lipid phase temperature of the binary lipid systems in the absence of protein was also carried out. As shown in Table 2-4, the phase transition temperatures of PG and d-PC in the binary lipid mixtures remained similar to those obtained when the pure lipids were examined. There was less variance in the calculated phase transition temperatures of d-DMPC in each mixture (within 0.4°C) than that for DPPG (within 2.0°C). The

1.0-2.0°C increase in the $T_m(\text{PG})$ would at first suggest a slight stabilization of the PG portion of the bilayer. However, this result is counterintuitive if the lipid mixture was homogeneous. Disordering in the acyl chains of d-PC should produce kinking in neighboring PG chains and promote PG melting at a slightly lower temperature. Prior to making any strong conclusions based on phase transition temperatures alone, which may involve a 2°C error, it was therefore necessary to evaluate the relative order of the lipid acyl chains in the gel and $L\alpha$ state when PG and d-PC were combined.

Table 2-4. Phase transition temperatures of PG and d-PC in liposomes of varied PG:d-PC composition. $T_m(\text{d-PC})$ and $T_m(\text{PG})$ were estimated from Boltzmann sigmoidal fits of $\nu(\text{CD}_2)$ and $\nu'(\text{CH}_2)$ versus temperature, respectively.

(PG:d-PC)	$T_m(\text{d-PC})/^\circ\text{C}$	$T_m(\text{PG})/^\circ\text{C}$
1:0	-	43.4 ± 0.2
3:1	20.3 ± 0.2	44.3 ± 0.2
1:1	20.1 ± 0.2	45.4 ± 0.2
1:3	20.3 ± 0.2	44.8 ± 0.2
0:1	20.5 ± 0.1	-

Summarized in Table 2-5, are the frequencies of the gel and $L\alpha$ states of PG and d-PC in the liposomal preparations. Related by Planck's constant, frequency (in cm^{-1}) is directly proportional to energy and therefore reflects the averaged order of the acyl chains. The frequency of the d-PC acyl chains when both lipids are in the gel state (15-19°C) remains constant within 0.4 cm^{-1} regardless of PG presence. Similarly, the $L\alpha$ state energy of d-PC remains constant within 0.4 cm^{-1} when PG is still in its ordered gel state (23-40°C). These results appear to match the lack of change in the phase transition temperature of d-PC when in the presence of PG. The larger changes seen in the gel and $L\alpha$ state energy of PG when the d-PC content exceeded that of PG (*i.e.*, 1PG:3d-PC mixture) may be due to the premature kinking of PG acyl chains neighboring the d-PC acyl chains already in a fluid state. This slight destabilization of the PG acyl chains prior to the system reaching the melting temperature of pure PG liposomes does not match the small increase noted for $T_m(\text{PG})$ when the d-PC content was increased (Table 2-3). Such a discrepancy may have arisen from the approximate method chosen to calculate phase transition temperatures, however

it is more likely that this discrepancy exists because the phase transition temperature is a global measurement of the system (*i.e.*, sensitive to both the interfacial hydration and acyl chain fluidity) while the frequency of the acyl chains is a localized parameter (*i.e.*, probing only the acyl chain fluidity). Aside from the acyl chain length, other variables can contribute to the observed T_m of a lipid, such as the chemical nature of the headgroup and its interaction with the aqueous solvent (see discussion below). In a homogeneous binary lipid mixture, interactions that exist between the headgroups and the aqueous solvent can be disrupted. For example, the hydrophobic choline headgroups of PC in the binary PG:d-PC mixtures may have interrupted the extensive H-bonding network between the PG glycerol head groups and the solvent. Such a disruption can potentially decrease the solvent hydration at the location of the PG acyl C=O interface, resulting in an increase in the T_m (PG) when a predominant amount of d-PC was present. Dehydration of the interfacial region has been previously documented to produce an increase in the lipid phase transition temperature (Reinyl and Bayerl, 1993). To substantiate such a proposition, the interfacial hydration of the mixed bilayer (or H-bonded state of the acyl C=O's of the two lipids) should be investigated.

Table 2-5. Comparison of the gel and $L\alpha$ state frequency (proportional to energy) for d-PC and PG in the liposomal preparations.

(PG:d-PC)	$\nu(\text{CD}_2)^{\text{gel}}/\text{cm}^{-1}$	$\nu(\text{CD}_2)^{L\alpha}/\text{cm}^{-1}$	$\nu'(\text{CH}_2)^{\text{gel}}/\text{cm}^{-1}$	$\nu'(\text{CH}_2)^{L\alpha}/\text{cm}^{-1}$
1:0	-	-	2919.5 ± 0.1	2923.9 ± 0.1
3:1	2090.3 ± 0.1	2094.3 ± 0.1	2919.3 ± 0.1	2923.1 ± 0.1
1:1	2089.6 ± 0.2	2094.0 ± 0.1	2919.4 ± 0.1	2923.5 ± 0.1
1:3	2089.7 ± 0.1	2094.0 ± 0.1	2920.0 ± 0.1	2924.6 ± 0.1
0:1	2090.0 ± 0.1	2094.4 ± 0.1	-	-

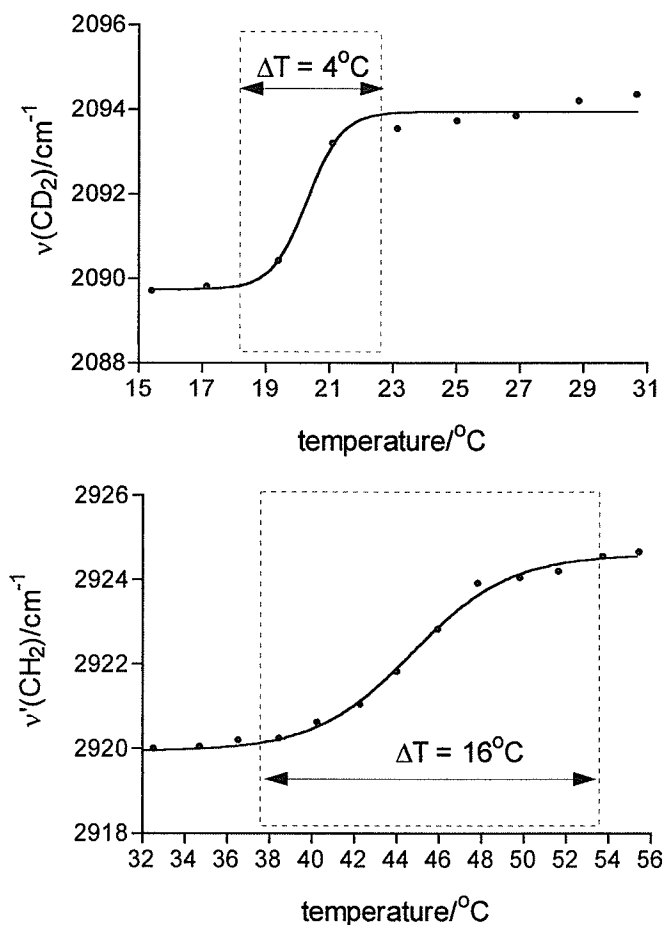
The actual hydration of the bilayer interface in the binary lipid mixtures could not be ascertained because the lipid acyl C=O absorptions of the d-PC and PG overlap one another. Isotopic ^{13}C substitution of the acyl groups of one of the lipids would shift the C=O absorption profile to lower frequency by nearly 50 cm^{-1} (Mantsch and McElhaney, 1991) and therefore allow the state of hydration of both lipids to be monitored simultaneously. However, such an isotopic substitution would not be practical for the study of a protein with

the lipid systems, since the ^{13}C -labeled C=O ($1700\text{-}1680\text{ cm}^{-1}$) of the lipid would overlap with portions of the amide I band profile of the protein. Regardless, comparison of the $\text{L}\alpha$ state acyl C=O stretching profile of d-PC liposomes to that of PG liposomes (Figures 2-7a, and 2-7b, dotted line) revealed the dramatic difference in the extent of interfacial hydration (H-bonding to water) for these two lipids. For example, there is a greater proportion of H-bonded acyl C=O (*ca.* 1730 cm^{-1}) to free C=O (*ca.* 1740 cm^{-1}) for PG than d-PC, indicating that the PG interfacial region is more hydrated than that of d-PC. The degree of water exposure experienced by the interfacial region is a direct consequence of the stability of the intermolecular H-bonding network between the headgroup region and water (Nabet *et al.*, 1994). Both PG and d-PC have a phosphate moiety as part of their respective headgroups which can H-bond to water, adding to the stability of the gel state (Casal and Mantsch, 1984). This hydrogen bonding network that exists between the phosphate moieties and water typically weakens during the phase transition of phosphatidic acids (Nabet *et al.*, 1994). Derivatized phosphatidic acids, like PG and PC, have an additional moiety in their headgroup region that can also participate in interactions with water. Due to the different polarities of the glycerol moiety of the PG headgroup and the choline moiety of d-PC headgroup different intermolecular hydrogen bonding networks can occur at the surface of the bilayer. While water at the surface of the bilayer cannot hydrogen bond to the nonpolar methyl groups of choline, water can hydrogen bond to the polar glycerol hydroxyl groups of PG. The hydrophobicity of the nonpolar methyl groups of the d-PC choline moiety may account for the decreased interfacial hydration of the fluid bilayer relative to that observed for PG (Figure 2-7a and 2-7b, dotted line). In addition, both the phosphate moiety and the glycerol moiety of the PG headgroup can provide additional stabilization to the gel state of the lipid. This strong H-bonding network that exists between the glycerol moieties of PG can provide stabilization against the phase transition. For example, in Figure 2-6, the temperature range of the PG melting interval (*ca.* $40\text{-}47^\circ\text{C}$) is greater ($\Delta T = 7^\circ\text{C}$) than that for d-PC (*ca.* $19\text{-}23^\circ\text{C}$, $\Delta T = 4^\circ\text{C}$) exemplifying the greater resistance PG has for the phase transition. The greater resistance of PG to the phase transition could have arisen from the extra methylene groups that DPPG has in its acyl chains in comparison to DMPC. However, from the frequency data summarized in Table 2-5, the shift of the acyl chain frequencies for the two pure lipids upon the phase transition were identical ($\Delta\nu(\text{PG}) = 4.4\text{ cm}^{-1}$ and

$\Delta v(\text{d-PC}) = 4.4 \text{ cm}^{-1}$). Thus, it is reasonable to propose that the greater resistance PG has for the phase transition arises from the chemical nature of the headgroups and their interaction with the aqueous solvent.

Although, the hydration state of the individual lipids cannot be implicitly examined in the binary mixture(s), a change in the interaction between the lipids and the solvent can be inferred from alterations in the temperature range of the melting interval of each lipid in the binary mixture(s). For example, as shown in Figure 2-8, the length of the melting interval of the PG component in the 1PG:3d-PC mixture was nearly doubled ($\Delta T = 16^\circ\text{C}$) that for pure PG, while that for the d-PC component of the mixture was similar in length ($\Delta T = 4^\circ\text{C}$) to the melting interval of pure d-PC. This broadening of the PG melting interval in the 1PG:3d-PC mixture suggests a greater resistance to the phase transition coincident with the slight increase observed in $T_m(\text{PG})$. A 30% increase in the PG melting interval ($\Delta T = 9^\circ\text{C}$) was also noted in the 1PG:1d-PC mixture, while little change in the PG melting interval was noted for the 1PG:3d-PC mixture ($\Delta T = 7^\circ\text{C}$) (data not shown). Since the nonpolar choline methyl groups cannot H-bond to water, an increase in the proportion of d-PC to PG may promote a strengthening of the H-bonding network amongst glycerol headgroups (*i.e.*, solvent dehydration of the PG interfacial region) which may offset destabilizing effects of neighboring d-PC chains already in the $L\alpha$ state. The $T_m(\text{PG})$, a global parameter, was observed to only be slightly increased relative to pure PG liposomes because of the combination of stabilization by d-PC induced dehydration and destabilization induced by d-PC acyl chain disordering. Similarly when the PG content was equal (1PG:1d-PC) or in excess (3PG:1d-PC) to that of d-PC, the d-PC phase transition also experienced broadening ($\Delta T = 7^\circ\text{C}$ and $\Delta T = 8^\circ\text{C}$, respectively; data not shown). Therefore, the interaction that exists between the phosphate moieties of d-PC and the solvent was also strengthened by the increased presence of PG. Rather than a small change in $T_m(\text{d-PC})$, little change was not noted in $T_m(\text{d-PC})$ for the binary mixtures, illustrating the lack of sensitivity of the phase transition temperature to discrete changes in different regions of a bilayer.

Figure 2-8. Comparison of the length of the melting interval for d-PC and PG in the 1PG:3d-PC liposomal mixture. The melting interval of PG in the presence of d-PC (bottom) is double that for pure PG (Figure 2-6) while the melting interval for d-PC in the presence of PG (top) remains the same as that for pure d-PC (Figure 2-6)



Such a change in the melting interval(s) also suggests that the binary liposomes were mixed homogeneously. In a homogeneous mixture of two lipids, one may anticipate that as one lipid reaches its fluid state (*i.e.*, d-PC) kinking of its acyl chains propagates disorder in neighboring chains of the other lipid (*i.e.*, PG). The melting behavior of a homogeneous mixture of two lipids is, however, dependent on the type of mixture formed. For example, for two lipids with the same acyl chain length (*i.e.*, DMPC and DMPG), perfect mixing is expected and there would be little or no difference in the individual T_m 's of the two lipids or one single T_m of the mixture (CRC Handbook of Lipid Bilayers, 1990). How-

ever, for a homogeneous mixture of two lipids with different acyl chain lengths (*i.e.*, DMPC and DPPG), nearly ideal mixing is expected, the mixture will have two distinct T_m 's, and the phase transition of each lipid in the mixture will be broadened (*i.e.*, less cooperative) in comparison to that of either pure lipid (CRC Handbook of Lipid Bilayers, 1990). The latter case holds for the lipid mixture(s) examined in the current study. That is, although the T_m 's of DMPC and DPPG appeared to remain unchanged in the binary mixture(s) in comparison to that of either pure lipid, this is not unusual for a homogeneous mixture of these two lipids. DMPC and DPPG mixed together in equal proportion are expected to exhibit high miscibility in aqueous solution with the two individual T_m 's separated by about 17°C (CRC Handbook of Lipid Bilayers, 1990). The effect of per-deuteration on the phase behavior of DMPC can account for the 23 to 24°C difference between the T_m (d-PC) and T_m (PG) observed for each binary mixture (Table 2-4). The increase in the frequencies of the gel and $L\alpha$ states of PG in the presence of a predominate amount of fluid d-PC (*i.e.*, 1PG:3d-PC mixture) indicated that stability of PG was decreased by d-PC presence, suggesting that mixing had occurred. Finally, the broadening of the phase transitions of each lipid when mixed in equal and/or excessive proportion suggests that the binary liposomal bilayers were mixed fairly homogeneously. However, since a new method was used to prepare the binary liposomes used in this study (section 2.2.2), another technique (*i.e.*, electron microscopy) would be useful to externally validate that the PG/d-PC bilayers were completely homogeneously mixed. Upon such external validation, the method used in this study to prepare binary liposomes in the absence of any organic solvents, offers an alternative technique for introducing a protein into a binary lipid system without compromising the structural integrity of the protein.

2.3.2 The effect of MBP on liposomes of zero surface charge density.

MBP has net-positive charge and is believed to interact primarily by electrostatic association with acidic (or net-negatively charged) phospholipids (Cheifetz and Moscarello, 1985; Jackson *et al.*, 1993; Morell *et al.*, 1994). Thus, little interaction was predicted with the liposomes of d-PC which have a zero surface charge density (SCD). As shown in Table 2-6, the effect of MBP isoform interaction on the phase transition temperature of d-PC appeared negligible (constant within 0.4°C). The lack of change to T_m (d-PC)

due to isoform presence inferred that these positively charged protein isoforms do not interact with the zwitterionic liposomes to a profound extent.

Table 2-6. The effect of MBP isoform interaction on T_m (d-PC).

Sample	T_m (d-PC)/°C
d-PC	20.5 ± 0.1
MBP-C1/d-PC	20.4 ± 0.4
MBP-C2/d-PC	20.3 ± 0.4
MBP-C3/d-PC	20.7 ± 0.3
MBP-C5/d-PC	20.4 ± 0.2
MBP-C8/d-PC	20.5 ± 0.3

The lack of interaction between d-PC and the isoforms of MBP is supported by the results of Reiny and Bayerl, 1993, in which unfractionated MBP was not found to interact with pure DMPC bilayers. Reiny and Bayerl, 1993, reported that MBP presence did not affect the phase transition of per-deuterated DMPC as observed by ATR-FTIR spectroscopy and differential scanning calorimetry. The results of Reiny and Bayerl confirmed the results of an earlier study which found that MBP isoforms C1 and C2 did not induce aggregation of PC vesicles as detected by little change in the optical density of the protein-lipid mixtures at 450 nm (Cheifetz and Moscarello, 1985). In a later study however, interaction between unfractionated MBP and PC bilayers was detected using a ^3H -radioactivity assay on centrifuged MBP/ ^3H -DPPC samples (Roux *et al.*, 1994). Although Roux *et al.*, 1994, confirmed that unfractionated MBP did not bind to pelleted PC bilayers, the protein was found to disrupt multilamellar PC bilayers as evidenced by the presence of small, solvated MBP/PC complexes in the supernatant. The results of Roux *et al.*, 1994, suggest that MBP may probe the PC bilayer and intercalate with the acyl chains of the lipid through hydrophobic interaction. Given the conflicting results in the literature, the acyl chain order and bilayer interfacial hydration of gel and $L\alpha$ state d-PC in the presence of each MBP isoform was examined to provide further information (Table 2-7).

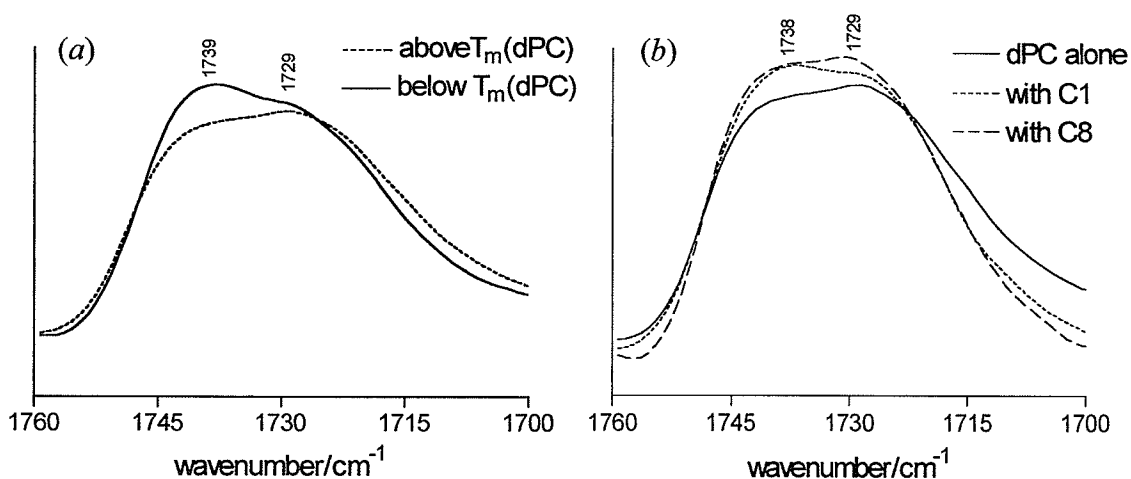
Table 2-7. The effect of MBP charge isoforms on d-PC acyl chain order as assessed by the methylene symmetric stretching vibration. Isoforms that stabilized the $L\alpha$ state of d-PC are shown in boldface. Upon protein interaction, $\Delta\nu$ from that of pure d-PC liposomes is given in brackets for $L\alpha$ state d-PC.

Sample	$\nu(\text{CD}_2)^{\text{gel}} (\text{cm}^{-1})$	$\nu(\text{CD}_2)^{L\alpha} (\text{cm}^{-1})$
d-PC	2090.0 \pm 0.1	2094.4 \pm 0.1
C1	2090.3 \pm 0.2	2095.0 \pm 0.2 (+0.6)
C2	2090.7 \pm 0.2	2095.1 \pm 0.1 (+0.7)
C3	2089.3 \pm 0.2	2092.3 \pm 0.1 (-2.1)
C5	2089.4 \pm 0.1	2091.8 \pm 0.1 (-2.6)
C8	2089.8 \pm 0.2	2092.6 \pm 0.1 (-1.8)

Contrary to the lack of change in $T_m(\text{d-PC})$ when MBP was introduced into the system (Table 2-6), the acyl chain order of the d-PC in both the gel and $L\alpha$ state did show substantial changes dependent on which MBP isoform was present (Table 2-7). The effect of MBP charge isoform presence on d-PC acyl chain order is based on the methylene symmetric stretching frequency of d-PC in the gel and $L\alpha$ state. The MBP isoforms with decreased positive charge (C3, C5 and C8) greatly decreased the energy (*i.e.*, lowered ν) of the $L\alpha$ state, while the most positively charged isoforms (C1 and C2) slightly increased the energy (*i.e.*, increased ν) of this fluid state. Prior to the phase transition, MBP-C3, C5 and C8 only slightly stabilized the gel state acyl chain order, indicating that acyl chain stabilization upon interaction with these isoforms was increased when the d-PC bilayer was fluid. The overall stabilization effect of the less positively-charged isoforms on the $L\alpha$ state d-PC acyl chains in decreasing capability of stabilization was: MBP-C5 > MBP-C3 > MBP-C8. These results indicate that MBP can interact with d-PC liposomes but the interaction is dependent on other factors aside from net-positive charge of the isoform. For further insight on the relative amount of d-PC stabilization by MBP surface association to destabilization by MBP bilayer penetration, bilayer perturbation had to be established separately. MBP bilayer penetration was examined by evaluating the hydration of the bilayer interfacial region upon interaction of each isoform with d-PC. The hydration of the d-PC bilayer inter-

facial region was assessed by the absorption profile of the d-PC acyl carbonyl stretch (*ca.*, 1735 cm^{-1}) upon interaction with each MBP isoform (see section 2.3.1). Comparison of the acyl carbonyl stretch of pure d-PC to that in the presence of each MBP isoform, confirmed that the isoforms interact with the d-PC liposomes differently. The effect of MBP-C1 and C8 presence on the ester C=O stretching profile of d-PC is shown in Figure 2-9.

Figure 2-9. Influence of protein interaction on acyl C=O stretch of d-PC. (a) d-PC acyl C=O stretch in the gel (solid line) and in the $L\alpha$ (dotted line) states. (b) The C=O of $L\alpha$ state d-PC alone and in the presence of MBP-C1 and MBP-C8.



As shown in Figure 2-9b, interaction of the unmodified isoform, MBP-C1, with $L\alpha$ state d-PC resulted in a near inversion of the H-bonded C=O/free C=O relative intensity in comparison to pure $L\alpha$ state d-PC, the acyl C=O absorption profile was more similar to pure d-PC in the gel state (compare to Figure 2-9a). In the presence of MBP-C8 however, the hydration of the bilayer interfacial region of $L\alpha$ state d-PC was nearly unchanged with only a slight decrease in the H-bonded C=O/free C=O relative intensity. The frequencies and relative intensities of the acyl C=O stretching component bands of d-PC in the $L\alpha$ state alone and in the presence of all of the MBP charge isoforms are summarized in Table 2-8.

Table 2-8. Influence of MBP on the relative contributions of the H-bonded and free acyl C=O stretch to the acyl C=O stretching profile of d-PC in the L α state (31°C). Peak positions were extracted from the FSD spectra. The component band of greater intensity is depicted in bold print. The relative intensity of the free to H-bonded C=O is presented in the bottom row. Note: the relative intensity of the free C=O to H-bonded C=O component band for d-PC in the gel state (15°C) was found to be 1.15.

Absorption	d-PC	With C1	With C2	With C3	With C5	With C8
free C=O (cm ⁻¹)	1739	1737	1739	1737	1740	1738
C=O \cdots H (cm ⁻¹)	1729	1730	1732	1732	1732	1731
C=O/C=O \cdots H	0.88	1.11	1.12	1.0	0.92	0.90

In contrast to the C=O stretch of pure d-PC liposomes (Figure 2-9a), all of the MBP isoforms decreased the bilayer interfacial hydration to different extents, as evaluated by the change in the relative intensity of the H-bonded C=O to the free C=O stretch of fluid L α state d-PC (Table 2-8). The most positively charged isoforms (MBP-C1 and C2) decreased hydration at the bilayer interfacial region to such an extent that the C=O stretching profile of L α state d-PC (31°C) more closely resembled the profile obtained for gel state d-PC (Figure 2-9). That is, the relative intensity of the free C=O to H-bonded C=O component bands of L α state d-PC upon MBP-C1 or C2 interaction increased by nearly 20% and was at a value closer to that for gel state d-PC (Table 2-8). For MBP-C3, the H-bonded C=O/free C=O relative intensity was unity (Table 2-8). Conversely, the hydration of the d-PC bilayer interface in the presence of MBP-C5 and C8 was nearly the same as that noted for pure d-PC liposomes since the H-bonded C=O component band remained a greater contributor to the overall C=O stretching profile (Table 2-8). The hydration of the d-PC bilayer interfacial region decreased in the presence of all the isoforms, indicative of some perturbation of the bilayer interfacial region by each isoform. However, d-PC interfacial hydration decreased in the following order of effective dehydration: MBP-C1/C2 >> MBP-C3 > MBP-C5/C8

(Table 2-8), indicating that the propensity the MBP isoforms to insert hydrophobic amino acids or backbone segments into the d-PC bilayer decreased in the following order: MBP-C1/C2 >> MBP-C3 > MBP-C5/C8.

Therefore, even though the phase transition temperatures calculated for d-PC in the presence of each MBP isoform did not indicate that protein-lipid interactions had occurred, analysis of more localized parameters that describe the gel and $L\alpha$ state d-PC, such as acyl chain order and hydration of the bilayer interfacial region, revealed that interaction(s) had taken place. As shown by the change in the $L\alpha$ state d-PC acyl C=O stretching profile, the propensity of the MBP isoforms to insert hydrophobic amino acids or backbone segments into the d-PC bilayer decreased in the following order: MBP-C1/C2 >> MBP-C3 > MBP-C5/C8. As revealed by changes in the acyl chain order, the overall stabilization effect of the MBP isoforms on the $L\alpha$ state d-PC decreased accordingly: MBP-C5 > MBP-C3 > MBP-C8 >> MBP-C1/C2. Considering these results on the phase behavior of d-PC together, MBP-C1 and C2 slightly destabilized the d-PC bilayer by intercalating with the hydrophobic portion of the d-PC bilayer. According to Boggs *et al.*, 1999a, hydrophobic labeling of the N-terminal halves of MBP-C1 and C2 in an aqueous solution with DPPC has been detected. For the less positively charged isoforms, MBP-C3, C5 and C8, which had an overall stabilization effect on the $L\alpha$ state d-PC acyl chains, the hydration of the d-PC interfacial region upon the phase transition was only slightly decreased relative to that of pure d-PC. Although a strong electrostatic binding interaction between these isoforms and the d-PC headgroups is unlikely, MBP-C3, C5 and C8 carry less net-positive charge on their C-terminal halves and are more likely to have electronically neutral segments which may have been able to weakly interact with (or at least do not disturb) the zwitterionic d-PC head groups at the surface of the bilayer. However, MBP-C5 had a greater overall stabilization effect on the d-PC acyl chains than MBP-C3 which in turn was more stabilizing than MBP-C8, thus the interaction of the isoforms may be dependent on other factors aside from net-positive charge of the isoform. The difference between isoforms resides in the type and number of post-translationally modified amino acid residues (recall sequence in Figure 2-3). MBP-C3 and C5 are phosphorylated at two common sites in their C-terminal half (Thr97 and Ser164). These common phosphorylations to the C-terminal halves of MBP-C3 and C5, may account for why these isoforms stabilize the d-PC acyl chain order, while

MBP-C1 and C2 have an overall destabilizing effect. That is, these extra negative charges in MBP-C3 or MBP-C5 may seek out and neutralize positively charged residues in the C-terminal half of the protein, enabling interaction with the zwitterionic d-PC surface. In comparison to MBP-C3, MBP-C5 has two additional sites of phosphorylation (Ser7 and Ser54) on its N-terminal half (Zand *et al.*, 1998). These negatively charged amino acids side-chains in the N-terminal half of MBP-C5 are not likely to insert into the d-PC bilayer surface and may even prevent neighboring side-chains from inserting. Moreover, these extra negatively charged residues of MBP-C5 may pair up with positively charged amino acids in the protein sequence to more effectively neutralize segments of the protein, enabling interaction with the zwitterionic d-PC surface. A decrease in the number of amino acids penetrating the bilayer in combination with additional neutral fragments interacting with the zwitterionic bilayer surface, may account for the decrease in bilayer dehydration and an increase in acyl chain stabilization, observed for MBP-C5 interaction with d-PC. Finally, since the dehydration of the d-PC bilayer interface was less pronounced upon MBP-C8 interaction, yet MBP-C3 and C5 had greater overall stabilization effects on the d-PC acyl chains, MBP-C8 surface interaction must be weaker than that of MBP-C3 or MBP-C5. Unlike the other isoforms, 6 arginyl residues in MBP-C8 are citrullinated (Wood and Moscarello, 1989). Although citrullination would increase the hydrophobicity of MBP and promote surface interaction with neutral lipids, citrullination also reduces the multivalency of positive charges available that could potentially neutralize negatively charged amino acids. Thus, in comparison to MBP-C3 and C5, fewer intramolecular salt-bridges may form in MBP-C8 that are capable of interacting with the zwitterionic d-PC surface and stabilizing the d-PC acyl chains. In turn, slightly weaker interaction between MBP-C8 and the d-PC bilayer surface may prevent some hydrophobic amino acid side chains or backbone segments from inserting into the interfacial region, resulting in less dehydration of the bilayer interface.

Taken together, these results are supported by the literature taking the relative abundance of each isoform in unfractionated MBP under consideration. For example, in studies on MBP extracted from normal white matter, the unmodified isoform, MBP-C1 and the citrullinated isoform, MBP-C8, have been found in greater proportion to the other isoforms (Chou *et al.*, 1976) with the ratio of C8/C1 near 0.82 (Wood *et al.*, 1996). Therefore, unfrac-

tionated MBP would be expected to behave similarly to pure MBP-C1 and C2, such that unfractionated MBP would not affect the phase transition temperature of PC (Reinyl and Bayerl, 1993) and would not associate with PC head groups and aggregate neutral vesicles (Cheiftez and Moscarello, 1985). Since unfractionated MBP was found to disrupt multilamellar PC bilayers (Roux *et al.*, 1994), MBP-C1 and C2 penetration of the d-PC bilayer found in the current study is understandable and substantiates that hydrophobic interactions can occur between these isoforms and neutral lipids. The excess net-positive charge on the C-terminal halves of these proteins is not likely to interact with the zwitterionic head groups of d-PC. However, considering the interactions of all the isoforms with d-PC, the interactions appear not only sensitive to the absence or presence of post-translationally modified residues, which affect the net-positive charge of the protein, but also the type of post-translational modification. Reduction of the multivalency of positively charged residues upon modification (*i.e.*, MBP-C8), reduces the neutralization of negatively charged residues in the sequence. In contrast, increasing the multivalency of negatively charged residues (*i.e.*, MBP-C3 and especially MBP-C5), increases the neutralization of positively charged residues in the sequence. The greater the neutralization of charged residues by intramolecular shielding or salt-bridge formation, the greater the MBP interaction with d-PC on the surface of the bilayer.

2.3.3 The effect of MBP on liposomes of negative surface charge density.

Contrary to the lack of change in the phase transition temperature of d-PC upon MBP isoform interaction, changes in $T_m(\text{PG})$ were detected upon interaction of the MBP isoforms with PG liposomes (Table 2-9). The $T_m(\text{PG})$ data presented in Table 2-9 is in support of strong associative behavior between MBP-C3 and PG head groups since the calculated $T_m(\text{PG})$ was increased in comparison to that for pure PG liposomes. The other isoforms however, appeared to destabilize the PG liposomes as reflected by the decrease in $T_m(\text{PG})$ upon their presence (Table 2-9). An increase in the gel-to- $L\alpha$ -state phase transition temperature of acidic lipids is typically observed when a protein interacts purely by electrostatic association, such as that noted for the interaction of poly-L-lysine and DMPA (Boggs *et al.*, 1981). However, the effect of unfractionated MBP or MBP isoforms with acidic lipids has been under great debate. Reinyl and Bayerl, 1993, using differential scan-

ning calorimetry, reported that the phase transition temperature of acidic phospholipids was still increased in the presence of unfractionated MBP. Yet numerous reports have shown by DSC that the opposite effect is observed; that unfractionated MBP decreases the phase transition temperature of acidic phospholipids because its interactions with the lipids is not purely electrostatic (Papahadjopoulos *et al.*, 1975; Boggs and Moscarello, 1978; Boggs *et al.*, 1981; Nabet *et al.*, 1994; Jo and Boggs *et al.*, 1999). Since unfractionated MBP is predominantly composed of MBP-C1 and C8 (Chou *et al.*, 1976), the results of the current study are supported by the decrease in the phase transition temperature in acidic lipids noted by the majority of the previous studies.

Table 2-9. The effect of MBP interaction on the phase transition temperature of PG

Sample	$T_m(\text{PG})/^\circ\text{C}$
PG	43.4 ± 0.2
MBP-C1/PG	41.3 ± 0.2
MBP-C2/PG	40.7 ± 0.2
MBP-C3/PG	45.3 ± 0.1
MBP-C5/PG	41.3 ± 0.2
MBP-C8/PG	41.0 ± 0.2

Based solely on the $T_m(\text{PG})$ data of the current study, only MBP-C3 exhibited interaction primarily by electrostatic association with the negatively charged PG headgroups and increased $T_m(\text{PG})$, yet MBP-C3 is not the isoform of greatest net-positive charge. Since the $T_m(\text{PG})$ data in the current study did not exhibit a trend based on net-positive charge of the protein isoforms, a reasonable conclusion would be that there are other factors aside from purely electrostatic association involved in the lipid-isoform interaction. For MBP-C1, C2, C5 and C8, a combination of electrostatic association and hydrophobic interactions (by partial penetration in the PG bilayer) would lead to a mixture of stabilizing and destabilizing forces, respectively, which lead to an overall decrease in $T_m(\text{PG})$. The phase transition temperature measurement is a global measurement of liposomal stability and does not provide structural information on the order of the acyl chains or the extent the isoforms

perturb the bilayer interfacial region (section 2.3.1). Thus, the PG acyl chain order and the PG acyl C=O stretching profile were evaluated for further information on the relative contributions of electrostatic to hydrophobic interactions between each MBP isoform and PG.

Table 2-10. The effect of MBP charge isoforms on PG acyl chain order as assessed by the frequency of methylene asymmetric stretching vibration. Isoforms that stabilized the $L\alpha$ state of PG are shown in boldface. Upon protein interaction, $\Delta\nu$ from that of pure PG liposomes is given in brackets for $L\alpha$ state PG

Sample	$\nu'(\text{CH}_2)^{\text{gel}} (\text{cm}^{-1})$	$\nu'(\text{CH}_2)^{L\alpha} (\text{cm}^{-1})$
PG	2919.5 \pm 0.1	2923.9 \pm 0.1
C1	2918.9 \pm 0.1	2922.5 \pm 0.1 (-1.4)
C2	2917.3 \pm 0.1	2922.6 \pm 0.1 (-1.3)
C3	2918.9 \pm 0.1	2922.1 \pm 0.1 (-1.8)
C5	2918.9 \pm 0.1	2923.0 \pm 0.1 (-0.9)
C8	2919.5 \pm 0.1	2923.9 \pm 0.1 (0)

The effect of MBP interaction on PG acyl chain order is summarized in Table 2-10 based on the methylene asymmetric stretching frequency of PG in the gel and $L\alpha$ state. The methylene asymmetric stretch was used preferentially in this calculation as the symmetric methylene stretch at 2850-2852 cm^{-1} was subject to more interference from the D-O-D stretching absorption of the solvent (sections 1.3.1 and 2.3.1). MBP-C1, C2, C3 and C5 lowered the energies of both the gel and liquid crystalline state, while the least positively charged isoform MBP-C8 did not alter the PG states (Table 2-10). The most positively charged MBP isoforms, MBP-C1-C3 were most effective at stabilizing the PG $L\alpha$ state, an effect which arises primarily through electrostatic association. However, MBP-C3 was nearly 30% more effective at ordering the $L\alpha$ state PG acyl chains than either MBP-C1 or C2 (Table 2-10). In comparison to MBP-C3, the stabilizing effect of MBP-C1 and C2 on the $L\alpha$ state PG acyl chains is slightly reduced, perhaps due to some bilayer penetration accompanying electrostatic association. For the less-positively charged isoform, MBP-C5, an even smaller stabilizing effect (*ca.*, 50% of the effect observed during MBP-C3/PG interaction) on $L\alpha$ state PG acyl chain order was observed (Table 2-10). This latter observation implies that MBP-C5 interaction with PG occurs by both electrostatic association

and bilayer penetration, with a greater contribution from hydrophobic interactions than that observed for MBP-C1 and C2. The least positively charged isoform, MBP-C8, did not exhibit an effect on the acyl chain order of either gel or $L\alpha$ state PG (Table 2-10). MBP-C8 association may be so weak in comparison to bilayer perturbation that the effects of the two interactions on PG acyl chain order cancel each other out. These results indicate that net-positive charge does alter the ordering effect that MBP can have on the acyl chains of acidic phospholipids. The more positive isoforms may interact predominantly by electrostatic association, while the less positively charged isoforms interact predominantly by hydrophobic interactions with weak electrostatic association. However, the amount of net-positive charge available for electrostatic association does not appear to be the only factor involved. The extent of isoform penetration of PG bilayer had to be verified by examination of the hydration state of the PG bilayer interfacial region.

Protein perturbation of the bilayer interfacial region was evaluated by the temperature dependence of the overall acyl C=O band contour of PG in response to MBP isoform presence (summarized in Table 2-11). When the lipid was in the highly ordered gel state, the overall acyl C=O band contour experienced a slight shift to lower frequency (1-2 cm^{-1}) in response to MBP isoform presence (Table 2-11). This slight shift in the overall band contour to lower frequency, indicates that there was small increase in the hydration of the PG gel state interface upon interaction with MBP. However, for PG liposomes in the fluid $L\alpha$ state, the least positively charged isoforms, MBP-C5 and C8, decreased bilayer hydration as interpreted from the 4 and 10 cm^{-1} increase in the frequency of the acyl C=O absorption, respectively (Table 2-11).

Table 2-11. Influence of MBP on the PG acyl band contour in the gel (31°C) and liquid crystalline state (55°C). Peak positions were extracted from the buffer and water vapor subtracted spectra.

Absorption	PG	With C1	With C2	With C3	With C5	With C8
C=O (cm^{-1}) gel	1740	1738	1738	1739	1737	1739
C=O (cm^{-1}) $L\alpha$	1731	1731	1731	1731	1735	1741

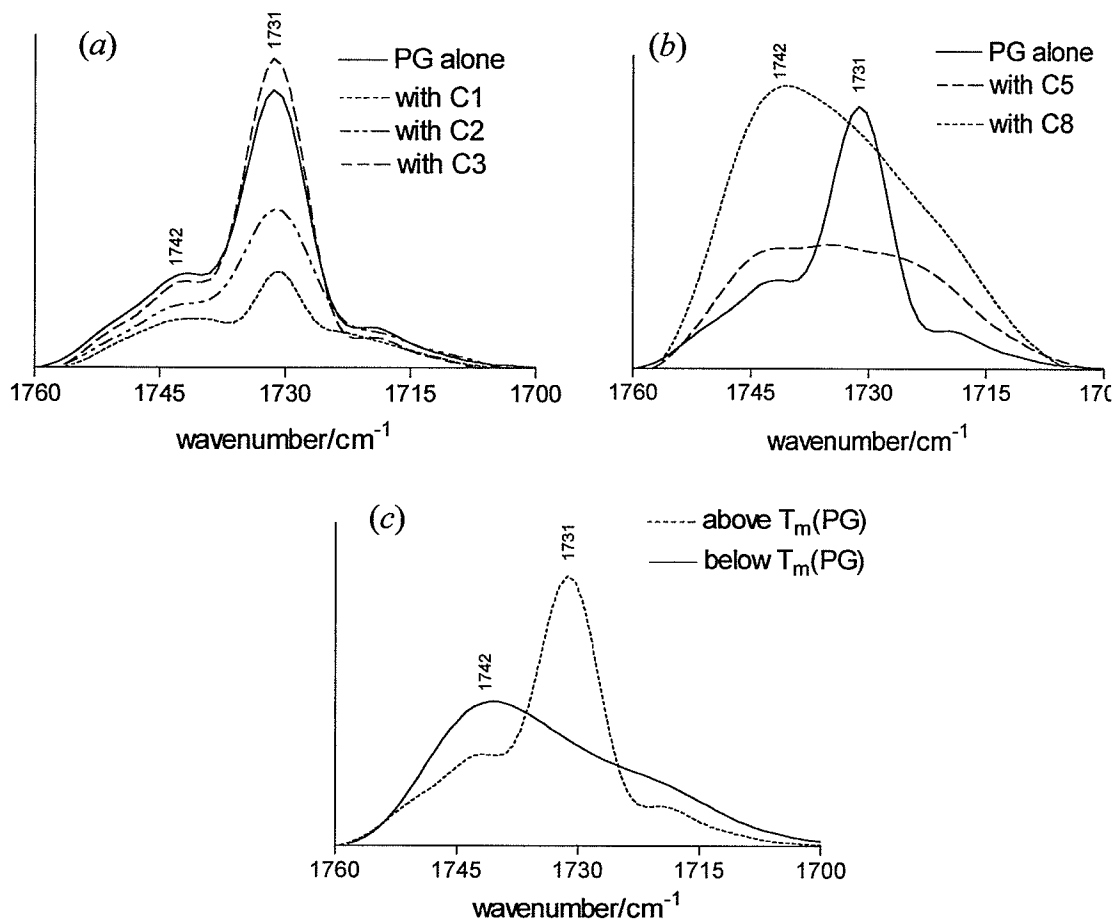
Upon FSD of the buffer-subtracted spectra, the influence of each isoform on the relative contributions of the H-bonded and free acyl C=O stretch of PG in the $L\alpha$ state (55°C) was determined (Table 2-12 and Figure 2-10). In the presence of MBP-C1 and C2, the C=O profile of PG was similar to that of fluid PG alone, however there appeared to a slight decrease in interfacial hydration as reflected by the decrease (*ca.* 50%) in the relative intensity of the H-bonded to that of the free C=O stretch of PG when in the presence of these isoforms (Table 2-12 and Figure 2-10*a*). MBP-C1 and C2 then restrict some water access to the bilayer interfacial region of $L\alpha$ state PG. In contrast, bilayer interface hydration appeared to increase slightly when $L\alpha$ state PG was in the presence of MBP-C3 as interpreted from the increase (*ca.* 20%) in the relative intensity of the H-bonded to that of the free C=O stretch (Table 2-12 and Figure 2-10*a*). In comparison to the more positively charged isoforms, the C=O stretch of $L\alpha$ state PG in the presence of MBP-C5 and in particular for MBP-C8 at 55°C was more similar to the acyl C=O stretching profile of PG liposomes in the gel state (Figure 2-10*b*); the H-bonded component band was no longer the predominant contributor (Table 2-12). As shown in Table 2-12, the relative intensity of the free to H-bonded C=O component bands of $L\alpha$ state PG in the presence of MBP-C8 (1.26) was near to that of the pure PG in the gel state (1.41). Therefore, the less positively charged isoforms, MBP-C5 and C8 decreased the interfacial hydration of $L\alpha$ state PG (restricted water access to the PG acyl carbonyls), MBP-C8 more so than MBP-C5.

Table 2-12. Influence of MBP on the relative contributions of the H-bonded and free acyl C=O stretch of PG in the $L\alpha$ state (55°C). Peak positions were extracted from the FSD spectra. The component band of greater intensity is depicted in bold print. The relative intensity of the free to H-bonded C=O is presented in the bottom row. Note: the relative intensity of the free C=O to H-bonded C=O component band for PG in the gel state (31°C) was 1.41.

Absorption	PG	With C1	With C2	With C3	With C5	With C8
free C=O (cm ⁻¹)	1742	1741	1741	1742	1741	1742
C=O····H (cm ⁻¹)	1731	1731	1731	1731	1728	1731
C=O/C=O····H	0.34	0.52	0.42	0.28	1.00	1.26

Figure 2-10. The influence of MBP interaction on the PG acyl C=O band profile.

(a) C=O profile of PG at 55°C in the presence of MBP-C1-C3. (b) C=O profile of PG at 55°C in the presence of MBP-C5 and C8. (c) Comparison of the C=O band profile of PG in the gel state (31°C) to the L α state (55°C).



The hydration of the PG bilayer interfacial region was enhanced by MBP-C3 presence, but decreased in the presence of the other isoforms in the following order of effective dehydration: MBP-C2 < MBP-C1 << MBP-C5 << MBP-C8. This suggests that the extent with which hydrophobic amino acid side-chains or hydrophobic segments of MBP penetrate the PG bilayer increases in the following order: MBP-C3 << MBP-C2 < MBP-C1 << MBP-C5 << MBP-C8. The overall stabilization effect of the MBP isoforms on the L α state PG acyl chains in increasing capability to stabilize was: MBP-C3 > MBP-C1/C2 >> MBP-

C5 >> MBP-C8. Thus, the relative contribution of isoform stabilization by electrostatic association to destabilization by bilayer penetration increased accordingly: MBP-C8 << MBP-C5 << MBP-C1 < MBP-C2 << MBP-C3. As opposed to MBP-C3 which interacts primarily by surface association, small hydrophobic segments (or hydrophobic amino acid side-chains) of MBP-C1 and C2 may have partially probed into the bilayer interface. Such partial probing into the $L\alpha$ state PG bilayer interface not only results in reduction of solvent access to the bilayer interface, but also decreases the stabilizing effect of surface association by introducing some conformational disorder in the first few methylene groups attached to the acyl C=O groups (Nabet *et al.*, 1994). This competition between electrostatic association and penetration of the $L\alpha$ state PG bilayer intensified in the presence of the less positively charged isoforms, MBP-C5 and C8. MBP-C5 and C8 appeared to participate in greater penetration of the PG bilayer than MBP-C1 and C2.

The following question then arises: "How can small perturbations to the bilayer surface, such as those suspected in the interaction of PG with MBP-C1 and C2 (and to a lesser extent MBP-C5), alter the fluidity of the bilayer (decrease T_m) yet increase the conformational order of the $L\alpha$ state PG acyl chains?". The answer to this question begins with understanding the difference between the two measurements. The T_m of a lipid represents the ease at which the melting event can ensue and once the process has begun it is typically cooperative. Electrostatic association of a protein to the headgroups of a lipid stabilize the lipid system against the phase transition and thus the T_m increases (Boggs *et al.*, 1981). This effect of electrostatic association on T_m (PG) was observed in the current study with MBP-C3. Penetration of the bilayer surface by a hydrophobic molecule, however, can only occur when the strong intermolecular H-bonding network between the lipid headgroups and water begin to weaken, typically near the beginning of the phase transition (Nabet *et al.*, 1994). As this H-bonding network begins to break down, a hydrophobic molecule may insert more readily, further destabilizing the bilayer and aiding in the propagation of an earlier melting event (T_m decreases). The effect of bilayer penetration on T_m (PG) was observed in the current study with MBP-C1, C2, C5 and C8. Therefore, regardless of the electrostatic association that can occur between MBP-C1, C2, C5 and C8 with PG, portions of these molecules can also insert into the weakened bilayer and even partial bilayer perturbation can weaken the system (like a weak link in a chain) propagat-

ing an earlier melting event. The conformational order of the acyl chains in the $L\alpha$ state (after the melting event is over) represents the stabilizing effect the protein has on the fluid membrane (not the stabilizing effect the protein has on the liposomes prior to melting). If the acyl chain order of the $L\alpha$ state lipid is increased (lower frequency) in the presence of protein, then the protein has a stabilizing effect on the fluid membrane. This stabilizing effect on the $L\alpha$ state lipid is most likely caused by electrostatic association to the head-group region. Alternatively, if the acyl chain order of the $L\alpha$ state lipid is decreased (higher frequency) in the presence of protein, then the protein has a destabilizing effect on the fluid membrane. Such a destabilizing effect on the fluid membrane most likely arises from perturbation of the bilayer surface and possible intercalation with the acyl chains mediated by hydrophobic interactions. Further to this point, if a protein can interact with the $L\alpha$ state lipid by a combination of electrostatic association and hydrophobic interactions, the net stability of the $L\alpha$ state is dependent upon the relative contributions of association and penetration. In the current study, MBP-C1, C2, C3 and C5 stabilized fluid PG, indicating that these isoforms interact predominantly by electrostatic association (Table 2-10). However, MBP-C3 stabilized fluid PG to the greatest extent and enhanced the hydration state of the interfacial region, indicating that the interaction between fluid PG and MBP-C3 is more purely electrostatic. In contrast to MBP-C3, MBP-C1 and C2 had a slightly less stabilizing effect on fluid PG and partially decreased the hydration of the PG interface, indicating the interaction between fluid PG and MBP-C1 or C2 is predominantly electrostatic with a minor contribution from partial penetration of the bilayer interface. The interaction between MBP-C5 and fluid PG was also predominantly electrostatic since $L\alpha$ state PG was still partially stabilized with respect to the $L\alpha$ state of PG in the absence of protein. In contrast to MBP-C1 and C2, MBP-C5 penetrated the $L\alpha$ state PG bilayer to a greater extent as indicated by further decrease in the PG interfacial hydration. Finally, the least positively charged isoform, MBP-C8, exhibited little effect on the conformational order of $L\alpha$ state PG while it nearly dehydrated the PG interfacial region. The latter observation indicates that MBP-C8 penetrates further into the $L\alpha$ state PG bilayer than MBP-C5. The little effect MBP-C8 has on the acyl chain order of $L\alpha$ state PG indicates that destabilizing effects of bilayer perturbation and the stabilizing effects of electrostatic association cancel each other out.

Comparison of the interactions between fluid PG and MBP-C1, C2 or C3, revealed the interaction between PG and MBP-C3 was predominantly electrostatic, while MBP-C1 and C2 have limited hydrophobic interactions (more so for MBP-C1) with the bilayer in addition to electrostatic attraction. These more positively charged isoforms differ in the type and amount of post-translational modification to the C-terminal half of their respective sequences (recall Figure 2-3, MBP sequence). MBP-C1 is unmodified, MBP-C2 is deamidated at Gln146 while C3 is phosphorylated at Thr97 and Ser164 (Zand *et al.*, 1998). Although the N-terminal portions of unfractionated MBP, MBP-C1 and C2 have been found to interact hydrophobically with acidic lipids more readily than the C-terminal portion (Boggs *et al.*, 1988; Boggs *et al.*, 1999a), this does not rule out insertion of hydrophobic amino acid side chains of the C-terminal half into the PG interfacial region. For example, electrostatic association of the C-terminal half may bring some hydrophobic amino acids in closer proximity to the bilayer surface for insertion. One speculation, for a decrease in penetration of the PG interfacial region by MBP-C2 and MBP-C3 may be that repulsion, between the phosphate moiety of PG and the extra negative charge(s) of MBP-C2 (at Glu146) and MBP-C3 (at Thr97 and Ser164), restricts these amino acids and perhaps neighboring amino acid side chains from entering the interfacial region. The MBP-to-PG ratio used (0.8 mol% MBP to PG, Table 2-2) was not high enough to fully saturate¹¹ the number of negative charges on the surface of the PG liposomes, thus repulsion between phosphorylated or deamidated residues and the PG surface is plausible. It would be of interest to investigate if dephosphorylation of MBP-C3 at pThr97 could decrease the hydration of the PG interfacial region to the same extent observed for MBP-C2. Even though the electrostatic association between MBP-C3 and PG may be the primary interaction, that does not mean that MBP-C3 is a more effective adhesive for the myelin membrane. That is, insertions of hydrophobic amino acids in concert with strong electrostatic association may more effectively bind MBP-C1 and C2 to an acidic bilayer, as suggested by numerous acidic vesicle aggregation assays (Cheifetz and Moscarello, 1985; Jo and

11. MBP-C1, C2, C3 and C5 have 31 positive charges/molecule while PG has one negative charge/molecule. Therefore, in a 0.8mol% protein-to-lipid mixture, the ratio of positive to negative charges would be 0.25 and there would be a net-excess of negative charge on the bilayer surface. For MBP-C8 there is a reduced multivalency of positive charges since six arginines are deaminated to citrulline (25 positive charges/molecule), thus the ratio of positive to negative charges would be decreased to 0.20

Boggs, 1995; Boggs *et al.*, 1997). Therefore, for MBP-C1 and C2 interaction with acidic phospholipids, there most likely is a synergy between surface association and partial penetration of the bilayer that maximizes the function of the protein as an adhesive for paranodal myelin.

In contrast to the more positively charged isoforms, MBP-C5 and C8 may not be as effective as a paranodal myelin adhesive. Perturbation of the interfacial region and possible intercalation with the hydrophobic portion of the bilayer was proposed to be their primary interaction with PG, more so for MBP-C8 than for MBP-C5. The C-terminal half of MBP-C5 is phosphorylated on the same residues as MBP-C3 (Thr97 and Ser164). However, the N-terminal half of MBP-C1 has been found to have a greater propensity for bilayer insertion (Boggs *et al.*, 1999a). The extra negative charges in the N-terminal half of MBP-C5 (pSer7 and pSer54) may experience repulsion from the unsaturated negative SCD on the PG bilayer surface, neutralize two positively charged residues in the sequence, and create a neutral fragment suitable for insertion. In contrast, the reduced multivalency of positive charges in MBP-C8 (Cit25, Cit31, Cit122, Cit130, Cit159 and Cit170), has a three-fold effect, especially in the C-terminal half: (i) a great reduction in the number of arginyl residues needed for electrostatic association with PG, (ii) increased hydrophobicity of residues, and (iii) increased repulsion between opposing leaflets of the PG liposomes with unsaturated negative SCD. The impact of (iii) is that negatively charged residues may be repelled from the excess negative SCD of the bilayer, seek positively charged residues to neutralize thus creating neutral segments suitable for insertion. Therefore, aside from a reduction in electrostatic association between MBP-C8 and PG bilayer surface, increased amphipathic character of MBP-C8 would lead to greater bilayer penetration. Just as hydrophobic interactions between unfractionated MBP (mainly MBP-C1) and neutral lipids can fragment multilamellar bilayers (Roux *et al.*, 1994), such predominant hydrophobic interactions between MBP-C8 and acidic lipids may disrupt the normal bilayer structure of myelin required for efficient nerve conduction. However, Boggs *et al.*, 1999b, found that only MBP-Cit-18, a unique isoform extracted from the myelin of individuals with fulminating Marburg-type multiple sclerosis, was capable of fragmenting large multilayered lipid vesicles into smaller vesicles. In comparison to MBP-C8, all the arginines in the C-terminal half of MBP-Cit-18 are deiminated to citrulline, which greatly

affects the multivalency of positive charge¹² in that half of the protein expected to interact at the aqueous phase with the head groups of acidic phospholipids. In addition, all the arginines in the N-terminal half of MBP-Cit-18 are converted to neutral citrulline, increasing the propensity of membrane insertion or disruption. Thus, although the MBP-C8/C1 ratio has been found to be increased in the myelin of individuals with chronic MS (Wood *et al.*, 1996), MBP-C8 is still amphipathic in nature (Boggs *et al.*, 1999b). MBP-C8 has also been localized to the intraperiod line in the myelin membrane (McLaurin *et al.*, 1993). PLP, another amphipathic myelin adhering protein, has also been localized to the intraperiod line of the myelin membrane (Morell *et al.*, 1994). Moreover, protein-protein interactions between PLP and MBP-C8 have been proposed (Wood and Moscarello, 1989). Perhaps the imbalance observed in the MBP-C8/C1 ratio of myelin from individuals with chronic MS is problematic not because of myelin fragmentation, but due to an imbalance in the distribution of MBP proteins in the major dense line and intraperiod line of the myelin membrane required for effective adhesion.

2.3.4 The effect of MBP on liposomes of varied net-negative surface charge density.

The myelin membrane is composed of a complex mixture of lipids (Morell *et al.*, 1994), thus the negative surface charge density is lower than that of a pure PG membrane. For better understanding of the interaction of the MBP with the myelin membrane, interaction of MBP isoforms with liposomes of varied net-negative SCD was investigated. Interactions between the MBP isoforms and liposomes prepared from binary mixtures of PG and d-PC were evaluated in a similar fashion to that described previously for the MBP isoforms with each of the pure lipids. That is, the interactions were evaluated by observed changes in the acyl chain order of PG and d-PC and by monitoring the temperature dependence of the methylene CH and CD stretching vibrations, respectively. Since absorptions due to the stretching of the acyl C=O moieties of PG and d-PC occur in the same region (1725-1745 cm⁻¹), evaluation of this region could not be used to assess the hydration of the bilayer interfacial region for the binary mixtures as was done previously for the pure lipids. Finally, the

12. For MBP-Cit (18) either 18 or 19 arginines are deaminated to citrulline, reducing the multivalency of positive charges to +12 or net-positive charge of the protein of +1. Unlike MBP-C8, the C-terminal half of MBP-Cit(18) would have excess negative charge due to the presence of 7 Glu/Asp residues, resulting in charge repulsion between opposing bilayer leaflets that have net-negative SCD.

data obtained on the effect of the isoforms on either pure d-PC or PG liposomes (sections 2.3.2 and 2.3.3) was used in conjunction with the phase transition temperature and acyl chain order measurements of d-PC and PG in the binary liposomes to discern whether phase separation (*i.e.*, demixing or microdomain formation) in the binary PG:d-PC liposomes could be induced by MBP interaction.

Evaluation of the phase transition temperature of each lipid in the liposomes of various SCD investigated indicated that the MBP isoforms exhibited preferential interaction with the PG portion of the binary lipid mixtures. Shown in Table 2-13, $T_m(\text{d-PC})$ remained constant (within 0.4°C) regardless of the PG content in the binary mixture. Moreover, the effect of MBP isoform interaction on $T_m(\text{d-PC})$ appeared to be negligible regardless of the liposomal composition (constant within 0.6°C). This lack of variability in $T_m(\text{d-PC})$ for d-PC in the binary mixtures was also observed when the isoforms were in the pure d-PC environment (section 2.3.2). Therefore, based on the $T_m(\text{d-PC})$ calculation alone (as seen in section 2.3.2), conclusions regarding the exclusion of MBP interaction with the d-PC component of the binary mixtures cannot be made with certainty without assessment of conformational order of the d-PC acyl chains in the liposomes of various SCD.

Table 2-13. The influence of PG on MBP interaction with d-PC liposomes of various surface charge density

(PG:d-PC)	$T_m(\text{d-PC})$ $^\circ\text{C}$	$T_m(\text{d-PC})$ with C1/ $^\circ\text{C}$	$T_m(\text{d-PC})$ with C2/ $^\circ\text{C}$	$T_m(\text{d-PC})$ with C3/ $^\circ\text{C}$	$T_m(\text{d-PC})$ with C5/ $^\circ\text{C}$	$T_m(\text{d-PC})$ with C8/ $^\circ\text{C}$
3:1	20.3 ± 0.2	20.3 ± 0.4	20.6 ± 0.3	20.4 ± 0.3	20.5 ± 0.4	20.4 ± 0.3
1:1	20.1 ± 0.2	20.5 ± 0.2	20.4 ± 0.2	20.5 ± 0.3	20.5 ± 0.4	20.5 ± 0.2
1:3	20.3 ± 0.2	20.4 ± 0.3	20.5 ± 0.3	20.4 ± 0.3	20.5 ± 0.4	20.8 ± 0.3
0:1	20.5 ± 0.1	20.4 ± 0.4	20.3 ± 0.4	20.7 ± 0.3	20.4 ± 0.2	20.5 ± 0.3

Contrary to the absence of intense alterations in the phase transition temperature of d-PC upon interaction with the MBP isoforms, variability in $T_m(\text{PG})$ was detected for liposomes of altered SCD (Table 2-14). This variability most likely arose by the combined sensitivity of $T_m(\text{PG})$ to both d-PC presence in the mixture and the type of interaction that

predominates between the isoform and PG. The influence of d-PC content on MBP interaction with PG can be examined by comparison of the $T_m(\text{PG})$ calculated for pure PG liposomes interacting with an isoform to the $T_m(\text{PG})$ calculated for PG:d-PC binary liposomes interacting with the same isoform (*i.e.*, reading the $T_m(\text{PG})$ from top to bottom in Table 2-14). The most noticeable trend in Table 2-14, is the decrease in $T_m(\text{PG})$ upon isoform interaction as the net-negative SCD of the liposomal mixture is decreased. Since $T_m(\text{PG})$ was shown to decrease in the presence of MBP-C1, C2, C5 and C8 for pure PG liposomes (section 2.3.3), due to the sensitivity of $T_m(\text{PG})$ to bilayer penetration, a reasonable conclusion is that d-PC presence may enhance both the electrostatic association and hydrophobic interaction between MBP and acidic lipids. Recall from Table 2-1, that greater d-PC content in the binary liposomes results in more saturation of the net-negative SCD by the multivalency of positive charges available on the isoforms. That is, when the MBP to PG content was raised to 3.1 mol%, the number of positive charges on MBP-C1, C2, C3 and C5 available was nearly equal to the number of negatively charged PG head groups at the surface of the 1PG:3d-PC mixture. Bilayer association and penetration with the proteins would proceed more readily when repulsion between opposing bilayer leaflets is reduced.

Table 2-14. The effect of MBP interaction on $T_m(\text{PG})$ in liposomes of various SCD.

Reading values from top to bottom shows the effect of d-PC presence on the interaction of MBP with PG. Reading values from left to right shows the effect of MBP interaction on the PG component of the mixed liposome.

(PG:d-PC)	$T_m(\text{PG})$ /°C	$T_m(\text{PG})$ with C1/°C	$T_m(\text{PG})$ with C2/°C	$T_m(\text{PG})$ with C3/°C	$T_m(\text{PG})$ with C5/°C	$T_m(\text{PG})$ with C8/°C
1:0	43.4 ± 0.2	41.3 ± 0.2	40.7 ± 0.2	45.3 ± 0.1	41.3 ± 0.2	41.0 ± 0.2
3:1	44.3 ± 0.2	41.2 ± 0.1	40.5 ± 0.3	39.2 ± 0.2	40.8 ± 0.4	40.5 ± 0.1
1:1	45.4 ± 0.2	34.7 ± 0.2	38.9 ± 0.2	32.4 ± 0.2	40.2 ± 0.1	39.2 ± 0.1
1:3	44.8 ± 0.2	36.5 ± 0.1	31.3 ± 0.3	32.2 ± 0.2	35.2 ± 0.2	31.1 ± 0.1

Upon a slight increase in the saturation of liposomal net-negative SCD (1.0 mol% MBP, Table 2-2) in the 3PG:1d-PC mixture (Table 2-14), the most dramatic decrease in $T_m(\text{PG})$ for the 3PG:1d-PC liposomes was observed when MBP-C3 was present (Table 2-14, $\Delta T_m(\text{PG}) = 45.3^\circ\text{C} - 39.2^\circ\text{C} = 6.1^\circ\text{C}$). Interestingly, the increase in $T_m(\text{PG})$ found upon the interaction of MBP-C3 and pure PG liposomes (Table 2-9), was no longer observed when PG liposomes contained 25% d-PC (3PG:1d-PC mixture, Table 2-14). Although the MBP to PG ratio in the 3PG:1d-PC mixture was only slightly increased (1.0 mol%) over that of the pure PG liposomes (0.8 mol%), it still was not high enough to saturate the net-negative surface density of the binary liposomes with available positive charges (saturation of SCD = 31%, Table 2-2). However, this slight decrease in net-negative SCD may have been enough to reduce repulsion between pThr97 or pSer164 of MBP-C3 and phosphate moieties of PG, allowing the C-terminal half of MBP-C3 to come in closer proximity to the bilayer surface to insert hydrophobic amino acid side-chains upon electrostatic association (see section 2.3.3). When saturation of the liposomal net-negative SCD was increased to nearly 50% (1PG:1d-PC, 1.5mol% MBP), the sharpest drop in the $T_m(\text{PG})$ observed was again upon MBP-C3 interaction (Table 2-14, $\Delta T_m(\text{PG}) = 45.3^\circ\text{C} - 32.4^\circ\text{C} = 12.9^\circ\text{C}$). Finally, upon saturating conditions of the liposomal negative SCD (1PG:3d-PC, 3.1mol% MBP), the largest difference between the $T_m(\text{PG})$ calculated for PG liposomes interacting with MBP and that of a binary mixture interacting with MBP was that observed during MBP-C3 interaction (Table 2-14, $\Delta T_m(\text{PG}) = 45.3^\circ\text{C} - 32.2^\circ\text{C} = 13.1^\circ\text{C}$). This suggests that $T_m(\text{PG})$ is extremely sensitive to both d-PC presence and protein association since MBP-C3 interaction with pure PG liposomes was found to be primarily electrostatic (section 2.3.3).

For the other MBP isoforms, a substantial decrease in $T_m(\text{PG})$ was only observed when the net-negative SCD of the binary liposomes was more saturated by the positive charges on the proteins. Even though MBP-C1 has the same number of positive charges as MBP-C3, a sharp decrease in $T_m(\text{PG})$ in the binary mixtures upon MBP-C1 interaction was not observed until the ratio of MBP-C1 to PG reached 1.5 mol% (*i.e.*, the 1PG:1d-PC mixture in Table 2-14, near 50% saturation). Moreover, although MBP-C2 presence decreased $T_m(\text{PG})$ to a greater extent than MBP-C5 and C8 for the 1PG:1d-PC mixture, a sharp decrease in $T_m(\text{PG})$ in the binary mixtures upon MBP-C2 interaction was not observed until

the ratio of MBP-C2 to PG reached 3.1 mol% (*i.e.*, the 1PG:3d-PC mixture in Table 2-14, near 100% SCD saturation). Near 100% saturation of the liposomal net-negative SCD was required for the presence of MBP-C5 or C8 to have a dramatic effect on $T_m(\text{PG})$ in the binary mixtures (1PG:3d-PC mixture in Table 2-14). It would be worthwhile to investigate the effects of each isoform on liposomes at protein concentrations between 1.5 and 3.1 mol%. Furthermore, the effect of dephosphorylating MBP-C3 at the Thr97 position on the liposomes of various SCD would be an interesting experiment to validate the differences observed in the associative behavior of MBP-C2 and C3. Regardless, it appears that saturation of the liposomal net-negative SCD by the multivalency of positive charges on the MBP isoforms was important for enhanced electrostatic association.

Overall inspection of the $T_m(\text{PG})$ data of Table 2-14 inferred that the d-PC component strengthens the interactions between the isoforms and PG component of the binary lipid systems. Alternatively, this dramatic decrease in $T_m(\text{PG})$, when the d-PC component of the binary liposomes was increased, could also be due to enhanced cooperativity of the PG phase transition in the presence of d-PC (what can be referred to as the “domino effect”). Recall that d-PC undergoes its phase transition at a temperature far below that of PG, thus at 31°C for example, PG is in the gel state while d-PC is completely fluid. The kinking of d-PC acyl chains in close proximity to PG acyl chains can then propagate the *trans* to *gauche* isomerization of PG acyl chains and initiate the phase transition of PG at a lower temperature. Even upon microdomain formation, this “domino effect” one acyl chain has upon another can still be dramatic when the lipid of lower phase temperature is the predominant lipid in the binary mixture. It appears that the decreased value for $T_m(\text{PG})$ derived for the binary liposomes in the presence of each MBP isoform can be at least partially attributed to this phenomenon since the most dramatic decrease observed for $T_m(\text{PG})$ occurred when the d-PC content was greater than that of PG (Table 2-14). It then may be surprising that the $T_m(\text{PG})$ calculated for the binary lipid systems in the absence of protein did not show a decrease due to the same “domino effect” phenomenon (section 2.3.1). This discrepancy was already addressed by the effect of dehydration of the PG acyl C=O interface (*i.e.*, a slight increase in $T_m(\text{PG})$) when a predominant amount of d-PC was present in the binary liposomes in the absence of protein (section 2.3.1). However, when a protein electrostatically associates with the headgroup of a lipid, electrostatic interactions replace

the stabilizing H-bonding network and restrict water-access to the headgroup (Nabet *et al.*, 1994). In the case of PG, MBP electrostatic association occurs with the phosphate moiety, while the bulk of the protein at the bilayer surface restricts the access of water to the glycerol moieties. As a result, electrostatic association between MBP and negatively charged phosphate moieties of PG interferes with the stabilizing network of hydrogen bonds that exists between the glycerol headgroups and water, an interference that can lower the phase transition temperature of PG (Nabet *et al.*, 1994). Taking this explanation under consideration, it would be expected that $T_m(\text{PG})$ would decrease even further when a protein primarily electrostatically associates with the PG component of the binary system while the headgroups of the other lipid (like d-PC) do not effectively hydrogen bond to water (*i.e.*, water interactions restricted by two sources). Any further conclusions based solely on the $T_m(\text{PG})$ calculated for the binary lipid mixtures in the presence of each MBP isoform at this point would be very difficult to make considering that only MBP-C3 interacts with PG primarily by electrostatic association with little contribution from hydrophobic intercalation (see section 2.3.3). From sections 2.3.1, 2.3.2 and 2.3.3, it was found that the order of the acyl chains was a more localized probe for monitoring the bilayer structure and stability in the presence and absence of MBP than the T_m calculated from the Boltzmann Sigmoidal function. Even though only the $T_m(\text{PG})$ varied under the influence of MBP interaction in the binary liposomes, the effect of MBP interaction and the possibility of microdomain formation upon preferential interaction with PG had to be verified by examination of the acyl chain order of d-PC and PG in the mixtures (Tables 2-15, 2-16 and 2-17).

Table 2-15. Acyl chain order of d-PC and PG in the presence of MBP-C1-C3, C5 and C8 for liposomal mixture 3PG:1d-PC. Shown in parentheses is $\Delta\nu$ between the lipid and protein-lipid preparations.

Sample	$\nu'(\text{CH}_2)^{\text{gel}}/\text{cm}^{-1}$	$\nu'(\text{CH}_2)^{\text{L}\alpha}/\text{cm}^{-1}$	$\nu(\text{CD}_2)^{\text{gel}}/\text{cm}^{-1}$	$\nu(\text{CD}_2)^{\text{L}\alpha}/\text{cm}^{-1}$
3PG:1dPC	2919.3 \pm 0.1	2923.1 \pm 0.1	2090.3 \pm 0.1	2094.3 \pm 0.1
C1	2920.1 \pm 0.1	2924.7 \pm 0.1 (+1.6)	2090.2 \pm 0.2	2094.4 \pm 0.2 (+0.1)
C2	2916.6 \pm 0.1	2920.5 \pm 0.1 (-2.6)	2090.5 \pm 0.2	2094.3 \pm 0.2 (0)
C3	2918.2 \pm 0.1	2923.7 \pm 0.1 (+0.6)	2090.0 \pm 0.2	2094.1 \pm 0.1 (-0.2)
C5	2918.5 \pm 0.1	2921.8 \pm 0.1 (-1.3)	2090.1 \pm 0.2	2092.6 \pm 0.1 (-1.7)
C8	2918.9 \pm 0.1	2922.3 \pm 0.1 (-0.8)	2089.7 \pm 0.2	2092.7 \pm 0.2 (-1.6)

Table 2-16. Acyl chain order of d-PC and PG in the presence of MBP-C1-C3, C5 and C8 for liposomal mixture 1PG:1d-PC. Shown in parentheses is $\Delta\nu$ between the lipid and protein-lipid preparations.

Sample	$\nu(\text{CH}_2)^{\text{gel}}/\text{cm}^{-1}$	$\nu(\text{CH}_2)^{\text{L}\alpha}/\text{cm}^{-1}$	$\nu(\text{CD}_2)^{\text{gel}}/\text{cm}^{-1}$	$\nu(\text{CD}_2)^{\text{L}\alpha}/\text{cm}^{-1}$
1PG:1dPC	2919.4 ± 0.1	2923.5 ± 0.1	2089.6 ± 0.2	2094.0 ± 0.1
C1	2916.7 ± 0.1	2923.0 ± 0.1 (-0.5)	2090.0 ± 0.2	2094.0 ± 0.1 (0)
C2	2919.4 ± 0.1	2923.1 ± 0.1 (-0.4)	2090.6 ± 0.2	2093.8 ± 0.1 (-0.2)
C3	2918.1 ± 0.1	2922.9 ± 0.1 (-0.6)	2090.4 ± 0.2	2094.4 ± 0.1 (+0.4)
C5	2918.8 ± 0.1	2922.0 ± 0.1 (-1.5)	2089.7 ± 0.2	2092.4 ± 0.1 (-1.6)
C8	2919.1 ± 0.1	2923.1 ± 0.1 (-0.4)	2089.7 ± 0.1	2092.5 ± 0.1 (-1.5)

Table 2-17. Acyl chain order of d-PC and PG in the presence of MBP-C1-C3, C5 and C8 for liposomal mixture 1PG:3d-PC. Shown in parentheses is $\Delta\nu$ between the lipid and protein-lipid preparations.

Sample	$\nu(\text{CH}_2)^{\text{gel}}/\text{cm}^{-1}$	$\nu(\text{CH}_2)^{\text{L}\alpha}/\text{cm}^{-1}$	$\nu(\text{CD}_2)^{\text{gel}}/\text{cm}^{-1}$	$\nu(\text{CD}_2)^{\text{L}\alpha}/\text{cm}^{-1}$
1PG:3dPC	2920.0 ± 0.1	2924.6 ± 0.1	2089.7 ± 0.2	2094.1 ± 0.2
C1	2918.1 ± 0.1	2922.1 ± 0.1 (-2.5)	2090.4 ± 0.2	2094.1 ± 0.2 (+0.1)
C2	2918.6 ± 0.1	2923.3 ± 0.1 (-1.3)	2090.0 ± 0.2	2093.7 ± 0.2 (-0.3)
C3	2918.0 ± 0.1	2922.9 ± 0.1 (-1.5)	2090.4 ± 0.2	2094.3 ± 0.1 (+0.3)
C5	2918.5 ± 0.1	2923.3 ± 0.1 (-1.3)	2089.5 ± 0.2	2092.2 ± 0.1 (-1.8)
C8	2920.3 ± 0.1	2924.1 ± 0.1 (-0.5)	2089.6 ± 0.1	2091.6 ± 0.1 (-2.4)

Preferential interaction of the most positively charged isoforms with the PG component of the binary liposomal mixtures was verified by examination of the effect of MBP-C1 and C2 interaction on the acyl chain order of both lipids in the binary mixtures. Examination of the acyl chain order of d-PC in the binary mixtures revealed that there was a reduction in the hydrophobic interactions between the more positively charged isoforms, MBP-C1 and C2, and d-PC even when d-PC was the predominant lipid (Tables 2-15, 2-16 and 2-17). For instance, the increase observed in the L α state energy of d-PC in the presence of the most positively charged isoforms, MBP-C1 and C2 (Table 2-7, $\Delta\nu = +0.6$ and $+0.7 \text{ cm}^{-1}$, respectively) was no longer observed for d-PC in the 3PG:1d-PC mixture (Table 2-15, $\Delta\nu = +0.1$ and 0.0 cm^{-1} , respectively), the 1PG:1d-PC mixture (Table 2-16, $\Delta\nu = 0.0$ and -0.2 cm^{-1} , respectively), and the 1PG:3d-PC mixture (Table 2-17, $\Delta\nu = +0.1$ and -0.3 cm^{-1} , respectively). In contrast, MBP-C1 and C2 interaction with the binary liposomes pro-

duced a substantial change in the acyl chain conformational order of PG (Tables 2-15, 2-16 and 2-17). Interaction between these isoforms and PG may have prevented the proteins from penetrating or disrupting the d-PC portion of the binary bilayer as previously implied by the lack of change in $T_m(\text{d-PC})$. In the presence of pure PG liposomes, MBP-C1 and C2 decreased the $L\alpha$ state frequency of PG (*i.e.*, increased the acyl chain order) by 1.4 cm^{-1} (Table 2-10). However, when a small amount of d-PC was added to the PG bilayer as in the 3PG:1d-PC preparation, the PG acyl chain order was increased by MBP-C2 interaction ($\Delta\nu = -2.6 \text{ cm}^{-1}$) but decreased by MBP-C1 ($\Delta\nu = +1.6 \text{ cm}^{-1}$) (Table 2-15). This difference between the interaction of MBP-C1 and C2 with the 3PG:1d-PC mixture is unusual, but is most likely due to the different contributions electrostatic association and hydrophobic interactions make towards interaction of these proteins with the acidic lipid. That is, in a pure PG environment, MBP-C1 restricted water access to the PG acyl C=O groups to a greater degree than MBP-C2 (section 2.3.3), thus PG may be more susceptible to penetration by MBP-C1 than by MBP-C2. Since these isoforms do not have favorable interactions with pure d-PC (section 2.3.2), a small amount of d-PC in the binary liposomes may further enhance both electrostatic and hydrophobic interactions of MBP-C1 and C2 with the dominant PG portion of the bilayer. When the d-PC content was raised, the $L\alpha$ state PG acyl chain order in 1PG:1d-PC bilayer upon interaction with either MBP-C1 or C2, was reduced (*ca.*, $\Delta\nu = -0.5 \text{ cm}^{-1}$) from that observed in the absence of d-PC (*ca.*, $\Delta\nu = -1.4 \text{ cm}^{-1}$), suggesting greater isoform penetration of the PG portion of the bilayer when the d-PC content was equal to that of PG (Table 2-16). The smaller effect of MBP-C2 presence on $T_m(\text{PG})$ of the 1PG:1d-PC lipid mixture (Table 2-14) may be explained by the observation that in pure PG liposomes MBP-C2 did not probe the interfacial region to same extent as MBP-C1 while the extent of electrostatic association may be equivalent (section 2.3.3). Although the hydration of the interfacial region of the PG portion of the bilayer could not be explored in the binary lipid mixtures without isotopic substitution, a decrease in perturbation of this region by MBP-C2 would result in less disordering of the first few methylenes. Under conditions where the liposomal net-negative SCD is nearly saturated (1PG:3d-PC), the degree of stabilization for the PG portion of the bilayer upon interaction with MBP-C2 was similar (Table 2-17, $\Delta\nu = -1.3 \text{ cm}^{-1}$) to when this isoform interacted with pure PG (Table 2-10, $\Delta\nu = -1.4 \text{ cm}^{-1}$), whereas upon MBP-C1 interaction the degree of stabilization nearly doubled

(Table 2-17, $\Delta v = -2.5 \text{ cm}^{-1}$). This observation suggests that when the net-negative SCD of the binary liposomes is saturated, the relative contribution of stabilization from electrostatic association to destabilization by bilayer penetration is greater for MBP-C1 than MBP-C2. The negative charge at Glu146 in the C-terminal half of MBP-C2 may decrease the associative behavior of MBP-C2 relative to MBP-C1. Overall, strong electrostatic association between MBP-C1 and MBP-C2 and PG, in combination with a lack of potentially favorable interactions with d-PC, appeared to induce the formation of PG microdomains as indicated by unaltered d-PC acyl chain order in all of the binary liposomal mixtures. Moreover, phase separation appears to be more complete when the net-negative SCD of the binary liposomes is saturated by the positive charges on the protein (*i.e.*, in the 1PG:3d-PC mixture) and unmodified MBP-C1 is slightly more effective at inducing PG microdomain formation than MBP-C2. Since deamidation at Gln146 of MBP-C2 is the only difference between MBP-C1 and C2, the C-terminal half of the protein is important for both stabilization by electrostatic association and PG microdomain formation in compact myelin (*i.e.*, high concentration of MBP to acidic lipid).

Preferential interaction of MBP-C3 with the PG component of the binary liposomal mixtures was also verified by examination of the effect of MBP-C3 interaction on the acyl chain order of both lipids in the binary mixtures. However, unlike MBP-C1 and C2, MBP-C3 was found to increase the acyl chain conformational order of both pure lipids (sections 2.3.2 and 2.3.3) and thus is potentially capable of interacting at the surface with PG or d-PC in a mixed bilayer. In a pure d-PC environment (section 2.3.2), MBP-C3 lowered the $L\alpha$ state energy of d-PC (Table 2-7). However, this stabilization of the fluid d-PC state by MBP-C3 in the pure d-PC environment (Table 2-7, $\Delta v = -2.1 \text{ cm}^{-1}$) was nearly obliterated in the 3PG:1d-PC environment (Table 2-15, $\Delta v = -0.2 \text{ cm}^{-1}$) and destabilized d-PC in the 1PG:1d-PC mixture (Table 2-16, $\Delta v = +0.4$), and the 1PG:3d-PC mixture (Table 2-17, $\Delta v = +0.3$). Similar to that observed for MBP-C1 and C2, as the d-PC content of the binary lipid mixtures was increased, MBP-C3 interaction resulted in a gradual lowering of the $L\alpha$ state energy of PG (Table 2-15, 3PG:1d-PC: $\Delta v = +0.6 \text{ cm}^{-1}$, Table 2-16, 1PG:1d-PC: $\Delta v = -0.6 \text{ cm}^{-1}$ and Table 2-17, 1PG:3d-PC: $\Delta v = -1.5 \text{ cm}^{-1}$). The overall stabilization of the PG portion of the 1PG:3d-PC bilayer was similar to that noted for MBP-C3 interaction with pure PG liposomes (Table 2-10, $\Delta v = -1.8 \text{ cm}^{-1}$). Therefore, although there appeared to be

some competition between d-PC and PG for interaction with MBP-C3 when the liposomal net-negative SCD was only partially saturated (*i.e.*, 3PG:1d-PC), saturation of the liposomal net-negative SCD (*i.e.*, 1PG:3d-PC mixture) promoted preferential interaction with PG. Moreover, since MBP-C3 interaction with pure PG liposomes was found to be primarily electrostatic (section 2.3.3), the increased order of the PG acyl chains as the d-PC content is raised infers that electrostatic interaction is enhanced by greater saturation of the liposomal negative SCD. However, when the liposomal net-negative SCD is saturated by the available positive charges on MBP-C3, the relative contribution of stabilization by electrostatic association to destabilization by bilayer penetration was similar to that observed for MBP-C2 interaction, but still less than that observed for MBP-C1 interaction (Table 2-17). The two sites of phosphorylation (Thr97 and Ser164) in the C-terminal half of MBP-C3 may decrease the associative behavior of MBP-C3 relative to MBP-C1. This further supports the notion that the C-terminal half of the protein is vital for both stabilization by electrostatic association and PG microdomain formation in compact myelin. An interesting observation is that MBP-C3 stabilization of the saturated net-negative liposomal mixture (1PG:3d-PC) was similar to that of MBP-C2, even though MBP-C3 has two phosphorylated residues in the C-terminal half. Therefore, the position of the modified residue in the C-terminal half of MBP-C2 and C3 appears to be important for defining the associative behavior of the isoform with compact myelin-like membranes.

In contrast to MBP-C1, C2 and C3, MBP-C5 and C8 did not induce the formation of PG microdomains in the binary liposomal mixtures (Tables 2-15, 2-16 and 2-17). Recall, that like MBP-C3, MBP-C5 and C8 can interact at either a d-PC (section 2.3.2) or PG (section 2.3.3) bilayer. In the binary lipid mixtures, MBP-C5 and C8, continued to lower the $L\alpha$ state energy of d-PC regardless of the PG content in the mixed liposomes. Simultaneously, MBP-C5 and C8 lowered the $L\alpha$ state energy of PG. Therefore, instead of MBP-C5 and C8 inducing the formation of PG microdomains, the two lipids of the binary mixture appeared to compete with one another for surface interaction with MBP-C5 and C8. However, this competition between d-PC and PG was less pronounced when MBP-C5 interacted with the binary liposomes. The stabilization of the d-PC acyl chains in the binary mixtures upon MBP-C5 interaction (Table 2-15, 3PG:1d-PC: $\Delta v = -1.7 \text{ cm}^{-1}$; Table 2-16, 1PG:1d-PC: $\Delta v = -1.6 \text{ cm}^{-1}$; Table 2-17, 1PG:3d-PC: $\Delta v = -1.6 \text{ cm}^{-1}$) was reduced by nearly

40%, compared to that obtained when MBP-C5 interacted with pure d-PC liposomes (Table 2-7, $\Delta v = -2.6 \text{ cm}^{-1}$). Concurrently, the stabilization of the PG acyl chains in the binary mixtures upon MBP-C5 interaction (Table 2-15, 3PG:1d-PC: $\Delta v = -1.3 \text{ cm}^{-1}$; Table 2-16, 1PG:1d-PC: $\Delta v = -1.5 \text{ cm}^{-1}$; Table 2-17, 1PG:3d-PC: $\Delta v = -1.3 \text{ cm}^{-1}$) was increased by 40%, compared to that obtained when MBP-C5 interacted with pure PG liposomes (Table 2-10, pure PG: $\Delta v = -0.9 \text{ cm}^{-1}$). Although d-PC and PG in the binary mixtures competed for interaction with MBP-C5, the interaction with PG was enhanced at the expense of interaction with d-PC, suggesting a preferential interaction between MBP-C5 and PG without obliterating interaction between MBP-C5 and d-PC. The presence of d-PC in the binary liposomes increased saturation of the liposomal net-negative SCD by the positive charges available on MBP-C5, resulting in enhanced interaction between MBP-C5 and the PG portion of the binary liposomes. When the liposomal net-negative SCD is saturated by the available positive charges on MBP-C5 (1PG:3d-PC mixture), the relative contribution of stabilization by electrostatic association to destabilization by bilayer penetration was similar to that observed for MBP-C2 and MBP-C3 interaction, but still less than that observed for MBP-C1 interaction (Table 2-17). The similar extent of PG stabilization exerted by MBP-C5 interaction with the 1PG:3d-PC mixture to that of MBP-C3, is understandable since MBP-C5 is phosphorylated at the same two residues (Thr97 and Ser164) in the C-terminal half as MBP-C3. In comparison to MBP-C3 however, MBP-C5 has two additional sites of phosphorylation (Ser7 and Ser54) in the N-terminal half of the sequence. These additional negative charges in the N-terminal half of MBP-C5 may be responsible for the lack of phase separation observed. Recall, that these negatively charged amino acids side-chains in the N-terminal half of MBP-C5 were thought to pair up with positively charged amino acids in the protein sequence to neutralize segments of the protein and enable interaction at the surface of pure d-PC liposomes (section 2.3.2). In a pure PG environment, these extra negative charges in the N-terminal half of MBP-C5 were thought to experience repulsion from the unsaturated negative SCD on the PG bilayer surface, neutralize two positively charged residues in the sequence, and create a neutral fragment suitable for bilayer insertion (section 2.3.3). Considering these results from the pure lipid systems, the N-terminal half of MBP-C5 may prefer to interact with the zwitterionic d-PC surface of binary liposomes, while the C-terminal half prefers to engage in electrostatic association with the

PG surface of the binary liposomes. In turn, preferential interaction of the N-terminal half of MBP-C5 with d-PC may minimize the destabilizing effects of the N-terminal modifications on PG, accounting for the increased stabilization effect of MBP-C5 on the PG acyl chains when d-PC was present. In contrast to MBP-C5, such a simple trend was not observed for the interaction between MBP-C8 and the binary liposomes. In the presence of MBP-C8, the relative stability of the d-PC portion of the binary liposomes to that of pure d-PC liposomes (Table 2-8: $\Delta v = -1.8 \text{ cm}^{-1}$) remained similar (Tables 2-14: $\Delta v = -1.7 \text{ cm}^{-1}$ and Table 2-16: $\Delta v = -1.5 \text{ cm}^{-1}$) rather than reduced. Moreover, when d-PC was the predominant lipid in the binary mixture the conformational order of the d-PC acyl chains increased (Table 2-17, $\Delta v = -2.4 \text{ cm}^{-1}$) over that obtained when MBP-C8 interacted with pure d-PC liposomes (Table 2-7, $\Delta v = -1.8 \text{ cm}^{-1}$), indicative of enhanced interaction between MBP-C8 and the zwitterionic head groups of d-PC. Yet similar to MBP-C5, MBP-C8 interaction also enhanced the conformational order of PG when d-PC was present (Table 2-10, pure PG: $\Delta v = 0.0 \text{ cm}^{-1}$; Table 2-15, 3PG:1d-PC: $\Delta v = -0.8 \text{ cm}^{-1}$; Table 2-16, 1PG:1d-PC: $\Delta v = -0.4 \text{ cm}^{-1}$; Table 2-17, 1PG:3d-PC: $\Delta v = -0.5 \text{ cm}^{-1}$); an enhancement that was less pronounced as the d-PC content was raised. Therefore, upon MBP-C8 interaction the competition between d-PC and PG was more fierce, but highly dependent on the relative amounts of PG and d-PC in the mixture. In contrast to the other isoforms, the presence of d-PC in the binary liposomes cannot increase the saturation of the liposomal net-negative SCD by the positive charges available on MBP-C8 to the same extent (*i.e.*, only 80% saturated in the 1PG:3d-PC mixture Table 2-2). When the liposomal net-negative SCD is maximally saturated by the available positive charges on MBP-C8 (1PG:3d-PC mixture), the relative contribution of stabilization by electrostatic association to destabilization by bilayer penetration was about 65% lower than that observed for MBP-C2, C3 and C5 and about 80% lower than that observed for MBP-C1 (Table 2-17). The four arginyl residues citrullinated (Cit122, Cit130, Cit159 and Cit170) on the C-terminal half of MBP-C8, reduce the multivalency of positive charges available for association of MBP-C8 with the PG portion of the binary mixtures. In addition, the multivalency of positive charges available in the N-terminal half of MBP-C8 (Cit25 and Cit31) is also reduced. Recall, in pure PG liposomes, it was suggested that this increased hydrophobicity of MBP-C8 could account for MBP-C8 insertion into the PG bilayer (section 2.3.3). However, in a pure d-PC

environment, the citrullinations of MBP were thought to result in electronically neutral segments which can weakly interact with (or at least not disturb) the surface of the zwitterionic d-PC bilayer (section 2.3.2). Considering these results from the pure lipid systems, the N-terminal half of MBP-C8 may prefer to interact with the zwitterionic d-PC portion of binary liposomes, and the C-terminal is shared between PG and d-PC. For example, in the binary liposomes of 80% saturated SCD (1PG:3d-PC), the acyl chain order of d-PC was increased (*i.e.*, stabilized) substantially beyond (*ca.*, 35%) that observed in the absence of PG (compare Table 2-8 to Table 2-17), suggesting a small amount of PG may have promoted greater surface interaction between MBP-C8 and d-PC. Thus, MBP-C5 and C8 are shared between the PG and d-PC and do not induce the formation of PG microdomains regardless of the liposomal composition. However in liposomes representative of compact myelin, the C-terminal half of MBP-C5 exhibited a preference for electrostatic association with PG while that of MBP-C8 exhibited a preference for d-PC. The restricted ability of MBP-C5 to induce formation of PG microdomains in the binary liposomes may in part be due to the preference of the N-terminal half of MBP-C5 for interaction with d-PC. This suggests that while the C-terminal half of the protein is vital for stabilization by electrostatic association, modifications to residues on the N-terminal half can also prevent PG microdomain formation in compact myelin. However, the restricted ability of MBP-C8 to induce formation of PG microdomains in the binary liposomes is more likely due to the combination of weaker electrostatic association between the C-terminal half with PG and preference of the N-terminal half to interact with d-PC. Therefore, either the number (*i.e.*, more than two) or the type (*i.e.*, citrullination) of post-translational modifications that reduce the multivalency of positive charges available in the C-terminal half of MBP-C8 is responsible for the decreased associative behavior of the isoform with compact myelin-like membranes.

The results of the current study infer that the net-positive charge of the C-terminal half of MBP can increase the relative amounts of PG stabilization by electrostatic association to destabilization by PG bilayer penetration in binary liposomes of saturated net-negative SCD. That is, the relative amounts of PG stabilization by electrostatic association to destabilization by PG bilayer penetration in the 1PG:3d-PC liposomal mixture decreased in the following order: unmodified MBP-C1 >> C2/C3/C5 >> C8. However, the multivalency of available positive charges in the C-terminal half of MBP is also important since MBP-

C2, C3 and C5 stabilized the PG portion of 1PG:3d-PC liposomal mixture to the same extent, while MBP-C8 barely had a stabilizing effect. Furthermore, the strong electrostatic association of MBP-C1, C2 and C3 with acidic lipids was able to induce the formation of PG microdomains when the net-negative SCD was saturated (1PG:3d-PC). Reduction of the multivalency of available positive charges in N-terminal half of MBP-C5 prevented PG microdomain formation in mixed bilayers of saturated net-negative SCD (1PG:3d-PC). Reduction of the multivalency of positive charges by multiple citrullinations in both halves of MBP-C8 had two effects: reduced electrostatic association and prevent PG microdomain formation. The idea of microdomain formation of acidic lipids in binary liposomes upon MBP interaction is controversial. Roux *et al.*, 1994, found that the fragmentation of PC bilayers into small lipoprotein particles observed upon interaction with unfractionated MBP was inhibited when binary liposomes containing 20 mol% phosphatidylserine interacted with the protein. This inhibition of fragmentation would only be possible if the strong interaction between MBP and PS favored exclusion of the protein from the PC portion of the binary liposomes. Since unfractionated MBP consists predominantly of MBP-C1 and C2, these observations of Roux *et al.*, 1994, are not in conflict with the current study which proposes that MBP-C1, C2 and C3 can impart PG microdomain formation in 1PG:3d-PC liposomes (25 mol% PG). In an earlier study, Reinyl and Bayerl, 1993, found that interaction of unfractionated MBP with single bilayers composed of DMPC and an acidic phospholipid (*ca.* 10 mol% DMPG, DMPS or DMPA) on a solid substrate did not support demixing in the binary systems in their ATR-FTIR experiments. However, Reinyl and Bayerl, 1993, evaluated MBP bound asymmetrically to one side of the bilayer and were looking for redistribution of the lipids between the two bilayer leaflets. Since MBP was accessible to both bilayer leaflets in the current study which supports MBP-induced formation of PG microdomains, comparison to the negative results of Reinyl and Bayerl is difficult.

2.3.5 Conformation of MBP charge isoforms in aqueous solution

Unfractionated and fractionated MBP in aqueous solution at physiological pH has been shown to be predominantly unordered or random coil with some turn structure (Choo, 1992; Jackson *et al.*, 1993; Morell *et al.*, 1994). This result for the highly net-positively charged MBP is not surprising given that similar results are observed for poly-L-lysine, a

protein typically used as a model polypeptide for studies on highly net-positively charged proteins. For example, when the lysine residues of poly-L-lysine are in an ionized state (neutral pH), charge repulsion between the positively charged lysine residues promotes a random coil conformation of the polypeptide backbone, while neutralization of the polypeptide (acidic pH) promotes solvated α -helical formation and heating (at basic pH) promotes β -sheet formation (Jackson *et al.*, 1989). Although MBP is not a homopolypeptide like poly-L-lysine, the high net-positive charge of the MBP, which ranges from +20 (MBP-C1) to +14 (MBP-C8), is mostly likely responsible for the lack of ordered secondary structure in aqueous solution.

In the current study, the conformation of the isoforms in buffer were to be compared to the conformation of the isoforms in the presence of the pure lipids (sections 2.3.6 and 2.3.7) and the binary liposomes (section 2.3.8). Temperature-ramped spectra of the isoforms were collected between 15-55°C to reproduce the conditions of the protein-lipid studies for direct comparison and to verify denaturation of the protein does not occur within this temperature range. Since bilayer fluidity can have an impact on protein conformation, the only temperatures required for comparison of protein conformation in buffer to that in a lipid environment are two temperatures representative of the gel state and the $L\alpha$ state of the lipid. From the plateau regions of the Boltzmann sigmoidal transition curves, three temperatures were chosen: 15°C for gel state d-PC, 31°C for $L\alpha$ state d-PC and gel state PG, and 55°C for $L\alpha$ state PG. For the binary liposomes however, PG reaches the fluid state at various temperatures depending on which isoform is present (*i.e.*, 31-37°C). Rather than compare isoform conformation at different temperatures, isoform conformation in the presence of the binary liposomes was only evaluated at two temperatures; when both lipids were in the gel state (15°C) and when both lipids were in the $L\alpha$ state (55°C). Therefore, for direct comparison of the isoform conformation in aqueous solution to that in any of the lipid environments used, the frequency of the amide I component bands and arginine side-chain vibrations for each MBP isoform, at 15, 31 and 55°C was all that was required (Table 2-18).

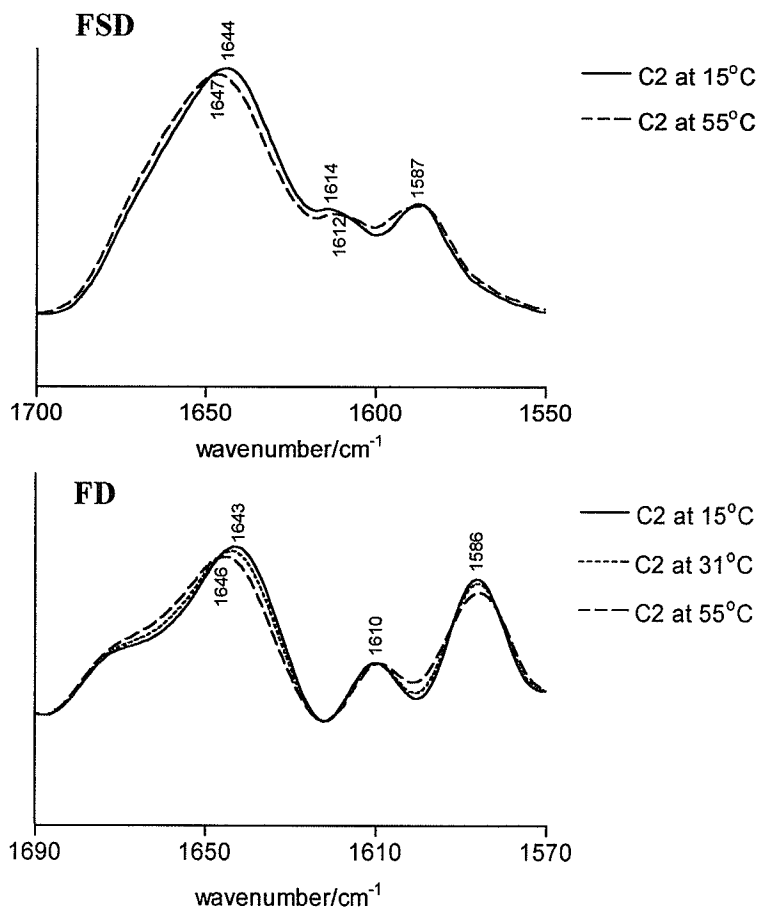
Table 2-18. Temperature dependence of MBP isoform conformation in aqueous solution as determined by the amide I vibration and side chain absorptions. Peak positions were extracted from second derivative spectra. The amide I maximum is marked with an asterisk. Abbreviations for assignments of the amide I component bands: (rc), random coil; (r, α), random coil or α -helix; (t), turns.

Isoform	Amide I 15°C (cm⁻¹)	Amide I 31°C (cm⁻¹)	Amide I 55°C (cm⁻¹)	Arginine 15°C (cm⁻¹)	Arginine 31°C (cm⁻¹)	Arginine 55°C (cm⁻¹)
C1	1643* (rc) 1671 (t)	1645* (rc) 1667 (t)	1648* (rc, α) 1667 (t)	1586 1611	1586 1611	1587 1612
C2	1643* (rc) 1670 (t)	1644* (rc) 1669 (t)	1646* (rc) 1668 (t)	1586 1610	1586, 1610	1586 1609
C3	1644* (rc) 1665 (t)	1645* (rc) 1663 (t)	1647* (rc) 1663 (t)	1586 1610	1586, 1610	1586 1610
C5	1643* (rc) 1668 (t)	1646* (rc) 1669 (t)	1648* (rc, α) 1671 (t)	1584 1609	1583, 1608	1583 1610
C8	1643* (rc) 1667 (t)	1644* (rc) 1669 (t)	1646* (rc) 1671 (t)	1584 1609	1583 1608	1584 1609

The frequencies of the amide I component bands summarized in Table 2-18 verify that the conformations of the MBP isoforms in aqueous solution are predominantly unordered or random coil with some turn structure. Component bands of the amide I band profile were assigned as follows: random coil structure was assigned to an amide I maximum between 1640-1645 cm⁻¹, α -helical structure was assigned to an amide I maximum between 1648-1658 cm⁻¹ and turn structure was assigned to component bands located above 1667 cm⁻¹ (Jackson and Mantsch, 1995). Recall however, that differentiation of unordered or random coil structure from that of α -helical is difficult because the accepted ranges for unordered and α -helical structures overlap near 1648 cm⁻¹ (section 1.5.1). Further to this point, parallel β -sheets and the low frequency component band of antiparallel β -sheets can absorb between 1625-1640 cm⁻¹ (Jackson and Mantsch, 1995), making differentiation of β -

sheet from random coil structure difficult if the component band is near 1640 cm^{-1} (section 1.5.1). Since MBP is thought to be predominantly random in aqueous solution at neutral pH (Choo, 1992; Jackson *et al.*, 1993; Morell *et al.*, 1994), the random coil and turn band assignments in Table 2-18 coincide with what is already known about the amide I band profiles of the isoforms in aqueous solution and ambient temperature. Some of the component bands in Table 2-18 absorb at the higher frequency side of the accepted range for random coil (*i.e.*, $1647\text{-}1648\text{ cm}^{-1}$), and for these bands it may be more appropriate to say that there was some gain in α -helical structure relative to that of random coil. Even with artificial band narrowing techniques (FD or FSD), a combination of helical structure and random coil may still yield an amide I maximum between $1647\text{-}1648\text{ cm}^{-1}$ simply because these two structures cannot be resolved from one another. The assignment of arginine side-chain absorptions was based on the accepted literature values for the symmetric and asymmetric vibrations of the δ -guanidino group vibration of arginine residues in D_2O , reported to be 1586 cm^{-1} and 1608 cm^{-1} , respectively (Chirgadze *et al.*, 1975). Second-derivative spectra were used in preference to the FSD spectra to extract the frequency of the component bands from the wide amide I band profile in Table 2-18. In comparison to second-derivative spectra, there was significantly more overlap amongst component bands in FSD spectra of the isoforms, making the extraction of peak frequencies by IR software programs more difficult. For example, turn structure (*ca.*, 1667 cm^{-1}) could not be resolved from the amide I maximum in an FSD spectrum of an isoform while in the second derivative spectrum turn frequencies could be extracted (Figure 2-11). Figure 2-11 illustrates the difference in the resolution of the amide I component bands in FSD and second-derivative spectra; the temperature dependence of the amide I band profile and side chain absorptions of MBP-C2 are shown as a typical example. Different degrees of smoothing were used after the application of the deconvolution function and after the second derivative calculation, which can affect the artificial resolution-enhancement obtained (*i.e.*, the greater the points of smoothing the more the overlap). A greater degree of smoothing was used in the FSD operation on the isoform spectra in order to ensure that the spectra were not “over-deconvolved” (see section 1.4.5).

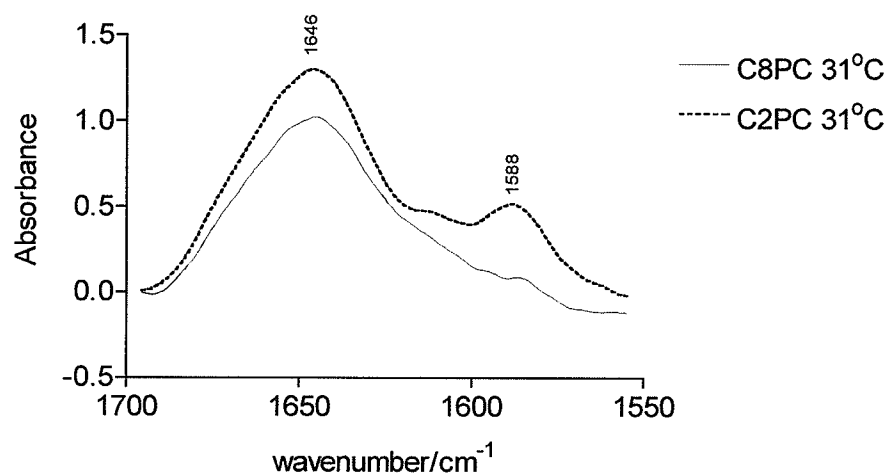
Figure 2-11. Amide I absorption profile of MBP-C2 at various temperatures. FSD spectra (top) and second derivative spectra (bottom) shown for comparison.



The amide I band profile and side-chain absorptions of the MBP isoforms in aqueous solution were similar, the main difference arising from the relative concentration of arginine to the other residues in the polypeptide backbone. The relative contribution of arginyl amide C=O to the amide I band for the different isoforms, can be approximated by the relative intensity of the arginine δ -guanidino side-chain absorptions to the amide I absorption. Comparison of relative intensities in spectra is best performed using FSD spectra rather than second-derivative spectra because the relative intensity information is lost in the latter when absorption bands of different natural widths are compared (Cameron and Moffatt, 1984). This relative intensity measurement of arginine side-chain absorptions to the amide I is only relevant for MBP-C8 in comparison to the other isoforms, since MBP-C8 is the only isoform that has some arginyl residues post-translationally modified to citrul-

line. Citrulline side-chain absorptions have been reported to appear at 1570 and 1590 cm^{-1} (Choo, 1992), however in Table 2-18, the side-chain absorptions of MBP-C8 were more typical of those attributable to arginine. Only 30% of the arginyl residues of MBP are citrullinated in MBP-C8 (Wood and Moscarello, 1989). Therefore citrulline may contribute to the side-chain absorptions observed for MBP-C8 but citrulline absorptions were overlapped and unresolved from those due to the arginine. However, the relative intensity of the arginyl peaks to the amide I absorption in the FSD spectra was decreased for MBP-C8 in comparison to the more positively-charged isoforms, such as MBP-C2 (Figure 2-12).

Figure 2-12. Comparison of the relative intensity of the amide I to the arginine side chain absorption for MBP-C2 and MBP-C8 at 31°C. FSD spectra shown.



The effect of temperature on the conformation of the MBP isoforms in an aqueous environment was again similar for the different isoforms (Table 2-18). The proteins did not denature at the higher temperature of 55°C, otherwise a rather narrow and predominant amide I component band around 1620 cm^{-1} would have been observed (*i.e.*, that due to aggregated peptides, see Table 1-3, section 1.5.1). Instead, there appeared to be a gradual 3-5 cm^{-1} shift of the random coil amide I maximum to higher frequency, suggesting a contribution from some α -helical structure (Table 2-18). Smaller temperature-dependent frequency shifts in the δ -guanidino group vibrations of arginine side-chains (*ca.*, 1587 cm^{-1} and 1612 cm^{-1}) were also observed, suggesting that there was also a change to the microen-

vironment in proximity to those arginyl residues due to conformational fluctuations (Table 2-18). A temperature-dependent shift of the amide I maximum of the MBP isoforms to higher frequencies near 1648 cm^{-1} has been reported before by Choo, 1992 and has been attributed to an increase in α -helical structure. However, an increase in temperature may also make a flexible protein in solution more dynamic, weakening some H-bonds within the structure. The weakening of some H-bonds may be better explanation for the shift of the amide I maximum to higher frequency. That is, a weaker H-bond to an amide carbonyl oxygen would pull less electron density away from the C=O group and more energy would be required for the amide C=O stretch (section 1.5.1).

2.3.6 Conformation of MBP charge isoforms upon interaction with neutral lipids

Since MBP has net-positive charge and interacts primarily by electrostatic association with acidic phospholipids (see sections 2.1.3 and 2.1.5), little associative interaction was predicted with the liposomes of d-PC which have a zero surface charge density (SCD). However, from the phase behavior of d-PC in the presence of MBP, it was noted that the more positively-charged isoforms, MBP-C1 and MBP-C2 perturbed the d-PC bilayer and were perhaps involved in hydrophobic interactions with the d-PC acyl chains (section 2.3.2). The hydrophobic photolabeling studies of Boggs *et al.*, 1999a, support the notion that segments or hydrophobic amino acid side-chains of MBP-C1 and C2 can at least partially insert into neutral lipid bilayers. Moreover, MBP-C3, C5 and C8 may have interactions at the surface of the d-PC bilayer since their presence was observed to increase the order of the d-PC acyl chains (section 2.3.2). Therefore, the amide I band profile of each MBP isoform in the presence of d-PC was examined below and above the phase transition temperature of the lipid to further substantiate the changes already noted for d-PC in section 2.3.2.

As shown in Table 2-19, the structure of the MBP isoforms in the presence of gel state d-PC ($15\text{ }^{\circ}\text{C}$) did not depart from the predominantly random coiled conformation found when the proteins were placed in aqueous solution at the same temperature (see section 2.3.5). As a typical example, the amide I band profiles of MBP-C2 in the presence of d-PC and in an aqueous environment are similar and show an amide I maximum of $1643\text{-}4\text{ cm}^{-1}$ due to a predominantly random coil structure (compare Table 2-18 with Table 2-

19). An exception was noted for MBP-C1 in which a shoulder at 1653 cm^{-1} , assigned to α -helical structure, was observable in the second-derivative spectrum (Table 2-19).

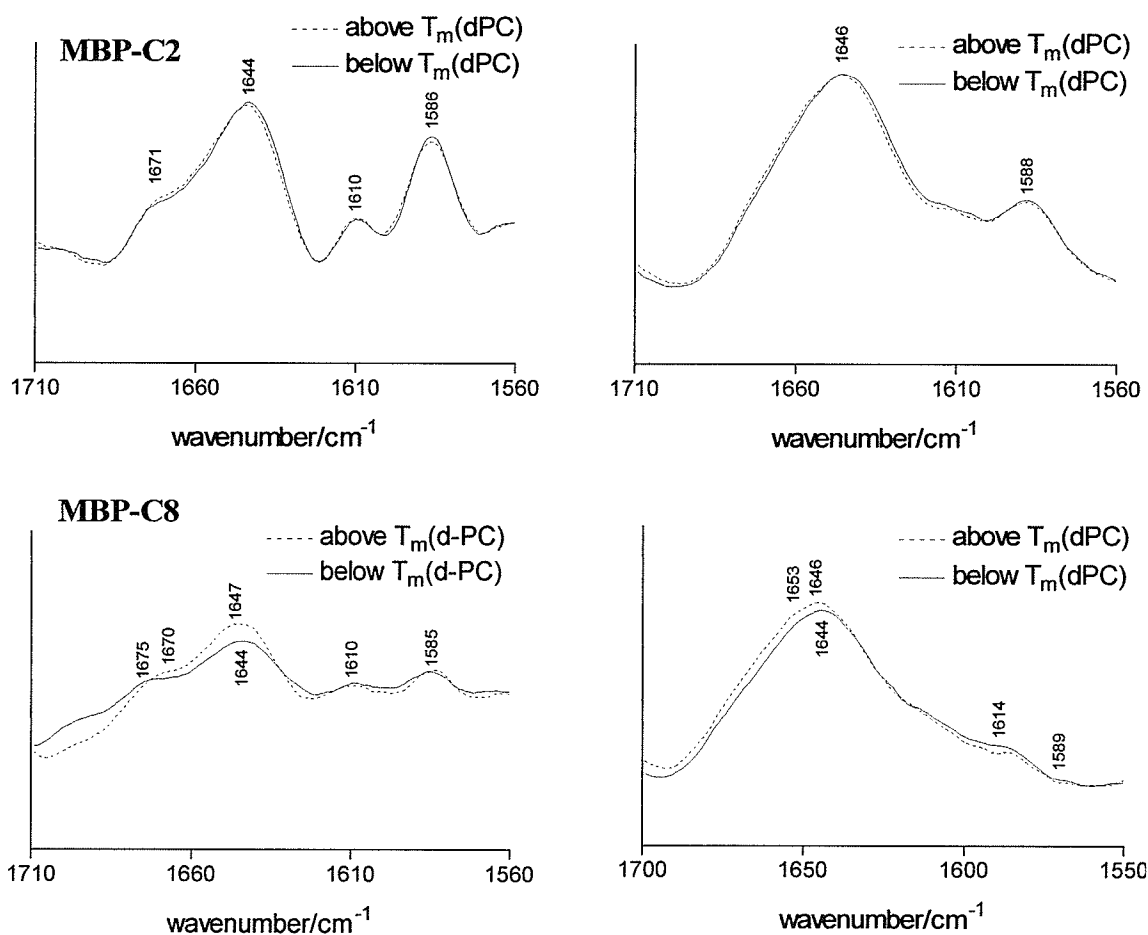
Table 2-19. The amide I profiles and arginine side chain absorptions of MBP isoforms in the presence of d-PC. Frequencies were extracted from second-derivative spectra and the amide I maximum is marked with an asterisk. Abbreviations used for assignment of the amide I component bands: (rc), random coil; (α), α -helix; (t), turns.

Isoform	Amide I 15 °C (cm^{-1})	Amide I 31 °C (cm^{-1})	Arginine 15 °C (cm^{-1})	Arginine 31 °C (cm^{-1})
C1	1643*(rc)	1643*(rc)	1585	1586
	1653(α)	1653(α)	1608	1608
	1671 (t)	1671 (t)		
C2	1644* (rc)	1644* (rc)	1586	1586
	1671 (t)	1671 (t)	1610	1610
C3	1643* (rc)	1643* (rc)	1586	1585
	1671 (t)	1671 (t)	1610	1610
C5	1642* (rc)	1643* (rc)	1584	1584
	1664 (t)	1667 (t)	1611	1612
C8	1644* (rc)	1646* (rc)	1586	1583
	1671 (t)	1671 (t)	1609	1610

Some differences are apparent when comparing the amide I profiles of the isoforms in the presence of L α state d-PC (31 °C) to those obtained in aqueous solution at 31°C (Tables 2-17 and 2-18). First of all, the temperature-induced shift of the amide I maximum to slightly higher frequency observed in aqueous solution was not as pronounced for the more positively-charged isoforms MBP-C1, C2, C3 and C5 in the presence of d-PC (compare Table 2-18 and 2-19). For example, when the temperature was raised to 31°C, the amide I profile of MBP-C2 in the presence of d-PC did not increase in frequency as was observed previously for the isoform in an aqueous environment (Figure 2-13, top). Therefore, the presence of d-PC prevented the conformational fluctuations of the more positively charged (or uncitrullinated) isoforms in response to a temperature

increase. In contrast, the amide I maximum of the least positively charged isoform (or citrullinated), MBP-C8, experienced the temperature-dependent shift to higher frequency when d-PC was present at a lower temperature (31 °C) than that observed for this isoform in aqueous solution (Table 2-19 and Figure 2-13, bottom). Shown in Figure 2-13, the amide I of MBP-C2 in the presence of d-PC did not change in response to temperature, while that of MBP-C8 still experienced a temperature-induced shift to higher frequency. Moreover, the frequencies of the amide I component bands of MBP-C8 in the presence of $L\alpha$ state d-PC was more similar to those of MBP-C8 in aqueous solution at 55 °C than at 31°C (Table 2-18 and Table 2-19). Therefore, MBP-C1, C2 C3 and C5 may have been conformationally restricted upon interaction with d-PC whereas the conformational flexibility of MBP-C8 was not affected or perhaps enhanced.

Figure 2-13. Amide I band profile of MBP-C2 (top) and MBP-C8 (bottom) above and below the T_m of d-PC. Second derivative spectra (left), FSD spectra (right)



Overall, the predominant conformation of the MBP isoforms upon interaction with d-PC was still random coil or unordered, but either a change in the isoform conformation upon exposure to d-PC or a change in the conformational flexibility of the isoform at higher temperatures, suggests an interaction with d-PC. For better understanding of the impact of d-PC on the conformation of the isoform, recall the changes observed in the d-PC acyl chain order and hydration of the d-PC bilayer interfacial region upon isoform interaction (section 2.3.2). For example, the overall stabilization effect of the MBP isoforms on the L α state d-PC acyl chains in decreasing capability to stabilize was: MBP-C5 > MBP-C3 > MBP-C8 >> MBP-C1/C2 (section 2.3.2). This suggested that the relative amounts of stabilization by surface interactions with the choline head group region to destabilization by bilayer penetration decreased accordingly: MBP-C5 > MBP-C3 > MBP-C8 >> MBP-C1/C2. Further to this point, the hydration of the d-PC bilayer interfacial region was decreased in the presence of all the isoforms in the following order of effective dehydration: MBP-C1/C2 > MBP-C3 > MBP-C5/C8 (section 2.3.2). This suggested that the ability of hydrophobic amino acids or hydrophobic segments of the MBP isoforms to penetrate the d-PC bilayer decreased in the following order: MBP-C1/C2 > MBP-C3 > MBP-C5/C8. Considering the results of the d-PC phase behavior together, MBP-C1 and C2 were thought to penetrate the d-PC bilayer and intercalate with hydrophobic acyl chains (section 2.3.2). The appearance of a resolved α -helical component band in the amide I band profile of MBP-C1 upon interaction with d-PC is an interesting observation since membrane-interacting domains of proteins are frequently α -helical (Brandon and Tooze, 1999). Such a resolved α -helical component band was not observed in the amide I profile of MBP-C2 upon interaction with d-PC. The only difference between MBP-C1 and C2 is the extra negative charge on the C-terminal half (Gln146 modified to Glu146) of MBP-C2, indicating that Gln146 is important for the formation of additional α -helical structure in MBP-C1 upon interaction with d-PC. One speculation for this discrepancy between MBP-C1 and C2, could be that the Glu146 carboxylate side-chain in MBP-C2 is involved in a long range intramolecular interaction, such as salt-bridge formation, which may restrict formation of some α -helical structure. Regardless, substantial penetration of segments of MBP-C1 and MBP-C2 into the bilayer can explain the reduced flexibility of these proteins in solution (*i.e.*, resistance to temperature-induced

conformational fluctuations). Contrary to the more positively charged isoforms, MBP-C3, C5 and C8 predominantly interacted with the zwitterionic d-PC bilayer surface bringing some hydrophobic amino acids in proximity to the liposomal surface for partial penetration of the bilayer interface (section 2.3.2). Similar to MBP-C2, MBP-C3 and C5 remained predominantly random coil in structure and exhibited a resistance to temperature-induced conformational fluctuations upon interaction with d-PC. However, unlike the more positively charged isoforms, MBP-C3 and C5 had an overall stabilization effect on the d-PC bilayer and did not dehydrate the bilayer interfacial region to the same extent (section 2.3.2). Thus, MBP-C3 and C5 may insert some hydrophobic amino acid side-chains into the bilayer interfacial region but they are primarily located at the surface. The phosphorylations at Thr97 and Ser164 in MBP-C3 and C5 may restrict the penetration of these amino acid side-chains into the bilayer (if not neighboring side chains as well) in comparison to MBP-C1 and C2. Moreover, the increase in the multivalency of negative charges in MBP-C3 or C5 may neutralize some of the positive charges in the C-terminal half of the protein, allowing interaction with the zwitterionic d-PC surface. The N-terminal half of MBP-C5 has two additional phosphorylations at Ser7 and Ser54 which may account for why MBP-C5 does not dehydrate (*i.e.*, penetrate) the d-PC bilayer interface to the same extent as that observed for MBP-C3 interaction. Insertion of hydrophobic amino acid side-chains in concert with interactions at the surface of the d-PC bilayer, may account for the restriction in the conformational dynamics of MBP-C3 and C5 (*i.e.*, resistant to temperature-induced conformational fluctuations). In contrast to the other isoforms, MBP-C8 exhibited a similar (if not increased) sensitivity to the temperature-induced conformational fluctuations in a d-PC environment to that observed in aqueous solution. Since there was little dehydration of the d-PC bilayer interface in the presence of MBP-C8 and MBP-C3/C5 had a greater overall stabilizing effect on the d-PC acyl chains, MBP-C8 was thought to penetrate the bilayer to a lesser extent and have weaker interaction at the surface of bilayer, respectively, than MBP-C3 and C5 (section 2.3.2). Since MBP-C8 has fewer positively charged amino acids due to citrullination, fewer intramolecular salt-bridges can be formed in comparison to MBP-C3 and C5 (see section 2.3.2). In turn, fewer intramolecular interactions may account for the greater conformational flexibility of MBP-C8 upon interaction with d-PC.

2.3.7 Conformation of MBP charge isoforms upon interaction with acidic lipids

Although numerous studies have explored the interactions of MBP upon interaction with acidic lipids, little is known about the secondary and tertiary structure of the protein in this environment. Some recent progress has been made with molecular dynamic simulations performed on data from low resolution transmission electron microscopy (TEM) images of MBP-C1 in the presence of a lipid monolayer composed from a myelin-like proportion of lipids (Beniac *et al.*, 1997; Ridsdale *et al.*, 1997). The three-dimensional reconstruction (4 nm resolution) of MBP-C1 presented by Beniac *et al.*, 1997, represented the protein as a “C”-shaped structure oriented parallel to the monolayer surface. When MBP-C1 was exposed to high salt buffer, the protein became more compact (“O”-shaped) and globular in shape (Beniac *et al.*, 1997). Ridsdale *et al.*, 1997, attempted to fit a severin-like 5-stranded antiparallel β -sheet backbone model to their TEM reconstruction, since both severin and MBP are actin- and lipid-binding proteins. The atomic model that Ridsdale *et al.*, 1997, reported was the best fit for their TEM reconstruction, comprised a five-stranded antiparallel β -sheet and a large amount of irregular coil packaged together. More recently, these molecular dynamics simulations were carried out MBP-C1, MBP-C8 and the Marburg variant MBP-Cit-18 (Pritzker *et al.*, 2000). Again the models supported a central antiparallel β -sheet with extensive loop regions (which may be able to accommodate α -helical segments) on either side of the sheet, the overall molecule bent into a “C”-shaped tertiary structure (Pritzker *et al.*, 2000). The interesting finding of Pritzker *et al.*, 2000 was that citrullination of the MBP arginyl residues lead to an opening of this “C”-shaped structure, making the protein more susceptible to enzymatic digestion by cathepsin D, a metalloproteinase that is elevated in MS brains. To substantiate the proposed antiparallel β -sheet and irregularly looped structure (which may also accommodate α -helical segments), as well as the changes observed in the PG phase behavior noted in section 2.3.3, the amide I band profile of each MBP isoform in the presence of gel and $L\alpha$ state PG was examined.

In comparison to the MBP isoforms in an aqueous environment at 31°C (Table 2-18), conformational changes from the purely random coil were evident when these isoforms were in a gel state acidic lipid environment (Table 2-20). In the presence of gel state PG, a gain in ordered secondary structure for MBP-C1, and C2 was observed. Aside from

a random coil amide I maximum, component bands attributable to β -sheet (1639 cm^{-1}) and α -helix (1650 cm^{-1}) formation were observed in the amide I band profile for MBP-C1 and MBP-C2, respectively (Table 2-20).

Table 2-20. Amide I profiles and amino acid side chain absorptions of MBP isoforms in the presence of PG. Peak positions were extracted from second derivative spectra. Amide I maximum marked with an asterisk. Abbreviations used for assignment of the amide I component bands: (rc), random coil; (rc, α), random coil and/or α -helix; (α), α -helix; (β), β -sheet; (t), turns.

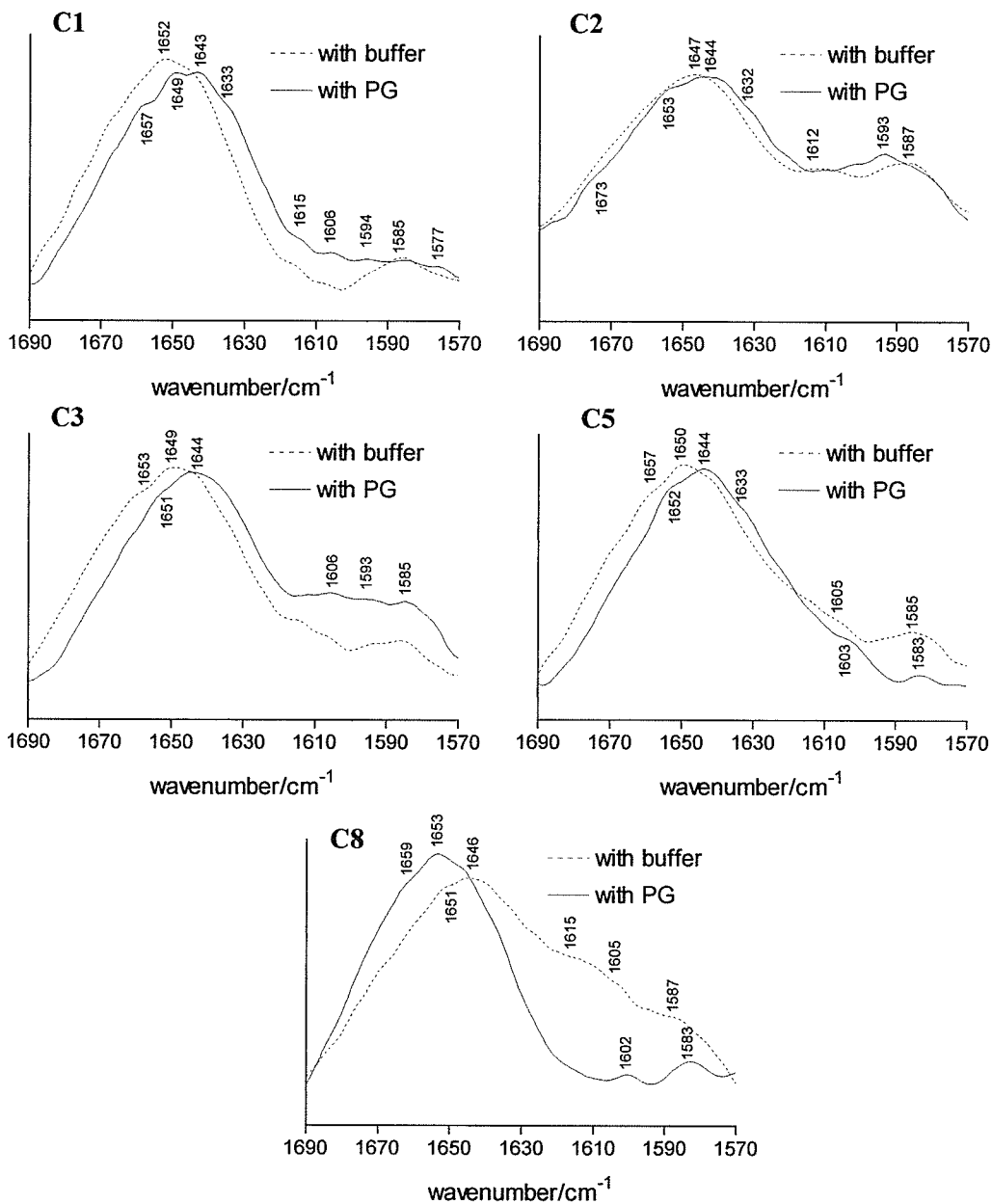
MBP	Amide I 31°C (cm^{-1})	Amide I 55°C (cm^{-1})	Arginine 31°C (cm^{-1})	Arginine 55°C (cm^{-1})
C1	1646* (rc) 1639 (β) 1663 (t) 1676 (t)	1645* (rc) 1639 (β) 1662 (t)	1581, 1587 1600, 1608	1581, 1586 1599, 1608
C2	1642* (rc) 1650 (α) 1672 (t)	1642* (rc) 1649 (α) 1656 (α) 1673 (t)	1587 1606	1584, 1591 1606, 1613
C3	1644* (rc) 1672 (t)	1644* (rc) 1651 (α) 1672 (t)	1583 1606	1582, 1594 1603
C5	1642* (rc) 1670 (t)	1643* (rc) 1650 (α) 1667 (t)	1580 1601	1581 1603
C8	1646* (rc) 1671 (t)	1652* (α) 1671 (t)	1583 1608	1581 1609

Changes in the conformation of MBP-C1 were also suggested by the appearance of two bands for each arginine absorption (Table 2-20). This appearance of two bands for each arginyl side-chain vibration suggests differences in the microenvironments in proximity to the arginines. Solvent dipoles can affect vibrations much in the same way that hydrogen bonds do; a strong solvent dipole, like at the aqueous surface of a protein, can

pull electron density from the vibrating group, causing the vibration to occur at a lower frequency (Lambert *et al.*, 1987; Jackson and Mantsch, 1995; Troullier *et al.*, 2000). For example, the appearance of two bands for the symmetric δ -guanidino stretch of MBP-C1, one at higher frequency (1587 cm^{-1}) and one at lower frequency (1581 cm^{-1}) may arise from arginines buried in an environment with a lower dielectric constant and those exposed to an environment with a high dielectric constant, respectively. Environments with a low dielectric constant may be either the protein interior or acyl chain portion of a bilayer. An environment with a high dielectric constant would be that on a protein surface, exposed to aqueous solvent. Electrostatic association between an arginine and a negatively charged amino acid may also extract electron density from the δ -guanidino group, causing the vibration to occur at lower frequency. Solvent dipoles can also affect the frequency of the amide I component bands assigned to different structural motifs of the protein, causing component bands to appear slightly out of the anticipated range (Jackson and Mantsch, 1995; see Chapter 1). For example, when poly-L-lysine adopts a helical conformation in aqueous solution at low pH, the amide I maximum (1638 cm^{-1}) was lower than anticipated for α -helical structures due to the significant hydration polar homopolypeptides frequently experience (Jackson *et al.*, 1989). Such a feature has also been found for apomyoglobin where a component band found at 1633 cm^{-1} has been assigned to solvated helical structure, well-resolved from the component band at 1650 cm^{-1} assigned to buried α -helix protected from solvent by inter-helix tertiary contacts (Gilmanshin *et al.*, 1997). Therefore, the assignment of the 1639 cm^{-1} component band of MBP-C1 (and MBP-C5) to β -sheet may not be correct and it could be argued that this component band could also arise from solvated helices. For now, although the formation of solvated helices is possible, the component band at 1639 cm^{-1} will be assigned to β -sheet structure, since antiparallel β -sheet formation is supported in the literature (Beniac *et al.*, 1997; Ridsdale *et al.*, 1997; Pritzker *et al.*, 2000). The absorption at 1639 cm^{-1} may be the low frequency component (LFC) band of an antiparallel β -sheet, but this cannot be confirmed by the presence of a high frequency component (HFC) band of an antiparallel β -sheet which normally appears 40-50 cm^{-1} higher than the LFC band (section 1.5.1). The HFC band of the antiparallel β -sheet would have appeared between $1690\text{-}1700\text{ cm}^{-1}$, but the high frequency edge of the lipid acyl C=O absorption (1735 cm^{-1}) overlapped the amide I in this region.

Upon an increase in temperature, differences were apparent in either the secondary structure and/or the conformational flexibility (*i.e.*, sensitivity to temperature) of the isoforms in the presence of PG (Table 2-20). The random coil amide I maximum of MBP-C1 remained at the same frequency regardless of temperature and only changes in the frequency of some turn structure changed. The frequency and splitting pattern of the arginine-side chain absorptions of MBP-C1 also remained the same upon the phase transition. Strong electrostatic binding between MBP-C1 and gel state PG (31°C) may restrict the conformational flexibility of MBP-C1 upon the phase transition (55°C). MBP-C2, C3 and C5 association with gel state PG (31°C) appears to have been slightly weaker than that of MBP-C1. That is, upon the phase transition, the predominantly random coil amide I maximum stayed at the same frequency but a new component band due to some α -helical structure appeared for MBP-C2 (1656 cm^{-1}), MBP-C3 (1651 cm^{-1}), MBP-C5 (1650 cm^{-1}). The arginine side-chain absorptions of MBP-C2 and C3 split only upon the phase transition (55°C) into the low and high frequency component bands observed for MBP-C1. In contrast, the amide I maximum of MBP-C8 in the presence of gel state PG (31°C) changed from predominantly random coil (1646 cm^{-1}) to predominantly α -helix (1652 cm^{-1}) upon the phase transition (55°C). The arginine side chain absorptions of MBP-C5 and C8 did not change upon the PG phase transition, but their occurrence at low frequency (1580-1583 cm^{-1}) suggests that they could be solvent exposed, involved in electrostatic interactions with PG, or involved in intramolecular salt-bridges. Since IR cannot differentiate between these similar dipole effects any change in the possible microenvironments of the arginines in MBP-C5 and C8 would be undetectable. Based on the conformational changes (or lack thereof) observed upon the PG phase transition, the conformational flexibility of the isoforms in the PG environment decreased accordingly: MBP-C8 > MBP-C3/C5 > MBP-C2 > MBP-C1. In turn, conformational flexibility in the presence of PG is most likely determined by the strength of the electrostatic binding between the isoforms and gel state PG; the weaker the binding, the greater the protein flexibility during the phase transition.

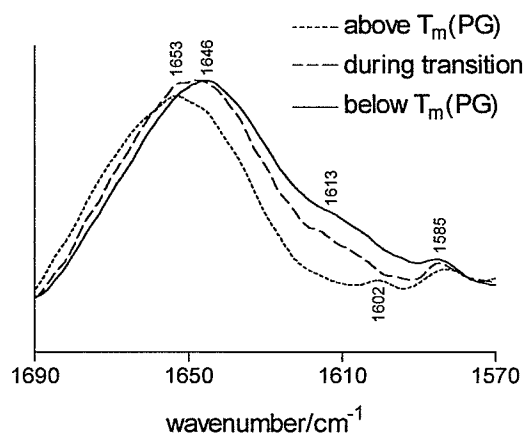
Figure 2-14. Comparison of the amide I band profile of MBP-C1-C3, C5 and C8 in aqueous (dotted line) and PG liposomal (solid line) environments at 55°C. FSD spectra shown



Aside from using the frequencies extracted from the second derivative spectra, the relative effects of PG on the conformation of each MBP isoform can also be examined by comparing the overall amide I band contour of the isoform in aqueous solution to that in a PG environment at the same temperature (Figure 2-14). In Figure 2-14, FSD spectra

of each the isoform in a PG and an aqueous environment at 55 °C are overlaid in each frame to illustrate the shift in the overall band contour induced by interaction with the lipid. For MBP-C1, C2, C3 and C5, the overall band contour of the amide I absorption shifted to lower frequency when these isoforms were exposed to PG (solid lines, Figure 2-14). Since the conformations of these isoforms in aqueous solution is considered to be predominantly random coil and turn structure, MBP-C1, C2, C3 and C5 gained β -sheet structure (1628-1640 cm^{-1} region) at the expense of turn structure (above 1663 cm^{-1}) upon interaction with PG. In contrast, the amide I of MBP-C8 experienced an overall shift to higher frequency upon interaction with PG, indicative of a structural change from the predominantly random coiled structure observed at 55°C in buffer (1646 cm^{-1}) to a predominantly α -helical structure (1653 cm^{-1}) in a PG environment. Further illustration of this gradual gain in α -helical structure at the expense of random coil structure for MBP-C8 as the bilayer fluidity increased is provided in Figure 2-15.

Figure 2-15. The amide I profile of MBP-C8 in the presence of PG illustrating the gradual gain in α -helical structure with concomitant loss in random coil structure as temperature and the bilayer fluidity increased. FSD spectra shown.



Conformational changes in the MBP isoforms upon interaction with a fluid PG bilayer were also suggested by the splitting of the arginine side-chain absorptions (Table 2-20 and Figure 2-14). Recall that the arginine absorptions were split for only MBP-C1 and C2 when PG was in the gel state (31°C). However, when the PG bilayer became fluid, a splitting in the arginine side chain absorptions was observed for MBP-C1, C2 and C3. Inter-

estingly, like the splitting in the arginine side-chain absorption, the additional α -helical component band in the amide I profiles of MBP-C2 and C3 appeared only when the bilayer was fluid. Since splitting of the arginine absorption band most likely arises from arginine side-chains exposed to different forces in their microenvironment (Chapter 1), MBP-C1, C2 and C3 have two types of arginine side-chain absorptions; arginine side chains that are proximal to external dipoles that extract electron density ($1581\text{-}1584\text{ cm}^{-1}$) and those that are shielded from external dipoles ($1586\text{-}1594\text{ cm}^{-1}$). The type of external dipoles responsible for the shifting of this vibration to lower frequency vary from H-bonding dipoles, dipoles from a polar solvent and electrostatic dipoles. Electrostatic interaction between MBP and acidic lipids is believed to proceed through both arginyl and lysyl residues (refer to sections 2.1.4 and 2.1.5). Therefore, the appearance of arginyl absorptions at higher frequency ($1586\text{-}1594\text{ cm}^{-1}$) suggests that not all of the arginyl residues are available for surface binding to PG in folded MBP-C1, C2 and C3, rather some are buried in the hydrophobic protein interior. This is extremely interesting since it suggests that the multivalency of positive charges available to interact with the surface of the fluid PG bilayer is not fully utilized during MBP-C1, C2 and C3 interaction. The arginine side-chain absorptions of MBP-C5 and C8 however, did not split regardless of bilayer fluidity and only the lower frequency absorption at 1581 cm^{-1} appeared. Therefore, the arginine side-chains of MBP-C5 or MBP-C8 are all in similar microenvironments, most likely electrostatically associated to the bilayer surface or involved in intramolecular salt-bridge formation. The microenvironments of arginines in MBP-C5 and C8 may still however be different because these two proteins are post-translationally modified in different ways. That is, since MBP-C5 is phosphorylated at Ser7, Ser54, Thr97 and Ser164 (Zand *et al.*, 1998), the excess multivalency of negative charges on MBP-C5 may be repelled by the unsaturated negative SCD¹³ of the PG bilayer and may compete with the PG phosphate moieties for positively charged residues in the protein sequence. If the extra negative charges located in the N-terminal half of MBP-C5 (pSer7 and pSer54) are repelled from the PG bilayer surface and salt-bridge formation with arginyl residues is promoted, this will neutralize part of the N-terminal half of MBP-C5, making it more suitable for insertion in the hydrophobic environ-

13. The negative SCD on the PG bilayer is at most 25% saturated when 0.8 mol% MBP is used (Table 2-2).

ment of bilayer. The appearance of an α -helical component band upon the phase transition may indicate this helix is formed from intramolecular charge neutralization. As for MBP-C8, citrullination reduces the multivalency of positive charges available for interaction with the negative SCD of the PG bilayer and/or with negatively charged residues in the protein¹⁴. This repulsion between negatively charged residues on the protein and the unsaturated negative SCD at the bilayer may be minimized by salt-bridge formation with positively charged residues. Electrostatic association with the bilayer and salt-bridge formation amongst residues would have the same dipole effect on the arginine side-chain absorption (*i.e.*, lower frequency of 1581 cm^{-1}), thus only one type of arginine absorption is observed for MBP-C5 and MBP-C8. Again, salt-bridge formation within the sequence of MBP-C8 would neutralize portions of the protein, making segments more suitable for insertion in the hydrophobic environment of bilayer. This latter postulation is supported by the greater amount of α -helical structure detected for MBP-C8 upon interaction with fluid PG, in comparison to that detected for the uncitrullinated MBPs.

The conformational changes detected in the MBP isoforms upon interaction with fluid PG are not in conflict with the changes observed in the PG phase behavior (section 2.3.3). The effect of the isoforms on the PG acyl chain order supported a synergy between electrostatic association and bilayer penetration, the relative contributions of each dependent on the type and presence of post-translational modifications on the isoform. The relative contributions of different structures (random coil, β -sheet and α -helix) detected for the isoforms also suggest various combinations of bilayer association and penetration for the isoforms. That is, membrane-inserting segments of proteins are frequently α -helical in structure, whether the helix traverses the bilayer in a perpendicular fashion or lies parallel to the plane of the bilayer and partially penetrates (Brandon and Tooze, 1999). Based on this generalization, the extrinsic portion of membrane proteins may be β -sheet and/or random coil in structure, but this does not rule out buried or solvated α -helix formation in the associated domain. The overall stabilization effect of the MBP isoforms on the $L\alpha$ state

14. MBP-C8 still has 12 Lys residues (5 in the N-terminal half, 7 in the C-terminal half) and 13 remaining Arg residues (8 in the N-terminal half, 6 in the C-terminal half). Like the other isoforms, MBP-C8 has 11 Glu/Asp residues (7 in the N-terminal half, 4 in the C-terminal half). From bovine sequence presented in Zand *et al.*, 1998 and sites of citrullination proposed by Wood and Moscarello, 1989.

PG acyl chains decreased accordingly: MBP-C3 > MBP-C1/C2 >> MBP-C5 >> MBP-C8 (section 2.3.3). This suggested the relative contribution of stabilization by electrostatic association to destabilization by bilayer penetration decreased accordingly: MBP-C3 > MBP-C1/C2 >> MBP-C5 >> MBP-C8. Further to this point, the hydration of the PG bilayer interfacial region was enhanced by MBP-C3 presence, but decreased in the presence of the other isoforms in the following order of effective dehydration: MBP-C2 < MBP-C1 << MBP-C5 << MBP-C8 (section 2.3.3). This suggests that ability of hydrophobic amino acids or hydrophobic segments of the MBP isoforms to penetrate the PG bilayer increased in the following order: MBP-C3 << MBP-C2 < MBP-C1 << MBP-C5 << MBP-C8. Taking the PG phase behavior under consideration, MBP-C3 acts primarily by surface association and few (if any) hydrophobic amino acids penetrate the bilayer, while from the conformational analysis, MBP-C3 was the isoform with the greatest contribution from random coil and β -sheet structure (Figure 2-14). MBP-C1 and C2 also acted primarily by surface association, but some hydrophobic segments and/or amino acid residues may partially penetrate the bilayer. In the conformational analysis, MBP-C1 and C2 had an α -helical feature resolved from the amide I maximum even though they were predominantly random coil and β -sheet in structure (Figure 2-14). This α -helical feature may arise from an amphipathic helix that lies parallel to and only partially penetrates the bilayer surface (*i.e.*, insertion of hydrophobic amino acid residues) since the PG acyl chains were still quite stabilized in the presence of MBP-C1 or C2. Similar to MBP-C1 and C2, the conformation of MBP-C5 in the $L\alpha$ state PG environment, was predominantly random coil, but the α -helical contribution was more prevalent and the β -sheet contribution appeared reduced to that observed for MBP-C1 and C2 (Figure 2-14). The random coil and residual β -sheet structure may have been that portion of MBP-C5 involved in surface association, but since the PG acyl chains were not as effectively stabilized by MBP-C5, an α -helical segment of the protein may have penetrated the bilayer to a greater extent, perhaps in a perpendicular orientation to the bilayer. For MBP-C8 and to lesser extent for MBP-C5, an observed increase in α -helical conformation at the expense of random coil and/or β -sheet structure upon interaction with $L\alpha$ state PG, a decreased ability to stabilize the PG acyl chains and dehydration of the bilayer interfacial region, suggests deep penetration of the bilayer by α -helical segments of the protein. Salt-bridge formation within the sequence of MBP-C5 and

C8 could make segments of these proteins electronically neutral and more suitable for insertion into the bilayer.

2.3.8 Conformation of MBP isoforms upon interaction with liposomes of altered SCD

Interpretation of the structural changes in the MBP isoforms upon interaction with the PG/d-PC liposomes, is more complicated than that with either pure lipid and thus must be approached more conservatively. The primary concern regarding structural analysis of the isoforms upon interaction with the PG/d-PC liposomes involves the unavoidable structural averaging in IR spectra. That is, any absorption (*i.e.*, amide I band or side chain absorptions), used to delineate structural information on the proteins, will be the composite absorption band from every protein molecule in the mixture. The observed amide I band profile will depend on the relative proportion of protein molecules that interact with PG and/or d-PC in the binary mixtures. In the absence of complete phase separation, the amide I band would be the composite amide I absorption of the different influences both lipids have on isoform structure. The result is a spectral “dilution” of the isoform structure induced by one specific lipid when the other lipid may have had an effect. For example, isoforms that did not have modifications in the N-terminal half of the sequence (MBP-C1, C2 and C3) were proposed to induce the formation of PG microdomains in the 1PG:3d-PC mixture (section 2.3.4). Therefore, for MBP-C1, C2 and C3, the 1PG:3d-PC liposomal mixture would lead to the least spectral “dilution” of protein structure induced by PG. In contrast, if the net-positive charge of the N-terminal half was reduced (MBP-C5 and C8), the N-terminal half exhibited substantial interaction with the surface of d-PC, and PG microdomain formation was inhibited in the 1PG:3d-PC mixture. Even though MBP-C1, C2 and C3 induce PG microdomain formation, the MBP to PG concentration may influence isoform structure. Saturation of the negative SCD of PG (*i.e.*, 1PG:3d-PC mixture) may influence the structure of the protein due to a reduction in repulsive forces from opposing PG leaflets experienced by the protein. For example, the extent of electrostatic binding between MBP-C1 and PG (*i.e.*, stabilization of the PG acyl chains) was increased by the saturation of the liposomal net-negative SCD (section 2.3.4). In the absence of PG leaflet repulsion, the excess positive charges in MBP-C1 may be more thoroughly neutralized by the PG head groups. Therefore, despite complete phase separation, MBP-C1 conformation

in a saturated liposomal SCD environment (*i.e.*, 1PG:3d-PC mixture) may be different to that observed in the pure PG environment where the negative SCD was unsaturated. Additional conformational changes may also result from charge modification to the C-terminal half of the protein. MBP net-positive charge reduction in the C-terminal half of the protein by deamidation or phosphorylation of 1-2 residues (MBP-C2, C3) reduced the extent of PG stabilization by electrostatic association in the 1PG:3d-PC mixture (section 2.3.4). Although it was believed that MBP-C2 and C3 still induced PG microdomain formation in the 1PG:3d-PC, increasing the multivalency of negative charges in the C-terminal half of the protein, reduced the extent of electrostatic association to PG. These extra negative charges on MBP-C2 and C3 may compete with the PG head groups for two positively charged residues in the sequence and result in a different structural change than that observed for MBP-C1. Comparison of the amide I band profiles of the isoforms in the 1PG:3d-PC mixture to those in either pure lipid environment would be further complicated by incomplete phase separation, and further charge modification (*i.e.*, MBP-C5 and C8). Therefore, it is best to begin with the structural changes observed in MBP-C1, C2 and C3 in the 1PG:3d-PC liposomal mixture, since this will at least remove the convoluted effects of d-PC and PG interaction on the isoform secondary and tertiary structure.

Upon saturation of the net-negative SCD of the 1PG:3d-PC liposomes, the amide I band profiles of MBP-C1, C2 and C3 did exhibit some contribution from ordered secondary structures (*i.e.*, α -helix and β -sheet) (Table 2-21). In comparison to the amide I band profiles in the unsaturated PG environment (Table 2-20), saturation of the liposomal negative SCD resulted in some discrete changes in secondary structure and overall conformational flexibility. First of all, in comparison to the conformational flexibility observed for MBP-C2 and C3 upon interaction with gel state PG (Table 2-20), all three isoforms were conformationally restricted in the 1PG:3d-PG environment (Table 2-21). For example, once these isoforms interacted with the binary liposomes in the gel state (15°C), their conformation remained the same regardless of an increase in temperature (55°C). Such decreased conformational flexibility suggests MBP-C1, C2 and C3 are more tightly bound to PG when the negative SCD of PG is saturated by the positive charges of the protein. Binding to the PG microdomains most likely involves a combination of electrostatic association to the PG head groups and some penetration of the PG interfacial region. Without isotopic labeling

of the acyl C=O groups of one lipid in the mixture, the hydration of the bilayer interface cannot be assessed. However, the relative contribution of stabilization by electrostatic association to destabilization by bilayer penetration was nearly twice as great for MBP-C1 than for MBP-C2 or C3 (Table 2-17, section 2.3.4), suggesting electrostatic association was greater for MBP-C1 interaction.

Table 2-21. Amide I band profile of MBP isoforms in 1PG:3d-PC liposomal environment. Data extracted from second-derivative spectra at temperatures where both lipids were in the gel state (15°C) and when both lipids were in the L α state (55°C). The amide I maximum is marked with a single asterisk. Abbreviations used for the assignment of the amide I component bands: (rc), random coil; (rc, α), random coil and/or α -helix; (α), α -helix; (β), β -sheet; (t), turns. Double asterisk depicts the splitting of arginine side chain absorption(s).

Isoform	Amide I 15°C (cm⁻¹)	Amide I 55°C (cm⁻¹)	Arginine 15°C (cm⁻¹)	Arginine 55°C (cm⁻¹)
C1	1643* (rc) 1658 (α) 1671 (t)	1642 * (rc) 1658 (α) 1671 (t)	1584 1607	1581 1607
C2	1639* (β) 1647 (rc) 1670 (t)	1640* (β , rc) 1647* (rc) 1665 (t)	1584 1605	1582** 1590** 1609
C3	1641* (rc) 1647 (rc) 1666 (t)	1641* (rc) 1647 (rc) 1670 (t)	1588 1610	1591 1611
C5	1639* (β) 1666 (t)	1642* (rc) 1667 (t)	1584 1610	1582 1605
C8	1642* (rc) 1670 (t)	1643* (rc) 1666 (t)	1583 1605	1581 1607

In addition, based on the splitting pattern and/or frequency of the symmetric δ -guanidino stretch of arginine, some arginyl residues of MBP-C2 and C3 may still be buried, while those of MBP-C1 are all exposed to a strong dipole (compare Table 2-20 to Table 2-21). The burial of some arginyl residues may account for the lessened effect MBP-C2 and

C3 had in stabilizing the PG acyl chains of the 1PG:3d-PC mixture in comparison to MBP-C1, even though they have the same number of positively charged residues. The appearance of one type of arginyl absorption at the low frequency of 1581 cm^{-1} suggests that saturation of the PG negative SCD allows electrostatic association to occur with all arginyl residues of MBP-C1. If all the arginines are involved in electrostatic association with PG, there would be less charge repulsion within the protein structure. Less charge repulsion within MBP-C1 may allow the protein to acquire a more ordered and compact structure, in comparison to MBP-C1 in the unsaturated negative SCD environment of pure PG. Moreover, in comparison to the unsaturated fluid PG environment (Table 2-20, 55°C), the amide I maxima of MBP-C1, C2 and C3 exhibited a $3\text{-}4\text{ cm}^{-1}$ decrease in frequency toward β -sheet structure (Table 2-21). For example, the amide I maximum of MBP-C1 was 1645 cm^{-1} when the MBP to PG concentration was low (Table 2-20), whereas saturation of the PG negative SCD promoted a shift of the amide I maximum to 1642 cm^{-1} (Table 2-21). Further to this point, in aqueous buffer (section 2.3.5) the amide I maxima were much higher in frequency ($1647\text{-}1648\text{ cm}^{-1}$) at 55°C . MBP-C2 and C3 still possess a component band at the frequency of random coil structure (1647 cm^{-1}) in the 1PG:3d-PC environment, whereas MBP-C1 lost some random coil structure and gained some α -helix (1658 cm^{-1}). Perhaps an increase in β -sheet structure (*i.e.*, shift of the amide I maximum to lower frequency) and a gain of α -helix is associated with more extensive neutralization of the positive charges in MBP-C1 upon electrostatic association to the PG. The restriction of protein conformational freedom indicates that tertiary structure of these isoforms may be more compact when they are bound to mixed bilayers of saturated net-negative SCD. Such a notion is supported by a molecular dynamics reconstruction using TEM data of MBP-C1 bound to a lipid monolayer, where the tertiary structure was reported to become more compact ("O"-shaped) and globular in shape upon exposure to high salt buffer (Beniac *et al.*, 1997). High salt buffer was thought to provide a shielding effect on MBP-C1 when bound to an acidic monolayer (Beniac *et al.*, 1997). Perhaps a large proportion of zwitterionic d-PC in the 1PG:3d-PC liposomes provides a similar shielding effect, allowing MBP-C1, C2 and C3 to become more compact.

In contrast to MBP-C1, C2 and C3, MBP-C5 did not induce PG microdomain formation in the 1PG:3d-PC mixture. However, the conformational flexibility of MBP-C5 was

reduced upon interaction with the gel state 1PG:3d-PC liposomes (Table 2-21). For example, in the unsaturated PG environment, an α -helical component band in the amide I of MBP-C5 appeared after the phase transition (Table 2-20), yet upon interaction with gel state 1PG:3d-PC a new component band did not appear upon the phase transition. Still, MBP-C5 is not as conformationally restricted as the more positively charged isoforms because the β -sheet amide I maximum (1639 cm^{-1}) observed at 15°C shifted to slightly higher frequency after the phase transition (1641 cm^{-1}) at 55°C . The amide I band profile of MBP-C5 upon interaction with the 1PG:3d-PC environment at 55°C was similar to that observed for MBP-C5 in fluid d-PC environment at 31°C (1643 cm^{-1} , 1667 cm^{-1}). However, the lower frequency of the amide I maximum (1641 cm^{-1}) suggests that MBP-C5 can interact with PG in addition to d-PC in the 1PG:3d-PC liposomes. The increased restriction in the conformational freedom of MBP-C5 may then be the result of surface interaction with d-PC and PG. A more dramatic structural change was observed for MBP-C8 once d-PC was present in excess of PG (Table 2-21). Instead of the α -helical structure (1652 cm^{-1}) observed for MBP-C8 in an unsaturated negative SCD PG environment (section 2.3.7), the isoform conformation exhibited a predominantly random coil amide I absorption profile, similar to that observed for MBP-C8 in a d-PC environment (section 2.3.6). In addition, MBP-C8 was conformationally restricted upon interaction with the 1PG:3d-PC, whereas the conformational flexibility of MBP-C8 was not affected by interaction with liposomes of zero SCD. In the absence of phase separation, the negatively charged head groups of PG may neutralize the excess positive charges in MBP-C5 and MBP-C8, which may improve isoform interaction with the zwitterionic d-PC head groups. Moreover, the lack of α -helical structure for MBP-C5 and MBP-C8 upon interaction with the 1PG:3d-PC liposomes suggests that the presence of d-PC prevented penetration of the N-terminal half of the isoforms near the PG acyl chains of the mixed bilayer. This lack of penetration, may account for why MBP-C5 and C8 can stabilize the PG acyl chain order of the 1PG:3d-PC mixture to a greater extent than that observed in the pure PG environment.

Several general inferences can be made with regards to changes in the amide I band profiles of the isoforms in the binary mixture where net-negative SCD was not saturated but when both lipids were present in equivalent proportions (*i.e.*, 1PG:1d-PC). When the d-PC content was equal to that of PG, there would be more charge repulsion between the neg-

atively charged PG head groups of opposing liposomal leaflets. Moreover, in comparison to the 1PG:3d-PC mixture, the d-PC charge shielding effect on the isoforms would be reduced in the 1PG:1d-PC mixture. Upon an increase in temperature, all of the isoforms exhibited less conformational restriction in the 1PG:1d-PC environment than the 1PG:3d-PC environment, indicating weaker protein-lipid binding when the liposomal negative SCD is not neutralized by the positive charges on the isoform(s). MBP-C3 experienced slightly more conformational restriction upon interaction with the 1PG:1d-PC liposomal mixture than the other isoforms. That is, the frequencies of the random coil amide I maximum and turn structure component band of MBP-C3 were the same at 15°C and 55°C (Table 2-22). The amide I band profile however, was more similar to that observed for MBP-C3 interacting with pure d-PC (section 2.3.6) since the α -helical component band observed in the amide I band profile of MBP-C3 upon interaction with the 1PG:3d-PC mixture (Table 2-21) was no longer present. Greater restriction to the conformational freedom of MBP-C3 may arise because the d-PC and PG content in the 1PG:1d-PC mixture is equivalent and MBP-C3 can interact at the surface with both lipids simultaneously. Interestingly, isoforms with an increased multivalency of negative charges in the C-terminal half of the sequence (MBP-C2, C3 and C5) appeared to experience some loss of secondary structure (Table 2-22). For example, while a predominantly β -sheet amide I was detected for MBP-C2, C3 and C5 in a 1PG:3d-PC environment at 55°C, a predominantly random coil (1644-1648 cm^{-1}) amide I can be seen in the 1PG:1d-PC environment (Table 2-22). In addition, splitting in the arginine side chains absorption of MBP-C2 and C3, was not detected and the absorption was at a low frequency (1584 cm^{-1}). A greater proportion of arginyl residues in MBP-C2 and C3 were then involved in electrostatic association or intramolecular salt-bridge formation and/or solvent exposed. Conversely, the amide I maximum of MBP-C1 still contained elements of ordered secondary structure (β -sheet, α -helix), suggesting that MBP-C1 still prefers interaction with PG even in the absence of PG microdomain formation (Table 2-22). In comparison to MBP-C2, C3 and C5, MBP-C1 has fewer negatively charged residues and thus may experience less charge repulsion from unsaturated negative SCD of the 1PG:1d-PC bilayer. Moreover, the arginyl side chain absorption of MBP-C1 was still split into low and high frequency component bands (1585 and 1592 cm^{-1}), suggesting that even in the absence of phase separation some arginyl residues can still be buried (Table 2-22).

Table 2-22. Amide I band profile of MBP isoforms in 1PG:1d-PC liposomal environment. Data extracted from second-derivative spectra at temperatures where both lipids were in the gel state (15°C) and when both lipids were in the L α state (55°C). The amide I maximum is marked with a single asterisk. Abbreviations used for the assignment of the amide I component bands: (rc), random coil; (rc, α), random coil and/or α -helix; (α), α -helix; (β), β -sheet; (t), turns. Double asterisk depicts the splitting of arginine side chain absorption(s).

Isoform	Amide I 15°C (cm⁻¹)	Amide I 55°C (cm⁻¹)	Arginine 15°C (cm⁻¹)	Arginine 55°C (cm⁻¹)
C1	1641* (rc) 1672 (t)	1643* (rc) 1632 (β) 1657 (α) 1674 (t)	1585 1604	1585** 1592**
C2	1644* (rc) 1673 (t)	1648* (rc, α) 1671 (t)	1586 1607	1584 1607
C3	1642* (rc) 1672 (t)	1644* (rc, α) 1670 (t)	1584 1607	1584 1607
C5	1645* (rc) 1657 (α) 1672 (t)	1647* (rc, α) 1672 (t)	1583 1605	1582 1603
C8	1643* (rc) 1671 (t)	1642* (rc) 1647 (rc, α) 1671 (t)	1584 1608	1587 1607

Finally, for MBP-C8 the increase in conformational flexibility suggests that MBP-C8 electrostatic interaction with PG in the 1PG:1d-PC mixture (Table 2-22) decreased in comparison to that observed for the MBP-C8/1PG:3d-PC mixture (Table 2-21). Rather than having an increase in the number of negatively charged residues, MBP-C8 has a reduction in the multivalency of positive charges due to citrullination. Therefore, MBP-C8 cannot saturate the negative SCD of the 1PG:1d-PC mixture to the same extent as the uncitrullinated isoforms. Greater charge repulsion between the PG head groups of opposing liposomal leaflets of the 1PG:1d-PC mixture, may account for the appearance of an additional amide I component band typical of random coil for MBP-C8. Alternatively, the 1647

cm⁻¹ component band observed in the amide I band profiles of MBP-C5 and C8 in the 1PG:1d-PC environment, may be some residual α -helical structure from that observed for these isoforms in the unsaturated PG environment (section 2.3.7). Recall, that it was proposed that an α -helix in the N-terminal halves of MBP-C5 and C8 perturbed the interfacial region of unsaturated PG bilayers (section 2.3.7). Perhaps even 50% d-PC in the binary liposomes (similar to 75% d-PC) can prevent some disruption of the PG acyl chains in the 1PG:1d-PC mixture by reducing α -helical formation. Less penetration of the mixed 1PG:1d-PC bilayer may account for why MBP-C5 and C8 stabilized the PG acyl chains of the 1PG:1d-PC mixture to a greater extent (section 2.3.4) than that observed for the unsaturated PG environment (section 2.3.3).

When the negative SCD of the binary liposomes was not saturated but PG was in excess of d-PC (*i.e.*, the 3PG:1d-PC mixture), the conformation of the isoforms appeared more sensitive to the influence of the predominant lipid, PG (Table 2-23). However, the small amount of d-PC in the mixture still had some influence on either isoform secondary structure or conformational flexibility since the liposomal negative SCD was decreased (1.0 mol% MBP to PG). First of all, while MBP-C1 was just as conformationally inflexible in the 3PG:1d-PC environment as it was in the pure PG environment (Table 2-20, section 2.3.7), MBP-C2 was more conformationally inflexible in the 3PG:1d-PC environment (Table 2-23). In addition, the amide I band profiles of MBP-C1 and C2 in this 3PG:1d-PC environment (Table 2-23) more closely resembled those in the 1PG:3d-PC environment (Table 2-21) than those in the unsaturated PG environment (Table 2-20). For example, the amide I maxima of MBP-C1 and C2 were shifted to lower frequency (more β -sheet in structure) than the amide I maxima in the unsaturated PG environment. Therefore, a slight increase in the saturation of the liposomal negative SCD by the positive charges on the protein (3PG:1d-PC, Table 2-23; 1.0 mol% MBP to PG), promoted further β -sheet formation in MBP-C1 and C2. This indicates that the charge shielding provided by the small amount of d-PC enhanced the binding interaction between MBP-C1 or C2 with the PG portion of the 3PG:1d-PC bilayer. Note however, only the arginine absorption profile of MBP-C1 changed in response to the small presence of d-PC in the bilayer (compare Tables 2-20 and 2-23). For example, in comparison to the splitting of the arginine side chain absorptions of MBP-C1 in a pure PG environment, most of the arginines in MBP-C1 are exposed to strong

dipoles in the 3PG:1d-PC mixture and thus appear only at the lower frequencies of 1583 and 1607 cm^{-1} .

Table 2-23. Amide I band profile of MBP isoforms in 3PG:1d-PC liposomal environment. Data extracted from second-derivative spectra at temperatures where both lipids were in the gel state (15°C) and when both lipids were in the $L\alpha$ state (55°C). The amide I maximum is marked with a single asterisk. Abbreviations used for the assignment of the amide I component bands: (rc), random coil; (rc, α), random coil and/or α -helix; (α), α -helix; (β), β -sheet; (t), turns. Double asterisk depicts the splitting of arginine side chain absorption(s).

Isoform	Amide I 15°C (cm^{-1})	Amide I 55°C (cm^{-1})	Arginine 15°C (cm^{-1})	Arginine 55°C (cm^{-1})
C1	1642* (rc) 1653 (α) 1671 (t)	1643* (rc) 1652 (α) 1672 (t)	1583 1605	1583 1607
C2	1637* (β) 1649 (α) 1669 (t)	1637* (β) 1650 (α) 1669 (t)	1587**	1580** 1593**
C3	1647* (rc, α) 1638 (β) 1665 (t) 1677 (t)	1648* (rc, α) 1665 (t)	1587 1608	1591**
C5	1642* (rc) 1671(t)	1644* (rc) 1655 (α) 1672 (t)	1584 1607	1581 1607
C8	1642* (rc) 1648 (rc, α) 1672 (t)	1645* (rc) 1672 (t)	1583 1606	1584 1607

In contrast, the more modified isoforms, MBP-C3, C5 and C8, were just as conformationally flexible in the 3PG:1d-PC environment (Table 2-23) as they were in the pure PG environment (Table 2-20, section 2.3.7). Therefore, a slight increase in the saturation of the liposomal negative SCD did not augment the interactions between the more modified isoforms and the mixed bilayer. The amide I maximum of MBP-C3 shifted to higher frequency (1648 cm^{-1}) in the 3PG:1d-PC mixture than in either the 1PG:3d-PC mixture (1641

cm^{-1}) or the unsaturated PG environment (1643 cm^{-1}), suggesting that random coil formation was promoted when 25% d-PC was present. Therefore, the introduction of more than one negative charge in the MBP sequence (MBP-C3), may have sensitized the isoform conformation to the negative charge repulsion between the opposing liposomal leaflets of the 3PG:1PG mixture. Unlike, MBP-C3 however, MBP-C5 can associate more effectively with the head groups of d-PC (section 2.3.2) and may tolerate the small amount of d-PC in the 3PG:1d-PC mixture. For example, the amide I maximum of MBP-C5 in the 1PG:3d-PC mixture (1642 cm^{-1}) shifted to higher frequency (1644 cm^{-1}) in the 3PG:1d-PC environment, suggesting a slight increase in random coil formation, but an α -helical component band (1655 cm^{-1}) also appeared (Table 2-23). Since MBP-C5 did not quite stabilize the PG acyl chains of the 3PG:1d-PC mixture to the same extent as the 1PG:1d-PC mixture (section 2.3.4), perhaps this α -helical feature is still the residual helix left in the N-terminal half of MBP-C5 that can partially perturb the bilayer interfacial region of the unsaturated PG liposomes (section 2.3.7). It was also proposed from the phase behavior results that the N-terminal half of MBP-C8 has a preference for d-PC interaction, but in contrast to MBP-C5, the C-terminal half of MBP-C8 can interact with both PG and d-PC (sections 2.3.4 and 2.3.7). The dramatic disappearance of the predominantly α -helical amide I observed for MBP-C8 in an unsaturated PG environment (section 2.3.7, Table 2-20) in the 3PG:1d-PC environment (Table 2-23) may reflect the sensitivity of this citrullinated isoform to preferential interaction with d-PC.

2.4 CONCLUSIONS

In summary, FTIR biospectroscopic investigation of MBP-lipid interactions and dynamics was successfully implemented to address the objectives of the study (section 2.1.5). The main objectives were to (i) establish the relative contribution of electrostatic to hydrophobic interactions in isoform-mediated adhesion of acidic bilayers and (ii) contrast the impact of MBP charge modification in paranodal and compact myelin adhesion. In order to simultaneously maintain a myelin-like ratio of total lipid to MBP (dry weight ratio of 5:1) and alter the MBP to acidic lipid concentration, liposomal negative SCD was reduced by the addition of a neutral lipid (d-PC) to the acidic lipid (PG). However, since it was unclear whether MBP could interact with neutral lipids, the interactions between the

isoforms and liposomes of zero SCD (*i.e.*, d-PC) was investigated prior to examination of the MBP/PG/d-PC samples.

The isoforms were found capable of interacting with liposomes of zero SCD, either favorably (stabilizing) or unfavorably (destabilizing) depending on the charge modification(s) to the MBP sequence (section 2.3.2). It was hypothesized that only the isoforms with decreased net-positive charge or electronically neutral segments could stabilize an electronically neutral bilayer surface. It was established that MBP-C3, C5 and C8 could indeed interact with the d-PC bilayer and provide stabilization to the d-PC bilayer primarily by surface association, whereas MBP-C1 and C2 destabilized d-PC by penetrating the interfacial and perhaps the hydrophobic region of the bilayer (section 2.3.2). However, the overall stabilization effect of the isoforms on the fluid d-PC bilayer decreased accordingly: MBP-C5 > MBP-C3 > MBP-C8 >> MBP-C1/C2, suggesting that decreased net-positive charge was not the only factor involved in MBP association with d-PC bilayer surface. Instead, MBP association with d-PC appeared to depend on the number and type of modified residues. Modifications that maximized intramolecular neutralization of positively charged residues within the MBP sequence (*i.e.*, phosphorylations) increased the number of electronically neutral segments that could interact with the neutral PC bilayer surface. Since MBP-C5 has four sites of phosphorylation (pSer7, pSer54, pThr97 and pSer164) it could interact with the PC surface to a greater extent than MBP-C3 (pThr97 and pSer164). Although neutral citrulline residues can interact with the neutral bilayer, citrullination also decreases the number of positive charges available to neutralize negatively charged residues within the sequence. Therefore, MBP-C8 interaction with the PC surface was slightly weaker than that of MBP-C3 and C5 because fewer positive charges were available to neutralize negatively charged residues in the protein sequence. Previous researchers have shown that unfractionated MBP could disrupt multilamellar bilayers of PC (Roux *et al.*, 1994). Since unfractionated MBP would be primarily composed of the most positively charged isoforms (Chou *et al.*, 1976; Wood and Moscarello, 1989) this observation was more reflective of the impact of MBP-C1 intercalating with the PC acyl chains and destabilizing the multilamellar PC bilayer. It has been reported MBP-C1, C2 and C3 and C8 are not capable of aggregating vesicles of pure PC (Wood and Moscarello, 1989). However, MBP-C8 can promote PC vesicle aggregation when the vesicles were reconstituted with proteolipid pro-

tein (PLP), a protein thought to be involved in protein-protein interactions with MBP-C8 at the intraperiod line of myelin (Wood and Moscarello, 1989). PLP cannot promote PC vesicle aggregation in the absence of MBP-C8, but it can aggregate negatively charged vesicles (Wood and Moscarello, 1989). It was rationalized that the only likely explanation for PLP aggregation of PC vesicles in the presence of MBP-C8 was that MBP-C8 and PLP were involved in hydrophobic interactions (Wood and Moscarello, 1989). However, vesicle aggregation is believed to proceed by MBP binding the vesicles, followed by protein-protein interaction to form vesicle aggregates (Wood and Moscarello, 1989). In the current study MBP-C8 interaction with PC is thought to be slightly weakened due to reduction of the number of positively charged residues that can neutralize negatively charged residues in the sequence. Perhaps MBP-C8/PC vesicle aggregation in the presence of PLP is mediated by charge association between the positively charged residues of PLP and the negatively charged residues of MBP-C8.

Since MBP interaction with d-PC was possible, the role of MBP net-positive charge in isoform-mediated adhesion of acidic bilayers with unsaturated negative SCD was initially studied using pure PG liposomes (sections 2.3.3 and 2.3.7). Previous investigators reported that the most positively charged isoforms stabilize the unsaturated negative SCD bilayer of PG by strong electrostatic association only (Choo, 1992; Jackson *et al.*, 1993). Therefore, it was hypothesized that the isoforms of greater net-positive charge (C1, C2 and C3) would be more effective at stabilizing the PG bilayer by electrostatic association, while isoforms of less net-positive charge (C5 and C8) would interact less at the surface and penetrate the bilayer. The cationic nature of the MBP was verified to play a substantial role in the stabilization of the PG bilayer since order of the PG acyl chains was greater when the more positively charged isoforms were present (section 2.3.3). However, from the interfacial hydration of the PG bilayer (section 2.3.3) and the conformational analysis of the isoforms in the presence of PG (section 2.3.7), electrostatic association and partial penetration of the bilayer interface most likely act together to maximize the binding of the most positively charged isoforms with PG. For example, the phase behavior of PG revealed that the relative contribution of isoform stabilization by electrostatic association to destabilization by bilayer penetration increased accordingly: MBP-C8 \ll MBP-C5 \ll MBP-C1 $<$ MBP-C2 \ll MBP-C3 (section 2.3.3). While MBP-C3 was found to interact primarily by electro-

static association to the bilayer surface, strong electrostatic association in combination with partial insertion of hydrophobic residues into the bilayer interface were proposed to maximize the binding between MBP-C1 and C2 and PG liposomes. This enhanced binding of MBP-C1 and C2 to PG was supported by: (i) random coil structure accompanied by ordered secondary structures (β -sheet and α -helix) upon isoform interaction with gel state PG and (ii) decreased conformational flexibility of MBP-C1, and to a lesser extent MBP-C2, once exposed to gel state PG (section 2.3.7). In contrast, MBP-C3, C5 and especially C8 upon interaction with gel state PG were not as conformationally restricted as MBP-C1 and ordered secondary structures did not appear until the bilayer fluidity increased (section 2.3.7). Therefore, rather than net-positive charge affecting MBP electrostatic association to PG, it was the impact of net-positive charge on the synergy between electrostatic association and partial penetration of the bilayer interface that affected MBP-mediated adhesion of PG. Such a synergy between MBP electrostatic association and partial penetration of an acidic bilayer is supported by presence of hydrophobic photolabels on MBP-C1 and C2 upon interaction with acidic vesicles (Boggs *et al.*, 1999a).

As for the role of MBP net-positive charge in the adhesion of PG bilayers of unsaturated negative SCD, charge modifications in the C-terminal half and N-terminal half of the sequence may affect MBP electrostatic association and bilayer penetration in different ways. First of all, increasing the multivalency of negatively charged residues in the C-terminal half of the sequence may decrease the synergy between electrostatic association and partial insertion of residues into the interfacial region required for maximal MBP-mediated adhesion of the PG liposomes. For example, MBP-C2 (Gln146) and MBP-C3 (pThr97 and pSer164) did not bind PG liposomes of unsaturated negative SCD as effectively as MBP-C1 (section 2.3.7). Since the only difference between MBP-C1, C2 and C3 is the number of negatively charged residues in the C-terminal half, the synergy between surface association and partial interfacial penetration required for maximal adhesion to PG must depend on the type and number of modified residues in the C-terminal half of the MBP sequence. It was proposed that charge repulsion between the excess negative SCD of the PG bilayer and extra negatively charged residues in the C-terminal half of the protein may have prevented the partial insertion of some residues in the C-terminal half into PG bilayer interface (section 2.3.3). Secondly, modifications that increase the multivalency of negative charges

in the N-terminal half of the protein may promote intramolecular charge neutralization within the N-terminal half of the protein, making it more suitable for insertion in the hydrophobic environment of bilayer. The extent of MBP penetration of acidic lipids has been reported to be greater for N-terminal half of the protein than for the C-terminal half of the protein (Boggs *et al.*, 1999a). Since the C-terminal half of unmodified MBP has a net charge of +12 (4 negatively charged residues) and the N-terminal half has a net charge of +8 (7 negatively charged residues), the N-terminal half of the protein may have increased propensity for intramolecular neutralization than the C-terminal half (section 2.1.4). The only isoform that had an increase in the number of negatively charged residues in the N-terminal half was MBP-C5. Similar to MBP-C3, pThr97 and pSer164 in the C-terminal half of MBP-C5 may decrease the synergy between surface association and partial interfacial penetration required for maximal PG adhesion. In contrast to MBP-C3, MBP-C5 penetration of the PG bilayer was more extensive, only partial stabilization of the PG acyl chains was detected and MBP-C5 possessed a greater contribution from α -helical structure once the fluidity of the bilayer was increased (sections 2.3.3 and 2.3.7). The enhanced penetration of the PG bilayer, perhaps by a α -helical segment of the protein, was thought to arise from the intramolecular neutralization of two positively charged residues by pSer7 and pSer54 in the N-terminal half of MBP-C5. Finally, modifications that decrease the multivalency of positive charges in the N-terminal half and/or the C-terminal half of MBP (*i.e.*, citrullination) were found to diminish the ability of the protein to mediated adhesion of PG bilayers with unsaturated negative SCD. In contrast to the uncitrullinated isoforms, the retained conformational flexibility of MBP-C8 in the presence of gel state PG suggested decreased electrostatic binding between MBP-C8 and PG, and the appearance of a predominantly α -helical structure suggested insertion of an α -helix once the PG bilayer became fluid (section 2.3.7). The little detectable change in the PG acyl chain order upon MBP-C8 interaction was the result of extensive bilayer penetration in combination with decreased electrostatic association (section 2.3.3). The reduced multivalency of positive charges in MBP-C8 (Cit25, Cit31, Cit122, Cit130, Cit159 and Cit170), especially in the C-terminal half, was concluded to have a three-fold effect on MBP-mediated adhesion of unsaturated PG bilayers: (i) fewer arginyl residues are available for electrostatic association between MBP and the phosphate moieties of PG, (ii) a greater number of hydrophobic residues are

available for MBP penetration of the bilayer, and (iii) increased repulsion between opposing leaflets of the PG liposomes may promote the shielding of negatively charged residues by unmodified positively charged residues, simultaneously reducing MBP electrostatic association and increasing MBP bilayer penetration (section 2.3.3). The reduced multivalency of positive charges available on MBP-C8 to bind to the phosphate moieties of PG and increased amphipathic character of MBP-C8, may have decreased electrostatic association of the C-terminal half of the protein to the PG bilayer surface and increased the propensity of N-terminal half penetration of the bilayer, respectively.

The other main objective of the present study was to contrast the impact of MBP charge modification on MBP-mediated adhesion of paranodal and compact myelin-like membranes. The high concentration of MBP to acidic lipid in compact myelin was modeled by raising the d-PC content in the binary PG/d-PC liposomes while maintaining the proper lipid-to-protein dry weight ratio. Although myelin is composed of a variety of lipids (Morell *et al.*, 1994), MBP mediated adhesion of PG liposomes of unsaturated negative SCD was the better paranodal myelin model for FTIR evaluation (see section 2.3.8). For example, in the absence of lipid phase separation, PG and d-PC competed for interaction with the MBP isoforms as revealed from the liposomal phase behavior (section 2.3.4) and the conformation of the isoforms (section 2.3.8). Therefore, it was difficult to distinguish between the effects of partial saturation of the liposomal net-negative SCD and competition between PG and d-PC for isoform interaction. In the absence of phase separation the general trends were: (i) isoforms that had a disfavorable (destabilizing) interaction with d-PC and a highly favorable (stabilizing effect) interaction with PG (*i.e.*, MBP-C1 and C2), exhibited a preference for interaction with PG in the binary liposomes, (ii) isoforms that had a favorable (stabilizing) interaction with d-PC and only a moderately favorable (little stabilization) interaction with PG (*i.e.*, MBP-C5 and C8), were found to interact with both lipids in the binary liposomes, and (iii) MBP-C3 was the only isoform that had a highly favorable interaction (stabilizing) with either pure lipid, yet MBP-C3 still exhibited a preference for interaction with PG in the binary liposomes. The preference of MBP-C1, C2 and C3 for interaction with PG in the binary liposomes suggested that d-PC was excluded from the protein interaction with the liposome. PG microdomain formation in the binary liposomes was suggested as one mechanism that could exclude d-PC from interacting with

MBP-C1, C2 and C3. However, enhanced stabilization of the PG portion of the binary liposomes was not achieved until the liposomal net-negative SCD was nearly saturated by the positive charges on MBP-C1, C2 and C3. Therefore, it was unlikely that phase separation in the binary liposomes was complete until a 3.1 mol% MBP to PG was used (*i.e.*, 1PG:3d-PC). Since both PG and d-PC could influence the interaction between MBP and the binary liposomes, contrasting the impact of MBP charge modification in paranodal and compact myelin adhesion was best evaluated when d-PC was absent (pure PG liposomes) or when lipid phase separation was complete (1PG:3d-PC liposomes), respectively.

The PG/PC binary liposomes with 3.1 mol% MBP to PG (1PG:3d-PC) were used to evaluate the interaction between MBP and an acidic bilayer with a net-negative SCD that is nearly saturated by the 31 positive charges on the unmodified protein (*i.e.*, compact myelin). It was hypothesized that saturation of the liposomal net-negative SCD by the positive charges on MBP would enhance the electrostatic association of the isoforms with the PG and possibly lead to the formation of PG microdomains in the binary liposomes (section 2.1.5). From the phase behavior of PG in the 1PG:3d-PC mixture, the relative contribution of PG stabilization by isoform electrostatic association to PG destabilization by intercalation with the PG acyl chains decreased accordingly: unmodified MBP-C1 >> C2/C3/C5 >> C8 (section 2.3.4). In comparison to that observed for MBP interaction with the unsaturated PG liposomes (section 2.3.3), saturation of the liposomal negative SCD enhanced the PG stabilization achieved by MBP-C1, C5 and C8. This enhanced stabilization of PG in the 1PG:3d-PC mixture may have been imparted by different mechanisms. For example, it was concluded that the strong electrostatic association of MBP-C1, C2 and C3 with acidic lipids induced the formation of PG microdomains when the net-negative SCD was saturated (1PG:3d-PC) as inferred by the lack of change in the d-PC acyl chain order. Strong binding to the PG microdomains was suggested by the reduced conformational flexibility of MBP-C1, C2 and C3 in response to saturating the liposomal negative SCD (section 2.3.8). MBP-C1 stabilization of the PG microdomains was nearly twice as great that achieved by MBP-C2 and C3 (*i.e.*, as revealed by the PG acyl chain order). Thus, saturation of the liposomal net-negative SCD by the positive charges available on MBP-C1 enhanced the electrostatic association between the C-terminal half of MBP-C1 and the PG microdomains. The increased multivalency of negative charges in the C-terminal half of MBP-C2 and C3, may

slightly reduce association to PG, but the synergy between association and partial bilayer penetration still promotes tight binding of MBP-C2 to the PG microdomains. In contrast, MBP-C5 and C8 did not induce PG microdomain formation and stabilized both lipids in the mixed bilayer (section 2.3.4). Since the extent of PG stabilization by MBP-C2 and C3 interaction with the 1PG:3d-PC liposomes was similar to that achieved using MBP-C5, the lack of PG microdomain formation by MBP-C5 was attributed to preferential association of the N-terminal half of the protein with d-PC. Strong association to both lipids simultaneously can account for the restricted conformational flexibility of MBP-C5 upon interaction with the gel state 1PG:3d-PC liposomes (section 2.3.8). The preferential interaction of the N-terminal half of MBP-C5 with d-PC was attributed to two phosphorylations in the N-terminal half, which may neutralize two positively charged residues, creating neutral fragments that can interact with the neutral d-PC head groups. In turn, neutral segments within the N-terminal half of MBP-C5 can associate with neutral d-PC (section 2.3.2), rather than penetrate the mixed bilayer and disrupt the PG acyl chain order. The decrease in α -helical structure for MBP-C5 in the 1PG:3d-PC environment suggests that d-PC interaction with the N-terminal half of MBP-C5 prevented α -helical formation and penetration into the mixed bilayer. Similar to MBP-C5, MBP-C8 was also conformationally restricted upon interaction with the 1PG:3d-PC liposomes (section 2.3.8). However, the extent of PG stabilization by MBP-C8 was nearly reduced by three-fold in comparison to the extent of PG stabilization by MBP-C5 because of the multivalency of positive charges available to saturate the net-negative SCD of the 1PG:3d-PC liposomes is reduced (Table 2-17, section 2.3.4). Interestingly, the extent of d-PC stabilization by MBP-C8 in the 1PG:3d-PC liposomes (section 2.3.4) was greater than that obtained for pure d-PC liposomes (section 2.3.2). Since the liposomal net-negative SCD is more unsaturated in the presence of MBP-C8, the negatively charged residues of MBP-C8 may be repelled by the residual negative SCD on the mixed bilayer. In turn, these negatively charged residues may seek out unmodified positively charged residues, producing neutral fragments in a similar fashion proposed for MBP-C8 interaction with the unsaturated PG liposomes. In the 1PG:3d-PC mixture however, these neutral fragments of MBP-C8 (and neutral citrulline residues) can interact with the neutral d-PC headgroups rather than penetrate the bilayer and disrupt the PG acyl chain order. Finally, interaction between the N-terminal half of MBP-C8 and d-PC may

have prevented the penetration of the mixed bilayer by an α -helical formation, as suggested by the disappearance of the predominantly α -helical structure detected for MBP-C8 interacting with PG liposomes (section 2.3.8).

The conformational restriction of MBP-C1 in both the unsaturated PG environment and the saturated 1PG:3d-PC environment supports that this unmodified protein is the most effective isoform for paranodal and compact myelin adhesion, respectively. However, the relative contribution of MBP-C1 electrostatic association to bilayer penetration in the adhesion was shown to be dependent on saturation of the liposomal negative SCD by the positive charges on MBP-C1. Boggs *et al.*, 1997 reported that less KCl is required to maximize the MBP-C1-mediated aggregation of PC/PS vesicles when the concentration of MBP to PS is high because the excess negative charge on the surface of the MBP-bound PC/PS vesicles is reduced. This charge shielding by KCl only addresses the contribution of electrostatic association to MBP-mediated adhesion of acidic bilayers. In the present study, the relative contribution of MBP-C1 electrostatic association to acidic bilayer penetration was found to be enhanced when the concentration of MBP-C1 to PG was high (3.1 mol% MBP to PG versus 0.8 mol% MBP to PG). Therefore, for MBP-C1-mediated adhesion of paranodal myelin, a synergy between MBP-C1 electrostatic association and partial penetration of the bilayer interface may be required to maximize binding when there is negative charge repulsion between opposing membrane leaflets. Conversely, for MBP-C1-mediated adhesion of compact myelin, saturation of the negative SCD on the membrane may promote the formation of acidic lipid microdomains and increase the relative contribution of electrostatic association to partial penetration of the bilayer interface. Finally, extensive neutralization of MBP-C1 net-positive charge by electrostatic association to acidic lipid head groups may allow the protein to adopt a more compact and ordered (increased β -sheet and α -helix) structure in compact internodal myelin (section 2.3.8). Fluctuations between a compact and less compact MBP tertiary structure may be the dynamic mechanism responsible for controlling the amount of cytoplasm in the paranodal loops of myelin during nerve impulse generation (see section 2.1.3).

Based on the results of the present study, MBP charge modification can have a greater impact on the adhesive properties of the protein in paranodal myelin than in com-

compact myelin. One or two charge modifications that increase the multivalency of negative charges in the C-terminal half of MBP (MBP-C2 and C3) may slightly reduce the synergy between electrostatic association and partial interfacial penetration required for paranodal myelin adhesion, while this synergy is unaffected in MBP-C2 and C3-mediated adhesion of compact myelin. For example, even though the relative amount of electrostatic association to bilayer penetration was lower for MBP-C2 and C3 upon interaction with the 1PG:3d-PC liposomes in comparison to MBP-C1, MBP-C2 and C3 were more conformationally restricted upon binding to a bilayer of saturated negative SCD than upon binding to a bilayer of unsaturated negative SCD. Amplification of the adverse effects of MBP charge modifications, such as deamidation and phosphorylation, on the adhesive properties of the protein in paranodal myelin is supported by the MBP-mediated PC/PS vesicle aggregation assays of Boggs *et al.*, 1997 (see section 2.1.3). For example, the extent of PC/PS vesicles aggregation in the presence of KCl was nearly the same for MBP-C1 and isoforms modified by deamidation or phosphorylation (C2, C3 and C5) when the MBP to PS concentration was high (Boggs *et al.*, 1997). However, at lower concentrations of MBP to PS, post-translational modifications on MBP-C2, C3 and C5, reduced the extent of electrostatic binding between these isoforms and the PS head groups of the binary vesicles and aggregation decreased with decreasing net-positive charge of the isoform (Boggs *et al.*, 1997). Boggs *et al.*, 1997, proposed that an upset balance amongst MBP-C1, C2, C3 and C5 would likely have less of an effect on myelin adhesion in compact internodal myelin than in paranodal myelin. The results of the present study also suggest a diminished effect of deamidation and phosphorylation on MBP-mediated adhesion of compact myelin-like membranes since MBP-C2, C3 and C5 were able to stabilize the PG portion of the 1PG:3d-PC liposomal mixture to the same extent. However, the mechanism of MBP-C5 binding to myelin-like membranes may be different than that of MBP-C2 and C3. For example, MBP-C2 and C3 were shown to associate to PG microdomains in the 1PG:3d-PC liposomal mixture, whereas MBP-C5 was shown to associate simultaneously with PG and d-PC regardless of the PG/d-PC composition. The impact of zwitterionic lipids on MBP-C5 mediated adhesion of paranodal or compact myelin cannot be overlooked since phosphorylations in the N-terminal half of MBP-C5 allows association to zwitterionic lipid head groups. Preferential association of the N-terminal half of MBP-C5 to d-PC most likely enhanced the relative

contribution of electrostatic association to bilayer penetration by decreasing the intercalation between MBP-C5 and PG. The conformational flexibility of MBP-C5 was markedly reduced upon binding to the 1PG:3d-PC mixture (*i.e.*, compact myelin) than upon binding to liposomes where the concentration of MBP-C5 to PG was lower (*i.e.*, paranodal myelin). Even though paranodal and compact myelin both contain zwitterionic lipids, saturation of the negative SCD of the membrane by the positive charges on MBP-C5 may still diminish the adverse effects of the multiple phosphorylations within MBP-C5 in compact myelin adhesion. Finally, reduction of the multivalency of positive charges in the MBP sequence (*i.e.*, via citrullination) has been reported to have a more adverse effect on the adhesion of acidic bilayers than a decrease in MBP net-positive charge by phosphorylation (Boggs *et al.*, 1997). Although, Boggs *et al.*, 1997, did not carry out MBP-C8-mediated aggregation of the PS/PC vesicles using 3.7 mol% MBP to PS, vesicle aggregation was markedly decreased (30-40%) for MBP-C8 in comparison to MBP-C5 when a lower concentration of MBP to PS was used. In the present study, MBP-C8 adhesion of acidic bilayers (1PG:3d-PC) using a 3.1 mol% MBP to PG concentration revealed that the stabilizing effect of MBP-C8 on the PG portion of the mixed bilayer was merely a third of that observed for MBP-C5. In contrast to the uncitrullinated isoforms, electrostatic association between MBP-C8 and acidic bilayers is most likely reduced because fewer positively charged residues are available to saturate the negative SCD of the bilayer (Boggs *et al.*, 1997). From the results of MBP-C8 interacting with pure PG liposomes of unsaturated negative SCD, citrullination simultaneously increases the intercalative behavior of MBP-C8. However, MBP-C8 was shown capable of associating with both lipids in the PG/d-PC liposomes, regardless of the PG/d-PC composition. Therefore, it was proposed that reduction of the number of positively charged residues (*i.e.*, by citrullination) in the C-terminal half and N-terminal half of MBP reduced association to PG and increased association to d-PC, respectively. Since the conformational flexibility of MBP-C8 decreased as the saturation of the net-negative SCD of the mixed bilayer increased, MBP-C8 adhesion of compact myelin may be more effective than paranodal myelin adhesion. The maintenance of a greater ratio of the uncitrullinated MBP isoforms to MBP-C8 may be more critical for electrostatic association of MBP to acidic phospholipids in paranodal myelin than for compact internodal myelin. However, the amphipathic character of MBP-C8 and the preference of this isoform

for interaction with zwitterionic lipid head groups, signifies that the delicate balance between the zwitterionic and acidic phospholipids in the myelin membrane also plays a part in MBP-C8-mediated adhesion of myelin. Furthermore, since MBP-C8 is believed to interact with PLP at the intraperiod line for adhesion of concentric layers of myelin under normal conditions (Wood and Moscarello, 1989; McLaurin *et al.*, 1993), spatial localization of MBP-C8 may be important to maintain the ultrastructure of CNS myelin. Perhaps, in the myelin of individuals afflicted with chronic and fulminating MS, the enhanced MBP-C8 to C1 ratio (Wood and Moscarello, 1989), reflects an error in the spatial distribution of the MBP-C8 to the major dense line of myelin, where PLP is not found and subsequently effective adhesion of opposing cytoplasmic leaflets of the membrane cannot occur.

There are a number of directions in which future areas of research could take to further the investigation of this current study using FTIR spectroscopy. It would be advantageous to investigate whether the negative impact of MBP citrullination in compact myelin adhesion could be minimized even further by greater saturation of the PG/d-PC liposomal negative SCD. For example, the 25 positive charges on MBP-C8 could potentially saturate the liposomal net-negative SCD of a 1PG:4d-PC liposomal mixture (4 mol% MBP-C8 to PG). In turn, MBP-C8 may be able to stabilize the PG portion of the 1PG:4d-PC bilayer to a greater extent than that achieved when MBP-C8 was exposed to the 1PG:3d-PC liposomal mixture. Whether MBP-C8 could stabilize the PG portion of the 1PG:4d-PC liposomal mixture to the same extent as the uncitrullinated isoforms remains to be seen. Such an experiment would provide another platform to contrast the impact of different types of MBP charge modifications on compact myelin adhesion. Alternatively, charge shielding of the PG/d-PC liposomal net-negative SCD could be achieved by the addition of KCl to the isoform/lipid mixtures. Finally, it would be of considerable interest to expand this current study using polarized FTIR-ATR spectroscopy to establish the orientation of the isoform amide carbonyls involved in different structures (α -helix, β -sheet) upon MBP interaction with single bilayers on a solid support. Polarized infrared radiation can be utilized to selectively enhance molecular absorptions in which the dipole moment of the vibration is oscillating parallel to the oscillating dipole of the incident radiation. For example, oriented films of single planar bilayers can be prepared by condensation of small unilamellar vesicles on an ATR crystal (Reinl and Bayerl, 1993; Nabet *et al.*, 1994). ATR spectra acquired on pro-

tein-bilayer samples using incident radiation polarized parallel and perpendicular to the normal of the ATR crystal yields the dichroic ratio which can then be used to calculate the angle from the crystal normal at which the vibration occurs (Nabet *et al.*, 1994). From the angle of the vibration from the ATR crystal normal, the orientation of the lipid acyl chains, acyl C=O and structural motifs defined by the amide I component bands to the ATR crystal normal can be determined (Nabet *et al.*, 1994). Such a study could be carried out as the temperature is ramped as was done in the current study, using each MBP charge isoform and the various model lipid systems.

2.5 REFERENCES

- Beniac, D.R., Luckevich, M.D, Czarnota, G.J., Tompkins, T.A., Ridsdale, R.A., Ottensmeyer, F.P., Moscarello, M.A., Harauz, G. (1997) Three-dimensional structure of myelin basic protein I. Reconstruction via angular reconstitution of randomly oriented single particles. *J. Biol. Chem.*, **272**(7): 4261-4268.
- Boggs, J.M, Moscarello, M.A. (1978) Effect of basic protein from human central nervous system myelin on lipid bilayer structure. *J. Membr. Biol.*, **39**: 75-96.
- Boggs, J.M., Rangaraj, G., Koshy, K.M. (1988) Photolabelling of myelin basic protein in lipid vesicles with the hydrophobic reagent 3-(trifluoromethyl)-3-(m-[125I]iodophenyl) diazirine. *Biochim. Biophys. Acta.*, **937**: 1-9.
- Boggs, J.M., Rangaraj, G., Koshy, K.M. (1999a) Analysis of membrane-interacting domains of myelin basic protein by hydrophobic photolabeling. *Biochim. Biophys. Acta.*, **1417**: 254-266.
- Boggs, J.M., Rangaraj, G., Koshy, K.M., Ackerley, C., Wood, D.D., Moscarello, M.A. (1999b) Highly deiminated isoform of myelin basic protein from multiple sclerosis brain causes fragmentation of lipid vesicles. *J. Neurosci Res.*, **57**(4): 529-535.
- Boggs, J.M, Wood, D.D., Moscarello, M.A. (1981) Hydrophobic and electrostatic interactions of myelin basic proteins with lipid. Participation of the N-terminal and C-terminal portions. *Biochemistry*, **20**:1065-1073.
- Boggs, J.M., Yip, P.M, Rangaraj, G., Jo, E. (1997) Effect of postranslational modifications to myelin basic protein on its ability to aggregate acidic lipid vesicles, *Biochemistry*, **36**: 5065-5061.
- Boulias, C., Pang, H., Mastronardi, F., Moscarello, M.A. (1995) The isolation and characterization of four myelin basic proteins from the unbound fraction during CM52 chromatography. *Arch. Biochem. Biophys.*, **322**: 174-182.

- Brandon, C., Tooze, J. (1999) Introduction to Protein Structure, second edition, Garland Publishing Inc, New York, NY, USA, pp. 35 and 223.
- Bromberg, P.S., Gough, K.M, Jackson, M.J. (1997) FT-IR study of protein-lipid interactions: the surface binding and intercalating properties of myelin basic protein isoforms and their relation to multiple sclerosis, Abstract and poster presentation, *80th CSC Conference and Exhibition*, June 1-4, Windsor, Ontario, Canada.
- Bromberg, P.S., Gough, K.M, Moscarello, M.A. (1999) The influence of liposomal surface charge density on the interactions of various charge isoforms of myelin basic protein with model lipid systems as assessed by FT-IR spectroscopy. Abstract and oral presentation, *82nd CSC Conference and Exhibition*, June 1-4, Toronto, Ontario, Canada
- Cameron, D.G., Moffatt, D.J. (1984) Deconvolution, derivation and smoothing of spectra using Fourier transforms, *JTEVA*, 12(2): 78-85.
- Casal, H.L., Mantsch, H.H. (1984) Polymorphic phase behavior of phospholipid membranes studied by infrared spectroscopy. *Biochim. Biophys. Acta.*, 779:381-401.
- Cheifetz, S., Moscarello, M.A. (1985) Effect of bovine basic protein charge microheterogeneity on protein-induced aggregation of unilamellar vesicles containing a mixture of acidic and neutral phospholipids. *Biochemistry*, 24:1909-1914.
- Chirgadze, Y.N., Federov, O.V., Trushina, N.P. (1975) Estimation of amino acid residue side-chain absorption in the infrared spectra of protein solutions in heavy water. *Biopolymers*, 14: 679-694.
- Choo, L.-P. (1992) An investigation of the components of myelin basic protein in solution and in dimyristoylglycerol bilayers at 10°C and 30°C using Fourier transform infrared spectroscopy. Fourth year thesis. Hospital for Sick Children, Toronto, Ontario, Canada
- Chou, F.C.-H., Chou, J.C.-H, Shapira, R., Kibler, R.F. (1976) Basis of microheterogeneity of myelin basic protein. *J. Biol. Chem.*, 251:2671-2679.
- CRC Handbook of Lipid Bilayers (1990), Derek Marsh (editor), CRC Press Inc., USA, pp.136 and 153.
- Deber, C.M., Hughes, D.W., Fraser, P.E., Pawagi, A.B., Moscarello, M.A. (1986) Binding of human normal and multiple sclerosis-derived myelin basic protein to phospholipid vesicles: effects on membrane head group and bilayer regions. *Arch. Biochem. Biophys.*, 245:455-463.

- Deibler, G.E., Martenson, R.E., Kramer, A.J., Kies, M.W., Miyamoto, E. (1975) The contribution of phosphorylation and loss of carboxy terminal arginine to the microheterogeneity of myelin basic protein. *J. Biol. Chem.*, **250**:7931-7938.
- Dluhy, R.A., Mendelsohn, R., Casal, H.L., Mantsch, H.H. (1983) Interaction of dipalmitoylphosphatidylcholine and dimyristoylphosphatidylcholine-d54 mixtures with glycophorin. A Fourier transform infrared investigation. *Biochemistry*, **22**:1170-1177.
- Elliot, A., Ambrose, E.J. (1950) Structure of synthetic polypeptides. *Nature*, **165**: 921-922.
- Gilmanshin, R., Williams, S., Callender, R.H., Woodruff, W.H., Dyer, R.B. (1997) Fast events in protein folding: relaxation dynamics of secondary and tertiary structure in native apomyoglobin. *Proc. Natl. Acad. Sci. USA*, **94**: 3709-3713.
- Haris, P.I., Chapman, D. (1995) The conformational analysis of peptides using Fourier transform IR spectroscopy, *Biopolymers*, **37**: 251-263.
- Hille, B., Catterall, W.A. (1994) "Electrical excitability and ion channels", in Basic Neurochemistry, 5th edition, G.J. Siegel, B.W. Agranoff, R.W. Albers and P.B. Molinoff (editors). Raven Press, New York, pp.75-95.
- Jackson, M., L.-P. Choo, Boulias, C., Moscarello, M.A., Mantsch, H.H. (1993) Interaction of myelin basic protein isoforms with lipid bilayers studied by FTIR spectroscopy. *SPIE Biomol. Spec. III*, **1890**:9-12.
- Jackson, M., Haris, P.I., Chapman, D. (1989) Conformational transitions in poly(L-lysine): studies using Fourier transform infrared spectroscopy. *Biochim. Biophys. Acta.*, **998**: 75-79.
- Jackson, M.J., Mantsch, H.H. (1995) The use and misuse of FT-IR spectroscopy in the determination of protein structure. *Crit. Rev. Biochem. Mol. Biol.*, **30**:95-120.
- Jo, E., Boggs, JM (1995) Aggregation of acidic lipid vesicles by myelin basic protein: dependence on potassium ion concentration. *Biochemistry*, **34**: 13705-13716.
- Lambert, J.B. Shurvell, H.F., Lightner, D., Cooks, R.G. (1987). Introduction to Organic Spectroscopy, Macmillan Publishing Company, NY, pp.164-166.
- Lasch, P., Schultz, C.P., Naumann, D. (1998) The influence of poly-(L-lysine) and porin on the domain structure of mixed vesicles composed of lipopolysaccharide and phospholipid: an infrared spectroscopic study. *Biophysical Journal*, **75**: 840-852.
- Lowden, J.A., Moscarello, M.A., Morecki, R. (1966) The isolation and characterization of an acid-soluble protein from myelin. *Can. J. Biochem.*, **44**:567-577.

- Mendelsohn, R., Mantsch, H.H. (1986) "Fourier transform infrared studies of lipid-protein interaction", in *Progress in Protein-Lipid Interactions*, A. Watts and J.J.H.H.M. DePont (editors), Elsevier, Amsterdam, New York, Oxford, **2**:103-146.
- Mantsch, H.H., McElhaney, R.N. (1991) Phospholipid phase transitions in model and biological membranes as studied by infrared spectroscopy. *Chem. Phys. Lipids*, **57**:213-226.
- Martenson R.E., Deibler, G.E., Kies, M.W. (1969) Microheterogeneity of guinea pig myelin basic protein. *J. Biol. Chem.*, **244**:4261-4267.
- Martenson R.E., Deibler, G.E., Kies, M.W. (1983) Identification of multiple in vivo phosphorylation sites in rabbit myelin basic protein. *J. Biol. Chem.*, **258**:930-937.
- McLaurin, J., Ackerley, C.A., Moscarello, M.A. (1993) Localization of basic proteins in human myelin. *J. Neurosci. Res.*, **35**:618-628.
- Morell, P., Quarles, R.H., Norton, W.T. (1994) "Myelin formation, structure and biochemistry", in *Basic Neurochemistry*, 5th edition, G.J. Siegel, B.W. Agranoff, R.W. Albers and P.B. Molinoff (editors). Raven Press, New York, pp.117-143.
- Moscarello, M.A. (1990) "Myelin basic protein: a dynamically changing structure", in *Dynamic Interactions of Myelin Proteins*. Alan R. Liss, Inc., Toronto, pp. 25-48.
- Moscarello, M.A., Brady, G.W., Fein, D.B., Wood, D.D., Cruz, T.F. (1986) The role of Charge microheterogeneity of basic protein in the formation and maintenance of the multilayered structure of myelin. *J. Neurosci. Res.*, **15**: 87-99.
- Moscarello, M.A., Wood, D.D., Ackerley, C., Boulias, C. (1994) Myelin in multiple sclerosis is developmentally immature. *J. Clin. Invest.*, **94**:146-154.
- Nabet, A., Boggs, J.M., Pezolet, M. (1994) Study by infrared spectroscopy of the interaction of bovine myelin basic protein with phosphatidic acid. *Biochemistry*, **33**:14792-14799.
- Papahadjopoulos, D., Moscarello, M.A., Eylar, E.H., Isac, T. (1975) Effects of proteins on thermotropic phase transitions of phospholipid membranes. *Biochim. Biophys. Acta*, **401**: 317-335.
- Peterson, N.O., Kroon, P.A., Kainosho, M., Chan, S.I. (1975) Thermal phase transitions in deuterated lecithin bilayers. *Chem. Phys. Lipids*, **14**:343-349.
- Pritzker, L.B., Joshi, S., Gowan, J., Harauz, G., Moscarello, M.A. (2000) Deimination of myelin basic protein 1. Effect of deimination of arginyl residues of myelin basic protein on its structure and susceptibility to digestion by cathepsin D. *Biochemistry*, **39**: 5374-5381.

- Ramwani, J.J., Epand, R.M., Moscarello, M.A. (1989) Secondary structure changes of charge isomers of myelin basic protein before and after phosphorylation. *Biochemistry*, **28**: 6538-6543.
- Reinl, H.M., Bayerl, T.M. (1993) Interaction of myelin basic protein with single bilayers on solid support: an NMR, DSC and polarized infrared ATR study. *Biochim. Biophys. Acta*, **1151**:127-136.
- Ridsdale, R.A., Beniac, D.R., Tompkins, T.A., Moscarello, M.A., Harauz, G. (1997) Three dimensional structure of myelin basic protein II. Molecular modeling and considerations of predicted structures in multiple sclerosis. *J. Biol. Chem.*, **272**(7): 4269-4275.
- Roux, M., Nezil, F.A., Monck, M., Bloom, M. (1994) Fragmentation of phospholipid bilayers by myelin basic protein. *Biochemistry*, **33**:307-311.
- Troullier, A., Reinstadler, D. Dupont, Y., Naumann, D. Forge, V. (2000) Transient non-native secondary structures during the refolding of α -lactalbumin detected by infrared spectroscopy, *Nat. Struc. Biol.*, **7**(1): 78-86.
- Wood, D.D., Moscarello, M.A. (1989) The isolation, characterization and lipid aggregating properties of a citrulline-containing myelin basic protein. *J. Biol. Chem.*, **264**:5121-5127.
- Wood, D.D., Bilbao, J.M., O'Connors, P., Moscarello, M.A. (1996) Acute multiple sclerosis (Marburg Type) is associated with developmentally immature myelin basic protein. *Ann. Neurol.*, **40**:18-24.
- Zand, R. Li, M.X., Jin, X., Lubman, D. (1998) Determination of the sites of posttranslational modifications in the charge isomers of bovine myelin basic protein by capillary electrophoresis-mass spectrometry, *Biochemistry*, **37**: 2441-2449.

3

COLLAGEN REMODELING IN THE CARDIAC EXTRACELLULAR MATRIX OF THE CARDIOMYOPATHIC SYRIAN HAMSTER AS ASSESSED BY ATR-FTIR¹

3.1 INTRODUCTION

3.1.1 Chapter Overview

The present study exemplifies the use of FTIR spectroscopic examination of bulk tissue samples in the differentiation of diseased from normal tissue. In comparison to the *in vitro* biophysical study presented in Chapter 2, FTIR spectroscopic analysis of tissues is in general for biodiagnostic purposes since the actual tissue composition is unknown (see Chapter 1, section 1.5). The spectral differences between normal and diseased tissue are frequently subtle and can vary from sample to sample within a tissue and between specimens due to tissue microheterogeneity and heterogeneity within a group, respectively. Therefore, the numerous spectra that are collected in studies of this type are frequently subjected to isolate true discriminatory patterns that may otherwise be difficult or impossible to identify and validate. Information regarding the specific biochemical change(s) that give rise to spectral difference(s) between normal and diseased tissue must be obtained by traditional spectral interpretation. The first decision in a FTIR biodiagnostic study usually involves the selection of an appropriate disease where tissue biochemistry is believed to change from the normal state and some chemical information about the pathophysiology is already known. Since collagen deposition in the cardiac extracellular matrix (ECM) is believed to contribute significantly to myocardial dysfunction (Schlant and Alexander, 1994) and collagen has a well characterized mid-IR fingerprint (Jackson *et al.*, 1995; Liu *et al.*, 1996; Liu *et al.*, 1999), the decision was made to carry out FTIR spectroscopic analysis of heart tissue to characterize the condition of cardiomyopathy (CMP).

1. The majority of this study was presented at a conference (Bromberg *et al.*, 1998) and was published the following year: Bromberg, P.S., Gough, K.M., Dixon, I.M.C. (1999) Collagen remodeling in the extracellular matrix of the cardiomyopathic Syrian hamster heart as assessed by FTIR attenuated total reflectance spectroscopy. *Can J. Chem.*, **77**: 1843-1855.

The ventricular tissue used in the present study was extracted from the hearts of a well-known hamster model in which CMP develops spontaneously and is well established by 200 days of age. As a result of CMP, this hamster model exhibits increased collagen type I and III in the extracellular matrix (ECM) of the left ventricle (section 3.1.4). Collagen has a well-characterized pattern of absorption bands between 1000-1400 cm^{-1} (*i.e.*, 1032, 1082, 1202, 1240, 1283, 1315 and 1338 cm^{-1}) referred to as the collagen mid-IR fingerprint or signature (section 3.1.3). It should in principle be possible to exploit this spectral fingerprint of collagen to visually distinguish between spectra of the CMP and control (CON) hamster heart tissue. However, due to tissue heterogeneity and within-group variance, linear discriminant analysis (LDA) was employed to validate that the spectra acquired for CMP and CON tissues were different and to calculate the reproducibility of this difference for spectra collected on various individual tissue specimens (*i.e.*, the percent separation between classes). For LDA classification to be meaningful, the number of data points/spectrum must be substantially lower than the number of spectra in the smallest class under investigation, thus a data reduction methodology is required. The mid-IR data points were reduced by two methods: optimal spectral subregions for LDA discrimination were chosen either subjectively by manually choosing visually distinct features in the class average spectra (“user-selected” data reduction) or non-subjectively by a genetic algorithm (GA) (section 1.4.6). It was hypothesized that (*i*) non-subjective discrimination of CMP from CON heart tissue could be achieved using GA-LDA multivariate classification of the attenuated total reflectance (ATR)-FTIR spectral data and that (*ii*) the GA would preferentially select spectral subregions encompassing collagen absorptions. Difference spectra of the class average spectra (representing the bulk tissue) would be required to substantiate which tissue type under comparison possessed a higher collagen content. Classification trials complementing those produced by the GA-LDA would be obtained by subjecting “user-selected” spectral subregions of the tissue spectra to the same LDA algorithm. The final result in either approach was successful discrimination between the right and left ventricles of each heart type (CON and CMP) as well as discrimination between diseased and control ventricles (right and left, compared separately). The study confirmed that the CMP animals experienced LV collagen remodeling in the cardiac ECM, characterized by focal rather than diffuse fibrosis. More surprisingly, RV collagen remodeling (characterized by a

decreased RV collagen content) appeared to accompany the increased LV collagen deposition in the CMP animals.

3.1.2 Congestive cardiomyopathy

Cardiomyopathy, a disease of the heart myocardium, has an ill-defined etiology and a clinical treatment strategy has yet to be clearly defined. Several cardiomyopathies are inheritable or induced by alcohol toxicity, malnutrition or viral infection, however idiopathic congestive cardiomyopathy (CCM), classified as either hypertrophic or dilated cardiomyopathy, is of unknown etiology in humans (Schlant and Alexander, 1994). The incidence of CCM has been reported to be 5-8 cases/100000 population annually with a 5-year mortality of nearly half of those afflicted (Braunwald, 1997). CCM is typically clinically diagnosed by the presence of dilation and systolic dysfunction in the left ventricle when congenital, coronary, valvular, hypertensive or pericardial heart disease is not a predisposing factor (Schlant and Alexander, 1994). Essentially, CCM leads to left ventricle dysfunction and decreases the heart's efficiency to eject oxygenated blood into the arterial circulation, causing progressive accumulation of fluid in the lungs (congestion) and subsequent congestive heart failure. Histopathologically, CCM reveals myocyte hypertrophy and atrophy, myofilament loss, lymphocyte infiltration, intracellular changes such as large irregularly shaped nuclei and lipid droplet deposition as well as diffuse and focal fibrosis (Schlant and Alexander, 1994). The fibrotic event involves the increased deposition of the fibrillar collagens (types I and III), the predominant proteins in the interstitial space, resulting in abnormal accumulation of extracellular matrix (ECM) and thus myocardial hypertrophy (Liu *et al.*, 1999). Remodeling of the major components of the ECM, such as collagen, is believed to play a pivotal role in myocardial dysfunction, such that the change in the collagen content of a ventricle may compromise the stiffness, contractility and electrical properties of the heart muscle (Pelouch *et al.*, 1994a).

3.1.3 The mid-IR fingerprint of fibrous collagens

When one takes the traditional histological findings into account, a mid-infrared spectrum of CCM heart tissue may in turn show appreciable alterations in protein, carbohydrate, lipid and nucleic acid content and/or structure when compared to that of normal heart tissue (see Chapter 1). Recently, the absorption band assignment of collagen type I in

the mid-IR spectra of human breast tissue (Jackson *et al.*, 1995) and infarcted rat heart tissue (Liu *et al.*, 1996) have been documented. The latter investigators demonstrated that differences in the spectra of infarcted rat left ventricle, in comparison to those of control rats, were attributable to an increased deposition of collagen type I in the cardiac ECM as well to subtle differences in the lipid and nucleic acid content of the respective tissues (Liu *et al.*, 1996). Characteristic IR absorption bands between 1000-1400 cm^{-1} were assigned to the C-O stretching vibrations of the carbohydrate residues attached to collagen (1032 and 1082 cm^{-1}) and the amide III and CH_2 wagging vibrations of collagen (1202, 1240, 1283, 1315 and 1338 cm^{-1}) (Liu *et al.*, 1996). It has also been established that the amide I band profile (1610-1690 cm^{-1}) of collagen type I triple helix is distinct and can be characterized by predominant absorptions near 1662 cm^{-1} and 1628 cm^{-1} , where absorptions from the 3_1 helices and intermolecular hydrogen bonding interactions of collagen chains, respectively, are thought to occur (Jackson *et al.*, 1995; Liu *et al.*, 1996). Normal cardiac tissue can therefore be differentiated from diseased cardiac tissue with elevated collagen deposition simply by the simultaneous evaluation of the deviation of the amide band profile from a maximum near 1655 cm^{-1} , due to predominant contributions from α -helical proteins, to that expected for the collagen triple helix and inspection of the 1000-1400 cm^{-1} region of the spectrum.

3.1.4 The cardiomyopathic hamster

In the present study, ATR-FTIR spectroscopy (see Chapter 1) was utilized to monitor collagen-related changes/pathology in the cardiac extracellular matrix of a strain of cardiomyopathic hamsters (UM-X7.1 line). Substantial documentation is available denoting the predictable pathological course of progressive cardiomyopathy in the UM-X7.1 CMP hamster, such as dilation, left ventricle hypertrophy, left ventricle collagen deposition and congestive heart failure (Gertz, 1972; Jasmin and Proschek, 1982; Davison *et al.*, 1994; Dixon *et al.*, 1997). The UM-X7.1 hamster line has been shown to develop CMP in four definitive stages: cardiomyolysis resulting in myocyte necrosis (30-60 days), healing and fibrosis within sites of myocyte necrosis (60-90 days), left ventricle hypertrophy and dilation (90-150 days) and progression of dilation leading to CHF (Jasmin and Proschek, 1982; Dixon *et al.*, 1997). For our study, we examined the myocardial tissue of animals euthen-

ized by cervical dislocation at 200 days as this would enable analysis of the accumulated replacement fibrosis in the ECM associated with CHF.

3.1.5 Global data analysis

To facilitate objective classification of the cardiac tissue as cardiomyopathic (CMP) or as normal (CON) the spectra were subjected to multivariate analysis using a linear discriminant algorithm (Jackson and Mantsch, 1996; McLachlan, 1992). LDA is a multivariate statistical analysis which takes into account within-group and between-group variance to discriminate between assigned classes, resulting in an overall (%) separation of classes (see Chapter 1). Moreover, two methods were used to discriminate the most spectroscopically diagnostic subregions, namely GA-selected subregions and “user-selected” subregions for non-subjective and subjective classification, respectively. Selection of spectral subregions by a genetic algorithm has already been described in Chapter 1 (section 1.4.6). Manual selection of spectral subregions (“user-selected”) involved truncation of the subregions desired and “splicing” the chosen subregions together much in the same way nature removes the introns upon during transcription. Either method for data reduction (GA or manual “splicing”) provided the spectral subregions that would yield the highest linear discriminant analysis (LDA) separation between left and right ventricular tissue and between CMP and CON tissue. Subsequently, the spectral subregions chosen could be evaluated in terms of collagen remodeling in this animal model.

3.1.6 Objectives of the current study

FTIR spectroscopic analysis of CMP and CON hamster heart tissue, coupled to LDA multivariate analysis, was to be used to differentiate between CMP and CON tissue. First it was hypothesized that non-subjective classification of CMP from CON heart tissue could be obtained using GA-LDA multivariate analysis of the FTIR spectral data and the GA would preferentially selected spectral subregions where absorptions due to collagen are more prevalent in one of the tissue types under comparison. However, the difference spectra of the class average spectra of each tissue type under comparison would be required to substantiate which tissue type had a more pronounced mid-IR collagen signature. Verification of the GA-LDA results were to be obtained by LDA of “user-selected” spectral subregions of the tissue spectra. The optimal spectral regions for manual selection were to be

based on the difference spectra between the groups under comparison, the spectral subregions selected by the GA and the known regions in the mid-IR where collagen is expected to absorb. Although this hamster paradigm of human congestive cardiomyopathy was only expected to reveal more pronounced collagen deposition in the left ventricle, spectra acquired of the CMP and CON right ventricles were also compared to investigate the possibility of RV collagen remodeling. Finally, spectra collected of the right and left ventricles of each heart type (CON and CMP) were also compared in the global data analysis to gain information on the ventricular distribution of collagen in the normal and CMP heart.

3.2 EXPERIMENTAL

3.2.1 Materials

The UM-X7.1 strain of Syrian hamsters, supplied by the laboratory of Dr. Ian Dixon (Division of Cardiovascular Science, St. Boniface General Hospital and Research Centre, Winnipeg, Manitoba, Canada), was used in this study as a paradigm of human congestive cardiomyopathy. The excised hearts of male hamsters (Controls: 4 animals, 200 days old; Cardiomyopathic: 4 animals, 200 days old) were stored on dry ice prior to dissection. The left and right ventricular tissue were cut free of atria and spectra were collected from left and right ventricles (LV and RV, respectively) of cardiomyopathic (CMP, $N_{LV} = 30$, $N_{RV} = 27$ spectra) and control (CON, $N_{LV} = 20$, $N_{RV} = 15$ spectra) hearts.

3.2.2 FTIR-ATR spectroscopy and spectral preprocessing

Mid-IR spectra ($1000\text{-}4000\text{ cm}^{-1}$) were acquired from randomly sampled tissue (sample size *ca.*, $2 \times 2 \times 2\text{ mm}^3$) using a Bio-Rad FTS-40A infrared spectrometer equipped with a 'Split Pea' single reflection ATR accessory (Harrick Scientific). For each sample 256 interferograms were acquired, signal-averaged and Fourier transformed to generate spectra with a nominal resolution of 2 cm^{-1} . Spectra were then truncated between $1000\text{-}1800\text{ cm}^{-1}$ and the area under the curve was normalized to an arbitrary numerical value of 10 to compensate for inconsistencies in the ATR sampling method (section 1.2.3). Although the anvil of the ATR accessory was lowered onto each tissue sample to a numerical value of 2.0 tonnes, spectra were normalized as an extra precaution to compensate for pressure inconsistencies during tissue sampling. Second derivative spectra of the normalized raw data were then calculated prior to their use in multivariate analysis (LDA).

3.2.3 Data analysis

In the preliminary analysis, class average spectra were calculated as the arithmetic mean of all spectra in each of the following designated classes: LV(CON), LV(CMP), RV(CON) and RV(CMP). Difference spectra² between ventricles of the same tissue class (CON or CMP) and between tissue classes of the same ventricle (LV or RV) were calculated to ascertain the most diagnostic regions of the mid-IR. The difference spectra were utilized initially as a guide to user-selection of diagnostic subregions for multivariate analysis. It was established that the 1000-1800 cm^{-1} region, particularly subregions within this range, illustrated the most prominent differences between the class average spectra. In the final analysis, the difference spectra were utilized to substantiate which class under comparison exhibited greater collagen deposition since multivariate analysis (discussed below) only verified whether the assigned classes were significantly different in the spectral subregions selected. It should be noted, not all peaks were assigned or discussed in the difference spectra and quantitative analysis was avoided because ATR spectral distortions can be amplified in a difference spectrum calculation. Recall that ATR can lead to spectral distortions at longer wavelengths due to the greater penetration depth of longer wavelengths into the tissue (section 1.2.3). Therefore, the difference spectra were used only to determine the tissue group that had a more pronounced collagen fingerprint. Although the fingerprint region (1800-1000 cm^{-1}) was chosen to discriminate between the tissue classes, the LDA algorithm used in the multivariate analysis had one limitation for successful class separation: the number of attributes (data points in each spectrum) had to be less than or equal to the number of observations (number of spectra). Since the number of data points in the mid-IR fingerprint region (800 data points) exceeded the total number of spectra to be classified in each application of the LDA program, further data reduction methodologies were investigated to prepare the normalized, second derivatives of the raw spectra for LDA.

2. A minus kB where k is a constant chosen so that the baseline is flat and near zero

3.2.4 Data reduction and LDA

Two data reduction methodologies were used: the use of a genetic algorithm and manual splicing of the derivative spectra. Data reduction was necessary due to the restriction of the LDA program, which required that the number of attributes (data points) be less than the number of spectra under comparison. In the first approach, the normalized, second-order derivative spectra were subjected to a genetic algorithm (Bangalore *et al.*, 1996; Nikulin *et al.*, 1998) to determine spectral subregions that were most diagnostic as inputs for LDA. Genetic algorithm (GA)-selected subregions for LDA served in the nonsubjective classification of the cardiac tissue in the following two-class problems:

LV(CON) vs. RV(CON)

LV(CMP) vs. RV(CMP)

RV(CMP) vs. RV(CON)

LV(CMP) vs. LV(CON)

The GA was programmed to choose fewer than ten spectral subregions within 50 iterations of the program until the LDA separation between the chosen classes was optimized. For each spectral subregion chosen by the GA, the program automatically averaged the data points to one value (attribute) prior to being fed into the LDA algorithm.³ By averaging the data points in one spectral subregion to one attribute, the GA was able to incorporate the majority of the mid-IR fingerprint region in the LDA analysis. However, it was unknown whether the shape of absorption band(s) within each GA-selected subregion could be retained by a single data point representing the spectral subregion.⁴ Therefore, manual "splicing" of the second derivative spectra, by "user-selection" of subregions in the absence of data averaging, was performed in a separate LDA classification strategy to verify the GA-LDA classification. In the manual "splicing" data reduction approach, spectral subregions within the 1000-1800 cm^{-1} fingerprint region were manually chosen based on the difference spectra between the groups under comparison (Figures 3-1, 3-2, 3-3 and

3. The GA and LDA programs were both developed "in house" by the Informatics Division of the Institute for Biomedicine (IBD), National Research Council of Canada (NRCC) in Winnipeg, Manitoba.

4. The GA (Nikulin *et al.*, 1998) had not been tested on IR derivative spectra prior to the current application.

3-5), the spectral subregions selected by the GA, and the known regions in the mid-IR where collagen is expected to absorb. Once the subregions were chosen, the corresponding subregions in the second derivative spectra were truncated and “spliced” using a program called “XPREP” (provided by the IBD). Subsequently these “spliced” spectra were used as input for the LDA to discriminate between the four two-class problems defined previously. Various combinations of spectral subregions were chosen and “spliced” until the LDA separation was optimized (>85%). That is, in this manual “splicing” data reduction approach, the user mimics a genetic algorithm, albeit with less objectivity. An advantage of the manual “splicing” data reduction approach is the absence of averaging the data points within one spectral region to one data point. However, aside from the subjectivity involved in “user-selection” of diagnostically relevant spectral subregions, a greater amount of spectral data is lost by the manual “splicing” data reduction than by the GA data reduction.

3.3 RESULTS AND DISCUSSION

3.3.1 Class average spectra, difference spectra and LDA

The class average spectra for LV(CON), RV(CON), LV(CMP) and RV(CMP), along with the relevant difference spectra, can be found under the results and discussion pertaining to each two-class comparison: RV(CON) minus LV(CON) (Figure 3-1, section 3.3.2); LV(CMP) minus RV(CMP) (Figure 3-2, section 3.3.3); RV(CON) minus RV(CMP) (Figure 3-3, section 3.3.4); LV(CMP) minus LV(CON) (Figure 3-5, section 3.3.5). In general, visual inspection of the 1000-1800 cm^{-1} portion of the class average spectra revealed subtle differences in several spectral subregions, mainly those concerning absorptions due to collagen, carbohydrate and lipid. Although differences were evident in the amide I (*ca.*, 1650 cm^{-1}) and amide II (*ca.*, 1545 cm^{-1}) band profiles of the groups under comparison, these spectral subregions exhibited a high within-group standard deviation especially in the LV(CMP) group (data not shown). Therefore, the amide I and amide II spectral subregions were left out of the user-selected subregion data reduction methodology. Sharp peaks in difference spectra are most likely due to variance in the signal-to-noise quality of the spectra rather than poor water vapor compensation since the ATR technique does not typically suffer from the atmospheric bands seen in traditional transmission spectroscopy (Harrick, 1967). The S/N quality of the spectra was quite high (< 2 mOD units of noise), but a differ-

ence spectrum calculation can degrade S/N quality because noise is random and cannot be subtracted out. Moreover, sharp peaks in the difference spectra may have arisen amplification of small ATR spectral distortions in the absorbance spectra by the difference spectrum calculation (section 3.2.3). The user-selected subregions used as input for LDA of the four defined two-class problems and the LDA separation achieved are summarized in Table 3-1. The LDA class separation (86-98%) obtained by the “manual splicing” data reduction methodology was not as high as that obtained using the GA-LDA (100%). However, the user-selected subregions used as LDA input verified that class discrimination by GA-LDA was primarily based on greater collagen content in one tissue type. The spectral subregions chosen nonsubjectively by the genetic algorithm and used as input for LDA of the four defined two-class problems are summarized in Table 3-2. The GA-LDA results lead to a 100% class separation in each two-class tissue comparison. Many of the spectral subregions chosen by the GA for optimized LDA class separation were attributable to the prevalence of mid-IR fingerprint of collagen (section 3.1.3) in the spectra of one tissue class in each two-class comparison (see sections, 3.2.2, 3.3.3, 3.3.4 and 3.3.5).

Table 3-1. LDA of control and cardiomyopathic heart tissue using manually spliced spectral subregions. Abbreviations: N_S , number of spectra under comparison; N_A , number of attributes used in the LDA.

Groups	N_S	N_A	Subregions selected /cm ⁻¹	Assignment	LDA Separation /%
LV(CON) vs. RV(CON)	35	24	1275-1285 1235-1240 1205-1210	Amide III/proline CH ₂ wagging	92.5
LV(CMP) vs. RV(CMP)	57	40	1720-1735 1330-1335 1310-1315 1020-1030	Side of phospholipid C=O stretch Amide III/proline CH ₂ wagging C-O-C stretching region due to carbohydrates or carbohydrate residues on collagen	85.8
RV(CMP) vs. RV(CON)	42	21	1735-1740 1205-1208 1155-1165	Phospholipid C=O stretch Amide III/proline CH ₂ wagging C-OH stretching due to carbohydrates or hydroxyPro residues on collagen	98.1
LV(CMP) vs. LV(CON)	50	31	1735-1745 1455-1465 1320-1325 1203-1205	Phospholipid C=O stretch CH ₃ bending and CH ₂ scissoring Amide III/proline CH ₂ wagging	98.3

Table 3-2. Genetic algorithm-selected spectral subregions that lead to nonsubjective classification of the heart tissue. Abbreviations: NA, nucleic acids; HFC, high-frequency component; LFC, low frequency component

CON (LV vs RV) subregions /cm ⁻¹	CMP (LV vs RV) subregions /cm ⁻¹	RV (CMP vs CON) subregions /cm ⁻¹	LV (CMP vs CON) subregions /cm ⁻¹	Assignment
–	1713-1743	–	–	C=O (NA) to C=O (lipids)
1708-1720	–	–	–	C=O (NA)
	1634-1712	1592-1670	1634-1711	Amide I
1667-1680	–	–	–	Amide I: β -sheet (HFC), turns, 3_1 -helix
–	–	–	1597-1633	Amide I: β -sheet (LFC) and intermolecular H-bonding between collagen chains (cross-linking)
1507-1513	1511-1633	–	–	Tyr (~ 1517 cm ⁻¹) and low frequency side of the amide I
–	1474-1500	–	–	Region between CH ₂ scissoring and amide II
–	–	1497-1578	–	Amide II region
–	–	–	1455-1468	CH ₃ asymmetric bend (1457 cm ⁻¹) and CH ₂ scissoring (1467 cm ⁻¹)
1431-1432	–	–	1429-1440	Procession of the CH ₂ bending vibrations
–	1364-1436	1360-1404	1397-1413	Centred or upon side of the COO ⁻ symmetric stretch
1276-1289	1316-1350	1294-1335	–	Amide III/ proline CH ₂ wagging
	1205-1238	1201-1238		
1155-1164	–	1156-1188	1160-1177	C-OH stretching due to hydroxyproline residues and carbohydrates on collagen
1112-1114	1070-1112	1084-1127	1088-1159	C-O-C stretching region due to carbohydrates or carbohydrate residues on collagen
1001-1013	1000-1032	1022-1071		

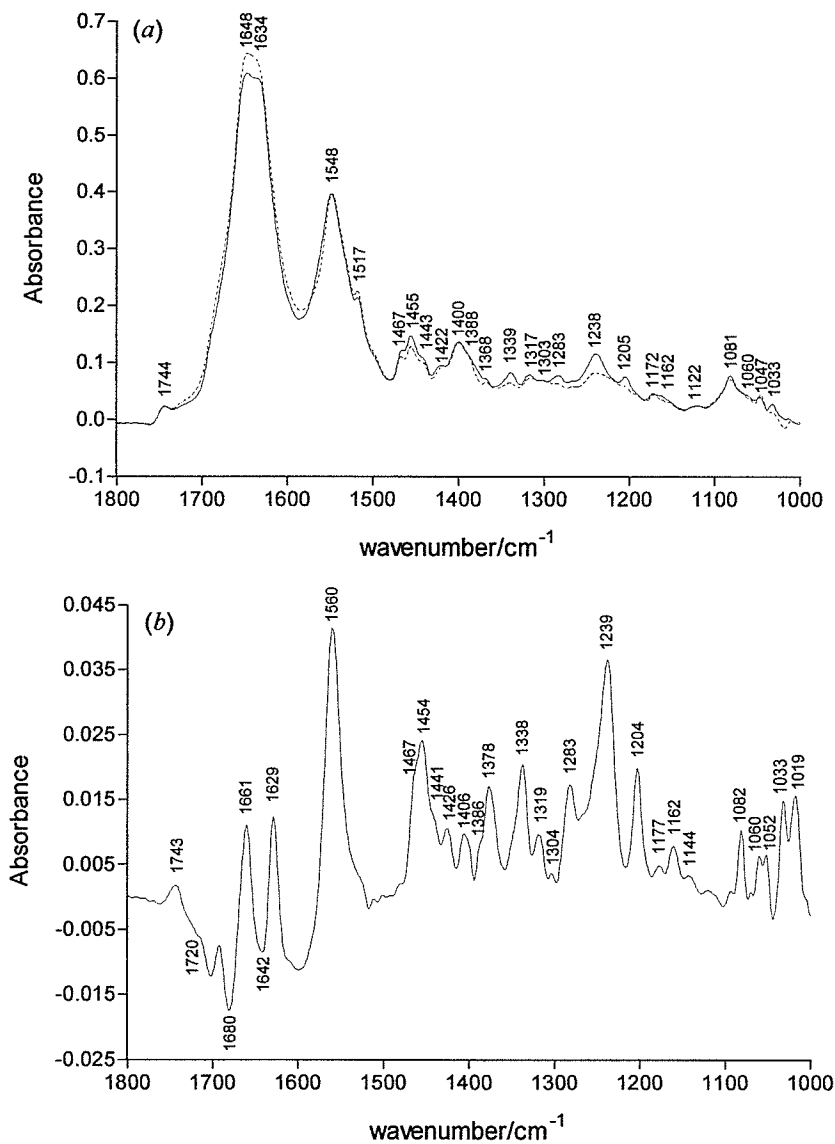
3.3.2 Comparison of the control ventricular tissue

Visual comparison of the class average spectra for the left and right ventricles of control hamster hearts (Figure 3-1a) suggested that compositional differences, especially in terms of collagen content, existed between the two ventricles of the normal heart. The difference spectrum, shown in Figure 3-1b, illustrated that the collagen type I content of control right ventricles was greater than that of the control left ventricles. Absorption bands that may be assigned to the C-O stretching vibrations of the carbohydrate residues attached to collagen (*ca.*, 1033 and 1082 cm^{-1}) and the amide III and CH_2 wagging vibrations of collagen (*ca.*, 1204, 1239, 1283, 1319, 1338 and 1378 cm^{-1}) were greater in RV(CON) than in LV(CON). Secondly, the relative intensity of the CH_2 scissoring vibration (*ca.*, 1467 cm^{-1}) to the COO^- symmetric stretch (*ca.*, 1400 cm^{-1}), upon visual inspection of the two class average spectra, was found to be greater in RV(CON) than in LV(CON). The high proline/hydroxyproline and glycine content of collagen (nearly 60% of the amino acid composition of collagen) in comparison to the lower aspartate/glutamate content may serve as an explanation for the enhancement of the CH_2 bending vibration over that of the COO^- symmetric stretching absorption (Jackson *et al.*, 1995). The difference spectrum (Figure 3-1b) also revealed that a lower frequency amide I component near 1629 cm^{-1} was more prevalent in RV(CON) than in LV(CON) which may be tentatively assigned to an amide I feature representative of the influence of strong intermolecular H-bonding between collagen chains (Liu *et al.*, 1996). The hydroxyl groups of the hydroxyproline residues are believed to stabilize the collagen triple helix by the formation of interchain hydrogen bonds (Creighton, 1993).

Confirmation of the distinction between RV(CON) and LV(CON) in terms of collagen content was provided by the LDA separation (92.5%) between the classes when regions of the second derivative spectra, representative of the amide III/ CH_2 wagging sub-region (1200-1285 cm^{-1}), were manually spliced together and used in the analysis (Table 3-1). Therefore, variations existed in the ventricular collagen content of control hearts in which the right ventricle contained a greater quantity of collagen in its ECM. The right ventricle, a smaller chamber with thinner walls than that of the left, may require greater collagen in its ECM perhaps as a means to increase the ventricular tensile strength and thus

enhance the contraction and relaxation phases of the ventricle. Greater collagen content in the right ventricle as opposed to the left ventricle of control rat hearts, detected by biochemical assay of the 4-hydroxyproline concentration of the myocardium, has been noted in other studies (Davison *et al.*, 1994; Pelouch *et al.*, 1994b; Robert *et al.*, 1994).

Figure 3-1. Comparison of the class average spectra from the left and right ventricles of the control animals. (a) Class average spectra; RV(CON), solid line; LV(CON), broken line. (b) Difference spectrum RV(CON) minus LV(CON).



The nonsubjective classification of the control heart tissue as either left or right ventricle, using spectral subregions selected by a genetic algorithm, yielded a 100% LDA separation based on attributes derived from spectral regions where the collagen signature in RV(CON) was found. The GA had a tendency to pick subregions that were found to lie upon the side of an absorption or between absorptions rather than centred upon a peak (Table 3-2). For instance, the subregions 1431-1432 cm^{-1} , 1112-1114 cm^{-1} and 1001-1013 cm^{-1} may be considered as subregions between the CH_2 scissoring and the COO^- symmetric stretching vibrations and subregions within or along the sides of the various C-O stretching vibrations of carbohydrates, respectively. However, the GA did select a spectral subregion (1276-1289 cm^{-1}) centred about an absorption of the amide III mixing with the proline side chain and glycine backbone CH_2 wagging vibrations (Jackson *et al.*, 1995). Furthermore, the GA also chose spectral subregions which did not correspond to those chosen subjectively for the LDA above. For example, the GA selected the subregion 1507-1513 cm^{-1} , which lies upon the side of the absorption which one would see for the residue tyrosine (1517 cm^{-1}), as well as that assigned to the side of the nucleoside base C=O stretch of nucleic acids (1708-1720 cm^{-1}). The absorption for tyrosine ring vibration would normally be expected to be of higher relative intensity in tissue containing a lower proportion of collagen (i.e., LV(CON) as opposed to RV(CON) in this instance), since tyrosine is not an abundant residue found in the collagen protein (Jackson *et al.*, 1995). The weak C=O absorption due to nucleic acids has been reported to appear at 1721 cm^{-1} , and in infarcted tissue this absorption is expected to be attenuated because extensive collagen type I deposition occurs after phagocytosis of cellular debris (Jackson and Mantsch, 1996). However, the difference spectrum between LV(CON) and RV(CON) in Figure 3-1a does not provide any significant information about whether the left or right ventricle contains more tyrosine or nucleic acids. The GA also selected the subregion corresponding to the C-OH stretching vibration (1155-1164 cm^{-1}). Absorptions in this subregion are commonly seen in the spectra of carbohydrates or of proteins high in hydroxyproline content, such as collagen, or proteins that contain a number of serine or threonine residues (Liu *et al.*, 1996). Furthermore, Liu *et al.*, 1996, found that the ratio of the 1159:1172 cm^{-1} absorptions was greatly increased in infarcted rat heart as opposed to that of control, suggesting that the 1159 cm^{-1} feature was due specifically to the C-OH stretching of hydroxyproline. Although this C-OH

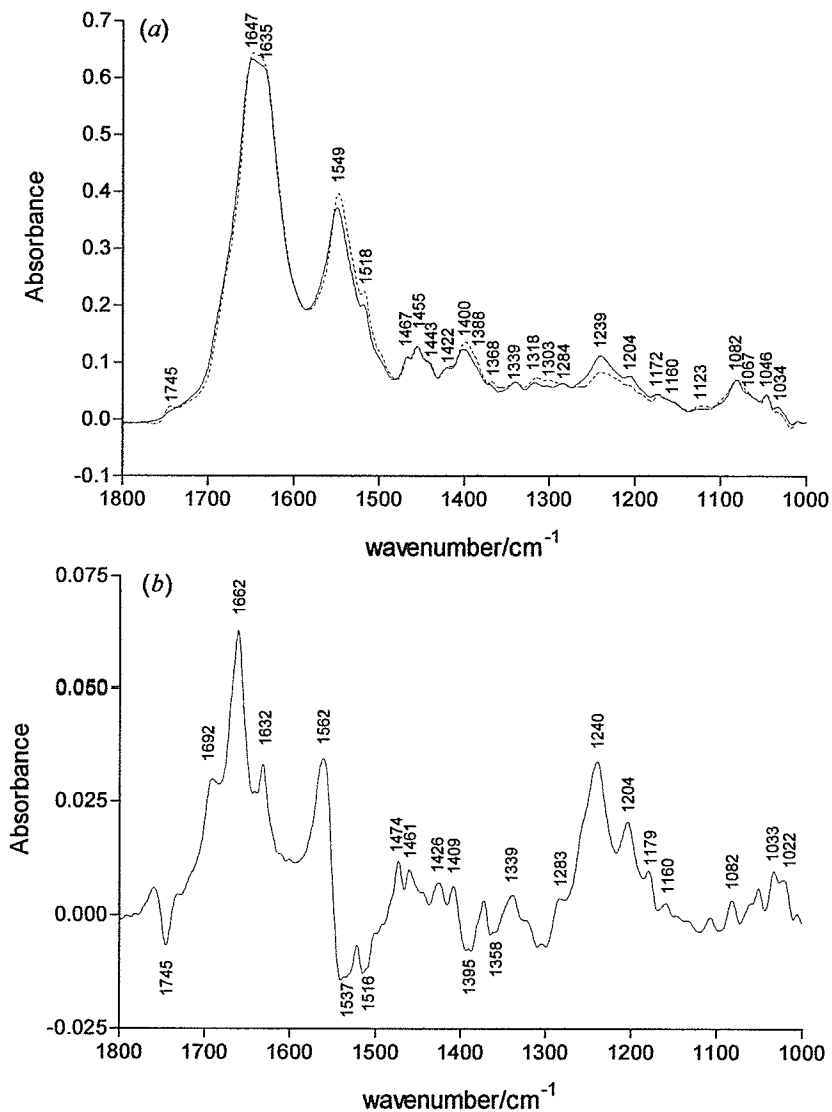
stretching subregion did not enhance the LDA separation when significant spectroscopically diagnostic subregion were user-selected, comparison of RV(CON) and LV(CON) revealed that the 1162:1172 cm^{-1} ratio was slightly greater in RV(CON) (Figure 3-1a). The GA-selected subregions may represent between-group spectral differences that were too subtle to be chosen by eye or lost in the difference spectrum calculation. The looping of the GA to the LDA algorithm allows for the diagnostic capabilities of all spectral subregions within the entire 1000-1800 cm^{-1} region to be assessed at the onset. In the GA-LDA classification, information contained within each spectrum of each tissue class is not lost by the calculation of the class average spectrum and taking the difference spectrum of class average spectra. Therefore, the GA not only provided a nonsubjective classification of control ventricular tissue, but it also used subregions for LDA classification that were distinct from those chosen manually.

3.3.3 Comparison of cardiomyopathic ventricular tissue

In contrast to the differences observed in the class average spectra of the control ventricular tissue, the cardiomyopathic ventricular tissue spectra were not as distinct upon visual comparison, based on the prevalence of the collagen fingerprint between 1000-1500 cm^{-1} (Fig. 3-2a). The difference spectrum between the class average spectra for the groups LV(CMP) and RV(CMP), shown in Fig. 3-2b, illustrated the minute difference in collagen content of the two ventricles. Both class average spectra, LV(CMP) and RV(CMP), displayed the collagen fingerprint (*i.e.*, absorptions at 1033, 1081, 1205, 1238, 1283, 1317 and 1339 cm^{-1}). However, the difference spectrum (Fig. 3-2b) indicated a slight difference between these spectral subregions of the two class average spectra, whereby the collagen fingerprint was found to be slightly more pronounced in the LV(CMP) class average spectrum. Upon subtraction of RV(CMP) from LV(CMP), a collagen-like fingerprint remained just above a zero difference. Furthermore, the difference spectrum illustrated a less prominent phospholipid ester C=O stretching vibration (*ca.*, 1745 cm^{-1}) in LV(CMP). The phospholipid content of a tissue typically decreases when the content of another component (*i.e.*, collagen) increases (Jackson and Mantsch, 1996). The LDA separation using the user-selected subregions to classify the groups LV(CMP) and RV(CMP) was satisfactory (85.8%) when subregions such as those representing the phospholipid ester C=O (1720-

1735 cm^{-1}), amide III/ CH_2 wagging (1310-1315 cm^{-1} and 1330-1335 cm^{-1}) and C-O stretching of carbohydrates (1020-1030 cm^{-1}) were used (Table 3-1). Together, the difference spectrum and the lower LDA class separation (85.8%) achieved suggest the collagen content in the ECM of the left and right ventricles of the CMP hearts does not differ to the extent observed with the control ventricles. This is perhaps due to collagen remodeling in both ventricles wherein the left ventricular collagen increased and the right ventricular collagen remained similar to control levels or decreased.

Figure 3-2. Comparison of the class average spectra from the left and right ventricles of the CMP animals. (a) Class average spectra; LV(CMP), solid line; RV(CMP), broken line. (b) Difference spectrum LV(CMP) minus RV(CMP).



The nonsubjective classification of the CMP tissue yielded a 100% separation of subregions that were GA-selected. However, in contrast to the subregions chosen by the GA for the control spectra, the CMP spectral subregions were of rather a broad range ($>30\text{ cm}^{-1}$) such that classification was based on nearly the entire fingerprint region (Table 3-2). Since the GA program "averaged" each spectral range to a single point (attribute), the GA/LDA 100% separation of the LV(CMP) group from the RV(CMP) group may have been an artifact. The rather large subregions selected by the GA that generated a 100% separation between the left and right CMP ventricles included the lipid/nucleic acid C=O stretching subregion ($1713\text{-}1743\text{ cm}^{-1}$), the amide I and II band profiles ($1511\text{-}1712\text{ cm}^{-1}$), the subregion between the CH₂ scissoring and the amide II ($1474\text{-}1500\text{ cm}^{-1}$), the subregion containing the COO⁻ symmetric stretching vibration ($1364\text{-}1436\text{ cm}^{-1}$), the amide III/ proline CH₂ wagging subregion ($1316\text{-}1350\text{ cm}^{-1}$ and $1205\text{-}1238\text{ cm}^{-1}$) and the C-O stretching subregion of carbohydrates or carbohydrate residues of collagen ($1000\text{-}1032\text{ cm}^{-1}$ and $1070\text{-}1112\text{ cm}^{-1}$). Therefore, although the GA was a useful method for reduction of the number of spectral attributes and for selection of subtle differences between the spectra for LDA input, manual selection of subregions from observable differences between the class average spectra was necessary to avoid possible artifactual distinctions between the groups under comparison.

3.3.4 Collagen remodeling in the right ventricle

Verification of collagen remodeling in the right ventricle of cardiomyopathic hamster hearts involved the direct comparison of the groups RV(CMP) and RV(CON). Visually, the most apparent differences between the class average spectra RV(CMP) and RV(CON) concern the IR subregions where absorptions due to phospholipid and collagen occur (Fig. 3-3). The subregions chosen and manually spliced for LDA input that generated an LDA separation between classes of 98.1% are shown in Table 3-1. Absorptions in the subregions $1735\text{-}1740\text{ cm}^{-1}$ (side of lipid C=O), $1205\text{-}1208\text{ cm}^{-1}$ (amide III/ CH₂ wagging) and the ratio of the $1162\text{:}1172\text{ cm}^{-1}$ (contribution from the C-OH stretching of hydroxyproline) were greater in RV(CON) than in RV(CMP). Further differences between the groups RV(CMP) and RV(CON) were noted upon visual inspection of Fig. 3-3; the C-O stretching of carbohydrates or carbohydrate residues attached to collagen (1031 and 1081 cm^{-1}) was

more prevalent in RV(CON); the CH₂ scissoring (1466 cm⁻¹) was greater than the COO⁻ symmetric stretch (1398 cm⁻¹) in RV(CON); and the amide I maximum had shifted to lower frequency in RV(CON) in comparison to RV(CMP). Thus, although the model used in this study was expected to be a paradigm of LV cardiomyopathy in which collagen remodeling of the ECM occurs primarily in the left ventricle, the greater phospholipid and collagen type I content in the right ventricle of control rather than in right ventricle of the CMP hearts, supported the likelihood of collagen remodeling (*i.e.*, collagen loss) in the ECM of the right ventricle as well. However, while RV(CMP) was found to have decreased collagen deposition in comparison to RV(CON), little difference was found in the collagen deposition of RV(CMP) and LV(CMP) in comparison to the noticeable difference between RV(CON) and LV(CON). A likely explanation for the smaller difference between RV and LV collagen deposition in the CMP hearts than that between the control heart ventricles is that collagen remodeling occurred in both the RV (*i.e.*, collagen loss) and LV (*i.e.*, collagen gain) in response to cardiomyopathy (see Figure 3-4 and section 3.3.5).

The nonsubjective classification of the right ventricles as either CON or CMP, using GA-selected subregions, yielded a 100% LDA separation based on attributes derived from spectral subregions that mainly involved absorptions due to collagen (Table 3-2). In contrast to the subregions chosen manually, the GA did not select the lipid C=O absorption. The GA, however, did choose the C-OH stretching subregion due to carbohydrates and/or hydroxyproline (1156-1188 cm⁻¹) and the amide III/ proline CH₂ wagging subregion (1294-1335 cm⁻¹ and 1201-1238 cm⁻¹), similar to those subregions selected by the manual splicing methodology. In addition, the GA selected subregions in the C-O stretching region due to carbohydrates or carbohydrate residues on collagen (1084-1127 cm⁻¹ and 1022-1071 cm⁻¹), the side of the COO⁻ symmetric stretch (1360-1404 cm⁻¹), and the amide I and amide II band profiles (1592-1670 cm⁻¹ and 1497-1578 cm⁻¹, respectively), all of which were found to differ between RV(CMP) and RV(CON) as illustrated in the difference spectrum in Fig. 3-3b.

Figure 3-3. Spectral comparison of control and CMP right ventricular tissue indicative of decreased collagen deposition in RV(CMP). (a) Class average spectra; RV(CON), solid line; RV(CMP), broken line. (b) Difference spectrum RV(CON) minus RV(CMP).

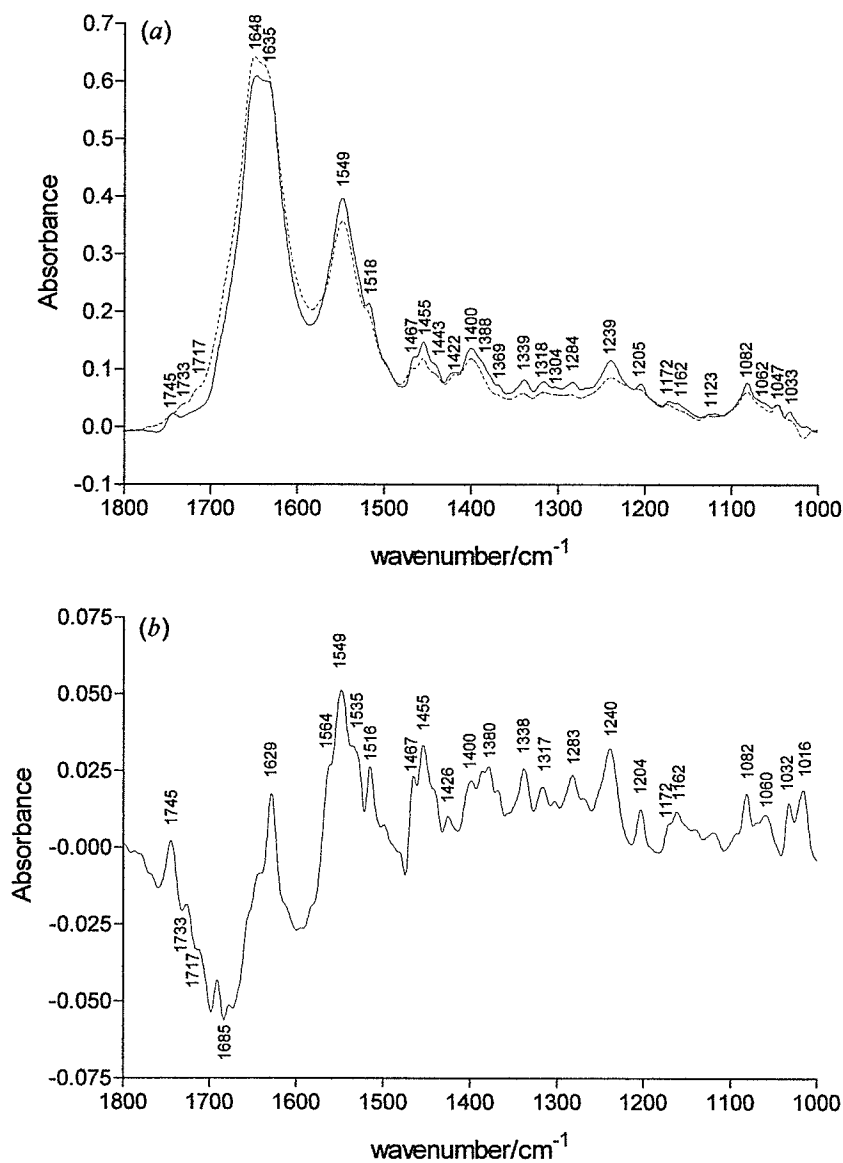
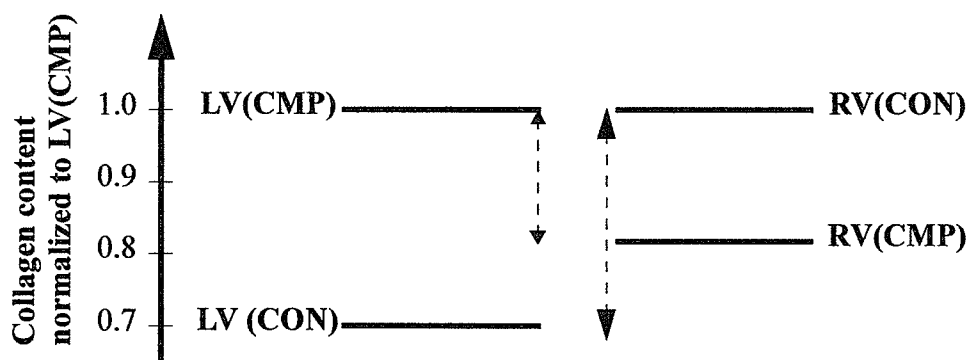


Figure 3-4. Schematic diagram illustrating the difference in ventricular collagen content in the CMP and CON hearts. Since collagen in RV(CON) is greater than in RV(CMP), and collagen in LV(CMP) is greater than in LV(CON), the difference in ventricular collagen content in the diseased hearts is smaller than that in the control hearts. Horizontal lines represent the normalized collagen content in the tissue class. The scale normalized to the collagen content in LV(CMP) approximated by intensity of 1204 cm^{-1} peak (80 mOD units) in the class average spectrum of LV(CMP).

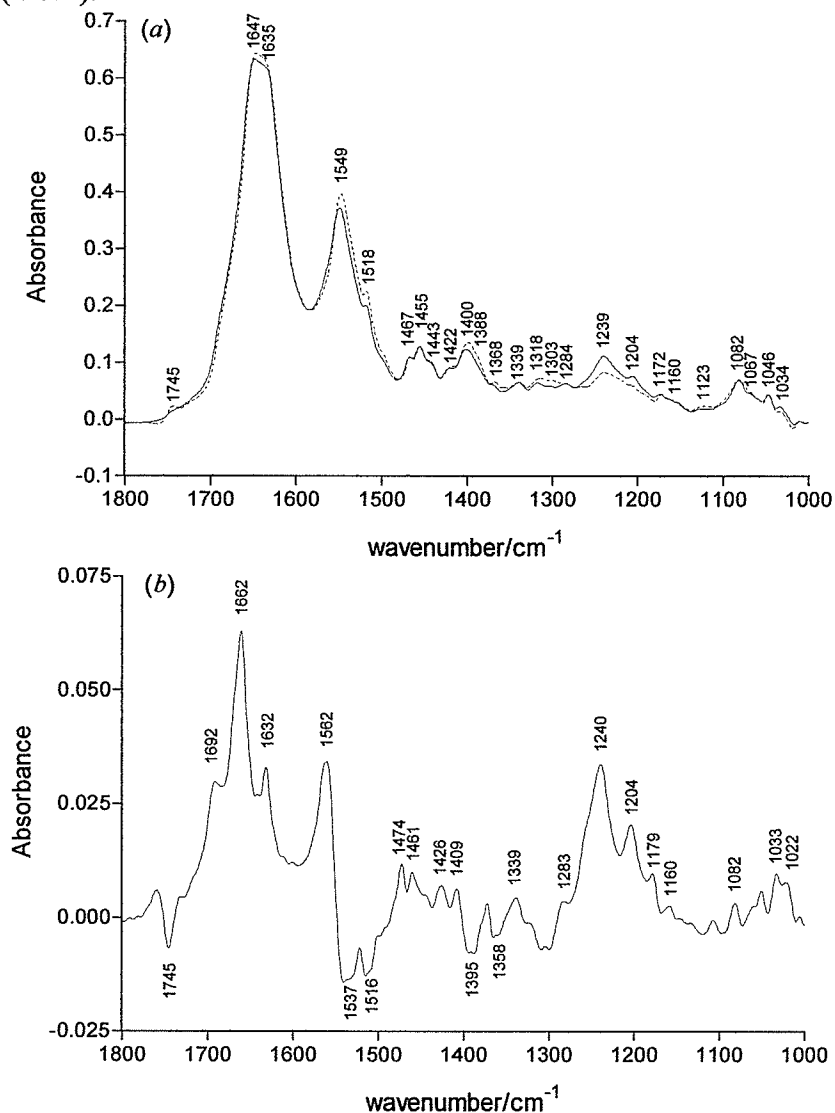


3.3.5 Collagen remodeling in the left ventricle

Finally, evidence for collagen remodeling in the left ventricle of the cardiomyopathic hamster hearts was derived initially from the direct comparison of the groups LV(CON) and LV(CMP). Visual comparison of the fingerprint region of the class average spectra for LV(CON) and LV(CMP) revealed that the groups differed predominantly in spectral subregions where absorptions due to collagen and phospholipid occur (Fig. 3-5a). For instance, deposition of a greater amount of collagen in the group LV(CMP) was inferred from the presence of more prevalent absorptions in the amide III/ proline CH_2 wagging region (1339, 1283, 1240, 1204 cm^{-1}) and by attenuation of the phospholipid $\text{C}=\text{O}$ (1745 cm^{-1}) stretching absorption in LV(CMP). In addition, the enhanced relative intensity of the CH_2 scissoring absorption (1467 cm^{-1}) to the COO^- symmetric stretching absorption (1400 cm^{-1}) in LV(CMP), visually detected upon comparison of the group-mean spectra further supported elevated collagen deposition in LV(CMP). The CH_3 bending/ CH_2 scissoring subregion (1455-1465 cm^{-1}), sides of bands within the amide III/ proline CH_2 wagging subregion (1320-1325 and 1203-1205 cm^{-1}) and the $\text{C}=\text{O}$ stretching subregion (1735-

1745 cm^{-1}) were found to augment the separation between classes in the LDA resulting in a LDA class separation of 98.3% (Table 3-1). Differences in the C-O and C-OH stretching regions (1030-1175 cm^{-1}) and in the absorption due to tyrosine (1515 cm^{-1}), wherein the former was found to be greater in LV(CMP) and the latter was found to be greater in LV(CON), could be detected visually (difference spectrum, Fig. 3-5b) but were not found to further enhance the LDA separation between the classes beyond that reported.

Figure 3-5. Spectral comparison of the control and CMP left ventricular tissue indicative of increased collagen deposition in LV(CMP). (a) Class average spectra; LV(CMP), solid line; LV(CON), broken line. (b) Difference spectrum LV(CMP) minus LV(CON).



Nonsubjective classification of the left ventricles as either CON or CMP, using GA-selected subregions, generated a 100% LDA separation based on attributes derived from spectral subregions that contained collagen absorptions (Table 3-2). Interestingly, the GA selected the CH₃ bending/CH₂ scissoring subregion (1455-1468 cm⁻¹) in this class comparison. The relative intensity of the CH₂:CH₃ absorptions has been previously reported to increase in infarcted tissue where increased collagen deposition may be found (Liu *et al.*, 1996). Although a difference in the relative intensity of the CH₂ to CH₃ deformation could not be detected visually in the class average spectra (Figure 3-5), this subregion (1455-1465 cm⁻¹) was selected in the user-selected data reduction methodology. In turn, the 1455-1465 cm⁻¹ subregion was found to improve the LDA separation. Once again this exemplifies how spectral information can be lost when only the class average spectra are examined to determine the most spectroscopically diagnostic subregions. Instead of differentiating between class average spectra, the GA-LDA is able to discern between-group differences by examination of all the spectra in each group. Aside from the CH₃ bending/CH₂ scissoring subregion, the GA selected a subregion containing the procession of CH₂ scissoring vibrations (1429-1440 cm⁻¹) and a subregion centered about the COO⁻ symmetric stretching vibration (1397-1413 cm⁻¹). Therefore, the LDA that utilized the GA-selected subregions may have also based its classification on the differences in the relative intensity of CH₂ scissoring (proline/glycine) to the COO⁻ symmetric stretching (aspartate/glutamate) in tissue with elevated collagen deposition due to the high glycine and proline residue count in the collagen sequence. Contrary to the subregions chosen manually, the GA did select the subregions due to the C-O stretching of carbohydrates and carbohydrate residues on collagen and the C-OH stretching of carbohydrates and/or hydroxyproline (1088-1177 cm⁻¹) to distinguish between the classes, while it did not select the lipid C=O subregion nor the amide III/ proline CH₂ wagging subregion (Table 3-2). Although the latter regions were not chosen by the GA, both the difference spectrum (Fig. 3-5b) and the LDA performed upon the user-selected subregions (Table 3-1) validated that class distinction could be augmented by use of these regions. Instead of subregions containing absorptions reflective of phospholipid content or absorptions containing the many overlapping bands due to the amide III/ proline CH₂ wagging vibrations, the GA chose subregions that contained the amide I absorption (1597-1633 cm⁻¹ and 1634-1711 cm⁻¹) which were not utilized in the LDA performed on

the manually-spliced spectral subregions. The LV(CMP) group exhibited a high standard deviation in the amide I subregion (data not shown), thus this subregion was not considered as reliable in class distinction strategies as some of the other spectral subregions already mentioned. However, the difference spectrum in Fig. 3-5b supported the GA selection of subregions within the amide I absorption for LDA separation of the LV(CMP) and LV(CON) classes since the greatest difference was found to lie within the amide I band profile. In Fig. 3-5b the amide I region of LV(CMP) contained significant contributions from components that may be attributed to structure of the collagen triple helix. That is, the enhanced absorptions near 1632 cm^{-1} and 1662 cm^{-1} in LV(CMP) as opposed to LV(CON) were representative of the amide I absorptions due to the cross-linking intermolecular hydrogen bonding network between collagen chains and the 3_1 -helix structural motif of collagen, respectively (Liu *et al.*, 1996).

Therefore, implementation of a genetic algorithm to select spectroscopically diagnostic subregions of spectra for LDA classification allowed for the distinction of the two classes LV(CMP) and LV(CON) primarily based on differences in the amount of collagen deposited in the ECM of the two tissue types. However, visual examination of the class average spectra and the difference spectrum between LV(CMP) and LV(CON) was still required to discern the tissue type where collagen deposition was increased. The difference between the class average spectra indicated that collagen was elevated in the extracellular matrix of the cardiomyopathic left ventricular tissue. Elevated LV collagen was expected in this CMP hamster line that is a model for human CCM (Gertz, 1972; Jasmin and Proschek, 1982; Davison *et al.*, 1994; Pelouch *et al.*, 1994a; Dixon *et al.*, 1997). As a consequence of CMP, collagen remodeling in the left ventricle progressively worsens in the living animal, until the contractility of the left ventricle is so compromised that congestive heart failure ensues (sections 3.1.2 and 3.1.4).

3.4 CONCLUSIONS

The results of the current study illustrated that the use of a genetic algorithm to select diagnostic spectral subregions of tissues with varied composition coupled to multivariate analysis (LDA) for non-subjective classification of the cardiac tissue. However, the 100% LDA separation achieved for the four group comparisons may give an overoptimistic impression since a “perfect” classification is more likely the result of “over-fitting”. In order to avoid “over-fitting”, the number of spectral subregions selected by a GA is typically chosen to be one-tenth the number of spectra in the smallest class under comparison (Nikulin *et al.*, 1998). That is, if there were 30 spectra in class A and 40 spectra in class B, then the maximum number of subregions selected by the GA for LDA input should be 3. In preliminary data analysis, the GA was directed to choose a smaller number of subregions (*i.e.*, 5 was attempted) in the 1000-1800 cm^{-1} region, however these subregions were large ($> 30 \text{ cm}^{-1}$) and thus vague with respect to assigning them to specific collagen absorptions (data not shown). Unfortunately, the GA program did not allow user-control for the maximum wavenumber range of the chosen subregions. Since the 100% separation obtained by GA-LDA classification strategy was suspected to be artificially high, spectral subregions for LDA classification were also generated by manually splicing the spectra of each tissue class.

The analysis of cardiac collagen deposition by IR spectroscopy confirmed those found by other studies of the hamster paradigm of congestive cardiomyopathy that utilized biochemical assays (Gertz, 1972; Jasmin and Proschek, 1982; Davison *et al.*, 1994; Pelouch *et al.*, 1994a; Dixon *et al.*, 1997), while in some instances further information was acquired. Specifically, left ventricular collagen remodeling in the cardiomyopathic ECM may be characterized by a more localized elevated collagen deposition rather than by diffuse fibrosis. For example, the LV(CMP) spectra exhibited the highest standard deviation spectrum of all the groups, especially in the amide I region (data not shown), suggesting that collagen deposition was variable (*i.e.*, not diffuse) in the LV(CMP) tissue sampled. Furthermore, the decreased collagen deposition observed in the right ventricles of cardiomyopathic hearts in comparison to control samples indicated that right ventricular collagen remodeling accompanied left ventricular collagen remodeling in this animal model. This observation of decreased collagen deposition in the CMP right ventricle was different

than that found in a recent FT-IR microspectroscopic study (Liu *et al.*, 1999) of hearts of the same hamster line. That is, Liu *et al.*, 1999, found increased focal fibrosis in the RV of the CMP hamster heart tissue examined at a spatial resolution of $50 \times 50 \mu\text{m}^2$ by IR microspectroscopy. The inferences made by Liu *et al.*, 1999, regarding an increase in RV collagen in the CMP hearts, refer to a localized concentration of collagen in the endocardium of RV, whereas collagen is spread out diffusely in the RV of control hearts. Such a microsampling technique cannot provide information regarding the collagen content overall in the RV tissue. That is, one tissue section ($< 10 \mu\text{m}$ in thickness) cannot statistically represent the entire right ventricle of a hamster heart (several mm in thickness and approximately 1.0 cm^2 in area) and tissue morphology can change abruptly within μm distances. Since the current study evaluated the collagen content in the RV of the CMP hamster heart using a larger sampling of the tissue (gross *in situ*), inclusive of statistical analysis rather than visual inference, it is still likely that the collagen content of RV(CMP) decreased in the ventricle (see Chapter 1, section 1.5 for differences regarding micro- and gross-sampling strategies). Regardless, the observed change in the spatial distribution of collagen in a thin section of RV(CMP) heart tissue, made by the microspectroscopy study of Liu *et al.*, 1999, is also of scientific interest.

Numerous FTIR approaches could further the research of this hamster paradigm of human CCM. If the aim of the study is for biodiagnostic purposes, an FTIR-ATR examination of CMP hamster heart tissue extracted at different stages of the disease (see section 3.1.5), followed by GA-LDA multivariate analysis, would enable the progressive necrosis and collagen remodeling of LV and RV to be followed as a function of time. Moreover, certain drugs, such as losartan, have been reported to attenuate the progression of CMP in the cardiomyopathic Syrian hamster (Dixon *et al.*, 1997). Therefore, a FTIR-ATR examination of heart tissue extracted from CMP hamsters treated with losartan, and comparison of this spectral group to CMP and CON spectra using GA-LDA, may provide further evidence of the effectiveness of losartan in the treatment of cardiomyopathy. Alternatively, if the aim of the research is to acquire information regarding the spatial distribution of collagen in the ECM of the CMP hamster hearts (akin to the study of Liu *et al.*, 1999), it may be of particular interest to examine thin sections of the heart myocardium (epicardium to the endocardium) at a greater spatial resolution (*i.e.*, $10 \times 10 \mu\text{m}^2$) using synchrotron FTIR

microspectroscopy (see Chapter 1, sections 1.2.5, 1.5 and 1.7.4). In turn, FTIR images, generated by the prevalence of the collagen fingerprint in each spectrum of the FTIR map, could be compared to a light microscopy image of the tissue section after histochemical staining (*i.e.*, trichrome stain can denote where collagen is deposited). Again, the spatial distribution of necrosis and collagen remodeling in the myocardium could be followed as a function of time by examining tissue sections extracted from the hearts of CMP hamsters at different stages of the disease. Note however, that dense necrotic tissue, which appears black under light microscopy, is typically opaque to IR light and can over-saturate the MCT detector of an IR microscope in reflectance mode. Finally, the effect of losartan on spatial distribution of either necrosis or collagen deposition in the CMP hamster line, could also be examined by synchrotron FTIR microspectroscopy.

3.5 REFERENCES

- Bangalore, A.S., Shaffer, R.E., Small, G.W., Arnold, M.A. (1996) Genetic algorithm-based method for selecting wavelengths and model size for use with partial least-squares regression: application to near-infrared spectroscopy, *Anal. Chem.*, **68**(23), 4200-4212.
- Braunwald, E. (1997) Heart Disease: A Textbook of Cardiovascular Medicine, W.B. Saunders Company, 1407-1408.
- Bromberg, P.S., Gough, K.M., Dixon, I.M.C (1998) Collagen deposition in the extracellular matrix of the cardiomyopathic Syrian hamster as assessed by attenuated total reflectance FT-IR spectroscopy, Abstract and poster presentation, *81st CSC Conference and Exhibition*, May 31-June 4, Whistler, British Columbia, Canada.
- Bromberg, P.S., Gough, K.M., Dixon, I.M.C. (1999) Collagen remodeling in the extracellular matrix of the cardiomyopathic Syrian hamster heart as assessed by FTIR attenuated total reflectance spectroscopy. *Can J. Chem.*, **77**: 1843-1855.
- Capellaro, D.F., Kapny, N.S. (1961) A hypodermic probe using fibre optics, *Nature*, **191**, 927- 928
- Creighton, T.E. (1993) Proteins. Structures and Molecular Properties, 2nd edition, W.H. Freeman and Company, New York, p.196-197.
- Davison, G., Hall, C.S., Miller, J.G., Scott, M., Wickline, S.A. (1994) Cellular mechanisms of captopril-induced matrix remodeling in Syrian hamster cardiomyopathy, *Circulation*, **90**, 1334-1342.

- Dixon, I.M.C., Ju, H., Reid, N.L., Scammell La Fleur, T., Werner, J.P., Jasmin, G. (1997) Cardiac collagen remodeling in the cardiomyopathic Syrian hamster and the effect of losartan, *J. Mol. Cell. Cardiol.*, **29**(7), 1837-1850.
- Faris, F., Rolfe, P., Thorniley, M., Wickramasinghe, Y., Houston, R., Doyle, M., O'Brien, S. (1992) Non-invasive optical monitoring of cerebral blood oxygenation in the foetus and newborn: a preliminary investigation, *J. Biomed. Eng.*, **14**(4), 303-306.
- Fogt, E.J. (1990) Continuous ex vivo and in vivo monitoring with chemical sensors, *Clin. Chem.*, **36**(8), 1573-1580.
- Gertz, E.W. (1972) Cardiomyopathic Syrian hamster: a possible model of human disease, *Progr. Exp. Tumor Res.*, **16**, 242-260.
- Harrick, N.J. (1967) Internal Reflection Spectroscopy, Interscience Publishers, 217-222.
- Jasmin, G., Proschek, L. (1982) Hereditary polymyopathy and cardiomyopathy in the Syrian hamster. I. Progression of heart and skeletal muscle lesions in the UM-X7.1 line, *Muscle and Nerve*, **5**, 20-25.
- Jackson, M., Mantsch, H.H. (1995) The use and misuse of FTIR spectroscopy in the determination of protein structure, *Crit. Rev. Biochem. Mol. Biol.*, **30**(2), 95-120.
- Jackson, M., Choo, L-P., Watson, P.H., Halliday, W.C., Mantsch, H.H. (1995) Beware of connective tissue proteins: assignments and implications of collagen absorptions in infrared spectra of human tissues, *Biochim. Biophys. Acta*, **1270**, 1-6.
- Jackson, M., Mantsch, H.H. (1996) "FTIR spectroscopy in the clinical sciences" in Biomedical Applications of Spectroscopy, R.J.H. Clark and R.E. Hester (eds.), John Wiley and Son Ltd., 185-215.
- Liu, K.Z., Jackson, M.J., Sowa, M.G., Dixon, I.M.C, Mantsch, H.H. (1996) Modification of the extracellular matrix following myocardial infarction monitored by FTIR spectroscopy, *Biochim. Biophys. Acta*, **1315**, 73-77.
- Liu, K.Z., Dixon, I.M.C., Mantsch, H.H. (1999) Distribution of collagen deposition in Cardiomyopathic hamster hearts determined by infrared microscopy, *Cardiovasc. Pathol.*, **8**, 41-47.
- Mantsch, H.H., McElhaney, R.N.(1991) Phospholipid transitions in model and biological membranes as studied by IR spectroscopy, *Chem. Phys. Lipids*, **57**, 213-226.
- McLachlan, G.J. (1992) Discriminant Analysis and Statistical Pattern Recognition, Wiley, New York.

- Nikulin, A.E., Dolenko, B., Bezabeh, T., Somorjai, R.L. (1998) Near-optimal region selection for feature space reduction: novel preprocessing methods for classifying MR spectra, *NMR Biomed.*, **11**, 209-216.
- Parker, F.S., Ans, R. (1967) Infrared studies of human and other tissues by the attenuated total reflection technique, *Anal. Biochem.*, **18**, 414-422.
- Pelouch, V., Dixon, I.M.C., Golfman, L., Beamish, R.E., Dhalla, N.S. (1994a) Role of extracellular matrix proteins in heart function, *Mol. Cell. Biochem.*, **129**, 101-120.
- Pelouch, V., Dixon, I.M.C., Sethi, R., Dhalla, N.S. (1994b) Alteration of collagenous protein profile in congestive heart failure secondary to myocardial infarction, *Mol. Cell. Biochem.*, **129**, 121-131.
- Robert, V., Van Theim, N., Cheav, S.L., Mouas, C., Swynghedauw, B., Deleayre, C. (1994) Increased cardiac type I and III collagen mRNAs in aldosterone-salt hypertension, *Hypertension*, **24**, 30-36.
- Robinson, M.R., Eaton, R.P., Haaland, D.M., Koepp, G.W., Thomas, E.V., Stallard, B.R., Robinson, P.L. (1992) Non-invasive glucose monitoring in diabetic patients: a preliminary evaluation, *Clin. Chem.*, **38(9)**, 1618-1622.
- Schlant, R.C., Alexander, R.W. (1994) Hurst's, *The Heart*, 8th edition, McGraw-Hill Inc., 1585-1590, 1609-1619.
- Taillandier, E., Liquier, F. (1992) Infrared spectroscopy of DNA, *Meth. Enzymol.*, **211**, 307-335.
- Wong, P.T.T., Cadrin, M., French, S.W. (1991) Distinctive infrared spectral features in liver tumor tissue of mice: evidence of structural modifications at the molecular level, *Exp. Mol. Pathol.*, **55**, 269-284.

4 PATHOPHYSIOLOGICAL CHANGES IN ALZHEIMER'S DISEASED HIPPOCAMPUS IMAGED BY SYNCHROTRON FTIR MICROSPECTROSCOPY¹

4.1 INTRODUCTION

4.1.1 Chapter Overview

The final project summarized in this thesis explored the utility of synchrotron FTIR microspectroscopy for detecting the biochemical changes associated with disease pathology on the microscopic level. In the previous chapter, FTIR biospectroscopic differentiation of abnormal from normal tissue was possible due to the sensitivity of ATR-FTIR to macroscopic changes in tissue biochemistry (*i.e.*, collagen content in the cardiac ECM). However, due to heterogeneity within the tissue and population sampled, multivariate statistical analysis of the spectral data was required to verify that this macroscopic change in tissue biochemistry was associated with the disease pathology (recall section 1.6). Alternatively, FTIR microspectroscopic examination of a tissue allows for evaluation of tissue biochemistry at the cellular and sub-cellular levels (sections 1.2.4. and 1.2.5). In addition, FTIR microspectroscopic mapping of a tissue section, followed by multidimensional analysis to generate a FTIR image, can provide information on the spatial distribution of cellular and extracellular constituents in a tissue section (sections 1.6 and 1.7.4). Finally, the spatial resolution in the FTIR image can be improved by using a synchrotron IR source, allowing for the examination of the spatial distribution of tissue constituents at the sub-cellular level. More specifically, this chapter describes the utility of synchrotron FTIR microspectroscopy for denoting pathophysiological changes in Alzheimer's diseased (AD) hippocampus *in situ*.

There are several reasons to study AD hippocampus by synchrotron FTIR microspectroscopy. The disease itself is of interest since AD is the most common form of

1. A portion of this project, the pathophysiological changes observed in one AD hippocampus, has been presented at one national conference (Bromberg *et al.* 1999a), one international conference (Bromberg *et al.* 1999b) and documented in Proceedings of SPIE, Accelerator-based Sources of Infrared and Spectroscopic Applications (Bromberg *et al.*, 1999c).

senile dementia yet the pathogenesis of AD is unclear (Siegal *et al.*, 1994). AD has long been known to be associated with localized accumulations of peptide aggregates (amyloid-bearing plaques and neurofibrillary tangles) in the brain (Alois Alzheimer, 1907). Moreover, amide I component bands of amyloid fibrils prepared *in vitro* (Fraser, 1991) and amyloid-bearing plaques *in situ* (Choo *et al.*, 1996) have been reported to occur between 1620-1628 cm^{-1} and 1632-1634 cm^{-1} , respectively. These studies served as a useful guide for generation of exploratory FTIR images on-site at the synchrotron beamline. In turn, these preliminary FTIR images guided the selection of subsequent tissue regions for FTIR examination. Finally, the well-defined morphology of the hippocampus (section 4.1.2) made the correlation of visibly distinct features of the tissue (*i.e.*, neuronal cell bodies, myelinated axonal projections, parenchyma, blood vessels, *etc.*) to certain spectral signatures fairly straightforward. Although histochemistry can be used to denote the presence of the classical lesions of AD, discrete structural changes at the subcellular or molecular level are beyond the detection limitations of the staining process. Therefore, synchrotron FTIR microspectroscopy was used to compare the molecular substructure of AD and normal hippocampus in an attempt to localize plaques and tangles, and to test the hypothesis that A β -peptide is deposited between plaques at concentrations too low for detection by conventional Bielschowsky silver staining.

Spectroscopic studies were performed at the Synchrotron Radiation Center (SRC), University of Wisconsin-Madison and at the National Synchrotron Light Source (NSLS), Brookhaven National Laboratory, Upton, Long Island. Three AD and two control brains were examined during 1999. FTIR images derived from the spectral maps collected were compared visually with a light microscopy image of the Bielschowsky-stained tissue. Data analysis revealed that fibrillar amyloid *in situ* was high in peptide aggregate structure (amide I component band between 1620-1625 cm^{-1}), while amorphous A β -peptide deposition was high in β -sheet structure (amide I component band between 1630-1637 cm^{-1}). Moreover, another unique spectral feature of fibrillar amyloid was also revealed, namely the appearance of strong COO⁻ stretching absorption (1397-1400 cm^{-1}) assigned here to truncated peptides. Tissue staining correlated with the location of fibrillar amyloid within neurons and regions containing diffuse amorphous plaques. In contrast to inconclusive staining, FTIR imaging was sensitive enough to denote a 10-20% greater contribution of

proteins with β -sheet structure in the gray matter of AD gray matter over that in control tissue. While the conclusions of the present data are only preliminary in nature, they support the hypothesis that seemingly unaffected areas in the AD hippocampal tissue may in fact encompass enhanced diffuse A β -peptide deposits which may be a marker for the initial stages of the disease.

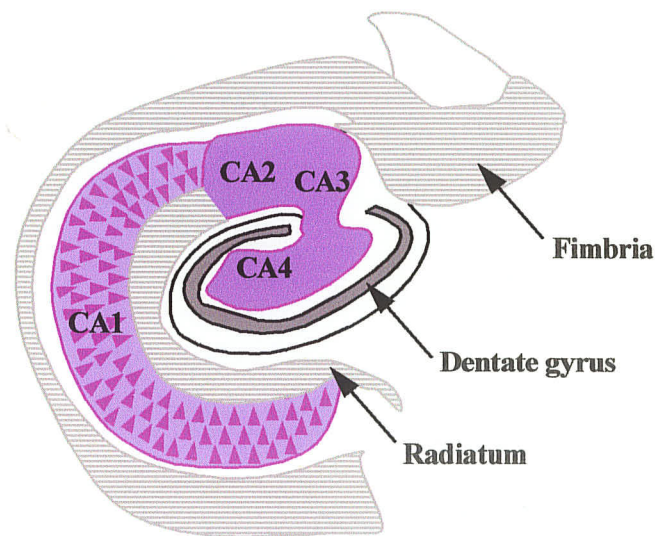
4.1.2 Alzheimer's Disease

Alzheimer's disease (AD) is the most common neurodegenerative disorder leading to late-life cognitive impairment. AD presents with the clinical symptoms of memory loss, disorientation in time, place and person, as well as progressive cognitive decline. As early as 1907 Alois Alzheimer called attention to the aberrant presence of amyloid-bearing plaques and neurofibrillary tangles in 50-70% of autopsied brains of patients clinically diagnosed with senile dementia (Siegal, *et al.*, 1994). Epidemiological studies since then have shown that AD can affect individuals of all races and ethnic groups; it is slightly more prominent in post-menopausal females than males. The majority of AD cases arise sporadically (> 60%) while 5-15% are of the genetically inheritable variety of early onset familial AD (Siegal, *et al.*, 1994). Clinical diagnosis of AD is tentative but post-mortem examination of the cortical and hippocampal regions of the brain can differentiate the disease from other forms of dementia. Histopathologically, these regions of the brain typically reveal neuronal and synaptic loss, reactive gliosis (activated astrocytes and microglia), β -amyloid angiopathy (vascular deposition of A β_{1-40}), extraneuronal amyloid-bearing neuritic plaques (mainly species A β_{1-42}) and neurofibrillary tangles (NFTs) located intra- or extra-neuronally (Esiri and Morris, 1997; Bobinski *et al.*, 1998).

The tissue morphology of the human hippocampus is quite distinct with reference to the relative spatial distribution of the neuronal cell bodies, axons and neurite extensions, and the parenchyma (*i.e.*, other cell types, such as astrocytes, microglia, oligodendrocytes, *etc.*). Shown in Figure 4-1 is a schematic illustration of a transverse section of the hippocampus. The white matter (fimbria) is found around the periphery of the gray matter composed of the CA1, CA2, CA3 and CA4 sectors (Figure 4-1). The pyramidal neurons in the gray matter are easily visualized by light microscopy and are spatially arranged in closer proximity in the CA2-CA4 fields than in the CA1 field. Encompassing the CA4 field of the

hippocampus is the dentate gyrus composed of a granular layer and a molecular layer (Figure 4-1). The granular layer of the dentate gyrus is composed of the dentate neurons which are oval in shape in contrast to the triangular-shaped cell bodies of the pyramidal neurons. The molecular layer of the dentate gyrus (or moleculare) is similar to white matter; it contains the myelinated axons of the dentate neurons along with the associated cells of the parenchyma. Neuritic plaques most typically appear in the gray matter, especially in the CA1 and CA2 fields, but they can also occur within or near the dentate gyrus. NFTs affect the pyramidal neurons of the gray matter and are most commonly found in the CA1 and CA2 fields. Finally, the radiatum houses myelinated axons extending from the pyramidal neurons of the hippocampus and is therefore compositionally similar to the fimbria.

Figure 4-1. Schematic illustration of a transverse section of the hippocampus. Pyramidal neurons of the CA1 represented by purple triangles.²



The pathological marker of AD is generally considered to be the observation of a large number of mature plaques in the hippocampus (and neocortex) because NFTs can be absent or few in 10-20% of AD cases (Siegal *et al.*, 1994). In addition, NFTs can appear in a variety of other etiologically distinct neurological disorders that do not display amyloid-bearing plaques, such as Pick's disease, Parkinson's disease and head trauma (Siegal *et al.*,

2. The illustration above was adapted from Esiri, M.M. and Morris, J.H. (1997) The Neuropathology of Dementia, p.24

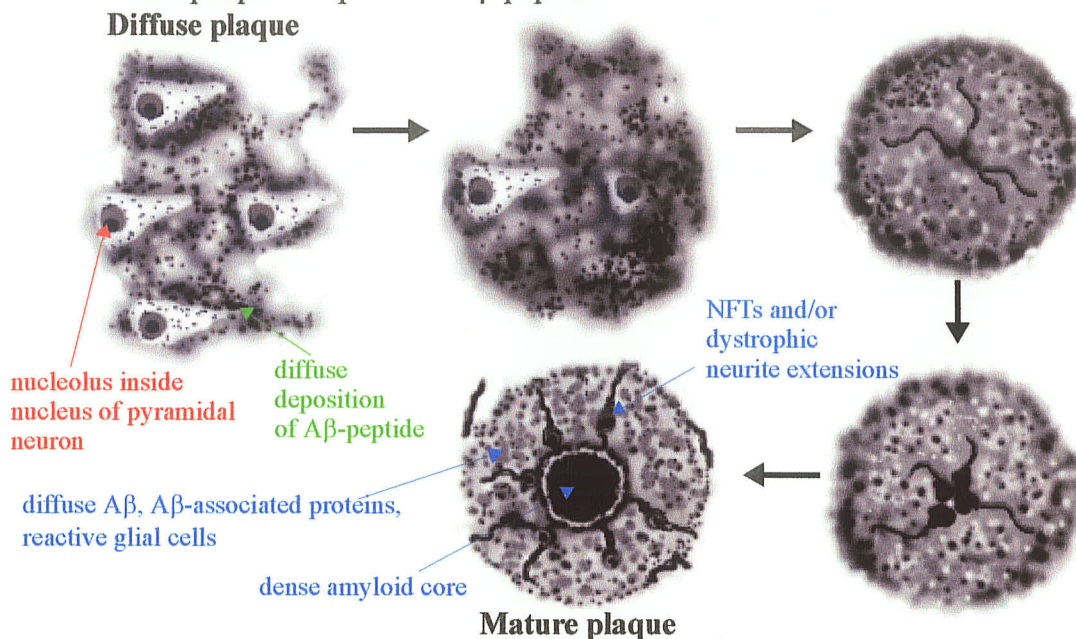
1994). Therefore, NFTs are frequently viewed as a marker of advanced neuronal dysfunction rather than due to a specific disease.

Neuritic plaques have been found to be composed primarily of amorphous aggregates of a peptide, 39-42 residues in length, denoted as A β ₃₉₋₄₂. This A β peptide is thought to arise from abnormal proteolytic processing of its parent protein β -amyloid precursor protein (β APP). β APP is a transmembrane glycoprotein with a short cytoplasmic C-terminus, a large extracellular N-terminus and membrane-spanning A β -domain (39-42 amino acids long) (Siegal *et al.*, 1994). Under normal conditions, β APP is enzymatically cleaved by α -secretase in the middle of its hydrophobic membrane-spanning domain, resulting in the secretion of a soluble form (sAPP) into the extracellular space (Mattson and Furukawa, 1997; John *et al.*, 1997). It has been suggested that sAPP has a neuroprotective role (Mattson and Furukawa, 1997). Under some pathological conditions, the N-terminal domain of β APP is cleaved by β -secretase, followed by the cleavage at the C-terminal end by γ -secretase, producing the A β -peptide (39-42 residues) found in amyloid-bearing plaques (Mattson and Furukawa, 1997; John *et al.*, 1997). The secretases (α , β , γ) responsible for the normal and abnormal proteolytic processing of β APP have been designated by their respective sites of action (John *et al.*, 1997). The identity of these secretases *in vivo*, has been of particular interest for development of potential drug therapies (De Strooper and Konig, 1999). Last year β -secretase, now known as β -site-APP-cleaving enzyme (BACE), was isolated *in vivo* and identified as a transmembrane aspartyl protease (Vassar *et al.*, 1999).

It has been suggested that the appearance of A β peptide marks the onset of AD-related neurodegeneration (Beyreuther and Masters, 1996). The temporal development of a mature neuritic plaque from diffuse A β peptide deposition is only partially understood, but is thought to proceed as presented in Figure 4-2 (Ulrich, 1993). Histopathological evidence supports the speculation that diffuse A β peptide deposition, derived from abnormal proteolytic processing of β APP, precedes the formation of insoluble, fibrillar aggregates of A β ₁₋₄₂ peptide that comprise the core of a mature neuritic plaque (Siegal *et al.*, 1994). Biochemically, diffuse plaques have been found to contain amorphous, non-fibrillar aggregates of A β peptides 39-43 amino acids in length (Siegal *et al.*, 1994, Choo *et al.*, 1996). In addition, the dense amyloid core of a mature plaque is surrounded by peripheral A β -

associated proteins (Apo E, heparan sulfate proteoglycans, laminin, ubiquitin, *etc.*) as well as activated microglia and reactive astrocytes, all of which are thought to be involved in the nucleation of diffuse A β -deposition into A β fibril formation *in vivo* (Ulrich, 1993; Choo *et al.*, 1996; John *et al.*, 1997; van Leeuvan *et al.*, 1998).

Figure 4-2. Formation of a mature neuritic plaque with a dense β -amyloid core from diffuse plaque composed of A β peptide.³

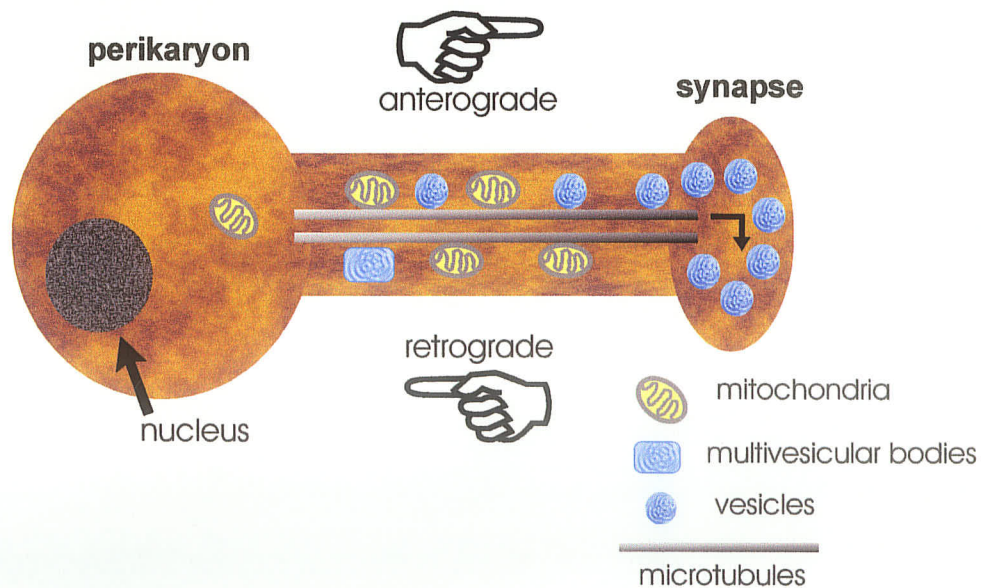


Alzheimer-type NFTs are cytoplasmic fibres formed from masses of paired-helical filaments (PHFs) and are most frequently found in neuronal cell bodies with axonal projections in close proximity to a neuritic plaque (Siegal *et al.*, 1994). PHFs are believed to be composed mainly of aggregates of a truncated portion of the microtubule-associated protein tau in a hyperphosphorylated state (Kidd, 1963; Kidd, 1964; Goedert *et al.*, 1996). Tau normally binds to α - and β -tubulins, facilitating microtubule assembly and stabilization *in vivo*, and thereby has a substantial role in microtubule-associated axonal transport mechanisms vital to neuronal functioning (Siegal *et al.*, 1994). As shown in Figure 4-3, microtubule assemblies are required for fast axonal transport of mitochondria and synaptic vesicles

3. Illustration based on the current view of neuritic plaque formation as described by Ulrich, J. (1993) Histochemistry and immunohistochemistry of Alzheimer's disease, volume 27, p.44.

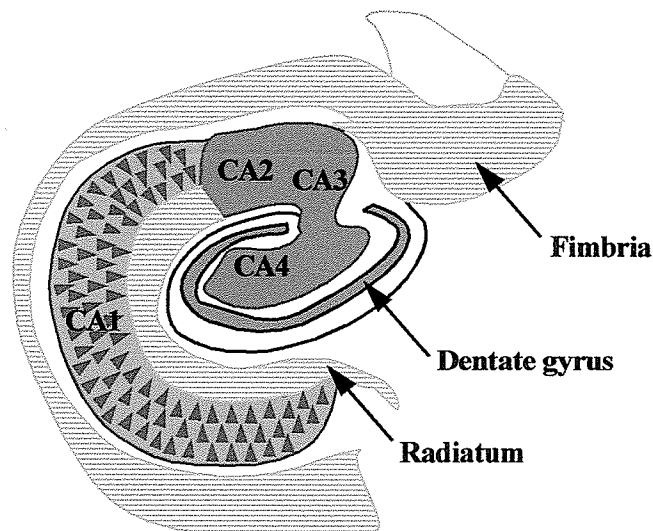
from the perikaryon to the synapse, as well as for disposal of foreign substances (Wiengarten *et al.*, 1975; Cleveland *et al.*, 1977; Siegal *et al.*, 1994). Hyperphosphorylated tau self-associates but can also sequester and bind normal tau (Iqbal *et al.*, 1998). Glycosaminoglycans (GAGs), such as heparan sulfate and heparin, have been shown to mediate assembly of tau into fibrils and stimulate tau phosphorylation, promoting microtubule disassembly *in vitro* (Beyreuther and Masters, 1996; Goedert *et al.*, 1996). It has been postulated that while neuronal membrane damage could occur because of A β neurotoxicity present in the plaque core, the associated GAGs gain access to the cytoplasmic tau present in neurite extensions, mediate NFT assembly and cause premature cell death through microtubule dissociation and inefficient axonal transport (Goedert *et al.*, 1996; Iqbal *et al.*, 1998). Further to this point, frameshift mutants of proteins directly or indirectly connected to plaque formation *in vivo*, such as β APP and ubiquitin-B, have been localized to NFTs as well as to neuritic plaques (van Leeuwen *et al.*, 1998).

Figure 4-3. Schematic representation of a neuron from perikaryon to synapse illustrating the role of microtubule assemblies (and tau) in fast axonal transport mechanisms. Failure of tau to stabilize microtubule assemblies would lead to the breakdown of these mechanisms and result in neuronal dysfunction.



hippocampus is the dentate gyrus composed of a granular layer and a molecular layer (Figure 4-1). The granular layer of the dentate gyrus is composed of the dentate neurons which are oval in shape in contrast to the triangular-shaped cell bodies of the pyramidal neurons. The molecular layer of the dentate gyrus (or moleculare) is similar to white matter; it contains the myelinated axons of the dentate neurons along with the associated cells of the parenchyma. Neuritic plaques most typically appear in the gray matter, especially in the CA1 and CA2 fields, but they can also occur within or near the dentate gyrus. NFTs affect the pyramidal neurons of the gray matter and are most commonly found in the CA1 and CA2 fields. Finally, the radiatum houses myelinated axons extending from the pyramidal neurons of the hippocampus and is therefore compositionally similar to the fimbria.

Figure 4-1. Schematic illustration of a transverse section of the hippocampus. Pyramidal neurons of the CA1 represented by purple triangles.²



The pathological marker of AD is generally considered to be the observation of a large number of mature plaques in the hippocampus (and neocortex) because NFTs can be absent or few in 10-20% of AD cases (Siegal *et al.*, 1994). In addition, NFTs can appear in a variety of other etiologically distinct neurological disorders that do not display amyloid-bearing plaques, such as Pick's disease, Parkinson's disease and head trauma (Siegal *et al.*,

2. The illustration above was adapted from Esiri, M.M. and Morris, J.H. (1997) The Neuropathology of Dementia, p.24

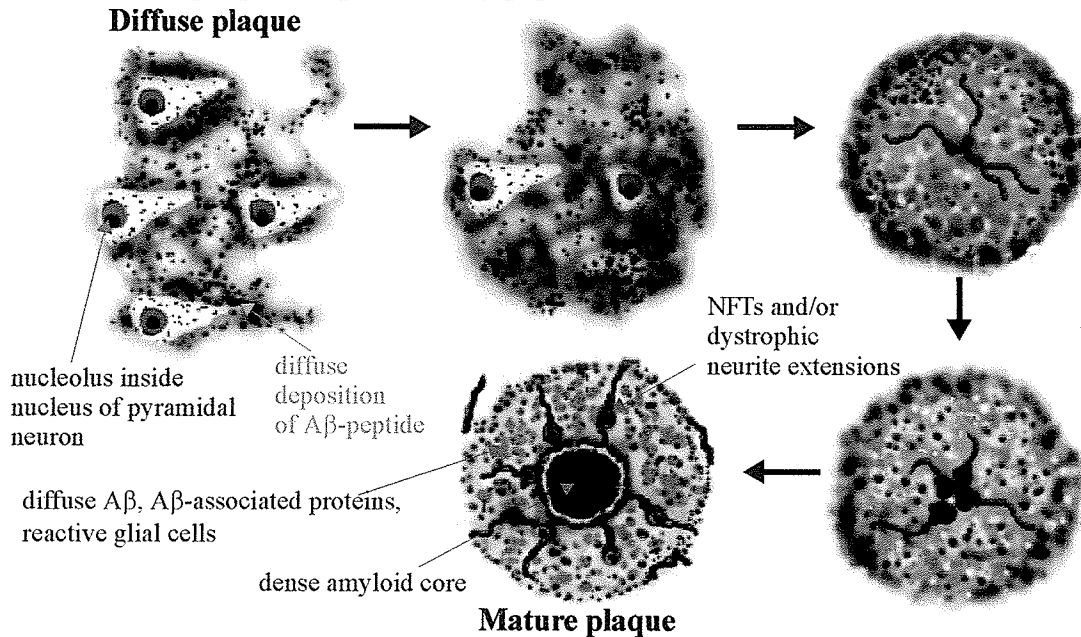
1994). Therefore, NFTs are frequently viewed as a marker of advanced neuronal dysfunction rather than due to a specific disease.

Neuritic plaques have been found to be composed primarily of amorphous aggregates of a peptide, 39-42 residues in length, denoted as A β ₃₉₋₄₂. This A β peptide is thought to arise from abnormal proteolytic processing of its parent protein β -amyloid precursor protein (β APP). β APP is a transmembrane glycoprotein with a short cytoplasmic C-terminus, a large extracellular N-terminus and membrane-spanning A β -domain (39-42 amino acids long) (Siegal *et al.*, 1994). Under normal conditions, β APP is enzymatically cleaved by α -secretase in the middle of its hydrophobic membrane-spanning domain, resulting in the secretion of a soluble form (sAPP) into the extracellular space (Mattson and Furukawa, 1997; John *et al.*, 1997). It has been suggested that sAPP has a neuroprotective role (Mattson and Furukawa, 1997). Under some pathological conditions, the N-terminal domain of β APP is cleaved by β -secretase, followed by the cleavage at the C-terminal end by γ -secretase, producing the A β -peptide (39-42 residues) found in amyloid-bearing plaques (Mattson and Furukawa, 1997; John *et al.*, 1997). The secretases (α , β , γ) responsible for the normal and abnormal proteolytic processing of β APP have been designated by their respective sites of action (John *et al.*, 1997). The identity of these secretases *in vivo*, has been of particular interest for development of potential drug therapies (De Strooper and Konig, 1999). Last year β -secretase, now known as β -site-APP-cleaving enzyme (BACE), was isolated *in vivo* and identified as a transmembrane aspartyl protease (Vassar *et al.*, 1999).

It has been suggested that the appearance of A β peptide marks the onset of AD-related neurodegeneration (Beyreuther and Masters, 1996). The temporal development of a mature neuritic plaque from diffuse A β peptide deposition is only partially understood, but is thought to proceed as presented in Figure 4-2 (Ulrich, 1993). Histopathological evidence supports the speculation that diffuse A β peptide deposition, derived from abnormal proteolytic processing of β APP, precedes the formation of insoluble, fibrillar aggregates of A β ₁₋₄₂ peptide that comprise the core of a mature neuritic plaque (Siegal *et al.*, 1994). Biochemically, diffuse plaques have been found to contain amorphous, non-fibrillar aggregates of A β peptides 39-43 amino acids in length (Siegal *et al.*, 1994, Choo *et al.*, 1996). In addition, the dense amyloid core of a mature plaque is surrounded by peripheral A β -

associated proteins (Apo E, heparan sulfate proteoglycans, laminin, ubiquitin, *etc.*) as well as activated microglia and reactive astrocytes, all of which are thought to be involved in the nucleation of diffuse A β -deposition into A β fibril formation *in vivo* (Ulrich, 1993; Choo *et al.*, 1996; John *et al.*, 1997; van Leeuvan *et al.*, 1998).

Figure 4-2. Formation of a mature neuritic plaque with a dense β -amyloid core from diffuse plaque composed of A β peptide.³

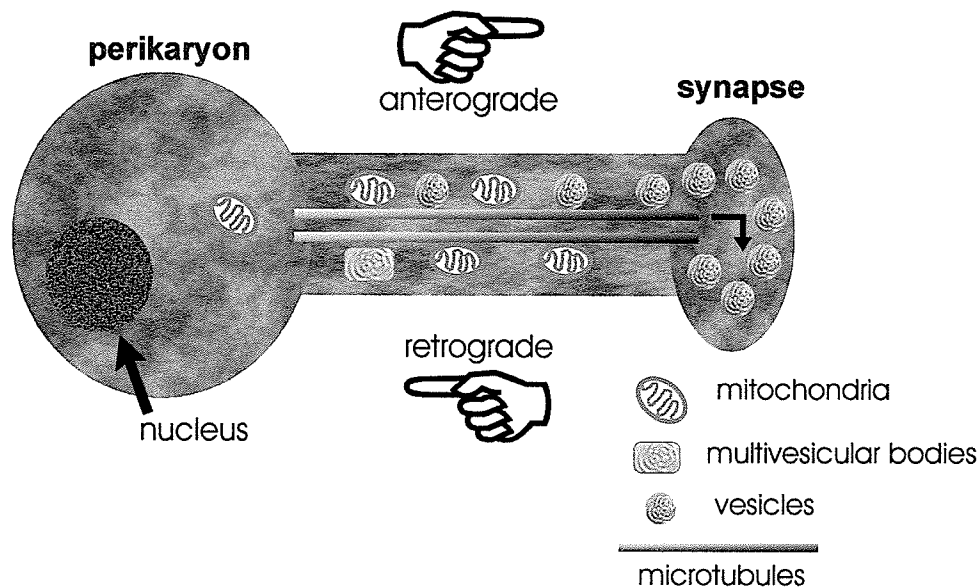


Alzheimer-type NFTs are cytoplasmic fibres formed from masses of paired-helical filaments (PHFs) and are most frequently found in neuronal cell bodies with axonal projections in close proximity to a neuritic plaque (Siegal *et al.*, 1994). PHFs are believed to be composed mainly of aggregates of a truncated portion of the microtubule-associated protein tau in a hyperphosphorylated state (Kidd, 1963; Kidd, 1964; Goedert *et al.*, 1996). Tau normally binds to α - and β -tubulins, facilitating microtubule assembly and stabilization *in vivo*, and thereby has a substantial role in microtubule-associated axonal transport mechanisms vital to neuronal functioning (Siegal *et al.*, 1994). As shown in Figure 4-3, microtubule assemblies are required for fast axonal transport of mitochondria and synaptic vesicles

3. Illustration based on the current view of neuritic plaque formation as described by Ulrich, J. (1993) Histochemistry and immunohistochemistry of Alzheimer's disease, volume 27, p.44.

from the perikaryon to the synapse, as well as for disposal of foreign substances (Wiengarten *et al.*, 1975; Cleveland *et al.*, 1977; Siegal *et al.*, 1994). Hyperphosphorylated tau self-associates but can also sequester and bind normal tau (Iqbal *et al.*, 1998). Glycosaminoglycans (GAGs), such as heparan sulfate and heparin, have been shown to mediate assembly of tau into fibrils and stimulate tau phosphorylation, promoting microtubule disassembly *in vitro* (Beyreuther and Masters, 1996; Goedert *et al.*, 1996). It has been postulated that while neuronal membrane damage could occur because of A β neurotoxicity present in the plaque core, the associated GAGs gain access to the cytoplasmic tau present in neurite extensions, mediate NFT assembly and cause premature cell death through microtubule dissociation and inefficient axonal transport (Goedert *et al.*, 1996; Iqbal *et al.*, 1998). Further to this point, frameshift mutants of proteins directly or indirectly connected to plaque formation *in vivo*, such as β APP and ubiquitin-B, have been localized to NFTs as well as to neuritic plaques (van Leeuwen *et al.*, 1998).

Figure 4-3. Schematic representation of a neuron from perikaryon to synapse illustrating the role of microtubule assemblies (and tau) in fast axonal transport mechanisms. Failure of tau to stabilize microtubule assemblies would lead to the breakdown of these mechanisms and result in neuronal dysfunction.



4.1.3 Synchrotron FTIR microspectroscopy of the AD and control hippocampus

As already discussed in Chapter 1, FTIR spectroscopic investigation of biological molecules, whether in model systems *in vitro* (section 1.5) or tissue components *in situ* (section 1.6), has become a recognized analytical method over the last few decades. For *in situ* studies, one key advantage is that characteristic absorptions due to each tissue component (lipid, carbohydrate, proteins and nucleic acids) may be detected in a single spectrum (section 1.6). This advantage was pointed out in Chapter 1 for simultaneous observation of absorption bands due to the protein and lipid constituents of hippocampal white matter (section 1.6). As explained there, the amide I profile ($1600\text{-}1700\text{ cm}^{-1}$) is particularly useful in identifying change in protein conformation such that structures involving strong H-bonds (*i.e.*, β -sheet proteins) will display amide I vibrations at lower frequency to those involving longer or weaker H-bonds (*i.e.*, α -helical proteins). Also discussed in Chapter 1 was the utility of an IR microscope attachment to the spectrometer (FTIR microspectroscopy, section 1.2.4) which permits spectral acquisition at focal spots (pixels) on a thin tissue section. Certain assigned spectral features found in the collection of pixels can then be compared upon calculation of 2D or 3D contour plots (section 1.7.4) to reveal the distribution of tissue constituents in the mapped section. Finally, as previously discussed, the use of a bright synchrotron source, rather than the conventional global, reduces the diffraction limit and allows for greater spatial resolution ($< 10\ \mu\text{m}$ spot diameter) in the FTIR image (section 1.2.5). Therefore, through the use of synchrotron FTIR microspectroscopy the structure of cellular to sub-cellular components of a tissue can be examined.

4.1.4 Objectives of current study

The classical lesions of AD (neuritic plaques and the NFTs) can be visualized microscopically by Bielschowsky silver staining of thin sections of brain tissue (Ulrich, 1993; Esiri and Morris, 1997). With serial stained sections as a guide for the general location of plaques and tangles FTIR synchrotron microspectroscopy was utilized in the current investigation to examine macromolecular structure in unstained AD and control hippocampal tissue. More specifically, it was hypothesized that synchrotron FTIR microspectroscopic imaging would be sensitive enough to (i) Discriminate between diffuse and fibrillar amyloid within plaques, (ii) Detect diffuse amyloid deposition outside the confines of a

plaque in the absence of positive staining, and (iii) Discriminate between fibrillar amyloid and the other protein aggregate of the disease, the neurofibrillary tangle, based on their respective spectral features. Dependent upon the success of these proposals, the long term goals address the overall question: will the IR signature(s) of the morphological features of AD (*i.e.* plaques, NFTs), if discernible, lead to a greater understanding of the disease state and its pathogenesis? Presented in this chapter are the results of the microspectroscopic examinations of the hippocampus from three individuals diagnosed with AD compared to two control individuals, obtained with the IR beamline at the SRC and IR beamline U10B at the NSLS. Due to the differences in the synchrotron stability and brightness an aperture of about 6-10 μm in diameter could be used at the NSLS as opposed to that of 15-20 μm at the SRC.

4.2 MATERIALS AND METHOD

Human brain tissue was acquired from the Neuropathology Department of the Health Sciences Centre (HSC, Winnipeg, Manitoba, Canada) and tissue extraction was carried out by Dr. M.R. del Bigio MD PhD. The excised hippocampus of autopsied brain (< 24 hours post-mortem) was flash frozen in liquid nitrogen, then freezer-stored (-70°C) until ready for sampling. AD diagnosed and age-matched control hippocampus were then warmed in a cryostat microtome to -30°C and mounted for cryosectioning at a section thickness of 8 μm . Sections were placed on low-e reflective MirrIR glass slides (Kevley Technologies, Chesterland OH) so that post-microspectroscopic staining could be carried out. For each sample collected on a MirrIR slide for the spectroscopic examination, a serial section was cut and placed on a standard glass slide and stained by the Bielschowsky method (carried out at the HSC Neuropathology laboratory) to illustrate the tissue morphology and the plaque/tangle locations. The morphology of each tissue section and the histopathology of any serial stains were assessed with guidance from Dr. del Bigio, prior to microspectroscopic analysis. Once IR microspectroscopic analysis was complete (sections 4.2.1 and 4.2.2), the samples on the MirrIR slides were stained by the Bielschowsky method (Ulrich, 1993) at the HSC neuropathology laboratory and unique spectral features were visually correlated to stained features (section 4.2.3). Histopathological assessment of the stained serial sections on glass and the stained sections on the MirrIR slides was carried

out by Dr. M.R. del Bigio at the HSC. Table 4-1 summarizes the hippocampal tissues examined, the identification number of the autopsied patient, the date the hippocampus was sectioned/placed on MirrIR slide, the synchrotron facility where the experiments were carried out and whether the post-microspectroscopic Bielschowsky stain was successful. Note in Table 4-1 that CON1 was lost during the staining process, therefore during subsequent stains the gelatin content of the water bath used to prepare the sample for staining was increased to prevent any further loss of samples.

Table 4-1. Hippocampal samples evaluated during doctoral thesis.

Brain	Identification number	Date sectioned	Date of spectroscopy	Synchrotron	Staining success
AD1	98R015	Jan. 1999	Jan., Mar. 1999	SRC	yes
AD2	99R003	May 1999	Aug. 1999	SRC	yes
AD3	99R028	Sept. 1999	Sept. 1999	NSLS	yes
CON1	98R016	Jan. 1999	Aug. 1999	SRC	no
CON2	98R013	Sept. 1999	Sept. 1999	NSLS	yes

4.2.1 Synchrotron FTIR microspectroscopy at the SRC beamline

FTIR microspectroscopy was carried out on samples AD1, AD2, and CON1 at the Synchrotron Radiation Center, Stoughton, WI, USA. Spectra were acquired in the reflectance mode on a Nicolet Magna 550 spectrometer equipped with a Nic-Plan microscope. Typically, 512 interferograms were collected, co-added and signal averaged with a nominal resolution of 4 cm^{-1} . In the course of a single 4-6 hour injection cycle, the 800 MeV beam current decayed from $\sim 260 \text{ mA}$ to $\sim 100 \text{ mA}$. In the absence of an upper aperture in the microscope, the illuminated area on the sample would have a diameter of about $30 \mu\text{m}$. Beam characteristics varied during the cycle, making it necessary to adjust the moving mirror velocity from time to time, in order to achieve the optimum signal-to-noise ratio in the fingerprint region. Decreasing the mirror velocity frequently improved the spectral quality in the fingerprint region of the spectrum ($1000\text{-}1800 \text{ cm}^{-1}$) but this increased spectral acquisition time. A transparent variable aperture (full field aperture, Spectra-Tech) was used for visualization of the peripheral tissue about the focal area. A $15 \times 15 \mu\text{m}^2$ to a $20 \times$

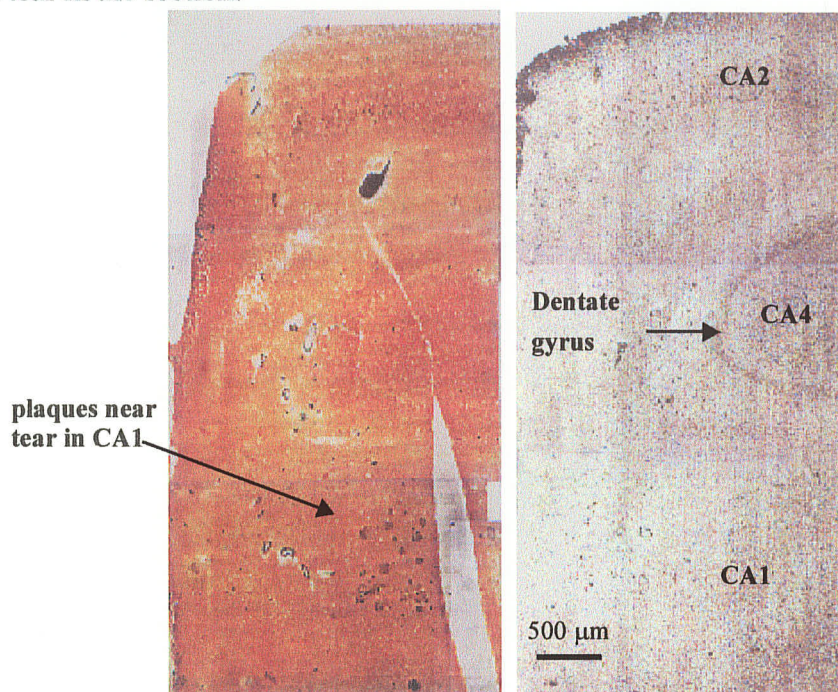
20 μm^2 aperture was used to gather focal spectra and line maps of pyramidal neurons with nearby tissue, as well as when area maps were acquired in tissue regions of interest. A single background was collected for each line map or area map to avoid stage whiplash, while for spot spectra a background was typically taken every hour.

The locations of the majority of plaques and tangles in the stained serial tissue sections from AD1 and AD2 were determined by light microscopic evaluation of the AD tissue pathology (summarized in Table 4-2). This preliminary inspection of the stained serial sections served as a guide for the subsequent IR microspectroscopy of the tissue sections placed on the MirrIR slides. The initial goal was to aim for regions of the tissue where amyloid deposition and NFTs were abundant. Therefore, numerous area maps were acquired in the CA1 and CA2 fields of the MirrIR tissue section from AD1 since these regions were rich in plaque and NFT formation (Table 4-2). Photomicrograph comparisons of the unstained section of AD1 used for spectroscopic examination and the stained serial section is presented in Figure 4-4. As can be seen in the photomicrograph of the serial stained section, hippocampus AD1 presented with a large number of plaques just to the left of the large tear in the CA1 below the dentate gyrus (Figure 4-4).

Table 4-2. Regions of interest in the hippocampal samples studied at the SRC

Brain	Identification number	Plaque locations	NFT locations	Number of area maps	Number of spectra in map data
AD1	98R015	CA1, CA2	CA1, CA2	11	247
AD2	99R003	CA1, CA4, molecule	CA1	21	987
CON1	98R016	-	-	7	217

Figure 4-4. Thin tissue section from Alzheimer's hippocampus AD1 on MirrIR slide (right) compared to stained serial section (left). The serial stain was used as a guide to localize the AD histopathology during the FTIR microspectroscopy. In this sample the majority of plaques (dark spots) were found in the CA1 field to the left of the tear in the section.



For the stained serial tissue section taken from AD2 however, a few plaques were localized to the CA4 field near the dentate gyrus and the molecular layer (Table 4-2). Thus the majority of spectral area maps were acquired in these regions on the MirrIR tissue section from AD2. Several spectral area maps were also acquired in the CA1 field of this tissue section from AD2 in an attempt to localize a large plaque identified in the stained serial tissue section. All spectral maps acquired on the section from the control hippocampus, CON1, were taken in the CA1 field for comparative purposes. The stained serial tissue section from CON1 did not present with any tissue pathology upon light microscopic examination, but the absence of tissue pathology in the MirrIR tissue section of CON1 could not be confirmed because the section was lost during the staining process after the IR microscopy had been carried out (Table 4-1). That is, even though the serial stain on glass of CON1 did not present with any tissue pathology, tissue morphology and pathology can

change abruptly within μm distances (*i.e.*, a neuron cell body is only 10-30 μm in diameter). In turn, stains of serial sections are only approximate guides to the tissue morphology/histopathology. FTIR images should only be compared to the stain of the tissue section examined by FTIR microspectroscopy. Unfortunately, the reflective coating on the MirrIR slide used for IR microspectroscopy in the present study was unpredictably sensitive to the chemicals used in the Bielschowsky staining method. Occasionally, a tissue section examined extensively by FTIR microspectroscopy would be lost during the staining process and the tissue histopathology could not be correlated to the FTIR image generated

4.2.2 Synchrotron FTIR microscopy at beamline U10B at the NSLS

Synchrotron FTIR microspectroscopy on samples AD3 and CON2 was carried out at beamline U10B at the NSLS, Upton, New York (Table 4-1). At the time of our experimentation the U10B port, located on the VUV ring, delivered the synchrotron radiation to a Spectra-Tech Ir μs TM scanning infrared microscope. In the absence of an upper aperture in the microscope, a sample area of 20 μm in diameter could be illuminated. Injection times were variable (ranging from every 2-5 hours) but during these short injection periods spectral acquisition could be paused and then resumed a few minutes later after the top-off was complete. The 800 MeV ring current was nearly 1000 mA with a 5 hour lifetime on average. Therefore, during spectral acquisition the current rarely fell below 450 mA before the acquisition was paused and the VUV ring was re-injected with electrons. Given these VUV ring parameters the brightness at the NSLS was substantially higher than that at SRC, thus the upper variable aperture used in the microscopy could be adjusted to between 6 and 10 μm in diameter. An aperture of 10 x 10 μm^2 was utilized for collection of most spectral maps except for two spectral maps in which the aperture was set to 6 x 6 μm^2 . These latter two maps were acquired with the aperture lower limit for the purpose of retrieving images of higher resolution in regions previously examined with the larger aperture.

Tissue pathology was assessed at HSC (Dr. M.R. del Bigio) in Winnipeg prior to spectroscopic examination at the NSLS. NFTs were not apparent in the stained serial section from the AD3 brain (not shown), thus localization of plaques and A β deposition was the primary focus of the spectroscopic examination of AD3. Shown in Figure 4-5 is the spectroscopically examined AD3 tissue section on the MirrIR slide before and after the

staining process. Similar to the stained serial stain on glass slide (not shown), the stained section on the MirrIR slide confirmed that the majority of plaques were localized to the moleculare near the dentate neurons and in the CA4 field of hippocampus AD3 (Figure 4-5). Therefore, the majority of spectral maps acquired on the AD3 tissue section were taken in the moleculare and in the CA4 field (Table 4-3). For comparative purposes, when the CON2 control hippocampus tissue section was examined, spectral maps were acquired in both the moleculare and the CA4 field as well as in the CA1 field. Upon post-microsopic staining, the CON2 tissue section on the MirrIR slide did not present with any tissue pathology.

Figure 4-5. Photomicrographs of the AD3 tissue section on the MirrIR slide examined spectroscopically prior to staining (left) and after staining (right). The majority of plaques (small brown spots) are localized to the moleculare in the stained photomicrograph.

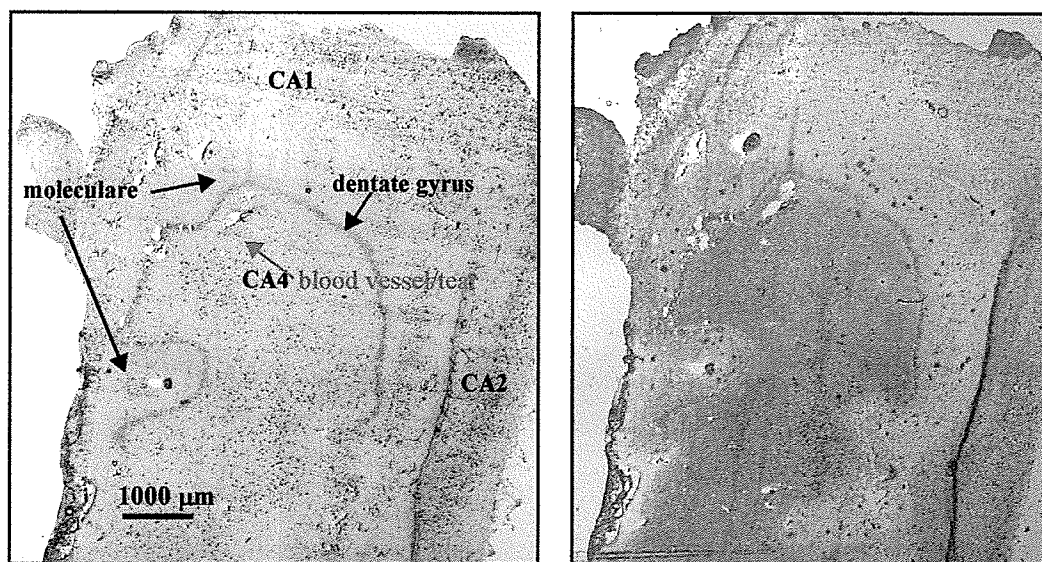


Table 4-3. Regions of interest in the hippocampal samples studied at the NSLS

Brain	Identification number	Plaque locations	NFT locations	Number of area maps	Number of spectra in map data
AD3	99R003	CA1, CA4, moleculare	none	6	1605
CON2	98R013	-	-	5	929

4.2.3 Spectral preprocessing and data analysis

Nicolet OMNIC/AtIµs™ software was used in data acquisition and data analysis. Residual water vapor was subtracted interactively from individual spectra using WIN-IR™ software. Individual spectra taken from different regions of the hippocampus were processed using WIN-IR™ software. Spectral processing details accompany individual spectra presented in section 4.3. For spectra within map files, the OMNIC™ automatic correction for water vapor was used. AtIµs™ software converted spectral map files into 2D contour plots derived by comparison of the relative peak height ratios found for each spectrum of the line or area maps (discussed in section 1.7.4). Profiling details can be found with their respective 2D contour plots presented in section 4.3. The 2D contour plots were derived by AtIµs™ and smoothed using Microcal™ Origin6.0 to improve the quality of the IR images for direct comparison to the light microscopy images of the stained tissue. Upon completion of IR microspectroscopic analysis and staining of the MirrIR sections, these IR images were visually compared to photomicrographs of the stained tissue and unique spectral features were correlated to tissue pathology.

4.3 RESULTS AND DISCUSSION

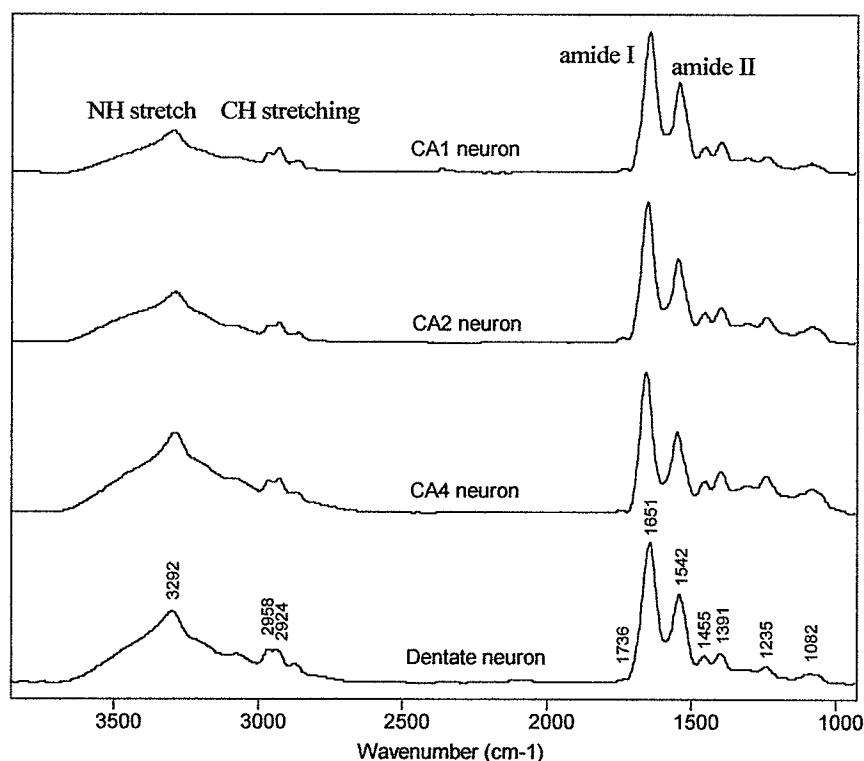
The morphological features detectable by FTIR microspectroscopy of the control hippocampus are presented in section 4.3.1. The spectra of pyramidal neurons and dentate neurons did not display significant differences. In contrast, spectra of the moleculare, radiatum and fimbria regions displayed in increasing order enhanced lipid to protein content. FTIR imaging of control hippocampus based on the relative contribution of lipid to protein also revealed some interesting results. For example, visual discrimination of neurons from

the neuropil and surrounding parenchyma in the gray matter and the dentate gyrus was possible in the FTIR images generated by the relative intensity of the CH₂ (lipid) to NH (protein) stretching absorptions in each spectrum (Figure 4-8). In addition, lipofuscin granules, a hall mark of the aging hippocampus, could be localized in the FTIR images (Figure 4-9) and distinguished from the location of the nucleus (Figure 4-10). The FTIR images of β -amyloid angiopathy (section 4.3.2) and β -amyloid plaque deposition (section 4.3.3) in AD hippocampus verified that the amide I band contour of fibrillar amyloid was similar to that suggested by *in vitro* studies of amyloid fibril formation (Fraser *et al.*, 1991). Moreover, the spectral signature of fibrillar amyloid *in situ* was found to include absorption bands typical of an aggregated protein composed of truncated peptides arranged in an antiparallel β -sheet conformation. In contrast, amorphous deposits of A β -peptide were found to have an increased amount of α -helical protein possibly due to the plaque-associated proteins involved in the seeding or nucleation of a fibrillar plaque core (Ulrich, 1993; Choo *et al.*, 1996). In section 4.3.4, diffuse deposition of A β -peptide outside the boundaries of plaque formation was detected by FTIR imaging in two tissue sections (AD1 and AD3), however additional AD and control samples would need to be examined to confirm this possibility.

4.3.1 FTIR microspectroscopic imaging of control hippocampal tissue

Prior to 2D contour analysis, individual focal spectra of pyramidal neurons, dentate neurons, and the layers of the hippocampus (moleculare, radiatum and fimbria) were examined. The mid-IR spectral features from the cell bodies of pyramidal neurons in CA1, CA2 and CA4 fields and neurons of the dentate gyrus were found to be very similar (Figure 4-6). As shown in Figure 4-6, the neurons exhibited a predominance of absorption bands assignable to protein, such as the NH stretch (3292 cm⁻¹), amide I (1651 cm⁻¹), amide II (1542 cm⁻¹) and the amide III (1235 cm⁻¹). In addition, the methyl to methylene stretching ratio (2958 cm⁻¹:2924 cm⁻¹) was found to be near unity and in the fingerprint region the methyl asymmetric (1455 cm⁻¹) and symmetric deformation (1391 cm⁻¹) slightly greater than that of the nearby methylene bending absorptions. The near equivalence of methyl to methylene absorption band intensities is additional spectral evidence that the protein content of a neuron predominates over the lipid content (see sections 1.5.1, 1.5.2 and 1.6).

Figure 4-6. Comparison of the mid-IR signature of pyramidal neurons from the CA1, CA2 and CA4 fields to the dentate neuron of the granular layer of the dentate gyrus illustrating the similar lipid to protein ratio.⁴ Absorption band assignments are as follows: [amide ν (NH) 3292 cm^{-1}]; [ν_{as} (CH₂) 2924 cm^{-1}]; [ν_{as} (CH₃) 2958 cm^{-1}]; [acyl ν (C=O), 1736 cm^{-1}]; [amide I 1651 cm^{-1}]; [amide II, 1542 cm^{-1}]; [δ_{as} (CH₃) and δ_{s} (CH₃), 1455 and 1391 cm^{-1} , respectively]; [amide III 1235 cm^{-1}]; [ν (C-O) 1082 cm^{-1}],

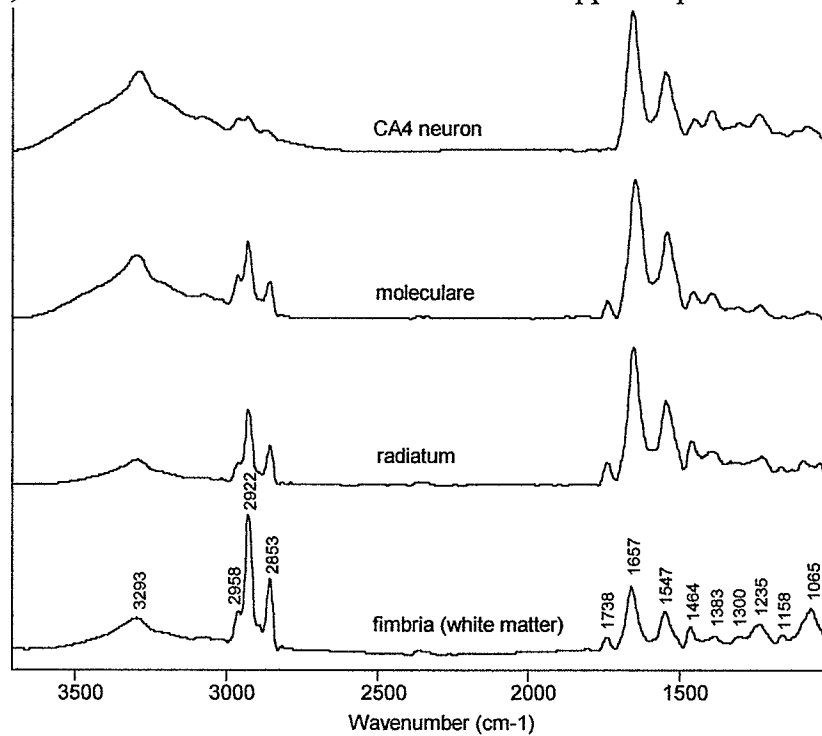


Spectra of the tissue regions peripheral to the neuronal cell bodies, which contains glial cells and axonal projections, exhibited noticeable features due to both protein and lipid (Figure 4-7). Spectra taken of the moleculare, radiatum and the fimbria displayed a progressive increase in absorptions due to lipid relative to those due to protein. For the moleculare, which neighbors the dentate neurons, the relative intensity of the NH stretch (3292 cm^{-1}) to the methylene CH stretch (2924 cm^{-1}) was found to be decreased in comparison to that observed for the CA4 field neuron. Furthermore, other lipid-associated bands were

4. Spectra were extracted from spectral maps taken on a tissue section from control hippocampus CON2 at NSLS with a 10 x 10 μm^2 aperture. Preprocessing included deconvolution and smoothing.

enhanced in this layer, such as the ester C=O stretch, methylene stretching (2922 and 2853 cm^{-1}) and methylene scissoring (1464 cm^{-1}).

Figure 4-7. Comparison of spectra taken of a CA4 pyramidal neuron, the moleculare, radiatum and white matter of the control hippocampal tissue.⁵



Similar changes were found to be apparent in spectra of tissue regions proximal to the pyramidal neurons of the CA1, CA2 and CA3 fields (data not shown), which is comprised of mainly astrocytes and neurite extensions (neuropil). Next to the moleculare is the radiatum (Figure 4-1), where axonal projections “radiate” towards the curve of the dentate gyrus. The radiatum was found to have a greater lipid to protein ratio than the moleculare. For example, the relative intensity of the methylene (2922 cm^{-1}) to methyl (2958 cm^{-1}) stretch is noticeably higher in the spectrum taken of the radiatum than the moleculare (Figure 4-7). In addition, the greater relative intensity of the methylene stretching (2922 cm^{-1}) to the NH stretch (3293 cm^{-1}) confirmed that the lipid content was greater than that of the

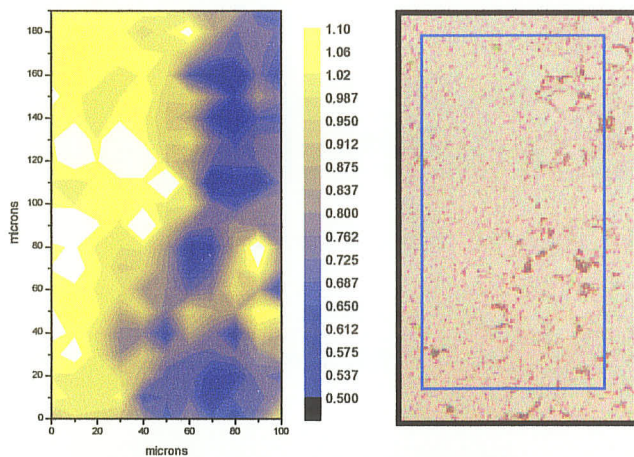
5. The fimbria and radiatum spectra from CON1 were taken at SRC with an $18 \times 18 \mu\text{m}^2$ aperture, while those of the CA4 pyramidal neuron and the moleculare of hippocampus CON2 were taken with a $10 \times 10 \mu\text{m}^2$ aperture at the NSLS. Spectral processing involved deconvolution and smoothing.

protein in the radiatum. These observed spectral changes for the radiatum layer were only further augmented in spectra taken in the fimbria with additional increases in other absorptions due to enhanced content of phospholipid (Figure 4-7 and recall Figure 1-13).

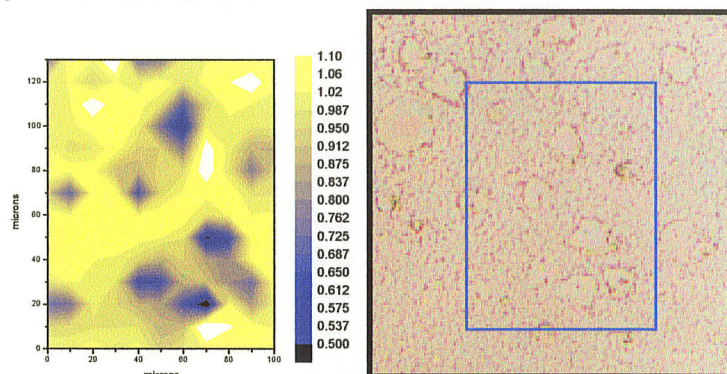
Given that the predominant spectral difference between neuronal tissue and neuropil was in the relative contributions of protein to lipid, FTIR microspectroscopic imaging proceeded by exploitation of this simple discriminating observation. Larger spectral maps with greater spatial resolution were obtained at the NSLS due to improved signal-to-noise, shorter spectral acquisition time and software capable of pausing map acquisition during injection. FTIR images were created from the 2D contour profiles calculated by taking the relative intensity of the lipid methylene asymmetric stretch (2923 cm^{-1}) to that of the protein NH amide stretch (3294 cm^{-1}) for each spectrum in a mapped array. Typical examples of the FTIR microspectroscopic images derived from spectral maps acquired in different regions of the control hippocampus CON2 are presented in Figure 4-8. The spatial distribution of the neurons in each of the five FTIR images (spatial resolution of $10\text{ }\mu\text{m}$) bore close resemblance to that seen in the light microscopy photomicrographs of the unstained MirriR tissue section (three of the five CON2 maps shown in Figure 4-8). In Figure 4-8a, the dentate neurons (navy) are easily distinguished from the moleculare (yellow to white) by differences in the relative contribution of lipid ($\nu_{\text{as}}(\text{CH}_2)$) to protein ($\nu(\text{NH})$) in each spectrum. In contrast, the pyramidal neurons of the CA1 field (Figure 4-8b) and the CA4 field (Figure 4-8c) are more spatially spread out in the tissue than the dentate neurons, similar to their spatial distribution revealed by light microscopy. In all of these 2D contour plots, the CH_2/NH stretching ratio decreases accordingly: white (> 1.1), light yellow (1.1), navy (0.5) and black (< 0.5). However, these ratios do not infer that the lipid-to-protein ratio is 1.1, 0.5, *etc.*, because the actual relative concentrations cannot be derived without calibration to a model lipid/protein film prepared *in vitro* or cross validation to a known biochemical assay (see section 1.7.1 in Chapter 1).

Figure 4-8. FTIR images (left) of control hippocampus tissue section compared to light microscopy photographs (right).⁶ See text for more details.

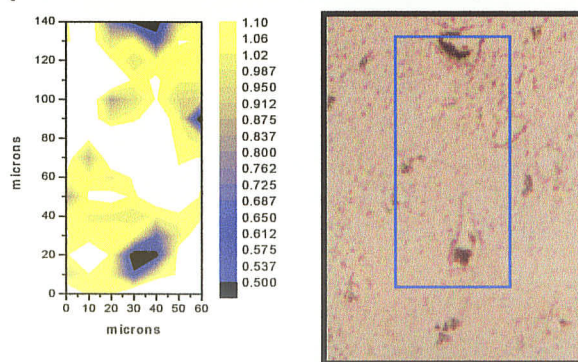
(a) Dentate gyrus: granular layer and molecular of CON2



(b) Pyramidal neurons in the CA1 field of CON2



(c) Pyramidal neurons in the CA4 field of CON2

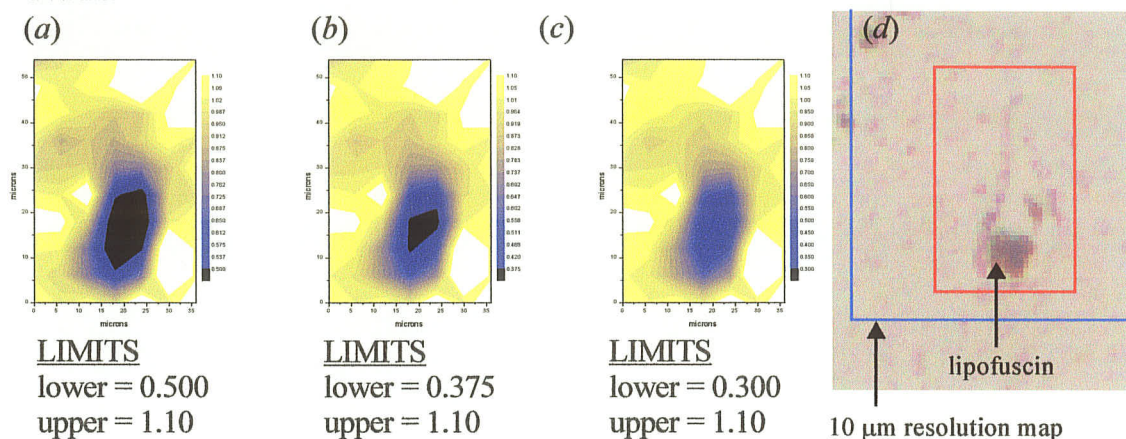


6. All FTIR images (left) are 2D contour profiles calculated by taking the relative peak height of the lipid CH_2 stretch (2923 cm^{-1}) to the protein NH stretch (3293 cm^{-1}).

In all of the FTIR images presented in Figure 4-8, the relative contribution of lipid to protein was found to decrease moving from the parenchyma (white to yellow) to the neuropil proximal to the neuronal cell body (gray), to the neuron cell body (navy) to the nucleus of the perikaryon (black). Interestingly, if the CH_2/NH stretching ratio in these spatial regions on the tissue could be translated into the relative concentration of lipid to protein, a ratio of unity would be equivalent to 50% lipid and 50% protein (parenchyma), a ratio of 0.8 would be equivalent to 40% lipid and 60% protein (neuropil), and a ratio of 0.5 would be equivalent to 25% lipid and 75% protein (perikaryon). The gray matter of the brain has been reported to be 50% lipid and 50% protein by dry weight, but this includes parenchyma and neuronal cell bodies which are unevenly distributed within the gray matter (Siegal *et al.*, 1994). In contrast, the relative contribution of lipid to protein in focal regions within the gray matter can be examined individually by synchrotron FTIR microspectroscopy (also see section 1.6). On a preliminary basis, details regarding gray matter heterogeneity and the relative contribution of molecular constituents *in situ* can be discerned by FTIR imaging, in the absence of histochemical staining (*i.e.*, without external validation) when the tissue morphology in the FTIR image and the light microscopy photomicrograph are similar.

Under light microscopy, the neurons of the normal hippocampus typically take on a featureless glassy appearance while still being distinct from the neuropil. Within the aging hippocampus however, the pyramidal neurons progressively accumulate lipofuscin granules (remnants of lysosomal waste) in their cytoplasm (Esiri and Morris, 1997). The presence of lipofuscin granules in the cytoplasm of the pyramidal neurons, depicted by the photomicrograph of the CA4 field of CON2 (CON2 was a 51 year old female), was also confirmed in the FTIR image by the blackened area inside the perikaryon (Figure 4-8c). In the 2D contour plot of Figure 4-8c this blackened region represented a position where the protein content increased beyond the lower limit of the CH_2/NH stretching ratio. To further examine this phenomenon, a second spectral map was acquired with greater spatial resolution (6 μm) of one of the CA4 field neurons that exhibited lipofuscin upon light microscopy (Figure 4-9).

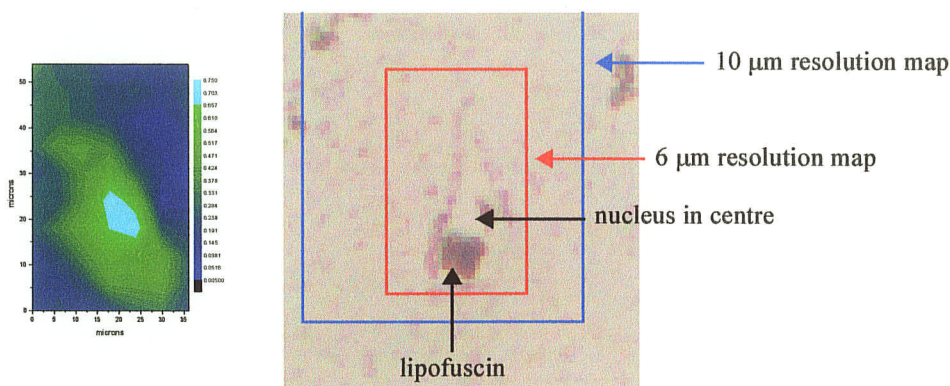
Figure 4-9. The relative contribution of lipid to protein in a CA4 field pyramidal neuron and surrounding neuropil (6 μm spatial resolution). The FTIR image was constructed using the CH_2/NH stretching ratio in each spectrum. The lowest ratio detected was in the perikaryon, perhaps due to lipofuscin. See the text for more details.



Similar parameters were used to create the 2D contour profile of this CA4 neuron map (displayed in Figure 4-9a) as were used in the creation of the FTIR images at 10 μm spatial resolution (Figure 4-8c). In order to estimate the distribution of protein inside the perikaryon, the lower limit for the 2D contour plot was decreased (Figure 4-9b and c). As is shown in Figure 4-9, the CH_2/NH stretching ratio inside the perikaryon at a position proximal to the lipofuscin granules in the light microscopy image, was 0.300, corresponding to an approximate protein composition of 85% in comparison to 15% lipid. This observation, however did not rule out a nucleic acid contribution from the nucleus. Therefore, a 2D contour profile was calculated to establish the relative distribution of protein and nucleic acid in this CA4 neuron map (Figure 4-10). The 2D contour profile shown in Figure 4-10 was prepared by calculating the relative intensity of the nucleic acid ribose sugar-base coupled vibration at 1418 cm^{-1} (see section 1.5.4) to the protein NH stretch at 3292 cm^{-1} . This ratio was highest in the centre of the perikaryon, rather than where the lipofuscin was located in the photomicrograph of the unstained tissue section. Similar results were obtained when the relative peak height intensity of either $1705\text{--}1710\text{ cm}^{-1}$ (due to base $\text{C}=\text{O}$ stretching) or 1375 cm^{-1} (due to dA:dG anti-glycosidic linkage) to the NH stretch was used

to create a 2D contour plot (data not shown). Therefore, the increased protein content found near the bottom tip of the perikaryon depicted in Figure 4-9*d* was due to lipofuscin content, while the position of nucleus of this pyramidal neuron may be centred in the cytoplasm (see Figure 4-10).

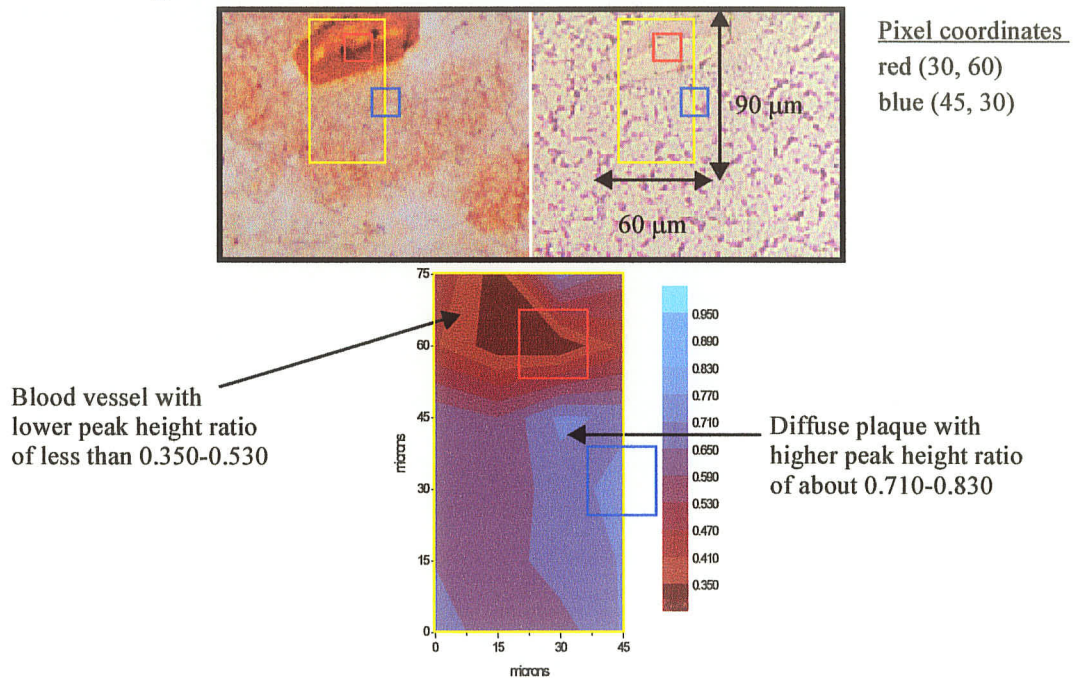
Figure 4-10. Relative contribution of nucleic acid to protein in CA4 pyramidal neuron in Figure 4-9. The FTIR image (left) of the pyramidal neuron is compared to the light microscopy image (right) of the unstained tissue. The upper and lower limits shown for the 2D contour depict peak height intensity of the ribose sugar-base coupled vibration at 1418 cm^{-1} to the NH stretch at 3292 cm^{-1} . This ratio was highest in the centre of the perikaryon. See the text for details.



4.3.2 FTIR imaging of amyloid angiopathy in the AD hippocampus

Recall from section 4.1.2, that $A\beta$ peptide can deposit within and near blood vessels in the brain (amyloid angiopathy). Amyloid angiopathy results in a weakening of the vessel walls and may promote stroke or cerebral hemorrhage (Maury, 1995). The frequency of $A\beta$ peptide deposition peripheral to blood vessels in AD brain, in combination with the ease with which blood vessels are recognizable by light microscopy, made major blood vessels a target for this current study. In the first hippocampus examined by FTIR microspectroscopic imaging, AD1, a diffuse plaque around a CA1 blood vessel was observed and confirmed by a faint staining of the area by the Bielschowsky method (Figure 4-11).

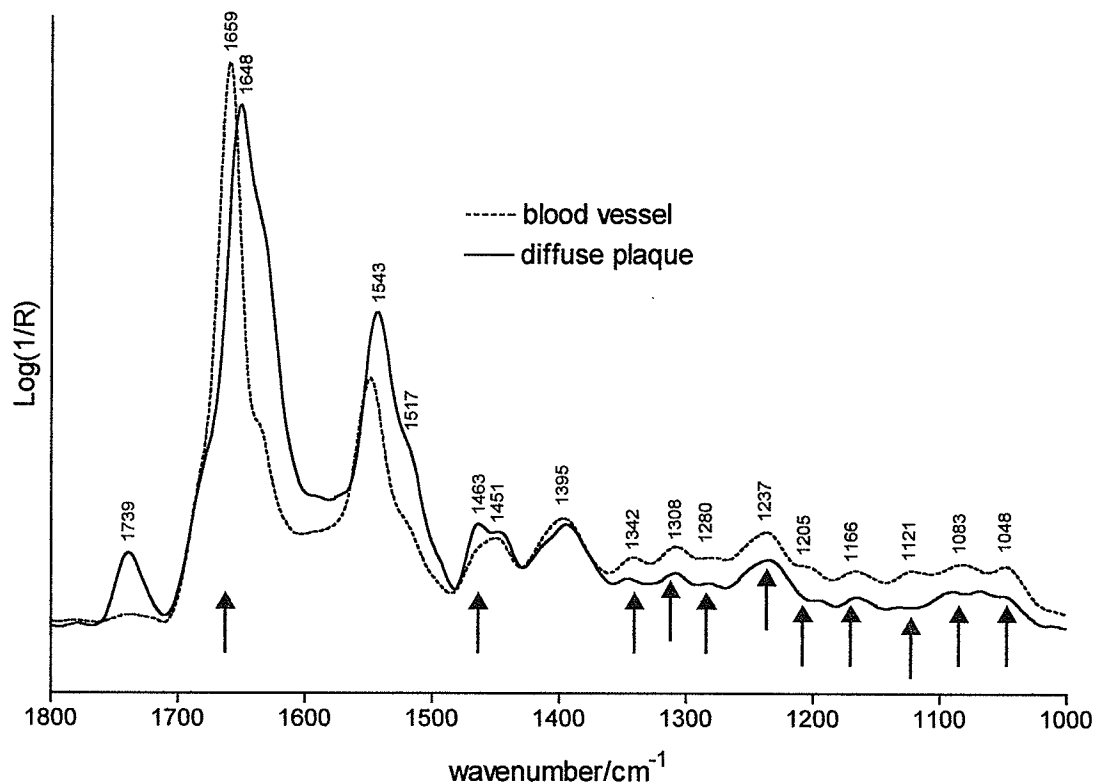
Figure 4-11. Diffuse A β peptide deposition peripheral to a blood vessel in AD1. The yellow box outlines the coordinates of the spectral map on the unstained tissue (right) with a step size of 15 μm , thus the area sampled extends by the length of one half the aperture in both the x and y directions. The 2D contour plot (below) can be compared to the photomicrograph of the stained tissue section (left). The 2D contour plot was calculated from the relative peak height intensity of 1637 cm^{-1} (β -sheet) to 1660 cm^{-1} (collagen and/or α -helical proteins). Spectra extracted from the pixels highlighted in red and blue for the blood vessel and diffuse plaque, respectively, are shown in Figure 4-12.



The 2D contour shown in Figure 4-11 was prepared by calculation of the relative peak height of the β -sheet component band of the amide I (1637 cm^{-1}) to that assigned to either collagen and/or α -helical proteins (1660 cm^{-1}) for each spectrum of the mapped array. Only blood vessels in the brain contain collagen. However, given the nominal spectral resolution used in this study (4 cm^{-1}), the 1660 cm^{-1} band represents collagen for a pixel focused on the blood vessel wall and α -helical proteins for a pixel focused on the surrounding parenchyma. As depicted in the 2D profile, dark brown to red represents the blood vessel which had a lower relative peak height ratio (0.350 to 0.530) than the diffuse plaque (0.710 to 0.830) represented by purple to blue (Figure 4-11). Direct comparison of a spec-

trum taken from the orange/red region (relative peak height = 0.410) to that from a lighter blue region (relative peak height = 0.830) in the 2D contour revealed that the collagen spectrum of the vessel was distinctive from that of the amyloid plaque (Figure 4-12).

Figure 4-12. Spectral comparison of a focal spectrum taken upon the CA1 blood vessel (dotted line) and that taken on a portion of the diffuse plaque about the vessel periphery (solid line). See Figure 4-11 for location of these focal spectra in the spectral map taken on tissue from hippocampus AD1. Arrows below the spectra denote the absorptions due to collagen content in the blood vessel.

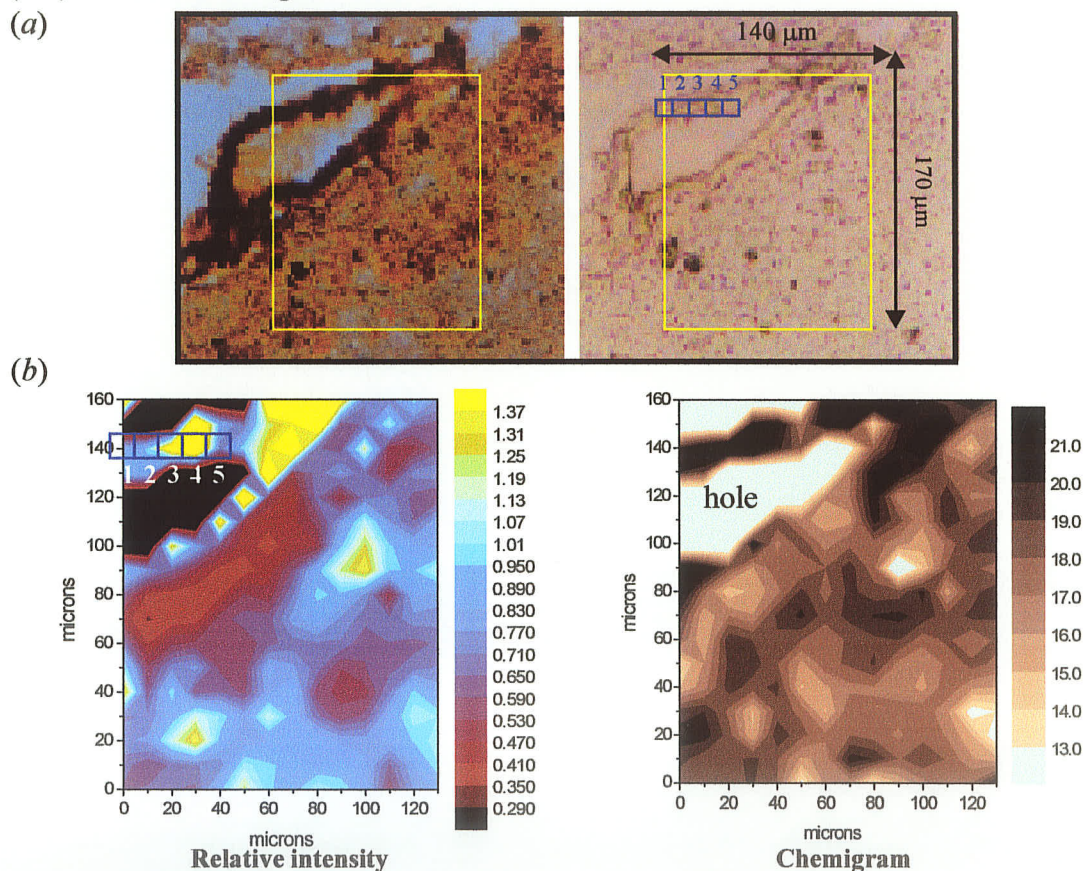


The arrows in Figure 4-12 denote the characteristic collagen fingerprint such as the collagen triple helix amide I (1659 cm⁻¹), amide III/proline wagging region (1205, 1237, 1280, 1308 and 1342 cm⁻¹) and enhanced carbohydrate absorptions (1048, 1083, 1121 and 1166) due to the glycosylated state of the protein (see Chapter 3). The spectrum taken within a region that contained diffuse amyloid deposition verified by post-spectroscopy staining, displayed an amide I with a broadened profile and a maximum at a lower fre-

quency, indicative of a loss of helical protein structure (Figure 4-12). This frequency shift to lower wavenumber was also apparent in the amide II vibration (1543 cm^{-1}). Furthermore, an amide I shoulder at about 1635 cm^{-1} accompanied the low amide I maximum at 1648 cm^{-1} (Figure 4-12). Finally, there was an enhanced absorption due to the ring vibration of tyrosine (1517 cm^{-1}) relative to the intensity of the amide II and β -amyloid has been shown to have a high amount of aromatic amino acid residues in its primary structure (Ulrich, 1993) in comparison to other proteins, such as collagen.

Aside from detecting diffuse $A\beta$ deposition near the CA1 blood vessel of hippocampus AD1, diffuse and core β -amyloid were detected in a CA4 blood vessel of hippocampus AD3 (Figure 4-13). Shown in Figure 4-13*b*, are two different types of 2D contour profiles used to create two FTIR images of the tissue area. In one of these profiles a “chemigram”, defined as the integrated intensity of a defined spectral subregion, was calculated for each pixel using the spectral subregion, $1605\text{-}1640\text{ cm}^{-1}$ to illustrate where predominant absorptions due to β -sheet and/or aggregated proteins occur. The “chemigram” profile (Figure 4-13*b*, right) depicts an image very similar to the photomicrograph of the stained tissue (Figure 4-13*a*, left). For example, holes in the tissue would result in relatively less absorbance. Therefore, holes and locations where the tissue is very thin can be observed in the FTIR image as a very faint blue (Figure 4-13*b*, right). Likewise, regions of the tissue predominated by protein absorption are represented in this FTIR image by shades ranging from tan to dark brown. Another interesting point to note in the “chemigram” 2D contour plot is that the location of the darkest areas correspond to dark staining in the photomicrograph of the stained tissue. These dark regions in the “chemigram” FTIR image in Figure 4-13*b*, correspond to possible amyloid deposition on and peripheral to the blood vessel. However, since the spectra in the “chemigram” image were not normalized to a common overall intensity, variation in sample thickness and changes in the synchrotron IR throughput during map collection may have created artifacts in the 2D contour constructed from the integrated intensity of a single absorption band. Moreover, verification was required to confirm that amyloid was the main contributor to the dark brown regions of this FTIR image rather than interchain H-bonded collagen triple helices (see Chapter 3).

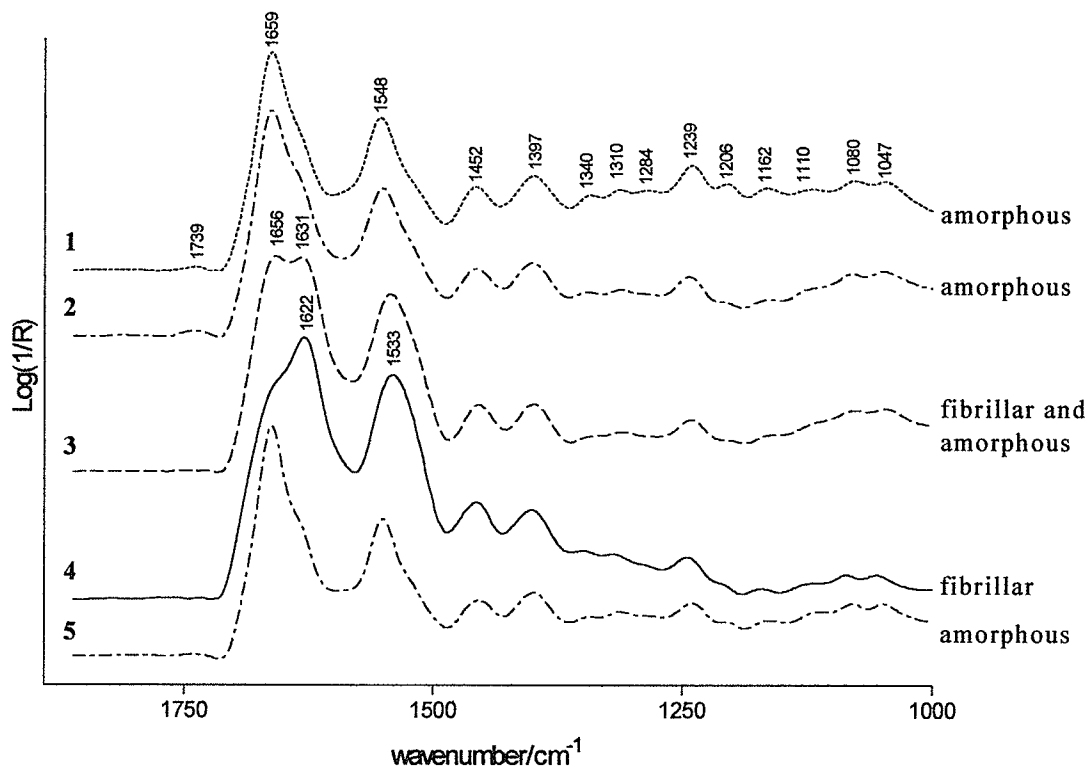
Figure 4-13. Detection of β -amyloid angiopathy in the CA4 field of hippocampus AD3. (a) Photomicrographs of the blood vessel and peripheral unstained tissue (right) and stained tissue (left). The area of the FTIR map is outlined in yellow ($10 \times 10 \mu\text{m}^2$ aperture is outlined in blue). (b) FTIR images: Left, the relative peak height intensity of 1625 (β -sheet and aggregated strands) to 1660 cm^{-1} (collagen amide I and or α -helical proteins) calculated for each pixel; Right, the integrated intensity of the spectral subregion, 1605 to 1640 cm^{-1} (β -sheet and aggregated strands), termed a “chemigram”, calculated for each pixel. Outlined on the unstained tissue in (a) and on the relative intensity profile in (b) is a series of 10 μm steps examined consecutively from left to right (1-5) on the blood vessel. The corresponding spectra (1-5) are shown in Figure 4-14.



Verification that the darker regions in the “chemigram” FTIR image were indeed due to amyloid was performed by constructing a second 2D contour plot (Figure 4-13b, left) to compare the relative contribution of β -sheet/aggregated strands to that of collagen

and/or α -helical proteins, as done previously for the CA1 blood vessel map of AD1. This relative intensity FTIR image was prepared upon calculation of the relative peak height intensity of 1625 cm^{-1} (β -sheet and aggregated strands) to 1660 cm^{-1} (collagen amide I and/or α -helical proteins) for each spectrum in the map (Figure 4-13*b*, left). A lower frequency for the numerator of this relative intensity profile, in comparison to that chosen to derive the FTIR image of diffuse amyloid angiopathy in Figure 4-11, was chosen for two reasons: (i) initial inspection of the individual spectra revealed that the amide I band of some pixels exhibited a resolved component band near $1622\text{--}1631\text{ cm}^{-1}$ (see discussion to follow for spectra in Figure 4-14), and (ii) the post-microspectroscopy stain of the tissue indicated dense amyloid was present along with diffuse amyloid, the former suspected to absorb at a lower frequency than the latter. Visually the distribution of β -sheet/aggregates to collagen and/or α -helical proteins in the relative intensity FTIR image added further support to the postulation that the dark regions in the “chemigram” FTIR image arose predominantly from enhanced amyloid deposition in those locations (Figure 4-13*b*). For example, the light blue to yellow shades in the relative intensity FTIR image (ratio = 0.830 to >1.37) correspond to the distribution of darker tones in the “chemigram” FTIR image, the exception being locations where the tissue was thin. Amyloid deposition tends to weaken the tissue, thus upon cryosectioning tissue regions high in amyloid deposition frequently tear or become thin. This latter point is exemplified by the higher β -sheet/aggregates to collagen/ α -helices ratio around the hole periphery (ratio = 1.01 to >1.37) in the relative intensity FTIR image in comparison to the “chemigram” FTIR image (Figure 4-13*b*, left and right, respectively). It should be noted that for the large hole inside the blood vessel, this ratio was set to zero (MicrocalTM Origin6.0) for contour pixels representing spectra with low S/N, to improve tissue morphology in the $1625\text{ cm}^{-1}/1660\text{ cm}^{-1}$ relative intensity FTIR image (Figure 4-13*b*, left). That is, spectra taken of the hole in the tissue section had a signal barely distinguishable from the noisy baseline. Thus, the $1625\text{ cm}^{-1}/1660\text{ cm}^{-1}$ ratio was set to zero for these pixels (black = 0) to distinguish the hole from the rest of the tissue. Interestingly, the inner portion of the blood vessel wall (light blue to yellow contours) appears to contain greater amyloid deposition than the outer portion of the blood vessel wall (red contours).

Figure 4-14. Spectral changes along a blood vessel in AD3 for discrimination of fibrillar amyloid from amorphous deposits of A β peptide. The spectra (1 to 5) were acquired consecutively from left to right in 10 μm steps of the aperture as outlined in blue on the unstained photomicrograph and the relative intensity FTIR image (Figure 4-13) of the CA4 field blood vessel.



In comparison to the profile calculated for the CA1 blood vessel that exhibited diffuse amyloid deposition (Figure 4-11), the relative intensity of the 1625 cm^{-1} amide I component band to that at of 1660 cm^{-1} more than doubled⁷ (Figure 4-13b, left). The main difference between this blood vessel in AD3 from that examined in AD1 was that diffuse plaque formation (ratio = 0.710-0.950) was accompanied by the presence of dense amyloid core (ratio = 1.01 to >1.37). Shown in Figure 4-14 are representative spectra that allowed discrimination of amyloid core and diffuse A β deposition from α -helix and the collagen triple helix. In these spectra, the amide I band was found to consist of two main component

7. In Figure 4-13b the 2D profile was differentiated up to a ratio of 1.37 for contrast in the contour plot, but the maximum ratio found for the 1625 cm^{-1} /1660 cm^{-1} relative peak height was 2.1.

bands, one due to β -sheet/aggregates ($1622\text{-}1635\text{ cm}^{-1}$) and the other due to either α -helix (1656 cm^{-1}) or the collagen triple helix (1659 cm^{-1}). Thus, the β -sheet component band in AD1 that was found at the higher frequency end of the $1622\text{-}1635\text{ cm}^{-1}$ range (Figure 4-12, *ca.*, 1637 cm^{-1}) may be indicative of diffuse amyloid deposition, while spectral pixels colored yellow in the FTIR image of the AD3 (Figure 4-13*b*) with a predominant amide I component band at 1622 cm^{-1} indicate the presence of protein aggregates contained within dense amyloid (Figure 4-14). With reference to pixels 1-5 in this FTIR image (Figure 4-13*b*) and the corresponding spectra in Figure 4-14, there was gradual increase in the intensity of β -sheet ($1631\text{-}1635\text{ cm}^{-1}$) relative to both α -helical proteins (1656 cm^{-1}) and collagen (1659 cm^{-1}) moving from pixel 1 to pixel 2 (blue, ratio = 0.83-0.95). Thereafter in pixel 3, the intensity of β -sheet (1631 cm^{-1}) relative to that of α -helical proteins (1656 cm^{-1}) was near unity, but in pixel 4 (yellow, ratio > 1.37) a component band attributable to aggregated peptides (1622 cm^{-1}) predominated the amide I profile. Finally, in pixel 5 (blue/purple, ratio = 0.77-0.89) the amide I band profile is similar to that of pixel 1 but the relative intensity of β -sheet proteins to α -helical proteins and collagen is slightly lower.

Based on these results, an amide I component band at 1622 cm^{-1} represents fibrillar amyloid deposition (plaque core), that near 1635 cm^{-1} represents amorphous/diffuse A β -peptide deposition, and an amide I component band at 1631 cm^{-1} is a combination of diffuse and fibrillar amyloid deposition (Figure 4-14). In the FTIR image of Figure 4-13*b*, blue (ratio = 0.83-0.95) represents a greater proportion of amorphous amyloid, while yellow (ratio > 1.37) represents a greater proportion of fibrillar amyloid in AD hippocampus. Moreover, yellow pixels in the FTIR image correspond to locations where the gray matter was darkly stained in the light microscopy image, while blue pixels correspond to regions where the stain lightened (Figure 4-13*b*). Therefore, visual discrimination between deposition of plaque core, diffuse amyloid, collagen and α -helical proteins in the FTIR image tissue appears to be possible due to alterations in the amide I band profile.

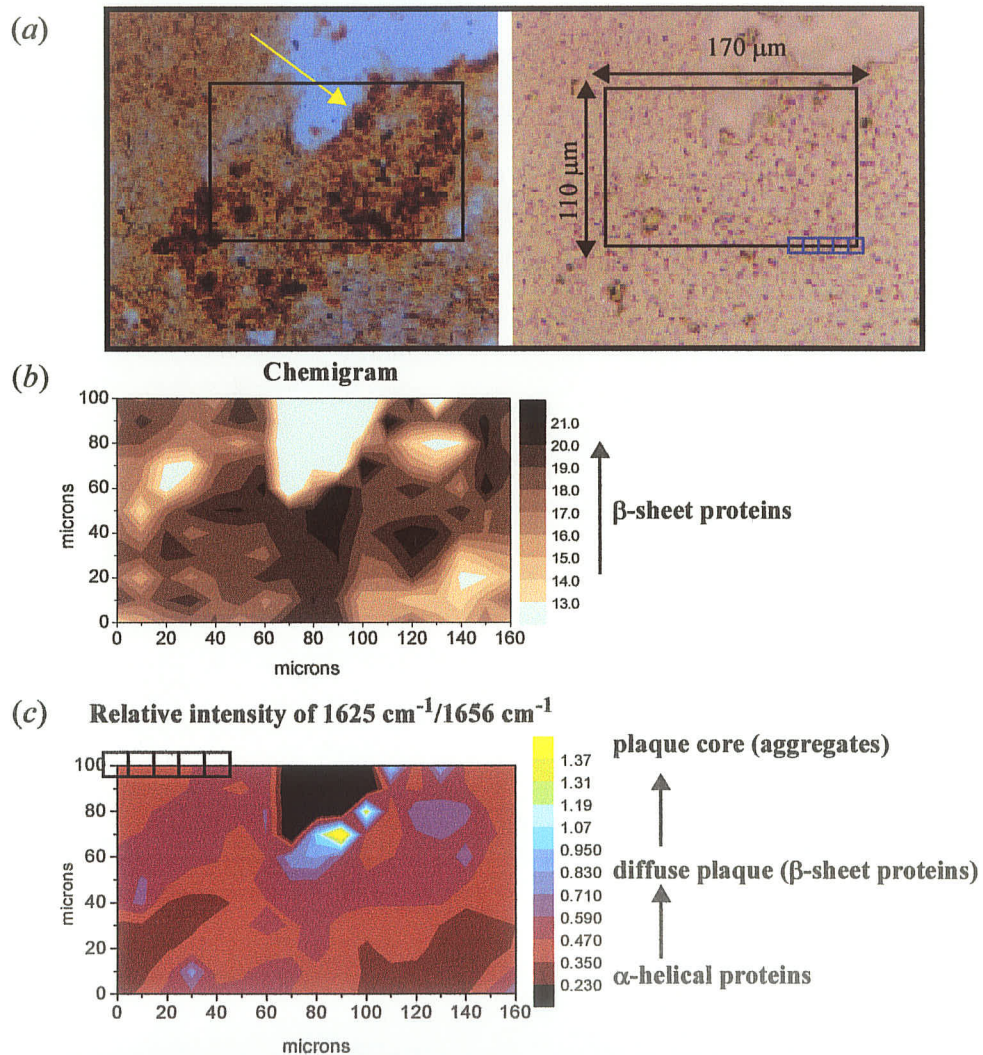
4.3.3 FTIR imaging of diffuse and mature neuritic plaques in the AD hippocampus

In all three AD tissue sections examined plaques were detected by Bielschowsky staining, the location of which has already been summarized in Tables 4-2 and 4-3. There was an observed difference in FTIR detection depending upon where the microspectros-

copy had been carried out, at the SRC or at the NSLS. Larger maps of better signal quality were acquired at NSLS as mentioned previously. Therefore, individual spectral maps presented in this section for samples AD1 and AD2 (SRC) were considerably smaller and with poorer spatial resolution (15-20 μm) than those acquired on sample AD3 at the NSLS (10 μm). In addition, some maps acquired at SRC were omitted from the 2D contour analysis due to occasional problems with beam power and stability that produced baseline artifacts and noise in the spectra. Nevertheless diffuse and neuritic plaques were detected on both samples AD2 and AD3. FTIR imaging of the areas examined in AD2 and AD3 revealed that amorphous and fibrillar amyloid coexist but can be distinguished based on a unique FTIR signature not seen in control hippocampus nor in regions where the amyloid deposition was merely diffuse. Unfortunately this unique FTIR signature was not detected in sample AD1, as the regions examined were just beyond the periphery of the amassment of plaques located in the CA1 field (Figure 4-4). Thus, the remaining FTIR images of sample AD1 will be presented in section 4.3.4 describing the detection of diffuse A β deposition outside of plaque locations which may be beyond the sensitivity of the staining technique.

In proximity to the CA4 blood vessel of AD3, an additional spectral map was collected at the bottom of the oval tear in the CA4 field (Figure 4-5) which confirmed the discrimination of plaque core from diffuse A β deposition and α -helical proteins. Shown in Figure 4-15 are photomicrographs of this spectral map along with the “chemigram” and relative intensity FTIR images. The “chemigram” FTIR image was again darkest in the regions that correspond to where the staining was most pronounced in the examined tissue area (Figure 4-15*a* and *b*). Areas where the tissue was thin were faintly colored in the “chemigram” image as before. However, the relative intensity image created by calculating the relative peak height intensity of 1625 cm^{-1} (β -sheet/aggregates) to 1656 cm^{-1} (α -helix) did not reveal dense amyloid core in all regions determined by staining as having dense amyloid deposits (Figure 4-15*c*). For example, regions about 30 μm below the tear appeared to have greater contributions from α -helical proteins than from either those that are predominantly β -sheet or composed of aggregated strands.

Figure 4-15. FTIR images representative of fibrillar and diffuse amyloid deposition in the CA4 field of hippocampus AD3. (a) Stained (left) and unstained (right) photomicrographs of the region examined using a 10 μm stepsize. Dark staining revealed dense fibrillar amyloid (yellow arrow). (b) Chemigram FTIR image using the spectral subregion between 1605-1640 cm^{-1} (β -sheet/aggregates). (c) FTIR image created by calculating relative peak height intensity of 1625 cm^{-1} (β -sheet/aggregates) to 1656 cm^{-1} (α -helix).



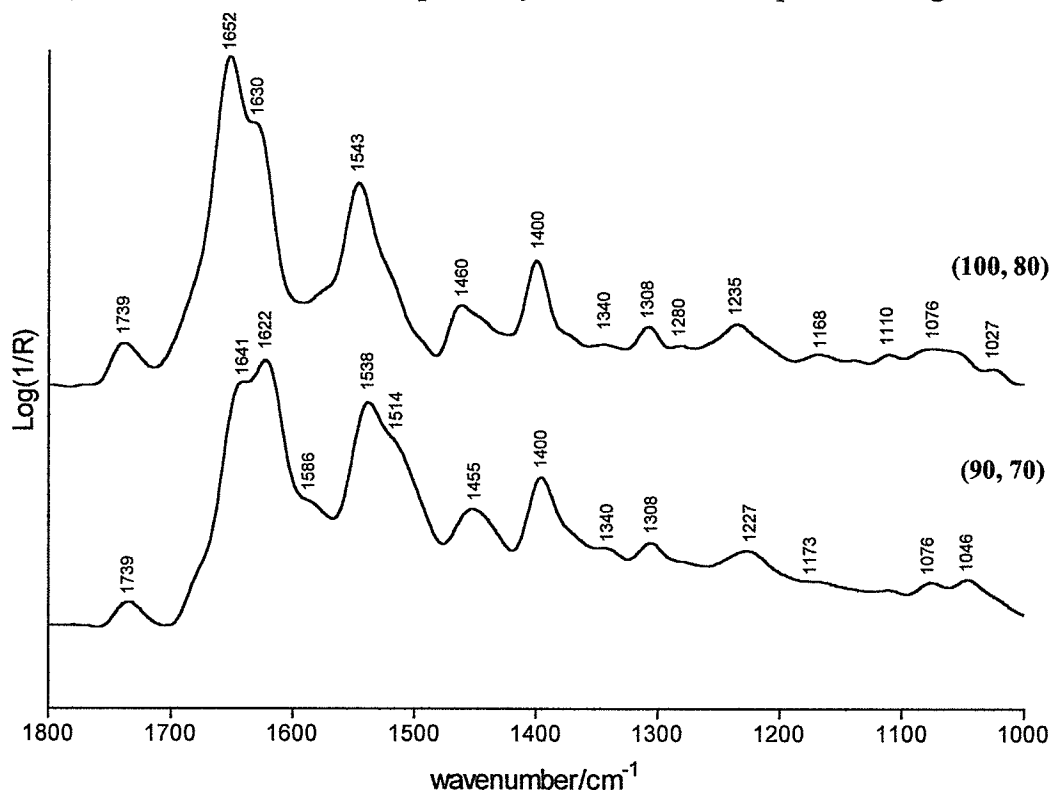
Overall these results suggest that the plaque seen in the Figure 4-15 may be more mature (*i.e.*, little diffuse A β -peptide deposition accompanied the plaque core). Recall from Figure 4-2 in section 4.1.2, that α -helical proteins are frequently found to associate to the periphery of mature plaques along with astrocytes and microglia (Ulrich, 1993; Choo *et al.*, 1996). The Bielschowsky stain in Figure 4-14a is also darker⁸ than that of Figure 4-13a, which confirms that the plaque in Figure 4-14a is more mature (*i.e.*, more fibrillar). The Bielschowsky stain is only sensitive to plaque and NFT formation, not to A β -associated α -helical proteins. In contrast, FTIR is sensitive to all the biochemistry in the tissue (section 1.6). Thus, if the relative contribution of A β -associated α -helical proteins to A β -peptide in a pixel is high, the FTIR image created by the 1625 cm⁻¹/1656 cm⁻¹ relative intensity would reveal a greater contribution of A β -associated α -helical proteins to A β -peptide as well (*i.e.*, red-purple pixels, ratio = 0.47-0.59).

The FTIR images in Figure 4-15 were similar to the FTIR images presented for the blood vessel in AD3 (Figure 4-13) such that amyloid deposition was detected in the relative intensity FTIR image at the same locations where the “chemigram” image indicated that the tissue was thin. However, the spectra acquired in locations that were most brightly colored in the relative intensity image (light blue to yellow) not only displayed a greater β -sheet/ aggregates absorption to that of α -helix, but also included unique absorptions that have yet to be characterized by other FTIR research investigations in the histopathology of AD tissue (Figure 4-16). Shown in Figure 4-16 are spectra extracted from the FTIR image in Figure 4-15c at coordinates (100, 80) and (90, 70) in the FTIR image. In comparison to spectra taken of amyloid angiopathy on the CA4 blood vessel (Figure 4-14), the spectra acquired at the coordinates (100, 80) and (90, 70) contained unique absorption bands in the fingerprint region besides a change in the amide I band profile. Of particular note are the prominent absorptions at 1400 cm⁻¹ and 1308 cm⁻¹, assigned to symmetric carboxylate (COO⁻) stretching and a contributing band (perhaps C=O in-plane bending) of the amide III combination of vibrations, respectively (see section 1.5.1). Since fibrillar amyloid is composed

8. The intensity of the background staining is similar in Figure 4-13a and Figure 4-15a since these regions are on the same stained tissue section (AD3), thus the intensity of the respective foregrounds can be directly compared to one another.

of a collection of A β peptides, intermolecularly H-bonded to each other to form the fibril aggregates, there would be an increase in the number of carboxy termini (in comparison to normal tissue) which could account for the increased intensity of the symmetric COO⁻ stretch. The asymmetric COO⁻ stretching vibration is typically found between 1610-1560 cm⁻¹ (Lambert *et al.*, 1987) near where absorptions due to glutamate, aspartate and arginine occur (see section 1.5.1). The absorption at 1586 cm⁻¹ in Figure 4-16 could tentatively be assigned to either glutamate, aspartate or arginine, however in light of the prominent absorption at 1400 cm⁻¹, and the lack of any known physiological explanation for an increase in Glu/Asp/Arg residues in the tissue, assignment of the 1586 cm⁻¹ band to the asymmetric COO⁻ stretch of terminal peptides is more plausible. The counterpart absorption from NH₃⁺ bending of the amino termini of truncated peptides may be partially masked by the amide II that arises from the NH bend of amide groups along the peptide backbone.

Figure 4-16. Representative spectra of fibrillar amyloid deposits in the CA4 field of hippocampus AD3. The spectra were extracted from map coordinates (100, 80) and (90, 70) which had 1625 cm⁻¹ (β -sheet and aggregated strands) to 1656 cm⁻¹ (α -helix) ratio of 1.17 and 1.37, respectively in the 2D contour profile in Figure 4-15b.



The characteristics of the amide I band profile in the fibrous amyloid spectrum acquired at the coordinates (100, 80) are in agreement with the results of synchrotron FTIR microspectroscopy of AD cortex, presented by Choo *et al.*, 1996. For example, Choo *et al.*, 1996, reported that the amyloid core of a plaque exhibited a β -sheet component band at 1632-1634 cm^{-1} along with an α -helical maximum at 1650-1656 cm^{-1} . Choo *et al.*, 1996, suggested that a higher frequency β -sheet component band at 1632-1634 cm^{-1} could be expected than that reported in FTIR *in vitro* studies (1620-1628 cm^{-1}) (Fraser et al, 1991), because A β -associated proteins *in situ* prevent close alignment of the A β -peptide aggregates. That is, longer/weaker intermolecular H-bonds between neighboring A β -peptide strands would shift the β -sheet component band to higher frequency. A similar argument could be made for the pixel at (100, 80) in the FTIR image presented in Figure 4-15. However, the fibrous amyloid spectrum acquired at coordinates (90, 70) exhibited an amide I maximum at 1641 cm^{-1} and component band at 1622 cm^{-1} , nearly 10 cm^{-1} lower in frequency than that suggested by Choo *et al.*, 1996 (Figure 4-16, bottom spectrum). This spectrum of fibrillar aggregates is in closer agreement with FTIR investigations *in vitro* which suggest the fibrillar aggregates absorb at significantly lower frequencies between 1620-1628 cm^{-1} (Fraser et al, 1991). Therefore, the 1641 cm^{-1} amide I maximum acquired at coordinates (90, 70) in Figure 4-15 may then be assigned to A β -peptide strands with weak intermolecular H-bonds (amorphous amyloid), while the component band at 1622 cm^{-1} may be assigned to A β -peptide strands with very strong intermolecular H-bonds (fibrillar amyloid). The 1652 cm^{-1} amide I maximum acquired at coordinates (100, 80) in Figure 4-15 may then be assigned to α -helical A β -associated proteins, while the component band at 1631 cm^{-1} may be assigned A β -peptide strands with a combination of weak and strong intermolecular H-bonds (amorphous and fibrillar amyloid). Recall from section 4.1.2, the A β -associated proteins are thought to participate in the nucleation of diffuse A β -deposition into A β -fibril formation, but in a mature neuritic plaque these A β -associated proteins are localized to the periphery of the plaque core (Ulrich, 1993). Therefore, the amide I band profile would depend on whether the IR microscope was focussed on diffuse A β -peptide with the associated α -helical nucleation proteins (β -sheet and α -helical component bands) or on the plaque core (aggregated strands). Moreover, the amide I band profile would depend on the relative contribution of diffuse A β -peptide, A β -associated proteins and

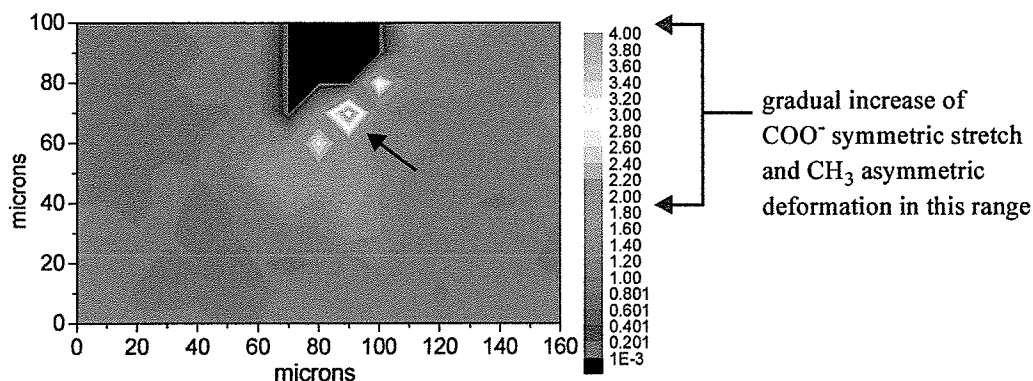
fibrillar amyloid in the plaque examined by FTIR microspectroscopy (*i.e.*, like tissue, plaques are heterogeneous). Finally, the amide I band profile would depend on the spatial resolution; the higher the resolution the less spectral “dilution” there would be of individual molecular constituents (see section 1.6). The FTIR image in Figure 4-15 was acquired at higher spatial resolution ($10 \times 10 \mu\text{m}^2$) than that of Choo *et al.*, 1996 ($12 \times 12 \mu\text{m}^2$), which means that spectra focussed onto a tissue region containing amyloid would experience less spectral “dilution” by other tissue constituents, such as A β -associated proteins. For example, in the amide I band profile acquired at coordinates (100, 80), the 1652 cm^{-1} and the 1631 cm^{-1} component bands most likely arose from the combination⁹ of a predominant amount of A β -associated proteins (1656 cm^{-1}) and diffuse A β -peptide (1641 cm^{-1}), and a smaller amount of fibrillar amyloid (1622 cm^{-1}). In contrast, in the amide I band profile acquired at coordinates (90, 70), most likely arose from a predominant amount of fibrillar amyloid (1622 cm^{-1}) and a smaller amount of diffuse A β -peptide (1641 cm^{-1}). The present results suggest that the intermolecular H-bonds between A β -peptides in diffuse amyloid are weakened from A β -associated proteins preventing close alignment of the β -strands, while the intermolecular H-bonds in fibrillar amyloid are stronger because the A β -associated proteins do not interfere with the close alignment of the A β -peptide strands. That is, the A β -associated proteins are localized to the periphery of the plaque core where they can then intermingle with the diffuse amyloid that surrounds the fibrillar amyloid.

Due to the observation of the new spectral feature of amyloid at 1400 cm^{-1} , assigned to the carboxy termini of peptide aggregates *in situ*, another 2D contour profile was created to differentiate between the amount of “regular protein structure” and truncated peptides responsible for fibril formation in the tissue section. Since truncated peptides and regular proteins would both be likely to contain the same proportion of methyl moieties, the main difference between them would be in their respective numbers of carboxy and amino termini. Moreover proteins typically contribute the most to the methyl vibrations aside from

9. Wavenumbers shown in brackets are the values of these structures when a resolved amide I component band can be observed. For example, in pixels colored brown in the FTIR image of Figure 4-15c, the amide I profile was found to consist of one observable component band at $1656\text{-}1657 \text{ cm}^{-1}$, whereas in the one pixel colored yellow (90, 70) the amide I profile consisted of two observable component bands, one at 1622 cm^{-1} and the other at 1641 cm^{-1} .

lipids (see sections 1.5 and 1.6). Therefore, a new 2D contour profile was created by calculating the relative intensity of the COO^- symmetric stretch ($1397\text{-}1400\text{ cm}^{-1}$) to the CH_3 asymmetric deformation ($1455\text{-}1457\text{ cm}^{-1}$) in each spectrum of the CA4 field map. This $\nu_s(\text{COO}^-)/\delta_{\text{as}}(\text{CH}_3)$ relative intensity FTIR image is shown in Figure 4-17. Again, portions of the hole where the spectra were noisy and low in signal were set to zero and therefore show up in the FTIR image as black. Bright yellow features in the FTIR image represent locations where spectra typical of those shown in Figure 4-16 occur.

Figure 4-17. FTIR image of the CA4 field map presented in Figure 4-15 using an alternative relative intensity profile of the $\nu_s(\text{COO}^-)$ at 1400 cm^{-1} to the $\delta_{\text{as}}(\text{CH}_3)$ at 1455 cm^{-1} . Fibrillar amyloid is localized to the side of the tear (arrow).



As can be seen in Figure 4-17, the locations of the most prominent absorptions due to carboxy moieties are at coordinates (80, 60), (90, 70) and (100, 80). The latter two pixels match the coordinates for the most prominent plaque absorptions based on the amide I band contour (Figure 4-15c). Although the photomicrograph does not show dense amyloid deposition in this region, it should be noted that during the staining process tissue sections can suffer mechanical stress especially near tears, therefore more fibril formation could have been present at the time of microspectroscopy. For example, observe the difference before and after staining in the tissue along the bottom of the hole (Figure 4-15a). After staining the bottom of the hole had a oval perimeter, whereas prior to staining (*i.e.*, during FTIR), the bottom of the hole had a “claw-like” shape. Further down from the tear, the $\nu_s(\text{COO}^-)/\delta_{\text{as}}(\text{CH}_3)$ FTIR image (Figure 4-17) also exhibited a subtle change in the shade of blue,

indicative of a $\nu_s(\text{COO}^-)/\delta_{\text{as}}(\text{CH}_3)$ ratio greater than unity. Recall, that the β -sheet/ α -helix FTIR image (Figure 4-15c) was red-purple in color at the corresponding location, suggesting α -helical protein A β -associated proteins predominate in this region, despite the dense amyloid staining detected in the photomicrograph of the stained section (Figure 4-15a). The subtle change in the shade of blue detected in the $\nu_s(\text{COO}^-)/\delta_{\text{as}}(\text{CH}_3)$ FTIR image (Figure 4-17) also suggests a gradual change towards development of AD-type histopathology, since in unaffected tissue with low lipid content these absorptions are near equal in intensity (Jackson and Mantsch, 1996).

Initially, the anomalous spectrum exhibiting enhanced carboxylate absorptions was thought to have been an abnormality in neuronal structure such as a neurofibrillary tangle (NFT). For instance, NFTs are also fibrillar and are composed of a truncated form of tau that is hyperphosphorylated. Upon microscopic inspection the anomalous spectra at coordinates (100, 80) and (90, 70) appeared to be located on a neuron in both the unstained and stained tissue section (Figure 4-15a). Even if a neuron was not present at those locations, "ghost" NFTs, or neurofibrillary tangles where the neuronal membrane has been destroyed (Bobinski *et al.*, 1998), could be responsible for the unique spectral signature. There are several reasons behind the rationale that this anomalous spectrum was not considered the FTIR signature of a tangle. First of all, another darkly stained neuron at coordinates (30, 10), which exhibited a blue contour in the FTIR image (Figure 4-15b), did not exhibit the additional spectral absorptions at 1400 or 1308 cm^{-1} even though the amide I was indicative of an enhanced contribution from β -sheet protein. Secondly, absorptions due to an increase in phosphate monoesters (970-980 cm^{-1}) were not observed in the spectra at locations where this anomalous spectrum was extracted. Furthermore, upon histopathological examination (Dr. M.R. del Bigio) the conclusion was made that classical tangles were absent from this region (if not all) of the tissue section from hippocampus AD3. Finally, this unique spectrum was observed in regions void of pyramidal neurons (*i.e.*, molecule) and NFTs are considered to be an affliction of the pyramidal neurons (Ulrich, 1993; Siegal *et al.*, 1994; Esiri and Morris, 1997). Therefore, the spectra presented in Figure 4-16 may be the spectral hallmark of fibrillar amyloid deposition but verification will proceed in the rest of this section with FTIR images constructed with both the β -sheet/ α -helix relative intensity and the $\nu_s(\text{COO}^-)/\delta_{\text{as}}(\text{CH}_3)$ relative intensity profile.

Several area maps acquired on the tissue section from AD2 further confirmed the spectral findings of this study, however problems were noticed after the staining of the MirrIR slide. The slides are covered with a reflective coating which was observed to chip and peel off from the glass slide upon exposure to acidic solutions. Although the MirrIR slides do not experience the extremes of pH during the staining process, the occasional loss of a tissue section, folding over of a tissue section or bubbling up of the reflective coating occurred. In the tissue section from AD2, gray-colored bubbled artifacts were observed which at times made it difficult to see if a plaque was present. Nevertheless, the microspectroscopy was done prior to staining and previous spectral sampling of tissue that stained properly sufficed to verify the results when the AD2 tissue staining appeared inconclusive. In addition, since several maps were typically acquired in the same region, frequently overlapping a portion of the same area, the ASCII XY data could be converted in Microcal OriginTM to one data sheet, allowing the generation of a single 2D contour plot for contiguous spectral maps. FTIR imaging of the tissue section from AD2 took place in several sectors of the hippocampus, namely the moleculare and granular layer of the dentate gyrus, the CA1 and the CA4. An overview of the AD2 tissue section, inclusive of the region in the moleculare and a portion of the CA4 field, is presented in Figure 4-18. A magnification of the moleculare where AD2 maps 1 to 6 were acquired is presented in Figure 4-19. Although plaques are easily distinguished from the golden background color of the peripheral tissue, gray streaks and bubbling artifacts from the staining (Figure 4-19, right) are also quite dark and at times made it difficult to distinguish a normal background from positive staining.

Figure 4-18. General location of spectral maps 1-9 obtained in the moleculare region of hippocampus AD2. Left, unstained; Right, stained.

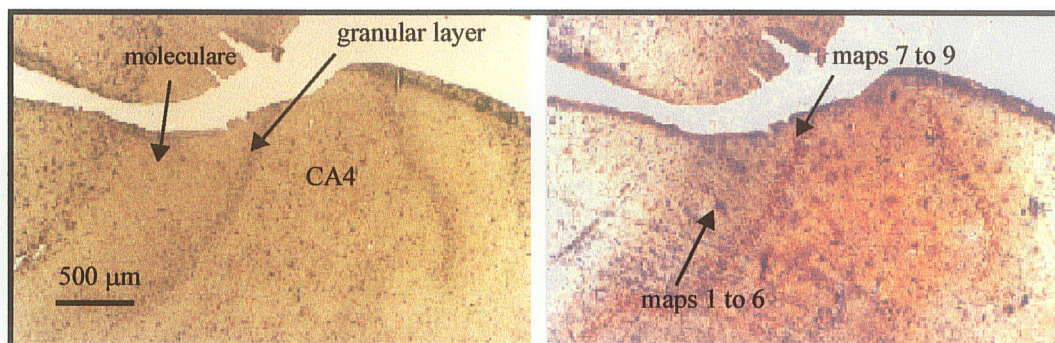
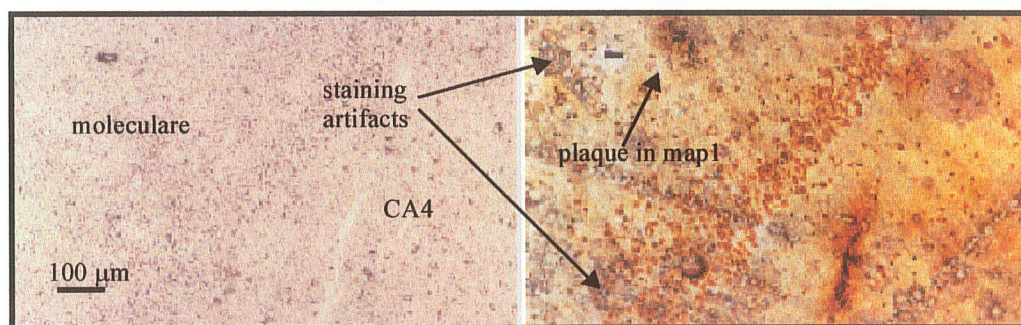


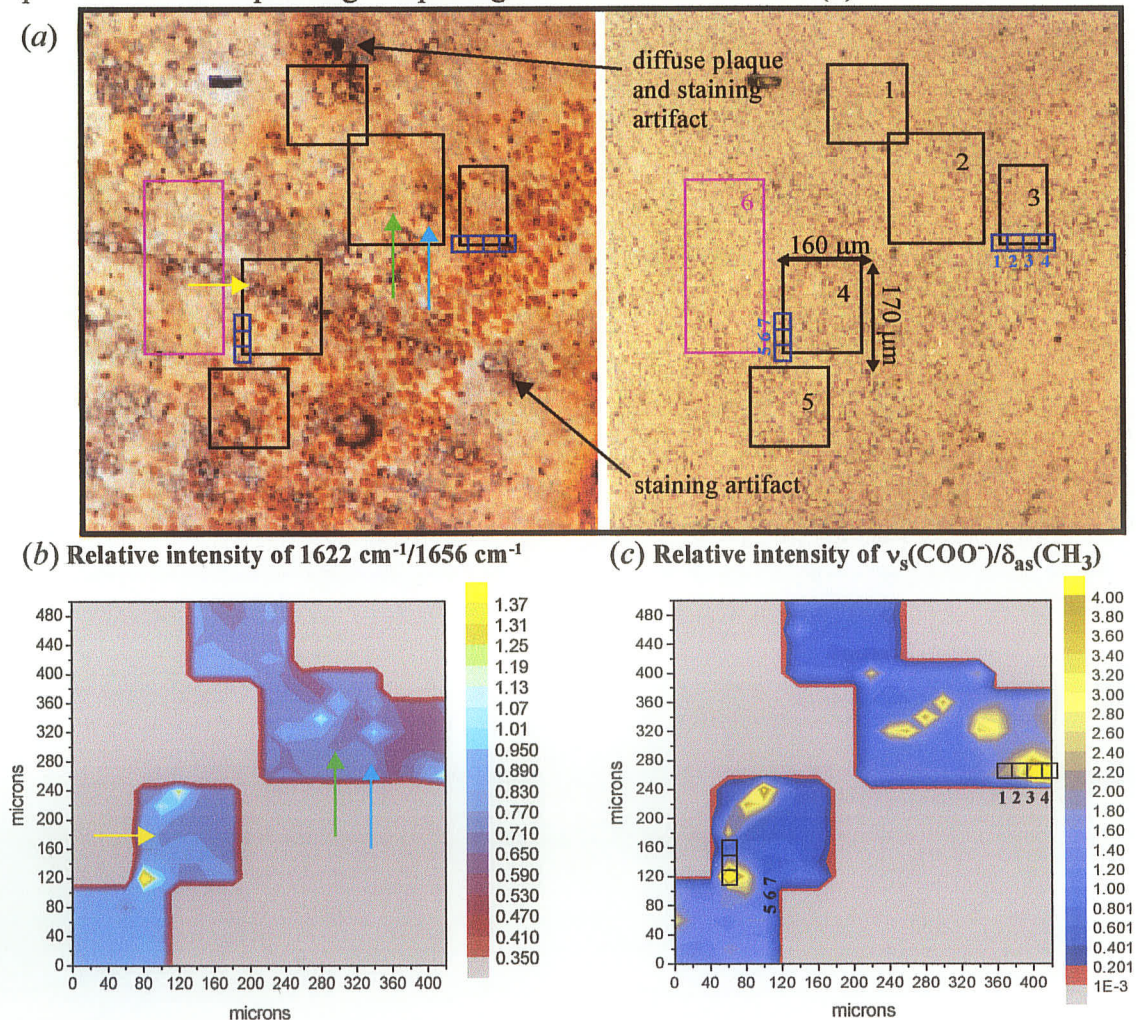
Figure 4-19. Photomicrographs of the unstained (left) and stained (right) region in the molecule where AD2 maps 1 to 6 were collected.



In comparison to the map acquired in the CA4 field of AD3, the molecule of AD2 displayed more pronounced plaque deposition based on the two relative intensity profiles used to generate the FTIR images of the tissue area (Figure 4-20). Very little contribution from α -helical protein can be inferred from the FTIR image in Figure 4-20b, as opposed to the CA4 field map of AD3. Recall, in the FTIR image of AD3 (Figure 4-15) the image was predominantly colored in the red and purple shades, assigned to a predominance of α -helical A β -associated proteins over diffuse A β -peptide deposition. In contrast, most of the tissue area in the β -sheet/ α -helix FTIR image of the molecule in AD2 (Figure 4-20b) is colored in the blue tones, suggesting a greater proportion of diffuse A β -peptide to A β -associated proteins. However, the diffuse plaque (cyan blue in centre) located between maps 2 and 3 was surrounded by tissue with a greater contribution from α -helical proteins. Plaque deposition defined as diffuse (ratio = 0.950 to 1.01, cyan blue) appeared to surround the more fibrillar deposition (ratio = 1.37, yellow). Although the stain looks dark, the more relevant feature in the photomicrograph is the irregular shape of the plaques, indicative of immature development (Ulrich, 1993). As a result, little tissue morphology is revealed by the β -sheet/ α -helix FTIR image since the molecule contains numerous amorphous plaques (see section 1.6). As reported in previous FTIR studies on AD cortex, the physiological relevance of α -helical structure near or within an AD amorphous plaque is that many of the plaque-associated proteins (ApoE, GAGs, *etc.*) involved in the nucleation of A β peptides into amyloid fibrils are α -helical in structure (Choo *et al.*, 1996). Brighter contours in the FTIR image of the relative intensity of the two amide I bands (Figure 4-20b),

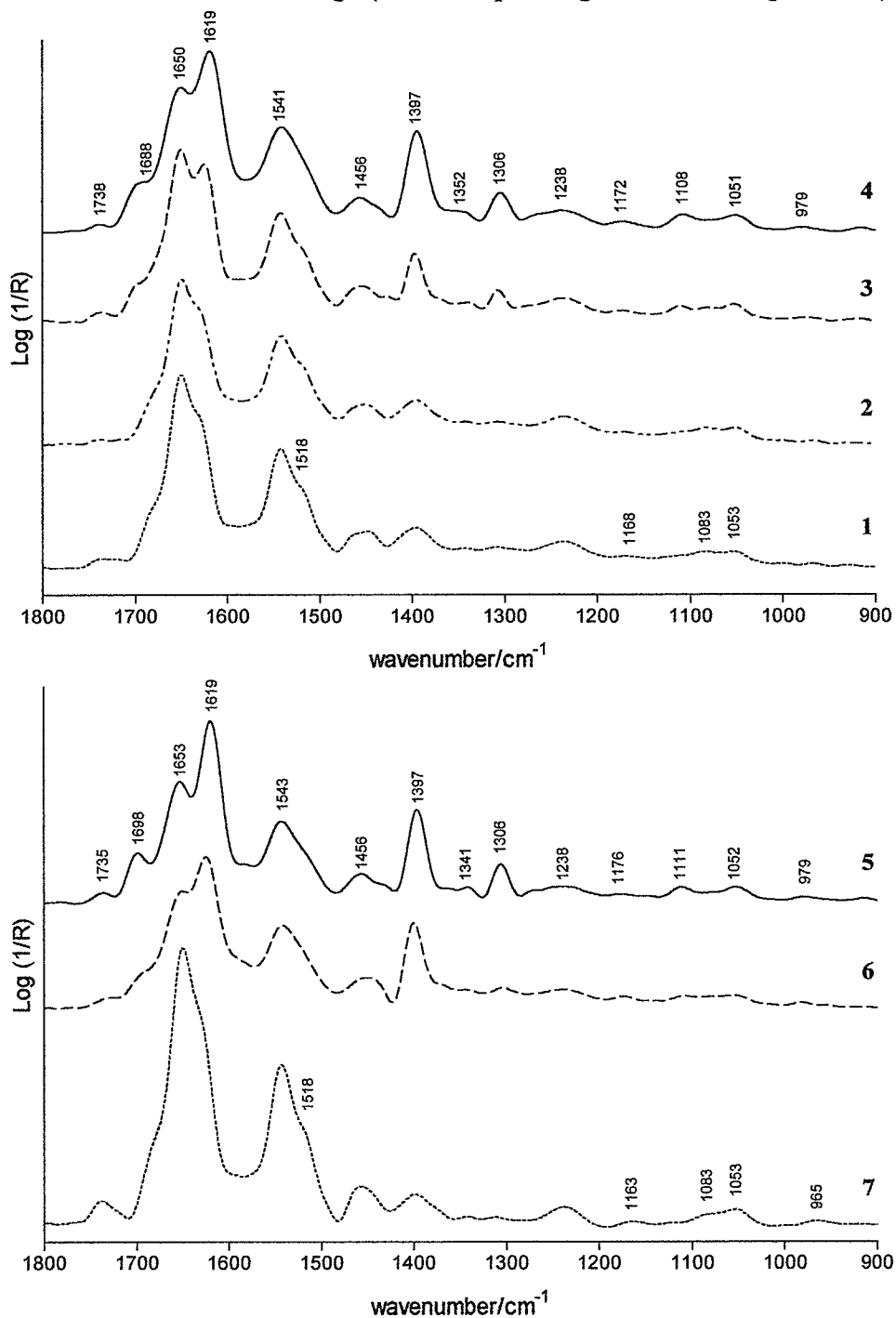
which indicate where amyloid deposition predominates in the tissue, corresponded to darkly stained dentate neurons in the photomicrograph of the stained tissue (Figure 4-20b).

Figure 4-20. FTIR imaging of five neighboring tissue areas in the molecule of hippocampus AD2. (a) The spectral maps (20 μm spatial resolution) are outlined in black on the stained (left) and unstained (right) tissue. (b) FTIR imaging calculated from the relative intensity of β -sheet/aggregates (1622 cm^{-1}) to α -helical proteins (1656 cm^{-1}). (c) $\nu_s(\text{COO}^-)/\delta_{\text{as}}(\text{CH}_3)$ FTIR image calculated from the relative intensity of 1400 cm^{-1} to 1455 cm^{-1} . Map 6 (purple outline) was omitted from both profile analyses due to poor S/N quality. Numbered positions show where spectra 1-4 and 5-7 were extracted from maps 3 and 4, respectively, in Figure 4-21. The yellow, green and blue arrows pointing to features detected in the FTIR image (b) point to the corresponding morphological features in the stain (a).



Further verification of predominantly diffuse A β -peptide deposition (ratio = 2.0) proximal to more fibrillar amyloid (ratio = 4.0) in the molecule of AD2 came from the $\nu_s(\text{COO}^-)/\delta_{\text{as}}(\text{CH}_3)$ FTIR image (Figure 4-20c). The $\nu_s(\text{COO}^-)/\delta_{\text{as}}(\text{CH}_3)$ FTIR image (Figure 4-20c) confirmed the location of truncated peptides in the same locations that dense amyloid deposition was inferred by the β -sheet/ α -helix FTIR image (Figure 4-20b). Again, some of the brighter contours appeared to correspond to the darker neurons of the dentate gyrus. However, upon greater magnification of the stained section, the neurons which were darkly stained did not appear to be classical NFTs, but instead were neurons that contained fibrillar amyloid deposits. Consecutive spectra extracted from maps 3 and 4 that exhibited light blue to yellow contours in the $\nu_s(\text{COO}^-)/\delta_{\text{as}}(\text{CH}_3)$ relative intensity profile (Figure 4-20c) are presented in Figure 4-21. From light blue to yellow contours (Figure 4-20c), the spectra display a gradual and concomitant increase in protein aggregates and truncated peptide in the tissue. However, aside from the synchronous increase in the β -sheet to α -helix relative intensity and the COO^- to methyl relative intensity moving from diffuse to fibrillar amyloid, there were other notable changes in the contiguous spectra, absent in the preceding CA4 field map of AD3. Of particular interest was the additional amide I component band that appeared on the high frequency end of the amide I band profile (Figure 4-21). In spectrum 4, this 1688 cm^{-1} band appeared 69 cm^{-1} higher in frequency than the component band assigned to β -sheet/aggregate structure (1619 cm^{-1}). These two absorptions can be assigned to the high and low frequency component (HFC and LFC, respectively) bands of antiparallel β -sheet structures as the HFC band typically appears 50-70 cm^{-1} higher in frequency than the LFC band (Jackson and Mantsch, 1995). Therefore, the type of protein detected in maps 3 and 4 was an aggregate of truncated peptides with a collective antiparallel β -sheet structure inclusive of strong H-bonding intermolecularly. This is not unlike the proposed model for fibril formation *in vitro*, called the " β -sheet-helix", wherein individual β -strands are thought to closely align in an antiparallel fashion to form a sheet that twists in a helical manner. (Blake and Serpell, 1996).

Figure 4-21. Representative spectra from the AD2 molecular. Note the gradual and concomitant increase in absorptions due to aggregated strands (1619 cm^{-1}) and COO^- termini (1397 cm^{-1}) compared to those due to α -helical proteins (1652 cm^{-1}) and CH_3 moieties (1455 cm^{-1}), respectively. Spectra extracted from blue to bright yellow contours in the FTIR image (see corresponding numbers in Figure 4-20).

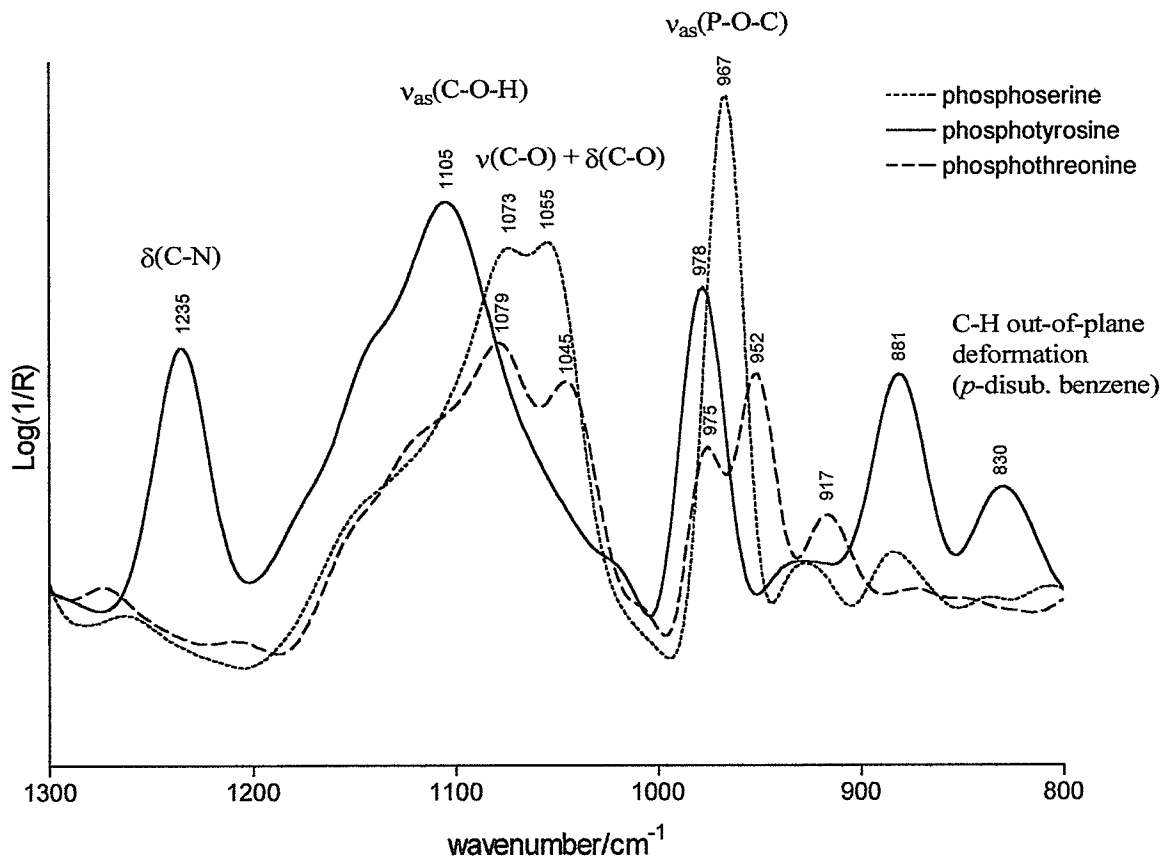


Other noticeable differences in the “ β -sheet-helix” spectra presented in Figure 4-21 from those in Figure 4-16 were alterations in the pattern of absorptions between 1000-1180 cm^{-1} . This spectral subregion is of primary interest for observation of carbohydrate absorptions *in situ* (sections 1.5.4 and 1.6). An apparent change in the carbohydrate absorption pattern in spectrum 4 may be indicative of a change in glycosylation state of the aggregated protein. For instance, the bands observed in spectrum 4 were 1051, 1108 and 1172 cm^{-1} (Figure 4-21), whereas in the spectrum of amyloid deposition in Figure 4-16 the 1108 cm^{-1} band lost intensity relative to the absorption at 1076 cm^{-1} . This alteration was even more apparent upon comparison of spectra 5 and 7 in Figure 4-21. Spectrum 5 displayed the amide I band contour of diffuse plaque formation along with the absorptions 1053, 1083 and 1168 cm^{-1} , whereas only 40 μm away the fibrillar amyloid spectrum 7 presented with the C-O-C and C-OH absorption pattern of 1052, 1111 and 1176 cm^{-1} . This increase in the C-OH vibrational frequency to 1176 cm^{-1} may be indicative of decreased H-bonding to hydroxyl moieties of carbohydrates or amino acids (serine, threonine and tyrosine). Perhaps serine, threonine or tyrosine underwent phosphorylation or glycosylation to account for the observed 8 cm^{-1} increase in the C-OH vibrational frequency (see section 1.5.4). β -amyloid, as an advanced glycation end product (AGE) has been found to bind to the receptor for advanced glycation end products (RAGE) located in the membranes of neurons and astrocytes (Yan *et al.*, 1996). In a recent immunohistochemical examination of AD hippocampus, β -amyloid has been found to co-localize with RAGE and AGE in the perikaryon of pyramidal neurons and some astrocytes (Sasaki *et al.*, 2001). Sasaki *et al.*, suggested that the binding of glycated β -amyloid to RAGE may comprise an AGE/RAGE lysosomal degradation pathway and contribute to neuronal dysfunction. Interestingly, the spectra in Figure 4-21 that had the 1619 cm^{-1} and 1688 cm^{-1} amide I bands (β -sheet helix), narrow bands at 1397 cm^{-1} and 1306 cm^{-1} ($\nu_s(\text{COO}^-)$ and C=O in-plane bend of amide III, respectively), and the C-O-C and C-OH absorption pattern of 1052, 1111 and 1176 cm^{-1} (*i.e.*, pixels 3, 4, 5 and 6) were acquired either partially or completely on a dentate neuron that stained positive for A β -aggregates (Figure 4-20). Perhaps, the fibrillar A β -peptide aggregates present inside these dentate neurons were glycosylated.

Phosphorylation of a tyrosine residue (Kozlowski *et al.*, 1992) and/or a threonine residue (Standen *et al.*, 2001) in the carboxy-terminus of the neurotoxic C-terminal frag-

ment of β APP (C-104) has been reported. C-104 is a neuronal membrane bound fragment of β APP, produced by β -secretase cleavage of β APP at the N-terminal end of the A β -domain of β APP (Furukawa *et al.*, 1996). The expression of C-104 peptide in neural cell cultures has been found to promote neuronal degeneration (Mattson and Furukawa, 1997). Moreover, the brain tissue of transgenic mice that express human C-104 exhibits similar histology to AD brain (Nalbantoglu *et al.*, 1997). Several pathways have been proposed for the C-104 amyloidogenesis, one of which is endocytosis of the C-104 peptide followed by endosomal/lysosomal proteolytic processing, producing amyloid fibrils inside the neuron (Furukawa *et al.*, 1996; Nalbantoglu *et al.*, 1997; Mattson and Furukawa, 1997; Standen *et al.*, 2001). The weak, broad absorption at 979 cm^{-1} , assigned to the phosphate monoester stretching of phosphorylated proteins, may further convey this enhanced state of phosphorylation in the fibrillar aggregate. The phosphate monoester moiety in pTyr, pThr and pSer are attached to different chemical groups (aromatic ring, methine and methylene group, respectively), thus the phosphate monoester stretch may occur at different frequencies. Therefore, a simple *in vitro* experiment was carried out to discern the phosphate monoester stretching frequencies of these different phosphoamino acids, under conditions similar to the tissue FTIR microspectroscopy. That is, a dry thin film of each phosphoamino acid on a Kevley MirrIR slide was prepared and spectra were acquired using synchrotron IR microspectroscopy and a $20 \times 20\ \mu\text{m}^2$ aperture (Figure 4-22). Based on the infrared signatures of phosphoserine, phosphotyrosine and phosphothreonine, the most likely candidate for phosphorylation in the truncated peptides comprising the fibrillar aggregate detected in the dentate neurons of AD2 may be phosphotyrosine (Figure 4-22). Phosphotyrosine has a phosphomonoester asymmetric stretch at 978 cm^{-1} which was the closest in frequency to the weak absorption (979 cm^{-1}) observed in the spectra of fibrillar amyloid (Figure 4-22). Moreover, amyloidogenic peptides have been shown to have a high amount of aromatic amino acid residues, especially tyrosine, in their sequence, in comparison to other cellular proteins (Ulrich, 1993).

Figure 4-22. Comparison of the phosphomonoester asymmetric stretch, $\nu_{as}(\text{P-O-C})$, for phosphoserine (967 cm^{-1}), phosphotyrosine (978 cm^{-1}) and phosphothreonine (975 and 952 cm^{-1}). Dried films of these phospho-amino acids were prepared by placing a couple of aqueous droplets of the solution on the MirrIR slide, allowing the solution to dry overnight before addition of another droplet. Spectra were acquired at SRC with $20 \times 20 \mu\text{m}^2$ aperture.¹⁰



Further microspectroscopic examination of sample AD2 was carried out close to the main tear of the sample inclusive of both the molecular and the granular layer of the dentate gyrus (Figure 4-18). The tissue area examined by spectral maps 7 to 9 is shown under greater magnification in Figure 4-23. In a similar manner to that carried out for diffuse and fibrillar amyloid analysis in the previously sampled regions, the FTIR images were prepared utilizing both the β -sheet/ α -helix profile and the $\nu_s(\text{COO}^-)/\delta_{as}(\text{CH}_3)$ profile to dis-

10. Band assignments based on those found in Lambert *et al.*, 1987 and Wong, *et al.*, 1991.

criminate diffuse from fibrillar plaque formation. Spectral map 8 was omitted from the 2D contour analysis due to poor S/N quality in the majority of the spectra (see below). Little more than diffuse A β -peptide deposition was noted in spectral map 7, but prominent plaque formation (consisting of both diffuse and fibrillar amyloid) was revealed in both FTIR images of map 9 in the granular layer of the dentate gyrus which contained the dentate neurons (Figure 4-23*b* and *c*). Although the dentate neurons stained quite darkly in sample AD2, an amorphous plaque was found to accompany them within the area examined by map 9 (see arrow, Figure 4-23*a*). In this region diffuse deposition (ratio = 0.95, cyan blue) and fibrillar amyloid (ratio = 1.13-1.31, pale green/green) were found to be again surrounded by proteins with a more α -helical character (ratio = 0.530-0.590, red/purple), as revealed by the FTIR image in Figure 4-23*b*. Contiguous spectra (numbered 1-4) taken across a portion of this plaque are shown in Figure 4-24. The spectral features found in this location were similar to those previously described in maps 3 and 4 further down into the molecular region, such as the simultaneous increase of the COO⁻ absorption with greater “ β -sheet-helix” fibril formation. However, a new absorption appeared in a spectrum collected on the amyloid core of the plaque (spectrum 3, Figure 4-24), namely the shift in the C=O to lower frequency (1727 cm⁻¹), suggesting an increased contribution of C=O in-plane stretching of nucleic acid bases to the tissue. This frequency is higher than expected for H-bonded base pairs (1721 cm⁻¹), suggesting base-pair H-bonding had decreased or nucleic acids were breaking down (*i.e.*, free bases absorb at higher frequency). Interestingly, spectrum 3 was acquired with the aperture partially on a brown discoloration of approximately the same size as a dentate neuron but a nucleolus was absent (the nucleolus typically stains black using the Bielschowsky method).

Figure 4-23. FTIR imaging of two neighboring tissue areas in the molecular and dentate neurons of AD2. (a) The spectral maps (20 μm spatial resolution) are outlined in black on the photomicrographs of the stained (left) and unstained (right) tissue. (b) FTIR imaging created by the relative intensity of β -sheet/aggregated strands (1625 cm^{-1}) to that of α -helical proteins (1656 cm^{-1}). (c) FTIR imaging created by the relative intensity of $\nu_s(\text{COO}^-)$ at 1400 cm^{-1} to $\delta_{\text{as}}(\text{CH}_3)$ at 1455 cm^{-1} . Map 8 (purple) was omitted from both profile analyses due to poor S/N quality. Numbered pixels indicate where adjacent spectra 1-4 were extracted from map 9 (presented in Figure 4-24).

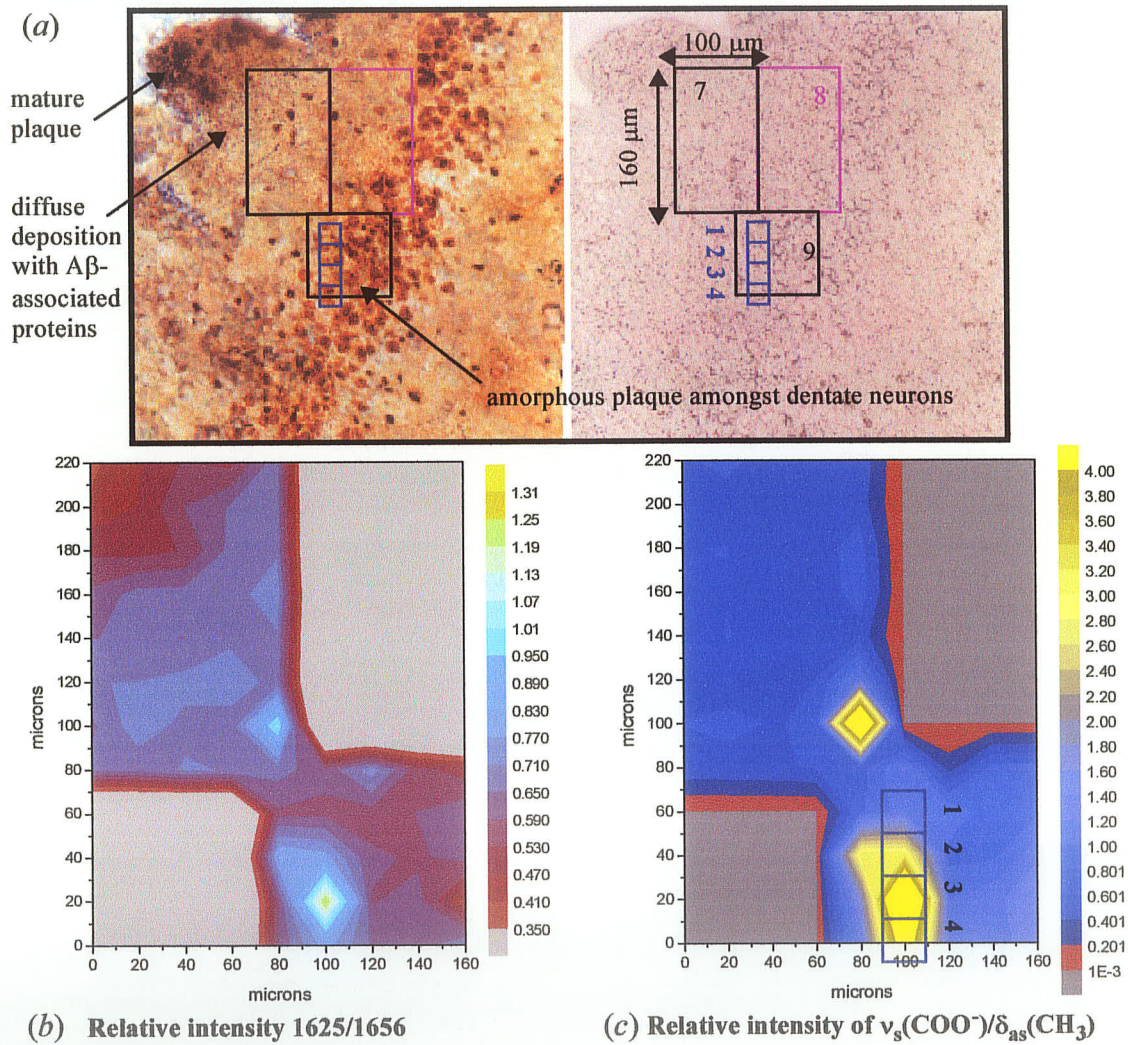
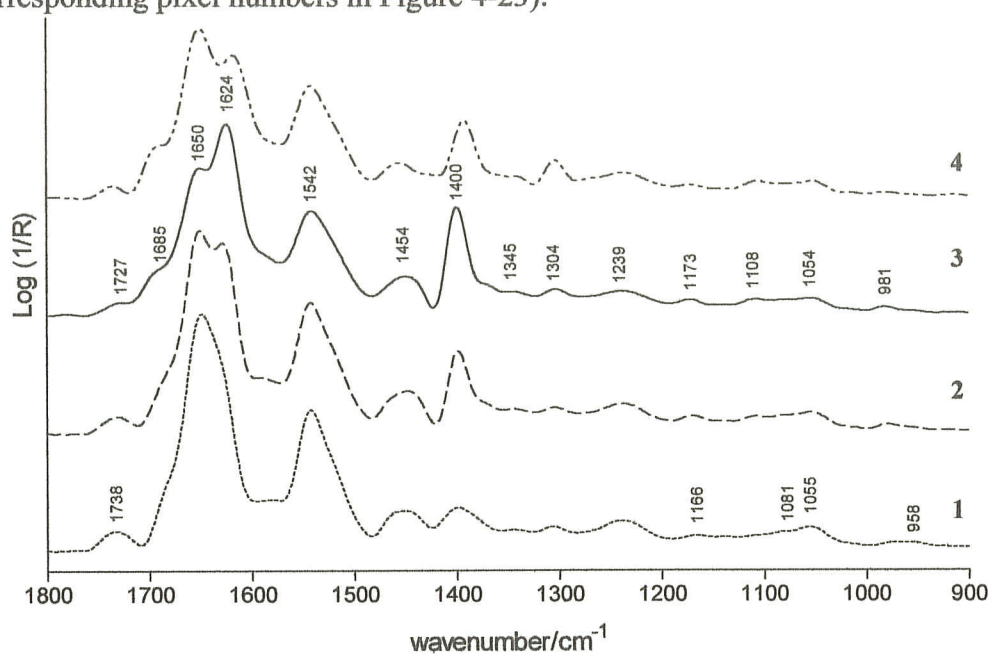


Figure 4-24. Representative spectra from the granular layer of the dentate gyrus accompanied by amyloid deposition in hippocampus AD3. The adjacent spectra illustrate the gradual and concomitant increase of aggregated strands and truncated peptides in areas where the staining was most intense in the photomicrograph of Figure 4-23a. Spectra were extracted from blue to bright yellow contours in the FTIR image prepared from the $\nu_s(\text{COO}^-)/\delta_{\text{as}}(\text{CH}_3)$ relative intensity profile (see the corresponding pixel numbers in Figure 4-23).

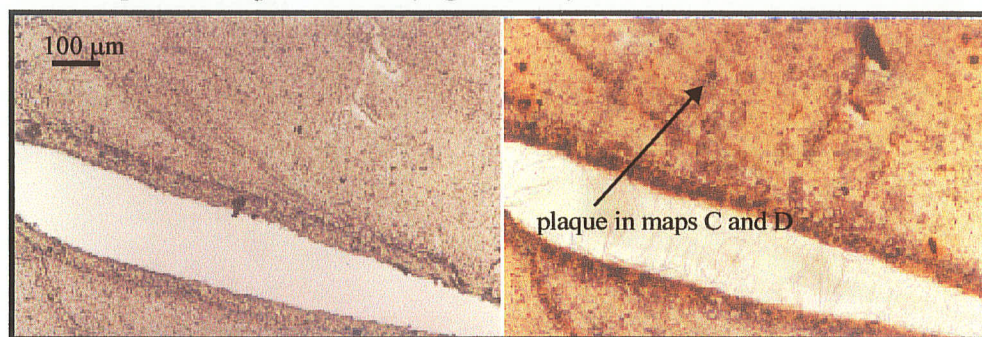


Recall, from Table 4-1, that AD2 was examined using the IR beamline at the SRC. The SRC is a first generation light source (*i.e.*, not as bright, not as stable) in comparison to the NSLS which is a third generation synchrotron. All maps that were discarded in this study due to poor S/N were recorded at the SRC. Moreover, the velocity of the moving mirror in the interferometer had to be decreased (from 3.15 cm/sec to 0.95 cm/sec) to move spikes (inherent ring noise from the harmonic chambers) out of the mid-IR fingerprint region in order to get high quality data in the absence of beam instability. High S/N quality came at a price, however, for it took approximately 7 minutes (rather than 2 min.) to collect each spectrum in a map (256 scans at 2 cm^{-1} resolution) at the SRC.

As opposed to the rather poor quality staining observed in the molecular and granular layer of the dentate gyrus, the CA1 of AD2 contained dense plaques which were easier

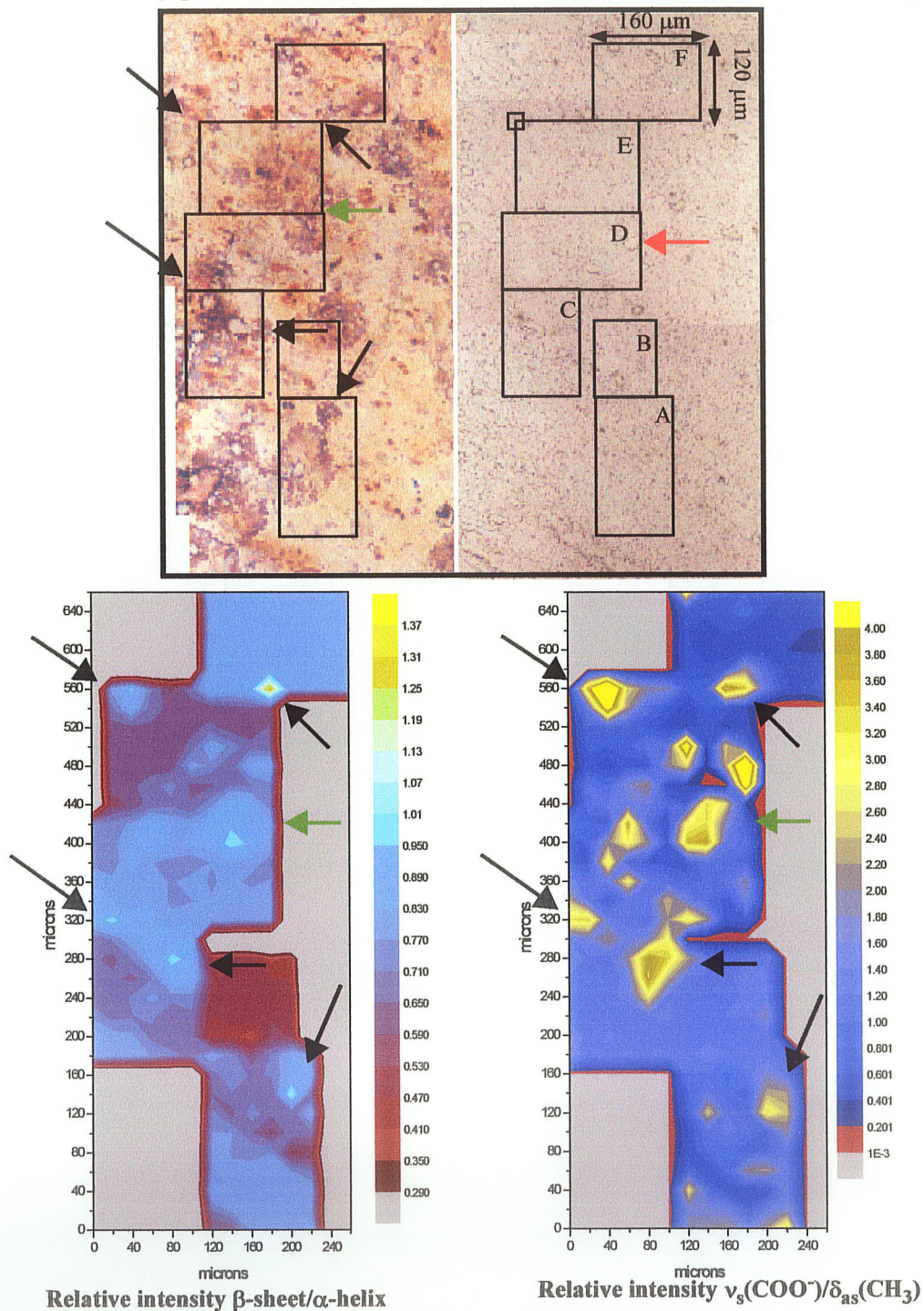
to distinguish from the staining artifacts. Shown in Figure 4-25 is an overview of the area examined spectroscopically in the CA1 field of hippocampus AD2. Six neighboring and occasionally overlapping spectral maps (labelled A to F) were collected in the CA1 and the same two relative intensity profiles used earlier for the molecular region were calculated (Figure 4-26).

Figure 4-25. Photomicrographs of the CA1 region examined in hippocampus AD2 unstained (left) and stained (right). The arrow points to a CA1 plaque which was recorded in spectral maps C and D (Figure 4-26).



The stained photomicrograph of the spectroscopically examined area confirmed the combination of diffuse deposition and fibrillar amyloid deposition in neuritic plaques detected in both relative intensity FTIR images (arrows, Figure 4-26). In the β -sheet (1622 - 1625 cm^{-1}) to α -helix (1656 cm^{-1}) relative intensity image (left), bright contours representative of diffuse/fibrillar amyloid were typically surrounded by the combination of diffuse amyloid and tissue with significant contributions from α -helical proteins (*i.e.*, A β -associated proteins and associated glial cells). In the $\nu_s(\text{COO}^-)/\delta_{\text{as}}(\text{CH}_3)$ FTIR image, location of fibrillar amyloid (bright yellow contours) was detected. If the two FTIR images were overlaid upon one another the differentiation between fibrillar and diffuse deposits is easily visualized. That is, although A β -associated proteins contribute to the amide I band, they primarily contribute to the 1455 cm^{-1} band ($\delta_{\text{as}}(\text{CH}_3)$) in comparison to the 1400 cm^{-1} band ($\nu_s(\text{COO}^-)$) in the $\nu_s(\text{COO}^-)/\delta_{\text{as}}(\text{CH}_3)$ FTIR image, while the opposite holds for fibrillar amyloid. Therefore, there is less spectral “dilution” of the fibrillar structure in the IR spectra when the $\nu_s(\text{COO}^-)/\delta_{\text{as}}(\text{CH}_3)$ relative intensity is used to construct the FTIR image.

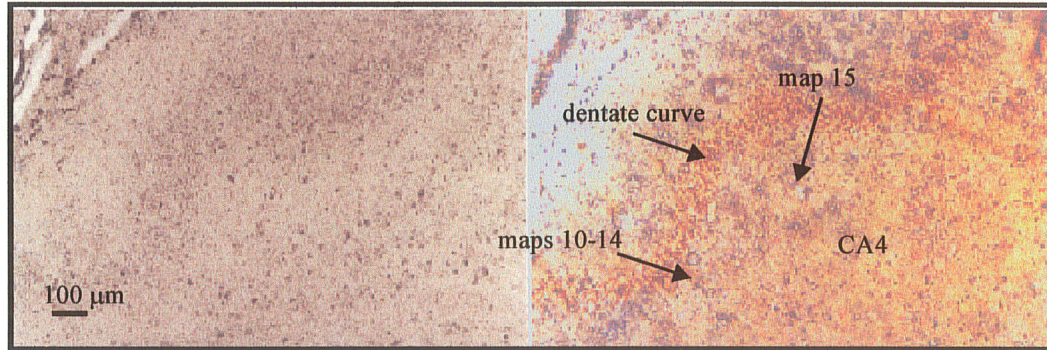
Figure 4-26. FTIR imaging of a plaque-infested area in the CA1 field of hippocampus AD2. Stepsize 20 μm . FTIR images were created with the same relative intensity profiles used earlier. (see Figure 4-23 and text for more details).



In comparison to the stained tissue then, the two FTIR images in Figure 4-26 superimposed on one another, provides more detail about the tissue constituents and plaque heterogeneity than the stain. For example, in the stain the plaque located on the right hand side of maps D and E (green arrow) appears predominantly amorphous with little contribution from fibrillar amyloid. However, the contours in the two FTIR images indicate the following: (i) in the centre of this oval plaque α -helical proteins (purple in IR image on left) predominate over diffuse A β deposition, (ii) the plaque periphery contains a predominant amount of fibrillar amyloid (yellow in the IR image on the right) over diffuse A β deposition (cyan blue in the IR image on the left), (iii) in peripheral tissue (unstained) along the top of this oval-shaped plaque, α -helical proteins (purple in IR image on left) again predominate over diffuse A β deposition, and (iv) in peripheral tissue (faintly stained) along the bottom of the plaque, diffuse A β deposition (cyan blue in the IR image on the left) predominates over the α -helical proteins and some fibrillar amyloid is detected (light purple, ratio > 2.0 in the IR image on the right). Therefore although the FTIR results of (iii) are in agreement with the stained photomicrograph, the FTIR result of (iv) is not, since only faint staining can be observed. In some focal locations the stain of the tissue correlates very well with the FTIR results. For example, within spectral maps D and E there are brown-stained neurons which were highlighted in yellow contours in the $\nu_s(\text{COO}^-)/\delta_{as}(\text{CH}_3)$ FTIR image. The location of one such neuron within map D is pointed out with a red arrow in the unstained photomicrograph of Figure 4-26. The light olive to bright yellow contours (ratio = 2.40 to > 4.0) in this image again corresponded to spectra (data not shown) suggesting the neurons contain fibrillar amyloid composed of truncated peptides that are glycosylated and phosphorylated (*i.e.*, pTyr) similar to that proposed for the dark-stained dentate neurons of hippocampus AD2 (Figures 4-20, 4-21, 4-23 and 4-24).

The last sector of AD2 hippocampus examined by FTIR microspectroscopy was the CA4 field near the curve of the dentate gyrus (Figure 4-27). The arrows in this photomicrographic overview of the region evaluated depict the locations of the five spectral maps collected. In one map (map 15) fibrillar amyloid deposition was detected by FTIR imaging and the histochemical stain. The other four spectral maps (maps 10 to 14), were acquired in a tissue region that exhibited little more than diffuse amyloid upon either staining or FTIR imaging.

Figure 4-27. AD2 overview of CA4 field examined, stained and unstained. Spectral maps 10 to 14 found in the CA4 with the curve of the dentate. Lower arrow points to hole in tissue just to the upper right of map 15.



The FTIR imaging and histochemistry of the CA4 field map15 of hippocampus AD2 are presented in Figure 4-28. Once again, the β -sheet/ α -helix and the $\nu_s(\text{COO}^-)/\delta_{\text{as}}(\text{CH}_3)$ relative intensities in each spectrum were used to construct the two FTIR images (left and right, respectively in Figure 4-28). As depicted in the stained photomicrograph of map 15, little fibrillar amyloid plaque was detected by the stain, however several neurons were darkly stained and a small amount of diffuse plaque can be seen in the lower right-hand corner of the spectral map (blue arrow). Notice that this plaque extends below the coordinates of the map with a hole artifact from staining in the centre. Interestingly, the periphery of this hole artifact stained darkly and thus may correspond to where a dense plaque was located prior to staining. The diffuse amyloid deposition surrounding the hole is quite regular (*i.e.*, round) which also suggests that this was a mature neuritic plaque. Both FTIR images exhibited brighter contours at map coordinates (60, 20) and (80, 40). FTIR spectra extracted from this region (Figure 4-29), exhibited spectral features that best represent the mid-IR signature of a predominant amount of fibrillar amyloid (*i.e.*, 1619 cm^{-1}), accompanied by a combination of diffuse $\text{A}\beta$ -peptides ($1637\text{-}1641\text{ cm}^{-1}$) and α -helical (1656 cm^{-1}) $\text{A}\beta$ -associated proteins (*i.e.*, resultant amide I component band at 1652 cm^{-1}). Furthermore, from the morphology of the unstained tissue section, a dentate neuron (map 15 is still close to the dentate gyrus) was originally at the coordinates (80, 40), but staining produced a bubble artifact in that region. Regardless, the spectrum at (80, 40) is similar to the dentate neuron spectra shown earlier that were darkly stained (Figures 4-19 and 4-24).

Figure 4-28. FTIR imaging in the CA4 field, close to the dentate gyrus, of hippocampus AD2. Spatial resolution of $20 \times 20 \mu\text{m}^2$. The bubble artifact from staining appeared near the coordinates where amyloid deposition was detected in the two relative intensity profiles below the photomicrographs; FTIR image (left) calculated from the relative intensity of β -sheet/aggregated strands (1622 cm^{-1}) to that of α -helical proteins (1656 cm^{-1}) and a FTIR image calculated from the relative intensity of $\nu_s(\text{COO}^-)$ at 1400 cm^{-1} to $\delta_{\text{as}}(\text{CH}_3)$ at 1455 cm^{-1} . The spectra at coordinates (60, 20) and (80, 40), outlined in black on the FTIR images, are shown in Figure 4-29.

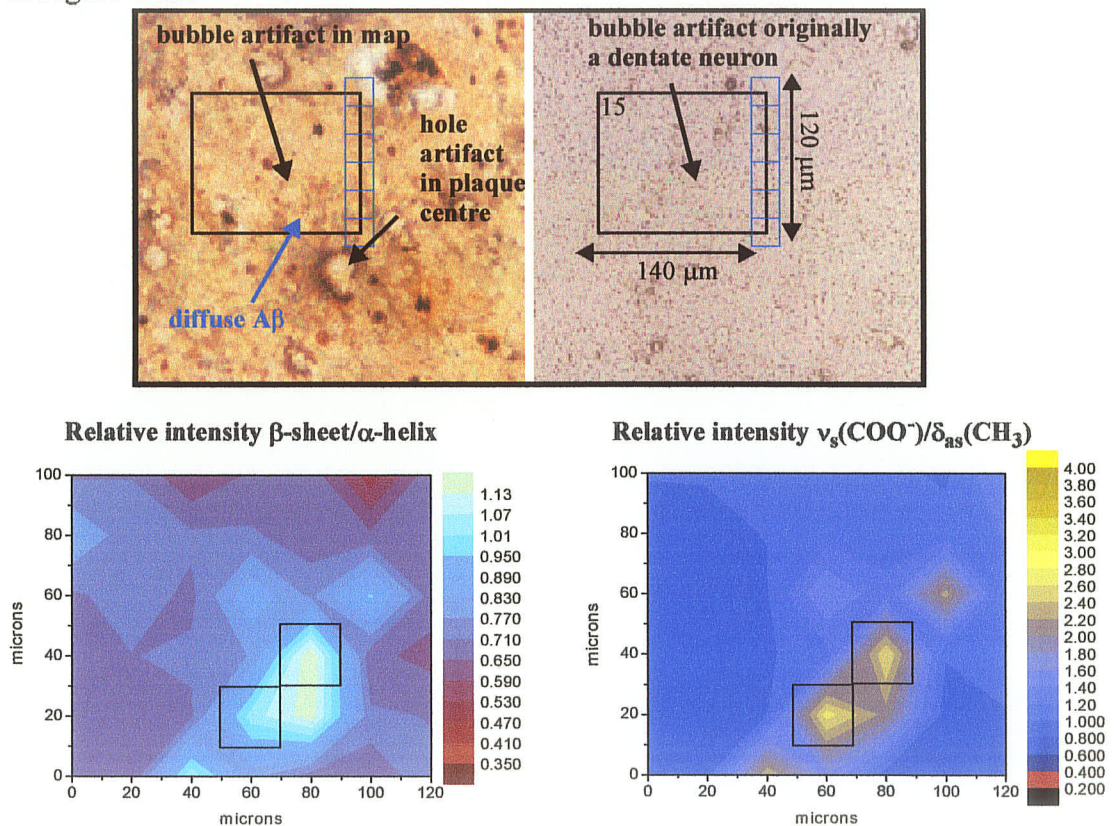
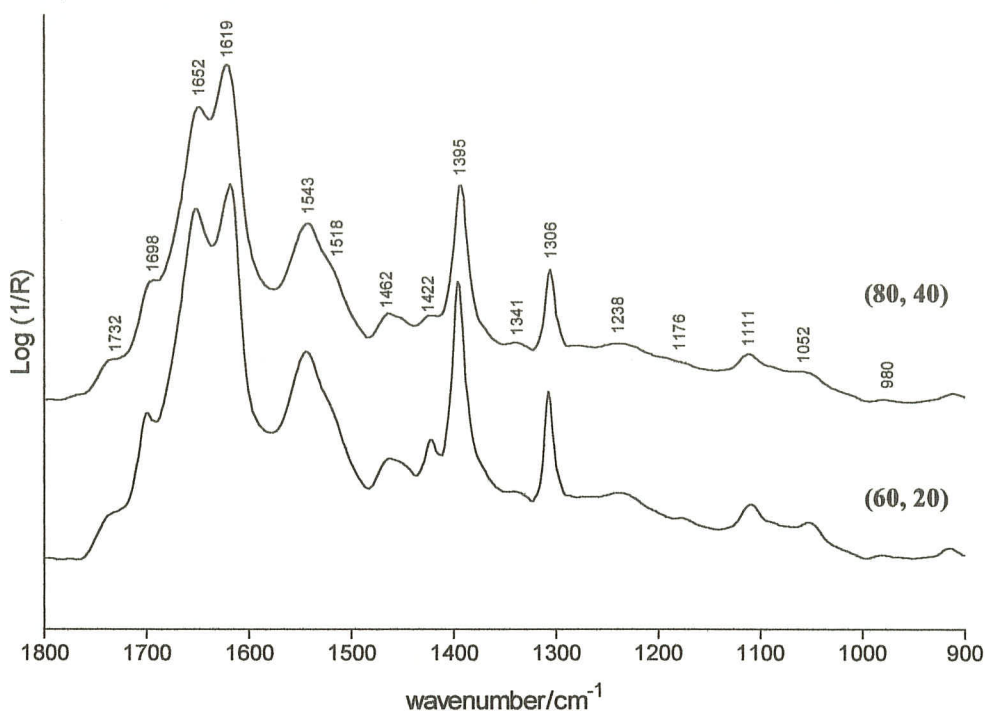


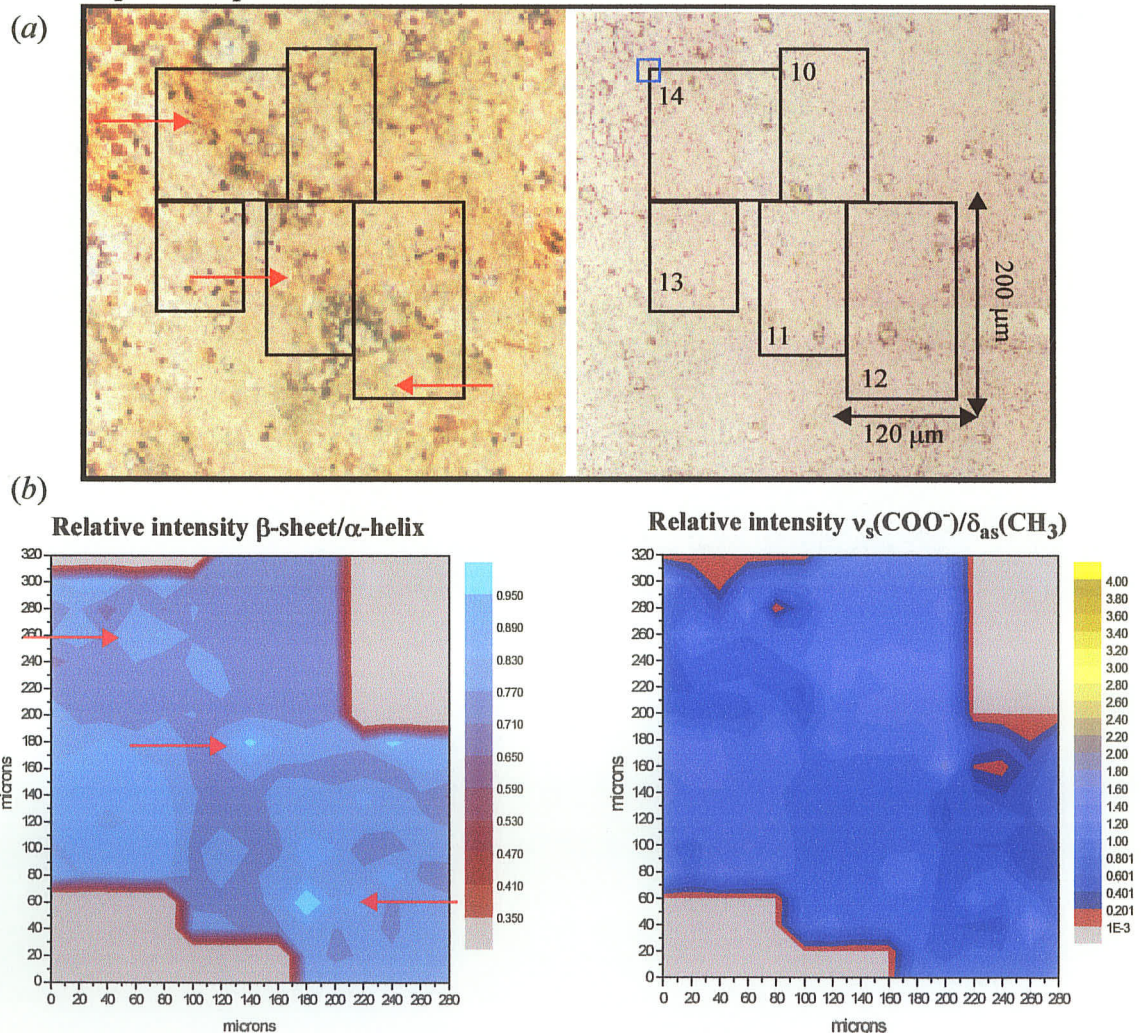
Figure 4-29. Representative spectra of amyloid deposition in the CA4 field close to the dentate gyrus of hippocampus AD2. Shown are spectra extracted from the coordinates (60, 20) and (80, 40) of map 15, which exhibited brighter contours in the relative intensity FTIR images presented in Figure 4-28. The pixel at coordinates (80, 40) contained a dentate neuron.



Contrary to map 15, the four other spectral maps collected in the CA4 field, near to the granular layer of the dentate gyrus (maps 10-14) did not display more than diffuse amyloid deposition (Figure 4-30). The photomicrograph of the stained tissue section in this region exhibited little positive staining for amyloid, aside from some faint brown in map 14. Upon preliminary examination of each spectrum, the amide I maximum was either at 1648 cm^{-1} or at 1656 cm^{-1} , in the absence of any other resolved component bands (data not shown). The amide I band profile of the spectra with an amide I maximum at 1648 cm^{-1} were similar to the diffuse plaque spectrum collected near the CA1 blood vessel of hippocampus AD1 (Figure 4-12). In order to obtain contrast in this amide I band profile FTIR image (Figure 4-30*b*, left) the relative intensity of the higher frequency β -sheet component band (1630 cm^{-1}) to that of α -helix (1656 cm^{-1}) was calculated for each of the pixel spectra (shown in Figure 4-30). The stain of the tissue section corroborated the presence of some

diffuse amyloid deposition (red arrows, Figure 4-30a) at the coordinates where diffuse A β -deposition was denoted in amide I band profile FTIR image. Fibrillar amyloid was not detected in the $\nu_s(\text{COO}^-)/\delta_{as}(\text{CH}_3)$ FTIR image (Figure 4-30, bottom right), nor in the tissue stain (*i.e.*, gray streaks/bubbles are artifacts from the staining process).

Figure 4-30. FTIR imaging of diffuse A β -deposition in the CA4 field of hippocampus AD2. Red arrows point to locations where the greatest diffuse deposition of amyloid was detected in both the FTIR images and the stained tissue section. For improved contrast in the amide I profile FTIR image (bottom left), the relative intensity of 1630 cm^{-1} (β -sheet) to 1656 cm^{-1} (α -helix) was calculated, rather than using the lower frequency β -sheet/aggregates absorption at 1622 cm^{-1} as carried out for previous profiles.



4.3.4 Detection of A β in tissue by FTIR when staining was inconclusive or between plaque regions

Based on the results from the FTIR imaging of amyloid angiopathy (section 4.2.3) and of diffuse and neuritic plaques (section 4.3.4), it was noticed that a number of contours in the images were brighter than expected by the results of the Bielschowsky stain. Furthermore, the amide I band profile of spectra from these contours, assigned to diffuse A β -peptide deposition, was slightly shifted to lower wavenumber when staining was inconclusive. Additional FTIR imaging in the CA4 field and the molecule of hippocampus AD3 denoted diffuse amyloid deposition in regions where the subsequent staining of the tissue suggested that amyloid deposition did not occur at those locations (Figures 4-31 and 4-32). These FTIR images, prepared from the relative intensity β -sheet (1630 cm⁻¹) to α -helix (1656 cm⁻¹), exhibited greater contrast with some lighter contours, while the relative intensity profile of the carboxylate symmetric stretch (1400 cm⁻¹) to the methyl asymmetric deformation (1455 cm⁻¹) was veritably featureless. Moreover, the characteristic spectrum of fibrillar amyloid (discussed in section 4.3.3) was not found in any spectra in this present section. Similar results were obtained in the FTIR images prepared from spectral maps located between plaques which were acquired in the CA1 of hippocampus AD1 (Figure 4-33). Verification that the brighter contours in these FTIR images were due to an abnormal increase in β -sheet (1630 cm⁻¹) was obtained by comparison of these FTIR images of AD hippocampus to the 2D contour analysis of spectral maps collected on the control samples, CON1 and CON2.

In the curl of the molecule of hippocampus AD3 (recall Figure 4-5, left of CA4), a spectral map was collected which indicated the presence of diffuse amyloid upon 2D contour analysis (Figure 4-31). Shown in Figure 4-31*b*, the amide I band FTIR image exhibited well-defined contrast with lighter contours (ratio = 0.95 to >1.07) corresponding to the upper portion of the spectral map (see arrow). However, after staining this location revealed only a background level of stain most likely due to the low sensitivity of the Bielschowsky staining method to little A β -peptide deposition. Since the relative intensity profile of the COO⁻ symmetric stretch to the methyl asymmetric deformation was veritably featureless (Figure 4-31*c*), the brighter contours in the β -sheet/ α -helix FTIR image indicate that a predominant amount of amorphous amyloid with some contribution from the α -helical A β -

associated proteins/glial cells deposited at that location. Moreover, the maroon to purple contours of this β -sheet/ α -helix FTIR image appear to surround the amorphous amyloid. These maroon to purple contours most likely result from a greater proportion of α -helical A β -associated proteins/glial cells to that of amorphous amyloid. An immunostain specific to non-fibrillar A β -peptide, glial fibrillary acidic protein from reactive astrocytes (Siegal *et al.*, 1994), GAGs, *etc.*, would be required to substantiate the relative proportion of these diffuse plaque constituents.

Figure 4-31. Diffuse amyloid deposition detected in the molecule of hippocampus AD3 where staining was inconclusive. (a) Photomicrographs of the stained (left) and unstained (right) tissue examined. Step size 10 μm . (b) FTIR image created using the relative intensity of β -sheet (1630 cm^{-1}) to α -helix (1656 cm^{-1}). (c) FTIR image created using the relative intensity of $\nu_s(\text{COO}^-)$ (1400 cm^{-1}) to $\delta_{\text{as}}(\text{CH}_3)$ (1455 cm^{-1}).

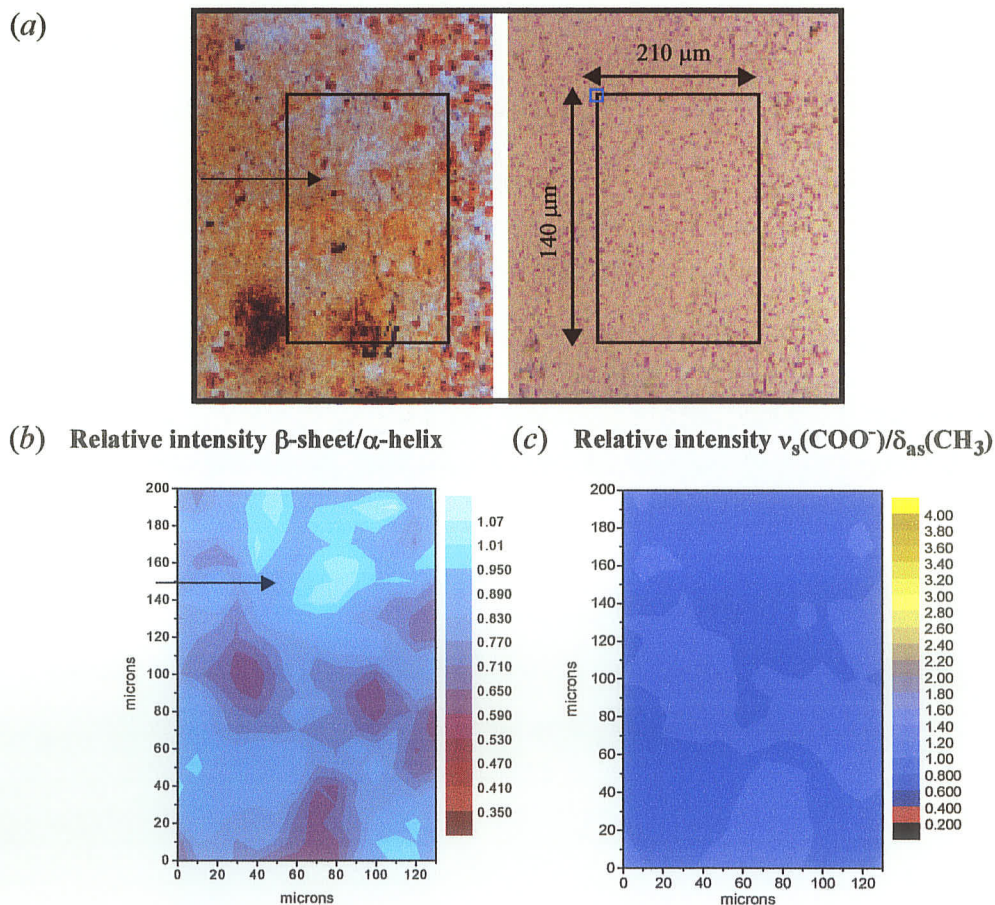
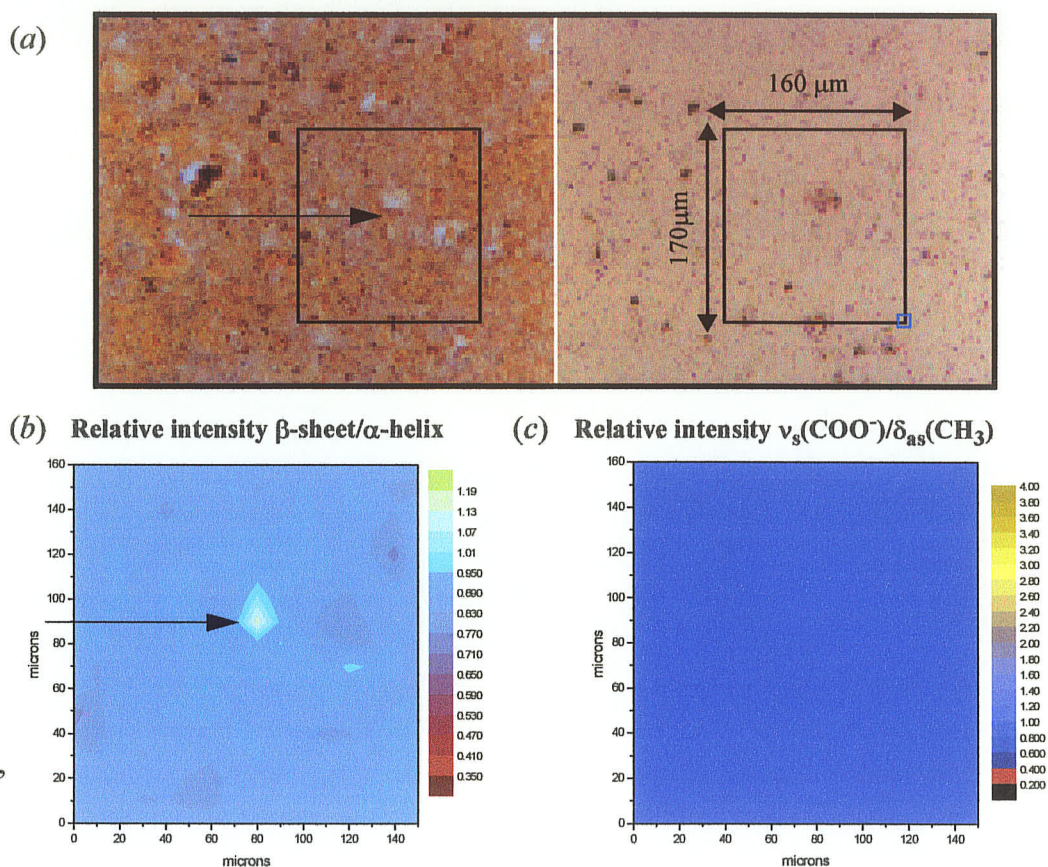


Figure 4-32. Diffuse amyloid deposition detected in CA4 of hippocampus AD3 where staining was inconclusive. (a) Photomicrographs of the stained (left) and unstained (right) tissue. Stepsize 10 μm . (b) FTIR image of the relative intensity of β -sheet (1630 cm^{-1}) to α -helix (1656 cm^{-1}). (c) FTIR image of the relative intensity of $\nu_s(\text{COO}^-)$ (1400 cm^{-1}) to $\delta_{\text{as}}(\text{CH}_3)$ (1455 cm^{-1}).



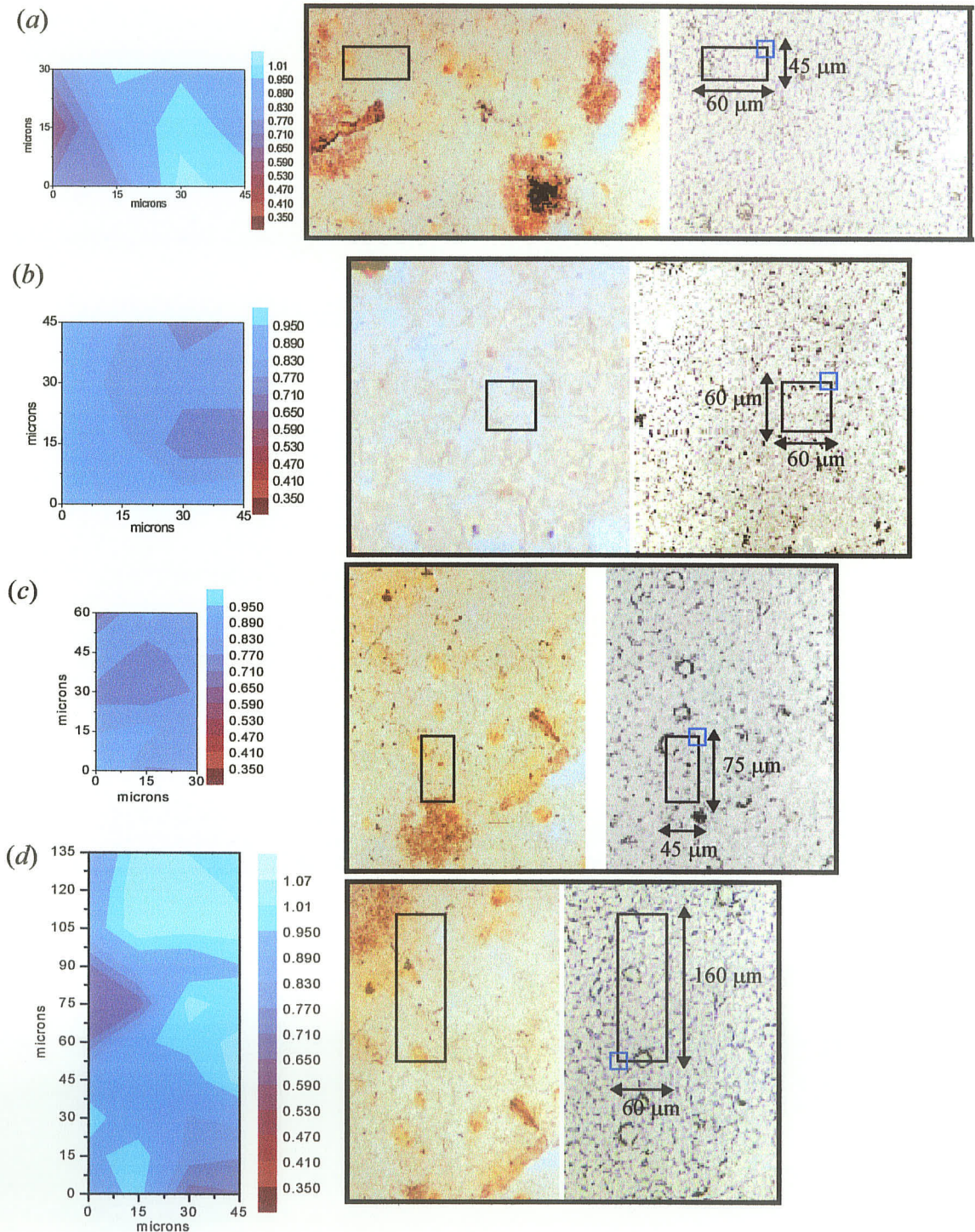
Similar results were obtained upon further spectral examination in the CA4 field of AD3. Shown above in Figure 4-32, is a map acquired in the upper right-hand side of the CA4 field (see Figure 4-5), in an attempt to localize the plaques that were present in the serial stained tissue section. Once again, the FTIR image prepared from the $\nu_s(\text{COO}^-)$ to the $\delta_{\text{as}}(\text{CH}_3)$ relative intensity was featureless indicating the absence of fibrillar amyloid, in agreement with the absence of dark staining in the tissue area examined. However, the majority of the FTIR image created from the relative intensities in the amide I band profile was a contour color reflective of a β -sheet/ α -helix ratio of greater than 0.890 (Figure 4-32b). Located in the centre of this image, a brightly colored collection of contours (ratio =

0.95 to >1.19) was observed, which corresponds to background staining below a hole in the photomicrograph of the stained tissue (arrows, in Figure 4-32). In this hippocampus, an unusual amount of background staining was noticed, especially in the CA4 field. A fibrillar-like matter appeared throughout much of this region, but it has yet to be identified and requires further investigation with more specific staining techniques.

In contrast to the tissue sections examined from AD2 and AD3, the staining of the MirrIR section from hippocampus AD1 exhibited far less background staining (Figure 4-33). This improved the interpretation of the FTIR imaging in determining whether diffuse amyloid was present in the vicinity of plaque formation. The tissue area examined (CA1 field) was infested with numerous immature and neuritic plaques (recall serial stain on glass, Figure 4-4). Unfortunately, the area maps collected were typically 15-100 μm from even the periphery of a plaque. Nevertheless, the maps were useful for investigating the possibility of diffuse amyloid deposition between plaques, in concentrations too low to be detected by Bielschowsky staining (Figure 4-33).

Shown in Figure 4-33 are several of these CA1 spectral maps and their corresponding FTIR images. The relative intensity of the amide I component band assigned to β -sheet (1635 cm^{-1}) to that of α -helical proteins (1656 cm^{-1}) was calculated for each spectrum in the area maps and used in the 2D contour analysis. A higher frequency for the β -sheet component band was chosen on the premise that if amyloid was there, it would be quite diffuse, resulting in very little of the inter-strand hydrogen bonding that was observed to lower the frequency of the β -sheet/aggregate band. As shown in Figure 4-33, two of the spectral maps acquired just beyond the periphery of a plaque (*a*, and *d*) did display an increase in the contribution of β -sheet to their amide I vibration over that of α -helix as revealed by the brighter contours (ratio of > 1.07) in their respective FTIR images. The third map (Figure 4-33*c*) was also just beyond the periphery of a plaque, but less of a β -sheet contribution was observed in the FTIR image (ratio = 0.77-0.95). The FTIR image of the map in Figure 4-33*b*, which was not in proximity to plaque formation, exhibited a diminished β -sheet contribution to that of α -helix, yet the predominant contour was within the range of a diffuse amyloid deposition (ratio = 0.77-0.95).

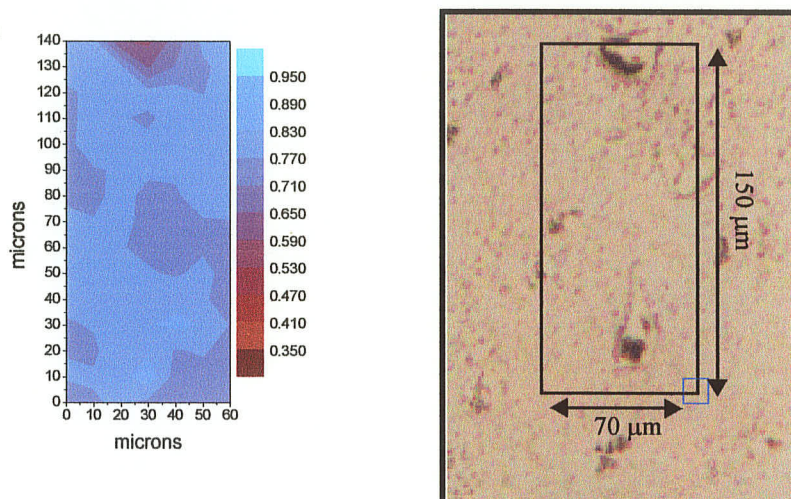
Figure 4-33. FTIR imaging of small spectral maps acquired in the CA1 field of AD1 that shows diffuse amyloid deposition that went unrecognized by the staining technique. Stepsize was 15 μm . The relative intensity of β -sheet (1635 cm^{-1}) to α -helix (1656 cm^{-1}) was used in the 2D contour analysis.



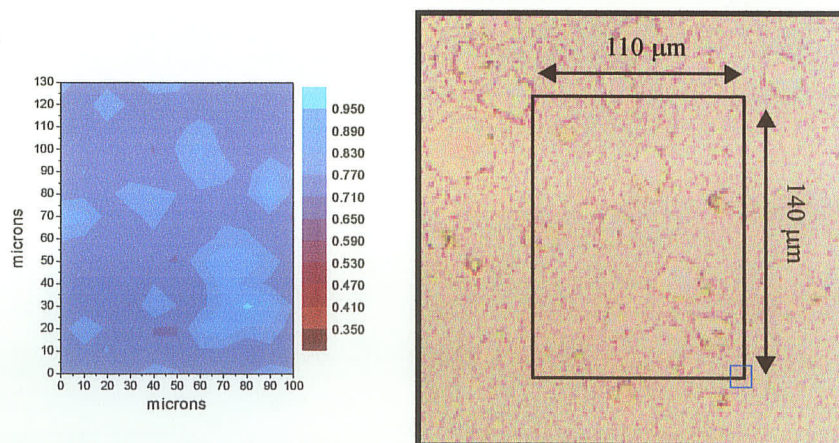
For full interpretation of these results on the AD hippocampal tissue, however, a similar 2D contour analysis had to be carried out on the spectral data acquired on control tissue, CON1 and CON2, in order to delineate a lower limit for the ratio that is indicative of diffuse deposition of a β -sheet protein. Upon 2D contour analysis, the spectral maps in the control gray matter were observed to have a greater contribution from α -helical proteins than from β -sheet (Figures 4-34 and 4-35).

Figure 4-34. FTIR imaging of control hippocampus (CON2) in the CA1 field to delineate the contribution of β -sheet protein to a normal aging hippocampus. Stepsize, 10 μm . FTIR images created from the relative intensity of β -sheet (1635 cm^{-1}) to α -helix (1656 cm^{-1}). Blue contours show the positions of the neurons where the predominant contribution from β -sheet proteins appears to occur.

(a) CA4 field

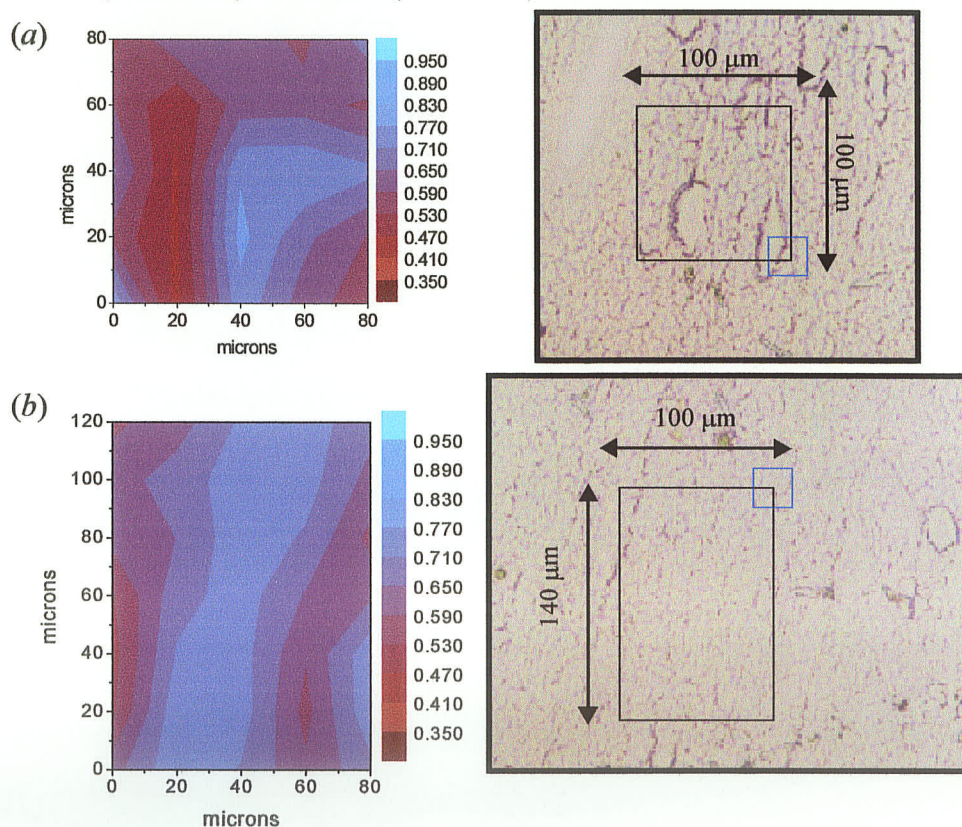


(b) CA1 field



Representative FTIR images from the CA1 and CA4 fields of hippocampus CON2 are shown in Figure 4-34. These spectral maps were previously analyzed for differentiation of protein and lipid content where the lipofuscin content of the neurons was found to contribute substantially to the higher protein content inside the neuron as opposed to the surrounding neuropil (recall section 4.3.1). In the amide I band profile FTIR images of control gray matter from hippocampus CON2, it was observed that the lighter blue contours (β -sheet to α -helix ratio = 0.830 to 0.950) fell on the positions of the neurons in the map, while darker blue to purple contours (ratio = 0.650-0.710) filled the neuropil (Figure 4-34).

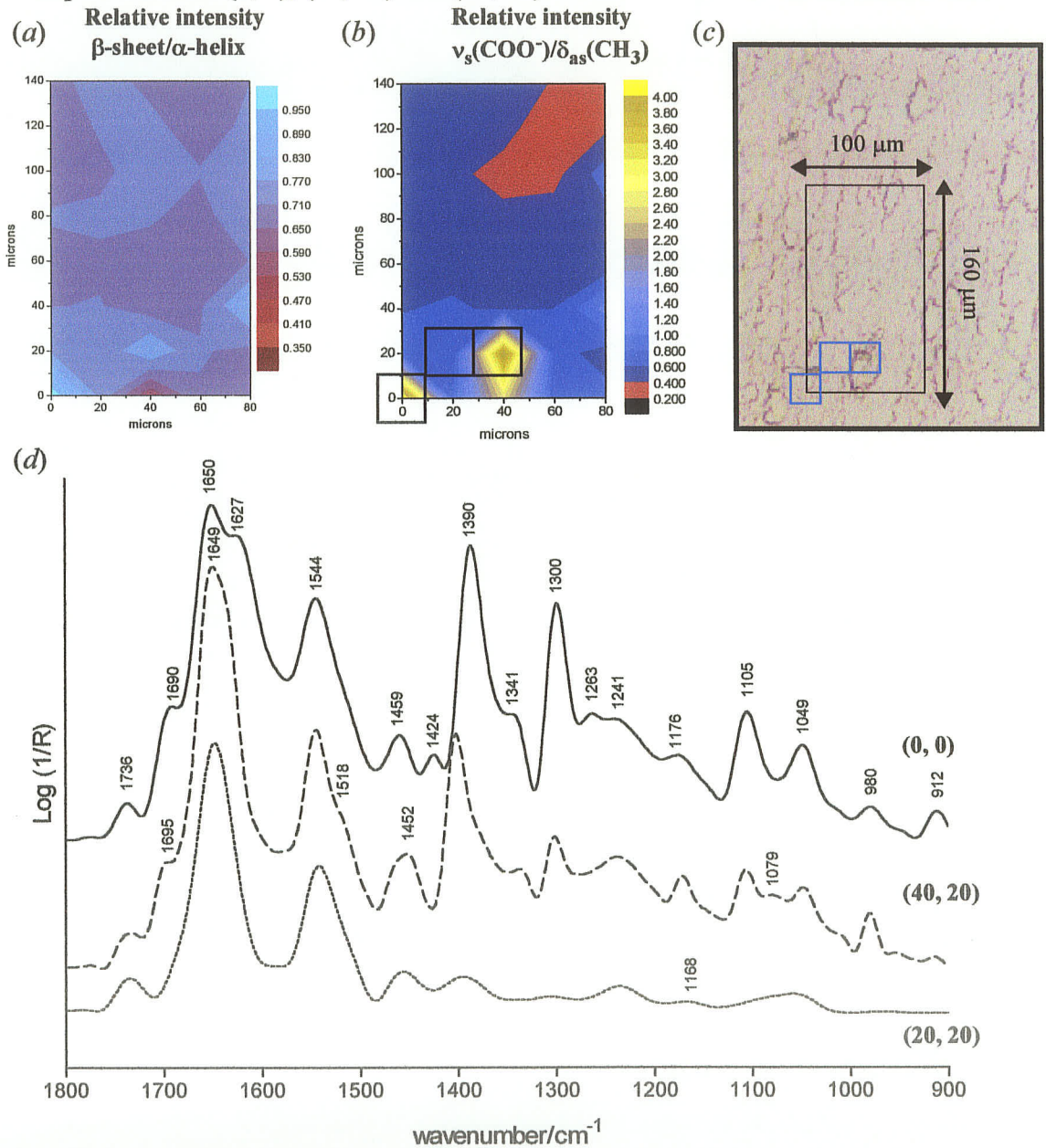
Figure 4-35. FTIR imaging of control hippocampus (CON1) in the CA1 field to delineate the contribution of β -sheet protein to a normal aging hippocampus. Spatial resolution, 20 μm . FTIR images created by calculation of the relative intensity of β -sheet (1635 cm^{-1}) to α -helix (1656 cm^{-1}).



In contrast, FTIR images prepared from spectral maps taken in the CA1 field of hippocampus CON1 (Figure 4-35) exhibited red to purple contours (ratio = 0.470-0.590) on the positions of the neurons and purple to dark blue contours (ratio = 0.530-0.710) in the surrounding neuropil. The relative intensity of β -sheet to α -helix in the CON2 hippocampus may have been due to the lipofuscin deposition inside the perikaryon. Regardless, the combined range for the relative intensity of β -sheet to α -helix in the neuropil in both of these control tissues was from 0.530 to 0.710. This result suggests that the lower limit for the β -sheet to α -helix ratio, indicative of a diffuse deposition of a β -sheet protein, is greater than 0.710. Since the FTIR images of AD1 and AD3 presented with a majority of the tissue area examined having a β -sheet to α -helix ratio of greater than 0.830, diffuse deposition of A β peptide between plaques was likely, yet low enough in concentration to escape histochemical detection.

Only two of the seven spectral maps acquired on the CON1 tissue section were shown for simplicity since spectra from one map in the control CA1 field were very similar to the spectra from another, the primary difference being whether the aperture was focused on a neuron or on the neuropil. However, one map was an exception in which spectra similar to the anomalous amyloid spectral signature (section 4.3.3) were obtained when the aperture was focused on the neuron in the lower portion of the map (Figure 4-36). Therefore, aside from preparing an FTIR image from the relative intensity of the two amide I component bands, an FTIR image was also prepared by calculating the relative intensity of the COO⁻ symmetric stretch (1400 cm⁻¹) to the CH₃ asymmetric deformation (1455 cm⁻¹). The neuron located at coordinates (40, 20) in the spectral map and an unidentified feature at (0, 0) correspond to the bright contours in the $v_s(\text{COO}^-)/\delta_{as}(\text{CH}_3)$ relative intensity image (Figure 4-36, top middle). The respective spectra obtained at these locations along with another spectrum at an adjacent location (20, 20) to them both are presented at the bottom of Figure 4-36.

Figure 4-36. Abnormal neuron revealed by FTIR imaging in the CA1 field of CON1. (a) β -sheet/ α -helix FTIR image, (b) $\nu_s(\text{COO}^-)/\delta_{\text{as}}(\text{CH}_3)$ FTIR image (c) Photomicrograph of the unstained tissue, and (d) FTIR spectra corresponding to the map coordinates (0, 0), (40, 20) and (20, 20) outlined in blue on the unstained tissue.



Although the spectra at (0, 0) and (40, 20) were similar to the amyloid signature spectrum discussed previously, there were some noticeable differences (Figure 4-36d). The COO⁻ absorption (1390 cm⁻¹), amide III band (1241-1341 cm⁻¹), carbohydrate absorptions (1049, 1105 and 1176 cm⁻¹) and the phosphomonoester stretch (980 cm⁻¹) were enhanced over that seen previously, while the band at 1650 cm⁻¹ remained as the amide I maximum. Moreover, the amide I band contour at coordinates (40, 20) displayed only two resolved bands, the amide I maximum at 1649 cm⁻¹ and a component band 45 cm⁻¹ higher in frequency (1695 cm⁻¹). In contrast, the spectrum from coordinates (0,0) had the usual antiparallel β -sheet absorption splitting at 1625 and 1690 cm⁻¹. The absorption at 1649 cm⁻¹ could be an unusually high in frequency LFC band of an antiparallel β -sheet structure, while the feature at 1695 cm⁻¹ is the HFC band. Unfortunately the identity of these structures can only be speculated since the stain of CON1 on the MirrIR slide was unsuccessful. Identified by their spectral similarity to fibrillar amyloid, the neuron in question could have been a non-Alzheimer's type tangle and the unidentified feature at (0, 0) could have been a "ghost" NFT (*i.e.*, neuronal membrane gone), or still yet another protein aggregate could have been involved.

4.4 CONCLUSIONS

In summary, synchrotron FTIR microspectroscopy was used successfully to localize and further characterize the diffuse and neuritic plaques of AD-related histopathology. Moreover, FTIR imaging of AD with a spatial resolution of 6-20 μm was achieved and enabled the localization of plaques and diffuse amyloid deposition in the tissue areas examined even before the spectra were thoroughly examined. In this manner, the 2D contour analysis allowed for quick preliminary analysis of the spectral data at the beamline so that the next spectral area could be chosen without having to spend beamtime evaluating hundreds of spectra between each map collection. The relative peak height intensity most successful at distinguishing diffuse from fibrillar amyloid was found to be the ratio of the carboxylate symmetric stretch at 1395-1400 cm⁻¹ to the methyl asymmetric deformation at 1455-1457 cm⁻¹. A concomitant increase in this relative intensity and that of the ratio of antiparallel β -sheets (LFC at 1619-1625 cm⁻¹) to α -helices (1652-1656 cm⁻¹) was indicative of fibrillar amyloid deposition in the tissue. From analysis of the unique spectral features

of fibrillar amyloid *in situ*, it was concluded that the aggregated peptides participate in stronger intermolecular hydrogen bonding than that found in a previous study (Choo *et al.*, 1996). Instead, the fibrils *in situ* were more structurally similar to fibrils examined by FTIR that were prepared *in vitro* (Fraser *et al.*, 1991). Other interesting observations were the spectroscopically detected alterations in glycosylation and phosphorylation state of the tissue as spectra were taken from areas containing diffuse amyloid compared to those containing fibrillar amyloid. With respect to the concept that diffuse A β -peptide deposition could occur between plaques, the data presented in the current study is supportive of that hypothesis. However, additional AD and control tissue sections should be evaluated, inclusive of statistical analysis of the cumulative results before this hypothesis can truly be validated. Finally, although the spectrum of an Alzheimer's type NFT *in situ* was not procured, the spectrum of the anomalous neuron in the CA1 field of a control hippocampus may have been a non-AD associated NFT, or yet another type of protein aggregate associated with neuronal dysfunction.

Future research in the application of FTIR imaging of Alzheimer's and control hippocampus could evolve in a variety of ways. For instance, utilization of a multichannel detector (focal plane array detector) and a microscope has been shown to generate FTIR images with a spatial resolution of less than 3 μm^2 (Kidder *et al.*, 1997). Therefore, an image of the entire tissue section would be possible in one experiment with better spatial resolution. However, it should be noted that nominal spectral resolution using focal plane array detection is typically 16 cm^{-1} , which would result in some loss of information regarding the component bands in the amide I band profile. With reference to the current study, the implementation of immunostaining specifically for hyperphosphorylated tau and β -amyloid would be of particular value. The Bielschowsky method is rather temperamental, such that the degree of background staining can vary along with the intensity of stained plaques and tangles. Finally, improvements in synchrotron FTIR microspectroscopy will coincide with improved stability in storage rings, better beamline design and further advances in instrumentation.

4.5 REFERENCES

- Beyreuther, K., Masters, C.L. (1996) Tangle disentanglement, *Nature*, **383**; 476-477.
- Blake, C., Serpell, L. (1996) Synchrotron x-ray studies that the core of the transthyretin amyloid fibril is a continuous β -sheet. *Structure*, **4**: 989-998.
- Bobinski, M., Weigel, J., Tarnawski, M., Bobinski, M., de Leon, M.J., Reisberg, B., Miller, D.C., Wisniewski, H.M. (1998) Duration of neurofibrillary changes in the hippocampal pyramidal neurons, *Brain Res.*, **799**; 156-158.
- Brandon, C., Tooze, J. (1999) Introduction to Protein Structure, 2nd edition, Garland Publishing, Inc., New York, pp. 288-289.
- Bromberg, P.S., Gough, K.M., Ogg, M., Hein, J., Del Bigio, M.R., Julian, R. (1999a) FT-IR spectromicroscopic investigation of structural changes in the hippocampus associated with Alzheimer's Disease. Abstract and poster presentation, *82nd CSC Conference and Exhibition*, June 1-4, Toronto, Ontario, Canada.
- Bromberg, P.S., Gough, K.M., Ogg, M., Del Bigio, M.R., Julian, R. (1999b) Synchrotron FTIR microspectroscopy of Alzheimer's diseased brain tissue at the SRC beamline. Oral presentation in Accelerator-based Sources of Infrared and Spectroscopic Applications, *SPIE's 44th Annual Meeting and Exhibition*, July 20, Denver, Colorado, USA.
- Bromberg, P.S., Gough, K.M., Ogg, M., Del Bigio, M.R., Julian, R. (1999c) "Synchrotron FTIR microspectroscopy of Alzheimer's diseased brain tissue at the SRC beamline", in Accelerator-based Sources of Infrared and Spectroscopic Applications, G.L. Carr and P. Dumas (editors), *Proceedings of SPIE*, **3775**: 118-126.
- Choo, L.P., Wetzel, D.L., Halliday, W.C., Jackson, M., LeVine, S.M., Mantsch, H.H. (1996) In situ characterization of β -amyloid in Alzheimer's diseased tissue by synchrotron Fourier transform infrared microscopy, *Biophysical Journal*, **71**; 1672-1679.
- Cleveland, D.W., Hwo, S.Y., Kirschner, M.W. (1977) Purification of tau, a microtubule-associated protein that induces the assembly of microtubules from purified tubulin, *J. Mol. Biol.*, **116**; 207-225; Physical and chemical properties of purified tau factor and the role of tau in microtubule assembly, *ibid*, **116**; 227-247.
- De Strooper, B., Konig, G. (1999) Alzheimer's disease: a firm base for drug development, *Nature*, **402**: 471-472.
- Dickson, T.C., King, C.E., McCormack, G.H., Vickers, J.C. (1999) Neurochemical diversity of dystrophic neurites in the early and late stages of Alzheimer's Disease, *Experimental Neurology*, **1**; 100-110.

- Esiri, M.M., Morris, J.H. (1997) The Neuropathology of Dementia, Cambridge University Press, U.K.
- Fraser, P.E., Nguyen, J.T., Surewitz, W.K., Kirshner, D.A. (1991) pH dependent structural transitions of Alzheimer's amyloid peptides, *Biophysical Journal*, **60**: 1190-1201.
- Furukawa, K., Barger, S.W., Blalock, E.M., Mattson, M.P. (1996) Activation of K⁺ channels and suppression of neuronal activity by secreted β -amyloid precursor protein. *Nature*, **379**: 74-78.
- Goedert, M., Jakes, R., Spillantini, M.G., Hasegawa, M., Smith, M.J., Crowther, R.A. (1996) Assembly of microtubule-associated protein tau into Alzheimer-like filaments induced by sulphated glycoaminoglycans, *Nature*, **383**: 550-553.
- Iqbal, K., Alonso, A.D., Gong, C.X., Khatoon, S., Pei, J.J., Wang, J.Z., Grundke Iqbal, I. (1998) Mechanisms of neurofibrillary degeneration and the formation of neurofibrillary tangles, *J. Neural Transmission Suppl.* **53**: 169-180.
- Jackson, M., Mantsch, H.H. (1995) The use and misuse of FTIR spectroscopy in the determination of protein structure, *Critical Reviews in Biochemistry and Molecular Biology*, **30(2)**, 95-120.
- Jackson, M., Mantsch, H.H. (1996) "FTIR spectroscopy in the clinical sciences", in Biomedical Applications of Spectroscopy, R.J.H. Clark and R.E. Hester (eds), John Wiley and Sons Ltd., pp.185-215.
- Jackson, M., Sowa, M.G., Mantsch, H.H. (1997) Infrared spectroscopy: a new frontier in medicine, *Biophysical Chemistry*, **68**: 109-125.
- John, V., Latimer, L.H., Tung, J.S., Dappen, M.S.(1997) "Alzheimer's disease: recent advances on the amyloid hypothesis", in Annual Reports in Medicinal Chemistry, Robertson (editor), Academic Press, pp.11-20.
- Kidd, M.(1963) Paired helical filaments in electron microscopy of Alzheimer's disease, *Nature*, **197**; 192-193.
- Kidd, M. (1964) Alzheimer's disease-an electron microscopical study, *Brain*, **87**; 307-320.
- Kidder, L.H., Kalasinsky, V.F., Luke, J.L., Levin, I.W., Lewis, E.N. (1997) Visualization of silicone gel in human breast tissue using new infrared imaging spectroscopy, *Nat. Med. (N.Y.)*, **3**: 235-237.
- Kozlowski, MR., Spanoyannis, A., Manly, SP., Fidel, S.A., Neve, R.V. (1992) The neurotoxic carboxy-terminal fragment of Alzheimer amyloid precursor binds specifically to neuronal cell surface molecule: pH dependence of the neurotoxicity and binding. *J. Neurosci.*, **12(5)**: 1679-1687.

- Lambert, J.B., Shurvell, H.F., Lightner, D., R.G. Cooks (1987) Introduction to Organic Spectroscopy, Macmillan Publishing Company, New York, pp. 175.
- Mattson, M.P., Furukawa, K.(1997) Short precursor shortens memory, *Nature*, **387**; 457-458.
- Maury, C.P.J. (1995) Biology of disease. Molecular pathogenesis of β -amyloidosis in Alzheimer's disease and other cerebral amyloidoses, *Lab. Invest.*, **72**: 4-16.
- Nalbantoglu, J. Tirado-Santiago, G, Lahsaini, A, Poirier, J., Goncalves, O., Verge, G., Momoli, F., Welner, S.A., Massicotte, G., Julien, J.P. Shapiro, M.L. (1997) Impaired learning and LTP in mice expressing the carboxy terminus of the Alzheimer precursor protein. *Nature*, **387**: 500-505
- Sasaki, N, Toki, S, Chowei, H., Saito, T., Nakano, N., Hayashi, Y., Takeuchi, M., Makita, Z. (2001) Immunohistochemical distribution of the receptor for advanced glycation end products in neurons and astrocytes in Alzheimer's Disease. *Brain Res.*, **888**: 256-262.
- Siegel, G.J., Agranoff, B.W., Albers, R.W., Molinoff, P.B.(1994) Basic Neurochemistry, 5th edition, Raven Press, New York, pp. 550-551, 913-933.
- Standen, C.L., Brownlee, J., Grierson, A.J., Kesavapany, S., Lau, K.F., McLoughlin, D.M., Miller, C.C. (2001) Phosphorylation of thr(668) in cytoplasmic domain of the Alzheimer's disease amyloid precursor protein by stress-activated protein kinase 1b (Jun N-terminal kinase-3). *J. Neurochem.*, **76**(1): 316-320.
- Ulrich, J. (1993) "Histochemistry and immunohistochemistry of Alzheimer's disease", in Progress in Histochemistry and Cytochemistry, volume 27, Stuttgart, New York.
- van Leeuwen, F.W., de Kleijn, D.P.V., van den Hurk, H.H., Neubauer, A., Sonnemans, M.A.F., Sluijs, J.A., Koycu, S., Ramdjielal, R.D.J., Saheli, A., Martens, G.J.M., Grosveld, F.G., Burbach, J.P.H., Hol, E.M. (1998) Frameshift mutants of β -amyloid precursor protein and ubiquitin-B in Alzheimer's and Down's patients, *Science*, **279**; 242-247.
- Vassar, R., Bennett, B., Babu-Khan, S., Khan, S., Mendiaz, E.A., Denis, P., Teplow, D.B., Ross, S., Amarante, P., Loeloff, R., Luo, Y., Fisher, S., Fuller, J., Edenson, S., Lile, J., Jarosinski, M.A., Biere, A.L., Curran, E., Burgess, T. Louis, J.-C., Collins, F., Treanor, J., Rogers, G., Citron, M. (1999) β -secretase cleavage of Alzheimer's amyloid precursor protein by the transmembrane aspartic protease BACE, *Science*, **286**: 735-741.
- Wiengarten, M.D., Lockwood, A.H., Hwo, S.Y., Kirschner, M.W. (1975) A protein factor essential for microtubule assembly, *Proc. Natl. Acad. Sci. USA*, **72**; 1858-1862.

Wong, P.T.T., Cadrin, M., French, S.W. (1991) Distinctive infrared spectral features in liver tumor tissue of mice: evidence of structural modifications at the molecular level, *Experimental and Molecular Pathology*, **55**, 269-284.

Yan, SD, Chen, X., Fu, J., Chen, M., Zhu, H., Roher, A., Slattery, T., Zhao, L., Nagashima, M., Morser, J., Migheli, A., Nawroth, P. Stern, D., Schmidt, A.M. (1996) RAGE and amyloid- β peptide neurotoxicity in Alzheimer's Disease. *Nature*, **382**: 685-691.

5 CONCLUDING REMARKS

In summary, unique information was accessible on the three independent biological systems studied, using FTIR biospectroscopy in the mid-IR as a single analytical tool. In Chapter 2, the possible intermolecular interactions between MBP and two lipids simultaneously, was accessed using transmission FTIR to determine the conformational dynamics of each macromolecular component in the mixture. The relative proportion of an electrostatic to an intercalative component to the overall MBP-liposome binding interaction was also accessible. In Chapter 3, non-subjective discrimination between diseased and healthy heart tissue was achieved by combining FTIR-ATR macro-sampling with multivariate statistical analysis, even prior to spectral interpretation. The biochemical change associated with the tissue pathology was determined from the spectral difference between class average spectra. In Chapter 4, the diverse quaternary structure of peptide aggregates *in situ* (fibrillar versus amorphous plaque formation) was determined using synchrotron FTIR microspectroscopy. Moreover, synchrotron FTIR microspectroscopy was sensitive enough to detect minute differences in the biochemical composition of seemingly unaffected AD gray matter and control gray matter of the hippocampus. The versatility of FTIR biospectroscopy originates from the IR phenomenon itself; a biophysical or biochemical change is detectable due to the sensitivity of vibrations to their microenvironment and the concentration dependence in the spectrum, respectively. The larger task is to deconvolute the massive amounts of spectral information into something meaningful about the biological system.

In all three projects, semi-quantitative information on the biological systems was accessible without curve-fitting any of the spectral data. The assumptions involved in curve fitting the spectral data in preparations *in vitro* have already been discussed in Chapter 1. Such assumptions also hold for spectral data acquired on tissue samples, but are magnified for two primary reasons: the exact biochemical composition of the tissue is unknown and intermolecular interactions change spectra. Tissue spectra can be “considered” the linear combination of the spectra belonging to each macromolecular constituent, but since the exact composition of the tissue is unknown, one cannot overlook that minor absorptions of one constituent can contribute to the strong overlapping absorptions of another. Moreover,

intermolecular interactions *in situ* can alter the intensity, bandwidth and frequency of absorption bands due to each macromolecular constituent. For example, based on the phosphate absorptions of phosphoamino acid thin films prepared *in situ* in Chapter 4, the assignment of the phosphomonoester asymmetric stretch in the dentate neurons of sample AD2 to phosphotyrosine, was interesting but tentative. The molar absorptivity (affecting band intensity) and bond connectivity and/or local microenvironments (affecting frequency and band shape) of phosphoamino acids *in vitro* and *in situ* may be different. In the end, making assumptions on the biochemical composition or overlooking the impact of intermolecular interactions and attempting to curve-fit tissue spectra, oversimplifies the deconvolution of spectral information.

With respect to the sensitivity of FTIR microspectroscopic mapping of tissue, few single techniques are available that can simultaneously extract biochemical information and the relative distribution of the tissue biochemistry on the microscopic scale *in situ*. This makes external validation of the FTIR results very difficult. One method for external validation may be to histochemically stain the tissue section for a number of tissue constituents simultaneously (*i.e.*, double staining). However, IR substrates (salt crystals or reflective slides) are not insusceptible to degradation by different histochemical techniques. Moreover, not all histochemical methods are compatible with one another and cannot be carried out on the same tissue section. Meanwhile, comparing the FTIR results to a stained serial section can lead to gross errors in external validation since tissue morphology can change abruptly within micron distances. Future progress in external validation of FTIR microspectroscopic mapping of tissue is definitely required. Secondly, the generation of FTIR images from the microspectroscopic mapping data, based on the histochemistry or what is known about the tissue histology, is subjective. As discussed in Chapter 1, unsupervised hierarchal clustering of FTIR microspectroscopic mapping data acquired by FPA detection is one recent method to combat this level of subjectivity. Perhaps hierarchal clustering of synchrotron FTIR microspectroscopic mapping data would also work, provided that enough spectra are contained within one contiguous spectral map for the unsupervised method to differentiate between similar and dissimilar spectra.

As for the future progress of FTIR biospectroscopy as a whole, with the advent of tissue microspectroscopy, the differentiation of tissues using gross macro-sampling methods has been receiving comparatively less attention in medical diagnostics. This is not terribly surprising since FTIR micro-sampling techniques require far less sample, and thus have the potential to make FTIR biodiagnostics less invasive. Moreover, FTIR microspectroscopy information on tissue biochemistry is site-specific and thus a more powerful tool than FTIR macro-sampling for associating the biochemical change with the tissue histopathology. Future progress in FTIR microspectroscopy of tissues will rest in improving spatial resolution and the approach to global data analysis. Finally, FTIR studies *in vitro* have become more commonplace in biophysics research laboratories over the last decade. Numerous biophysical research laboratories are using FTIR to examine macromolecular interactions and dynamics by a variety of novel techniques (*i.e.*, new isotopic substitutions, rapid-mixing sample cells for kinetic studies, *etc.*) to supplement their research by other solution spectroscopies.

Dedicated to my little "River" for taking the initiative to recycle old copies!

